DEPARTAMENTO DE ASTROFISICA

Universidad de La Laguna

# TRACING AND ISOLATING MAJOR MERGERS TRIGGERED IN GALAXY EVOLUTION: SPATIALLY RESOLVED PROPERTIES ALONG THE MERGER SEQUENCE

Thesis submitted by

Don Jorge Karolt Barrera Ballesteros

as a requirement for the degree of

Doctor of Physical Science


INSTITUTO Đ ASTROFISICA Đ CANARIAS

La Laguna, Mayo de 2015

Examination date: July 2015
Thesis supervisors: Begoña García Lorenzo and Jesús Falcón Barroso


ISBN: xx-xxx-xxxx-x
Depósito legal: xx-xxxx/xxxx

Some of the material included in this document has been already published in *Astronomy & Astrophysics*.

**Summary/Abstract**

Interactions and mergers have proved to be fundamental mechanisms for galaxy evolution. Galaxy-galaxy encounters could induce inflows of material as well as the enhancement of star formation. They could also lead to outflows by (stellar or active galactic nuclear) feedback. Despite the efforts to characterize and to understand the evolution of the galactic components in the course of the merging event, few studies have focused on the change of the spatially resolved properties of interacting galaxies. Spatially resolved observations are necessary for a comprehensive understanding of interacting and merging galaxies since the properties of their components could change drastically across the whole galaxy. To unveil how these components unfold as the interaction evolves, it is required to map these galactic properties in a sample of merging galaxies covering a wide range of the interaction parameter space (covering for example interaction stages stellar masses). To quantify the impact of mergers and to disentangle those processes induced by secular evolution from those related to mergers, it is also required to have a homogeneous sample of non-interacting galaxies (i.e., observed, reduced and analyzed using the same instrument, pipeline, and methodologies as for the interacting sample). The CALIFA (Calar Alto Legacy Integral Field Area) survey is the first integral field survey in the nearby universe that satisfies these requirements. This survey provides data cubes for $\sim$ 600 galaxies as a representative sample of the galactic population in the nearby Universe. It allows us to select a sample of interacting galaxies at different interaction stages and a well-match control sample, both sets of datacubes observed and reduced homogeneously.

In this thesis work we develop a common methodology to characterize and to analyze the spatially resolved information extracted from the CALIFA datacubes. In particular, we provide a method to measure the kinematic properties of velocity fields with no assumptions about the internal motions of galaxies. We also provide an estimate of the star formation and oxygen abundance of these two samples. Our studies are aimed at probing and to quantifying the impact of mergers on galaxy evolution. This is one of the first works aimed at statistically quantifying the impact of interactions and mergers in spatially resolved properties of galaxies. As a first step, we select a sample of 103 interacting galaxies at different stages of the interaction - from close pairs to merger remnants - and a sample of 80 non-interacting galaxies as control sample. We present our main three results as follows:

Using the methodology developed we determine the global major axis kinematic orientation (kinematic PA), the comparison between the receding and approaching kinematic sides (internal kinematic misalignment) and the radial deviations of the kinematic PA from a straight line ($\delta \mathrm{PA}_{\mathrm{kin}}$) for the stellar and ionized gas velocity fields of the 80 non-interacting galaxies. When we compare the global kinematic with the morphological major axis orientations, we find that morpho-kinematic position angle differences are smaller than 22 degrees in 90% of the sample for both stellar and ionised gas components. Moreover, internal kinematic misalignments are generally smaller than 16 degrees. The global kinematic orientation for the stellar and the ionized gas components present a tight relation, which are consistent with circular-flow pattern motions (90% of the sample has differences smaller than 16 degrees). This relation also holds, generally in barred galaxies across the bar and galaxy disc scales. Our findings suggest that even in the presence of strong bars, both the stellar and the gaseous components tend to globally follow the gravitational potential of the disk.

Results for non-interacting galaxies can be used to assess the degree of external distortions in interacting galaxies. Comparing these results with the sample of 103 interacting galaxies, we find that around half of the interacting objects show morpho-kinematic PA misalignments that cannot be found in the control sample. In particular, we observe those misalignments mainly in galaxies with evident signatures of interaction. On the other hand, the level of alignment between the approaching and receding sides for both samples is similar, with most of the galaxies displaying

internal misalignments comparable with those observed in the control sample. Radial deviations of the kinematic PA orientation from a straight line in the stellar component measured by $\delta PA_{kin}$ are large for both samples. However, for a large fraction of interacting galaxies the ionised gas $\delta PA_{kin}$ is larger than the typical values derived from isolated galaxies (48%), indicating that this parameter is a good indicator to trace the impact of interaction and mergers in the internal motions of galaxies. By comparing the stellar and ionized gas kinematic PA, we find that 42% (28/66) of the interacting galaxies have misalignments larger than 16°, compared to 10% from the control sample. Our results show the impact of interactions on the motion of stellar and ionized gas as well as the wide variety of their spatially resolved kinematic distributions. This study also provides a local universe benchmark for kinematic studies in merging galaxies at high redshift.

Finally, from the CALIFA datacubes we extract the H$\alpha$ equivalent width and the emission line flux maps, for several ions, of these two samples. H$\alpha$ equivalent width is a proxy for the specific star formation rate (sSFR, which provides an indication of the current star-formation activity compared to previous activity) while the 2D emission line flux distributions provide information about the gas-phase metallicity particularly the oxygen abundance. We confirm the moderate enhancement ($\times$ 2-3 times) of sSFR for interacting galaxies in central regions as reported by previous studies; however, this parameter is comparable to the control sample when observed over extended regions. We find that control and interacting star forming galaxies share similar oxygen abundances in their central regions, when normalized to their stellar masses. Oxygen abundances of these interacting galaxies seem to decrease with respect to the control objects at large aperture sizes in units of effective radius. Although the enhancement in central star formation and possible lower metallicities for interacting galaxies have been attributed to tidally induced inflows, our results suggest that other processes such as stellar feedback can contribute to the metal enrichment in interacting galaxies.

## Resumen

Las interacciones y fusiones galácticas son procesos fundamentales en la formación y evolución de galaxias. Los encuentros entre galaxias pueden generar flujos de material hacia el centro de las galaxias así como aumentar la formación estelar en estas. Los encuentros entre galaxias pueden dar lugar a un aumento de la formación estelar y a flujos de material hacia el centro de las galaxias, que pueden incluso inducir a actividad nuclear. A pesar de los esfuerzos para poder caracterizar y entender la evolución de las galaxias a medida que la fusión progresa, sólo algunos trabajos se concentran en estudiar las propiedades espacialmente resueltas de los objetos en interacción. La motivación para realizar estudios espacialmente resueltos en galaxias interactivas está en que sus propiedades pueden cambiar abruptamente en distintas regiones como consecuencia de las perturbaciones inducidas en el proceso de interacción. Además de realizar este tipo de observaciones, es necesario contar además con una muestra de galaxias que cubran distintos parámetros de la fusión galáctica (por ejemplo, distintos estados de la interacción así como rango de masas estelares los suficientemente amplio). Para poder diferenciar los procesos causados por la interacción de aquellos producidos por procesos internos, se hace necesario contar con una muestra homogénea de galaxias aisladas (i.e., galaxias cuyas observaciones hayan sido hechas, reducidas y analizadas de la misma manera que la muestra de galaxias en interacción). El cartografiado CALIFA (por sus siglas en inglés *Calar Alto Legacy Integral Field Area Survey*) ha permitido abordar este tipo de estudios ya que presenta las características anteriormente citadas. Este cartografiado proporciona información espacial y espectral (cubos de datos) para una muestra de $\sim$ 600 galaxias, que son representativas de la población total de galaxias en el universo cercano. CALIFA proporciona un marco adecuado para abordar el estudio de una muestra estadísticamente significativa de galaxias en distintos estados de interacción, además de permitir la selección de una muestra homogénea de galaxias aisladas.

La principal motivación de este trabajo está en la exploración y cuantificación del impacto de las interacciones/fusiones en la evolución de galaxias.Dadas las peculiaridades de los objetos a estudiar, en este trabajo de tesis doctoral se ha desarrollado una metodología específica para caracterizar y analizar la información que se extrae de los cubos de datos generados por CALIFA. En particular, en esta tesis se se desarrolla un método para determinar los parámetros cinemáticos de un campo de velocidad sin tener que asumir ninguna propiedad intrínseca de las galaxias. Además, se estima la tasa de formación estelar y la abundancia de oxígeno para todas las galaxias observadas. Este trabajo representa uno de los primeros esfuerzos por cuantificar estadísticamente el impacto en las propiedades especialmente resueltas de galaxias en el universo cercano. La muestra de objetos en interacción cuenta con 103 galaxias, mientras que la muestra de galaxias aisladas la forman de 80 objetos. A continuación, se presentan los resultados mas importantes de este trabajo doctoral:

Usando la metodología específica desarrollada para este trabajo, se caracterizaron los mapas de velocidades de las estrellas y del gas ionizado de las 80 galaxias aisladas a través de la medida de varios parámetros: 1) Orientación fotométrica, orientación cinemática (ángulo de posición del eje mayor cinemático), distorsión cinemática interna (comparando el ángulo de posición promedio del eje mayor cinemático a ambos lados de la galaxia), y 3) las variaciones radiales del ángulo de posición cinemático a distintos distancias galactocentricas ($\delta \mathrm{PA}_{\mathrm{kin}}$). El desalineamiento entre el ángulo de posición fotométrico y cinemático es inferior a 22 grados para el 90% de las galaxias , tanto en la componente estelar como en la cinemática de gas ionizado. Los desalineamientos internos en ambas componentes suelen ser menores que 16 grados. Además de esto, se encontró que los ángulos de posición cinemático de la componente estelar y del gas ionizado se encuentran bastante acoplados; el 90% de las galaxias aisladas presentan desalineamientos menores a 16 grados. Estos resultados sugieren que ambas componentes siguen movimientosmovimientos compatibles con discos en rotación. Estos alineamientos también se observan en galaxias barradas, dentro y fuera de la barra, sugiriendo

que, incluso en galaxias barradas, ambas componentes tienden, globalmente, a seguir el potencial producido por el disco.

Los resultados obtenidos en galaxies aisladas se utilizan como patrón de referencia para determinar el grado de distorsión producido en la cinemática debido a la interacción. Se encontró que alrededor de la mitad de las galaxias en interacción presentan desalineamientos entre el ángulo de posición cinemático y morfológico mayores que aquellos observados en la muestra de galaxias aisladas. La mayoría de estos desalineamientos se encuentran localizados en objetos que pertenecen a un par de galaxias interactivas. No obstante, el nivel de alineamiento cinemático interno es similar entre las dos muestras. De hecho, la mayoría de las galaxias en ambas muestras analizadas (interactivas + aisladas) presentan ambos lados cinemáticos bien alineados. Al analizar la variación radial de los ángulos de posición, encontramos que los valores de $\delta\mathrm{PA}_{\mathrm{kin}}$ para la componente estelar son altos para ambas muestras. Sin embargo, para una porción significativa (48%) de galaxias en la muestra de interactivas, los valores de $\delta\mathrm{PA}_{\mathrm{kin}}$ del gas ionizado son mas altos que aquellos que se encuentran en la muestra de galaxias aisladas, indicando que este $\delta\mathrm{PA}_{\mathrm{kin}}$ puede ser usado como parámetro para rastrear el impacto de la interacción y posible fusion en galaxias. Al comparar los ángulos de posición entre la componente estelar y del gas ionizado, se encuentra que el 42% (28/66) de las galaxias en la muestra en interacción posee desalineamientos mayores que 16 grados, comparado con sólo el 10% de los objetos en la muestra de galaxias aisladas. Estos resultados muestran el impacto de las interacciones en la cinemática de las galaxias así como la gran variedad de mapas de velocidades que presentan las galaxias en interacción. Este estudio proporciona un marco de referencia para futuros trabajos centrados en la cinemática de galaxias en el Universo temprano.

Además de la cinemática, se ha estudiado el impacto del proceso de interacción en la formación estelar. Para ello, se obtuvo la distribución de intensidad de distintas líneas de emisión presentes en los espectros y los mapas de anchura equivalente a partir de la línea en emisión de H$\alpha$ así como los mapas de distintas líneas de emisión. Por un lado, la anchura equivalente de la línea en emisión de H$\alpha$ es un indicador directo de la tasa de formación estelar específica (sSFR por sus siglas en en inglés), proporcionando una estimación de la formación estelar actual respecto a la formación estelar pasada. Por otro lado, los mapas de los flujos de las líneas de emisión dan información de la metalicidad del gas, en particular de la abundancia del oxígeno. En este estudio se confirma que en la parte central de las galaxias en interacción hay un incremento (moderado) de la formación estelar (2-3 veces) en comparación con galaxias aisladas. Sin embargo, la formación estelar es similar en las dos muestras cuando se mide en aperturas más grandes. Además, se determinó que en ambas muestras la parte central de las galaxias con formación estelar contiene una abundancia similar de oxígeno. A pesar del incremento en la formación estelar en la parte central encontrado para las galaxias en interacción, el hecho de que las galaxias aisladas y las interactivas presenten metalicidades similares sugiere que otros procesos (e.g. retroalimentación estelar o actividad nuclear) deben estar jugando un papel relevante para dar cuenta de la similitud en las abundancias químicas.

# Index

Chapter 1

# Introduction

*Interactions and mergers have played a paramount role in our current understanding of galaxy evolution. Despite its importance, little is known on how galaxies evolve in the course of the merger event and how they compare with processes driven by internal properties alone. In most of the cases, our knowledge of the merger event relies in integrated observations of only one specific stage of the merger. In this chapter, we signal the importance of interactions and mergers as mechanisms for the evolution of galaxies in the Universe. We start by giving a historical overview on the realization of the gradual discovery interactions and mergers are key players in galaxy evolution. Then, we revised the most important parameters that affect the merger. We also include a brief review of the studies aimed at characterizing the spatially resolved kinematics of non-interacting galaxies as well as studies of velocity field in interacting and merging galaxies. Finally, we present the impact of mergers an galactic star formation and gas phase metallicity including integrated and spatially resolved studies.*

## 1.1 Peculiar galaxies: Discovery and scenarios

Almost ninety years ago, Hubble determined the existence of diffuse objects that did not belong to our Milky Way and were morphologically similar to it. He later showed that they are receding from us and that the universe is expanding. In the coming years, many other extra-galactic objects were observed and tagged as galaxies. They were classified according to their morphology in the so called Hubble's morphological sequence of extragalactic nebulae (Hubble 1936).

To the left side of this morphological sequence are located galaxies with round or elliptical shapes (see Fig. 1.1). These featureless objects were named by Hubble "Elliptical Nebulae" . To the right hand side, the sequence divides disk-like objects often with spiral arms into barred and "normal" galaxies. These disk galaxies share similar properties: their material is confined in a thin disk (with a vertical thickness of $\sim 10\%$ of their diameters) and their stars and gas rotate around the disk center almost in circular orbits. On the other hand, elliptical galaxies look from roundly to oval shape, regardless of the direction from they are observed. Unlike the disk galaxies, these objects have little no gas. In these galaxies, the stellar kinematics are dominated by random motions.

In 1961 Sandage published *The Hubble Atlas of Galaxies*, showing regular well behaved galaxies. At abouts the same time, Eggen et al. (1962) deduced that halo stars in the Milky Way must have formed from free-falling clouds in a very short time scale ($\sim 10^8$ yr), while the stellar disk has

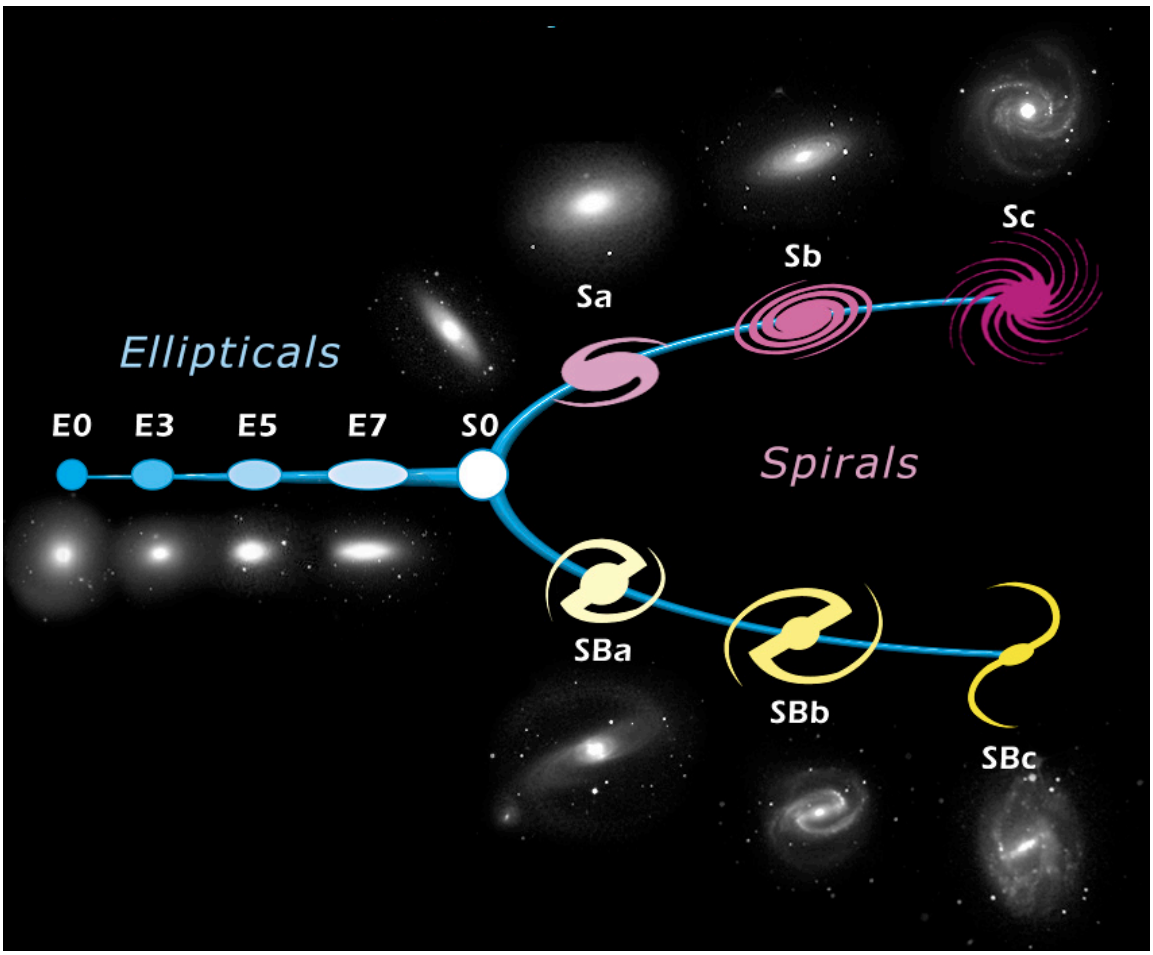


Figure 1.1: Hubble morphological sequence of galaxies in the nearby Universe (also known as the Hubble Tuning fork). The objects are divided in three different classes based on their appearance: ellipticals, lenticular and spirals. Image taken from Wikipedia.com

formed slowly from more accumulated gas. This scenario was rapidly generalized, suggesting that disk galaxies were formed from a protogalactic cloud right after the big bang. This scenario also included ellipticals, stars formed much faster than the collapse of the protogalactic cloud. However, this accepted view of galaxy formation could not explain why stars in ellipticals should have formed previous the collapse.

Some astronomers noted that some galaxies did not fit into any of the bins of the Hubble morphological classification. Individual photographic plates showed twisted shapes and extended lumps outside the main body of the galaxy (e.g., Duncan 1923; Keenan 1935; Wild 1953; Zwicky 1956). Later on, a large sample of photographs of these objects were gathered in the *catalog of interacting galaxies* (Vorontsov-Velyaminov 1959) and the *Atlas of peculiar galaxies* (Arp 1966). It was evident that many of these peculiar objects were companions of one or more galaxies. It was also clear that often thin filament were present between the companion galaxies (bridges) or in the opposite direction from them (tails).

Different scenarios were proposed to explain these filaments. Here we note some of them:

• **Supernovae Explosion:** The galactic collision would enhance the production of supernovae. The blasts caused by these supernovae would eject material away from the host galaxy (Zwicky 1962). However, this scenario failed to explained the presence of bridges between the interacting galaxies so it was ruled out.

• **Nuclear Jets:** Another scenario to explain galactic tails and bridges was jets (e.g., Arp 1967). Material ejecting by a pair of fast jets from the nucleus that would slow down as it found material along its path. The material dragged by the jet will condense at its tip and form a small companion. Then the jet would be the observed bridge connecting the small massive galaxy and its companion. The appearance of a companion in only one side of the jet (not companion in the tail) was explained by the dissolution, ejection into the ISM or delayed formation of the similar companion in the other side of the jet (Arp 1969). Holmberg (1958) note that condensation of gravitationally bound material is very unlikely to occur at tip of the jets since they could reach (and often they do) a velocity larger than the escape velocity.

• **Tidal Tails:** Another shade in the palette of scenarios to explain the formation of filaments was tides. The core idea is that an external gravitational field would not affect equally different parts of the galaxy. In other words, the closest side of one galaxy would be more affected by gravitational field of the companion than the opposite side. These differential forces would distort the original shape of the galaxy (e.g, Zwicky 1956). Some astronomers questioned the tide scenario arguing that elongation of tides was too large to be created by tides (e.g., Vorontsov-Vel'Yaminov & Arkhipova 1962). In any case, the majority of the astronomical community agreed that other processes than gravitational forces must play a role in shaping the features of peculiar galaxies (Arp 1966).

As we see in the next section, the outstanding study provided by the Toomre brothers showed galactic interactions as the mechanisms which produce tidal tails.

## 1.2 Creating bridges and tails: The Toomre sequence

About the time when the first catalogues of peculiar galaxies were published and the gravitational interaction between two galaxies was started to be accepted as the main mechanism for the origin of those peculiarities, numerical simulations of gravitationally interacting galaxies started to be available. Galaxies were represented as central point masses surrounded by test particles. These first simulations were able to reproduce tidal arms (e.g., Pfleiderer & Siedentopf 1961). However, the work presented by Alar and Juri Toomre (1972) has been of capital importance in our current understanding of galaxy evolution. The two major achievements of this study were to present specific models of observed modeled galaxies and to predict the evolution of merging galaxies. They suggested that interacting galaxies will merge rather quickly and their remnants will look quite similar to elliptical galaxies.

Toomre & Toomre (1972) noted that intense tidal field induced by close passage of a galaxy can strongly deform the shape of a disk galaxy leading in the formation of bridges and tails. By invoking only gravitational forces and by varying the interacting parameters such inclination of the disk and the eccentricity of the orbit, they could recover the morphological features observed in interacting systems. As Schweizer pointed out in his review of interacting and merging galaxies (in Kennicutt et al. 1996, Chapter 2), Toomre's work emphasized three fundamental concepts associated with tidal interactions: tidal friction, orbital decay, and violent relaxation. Tidal friction is expected if two N-body systems interact gravitationally. To produce the observed tidal features, energy must be exchanged between these systems. This transfer of energy would lead to an orbital decay with

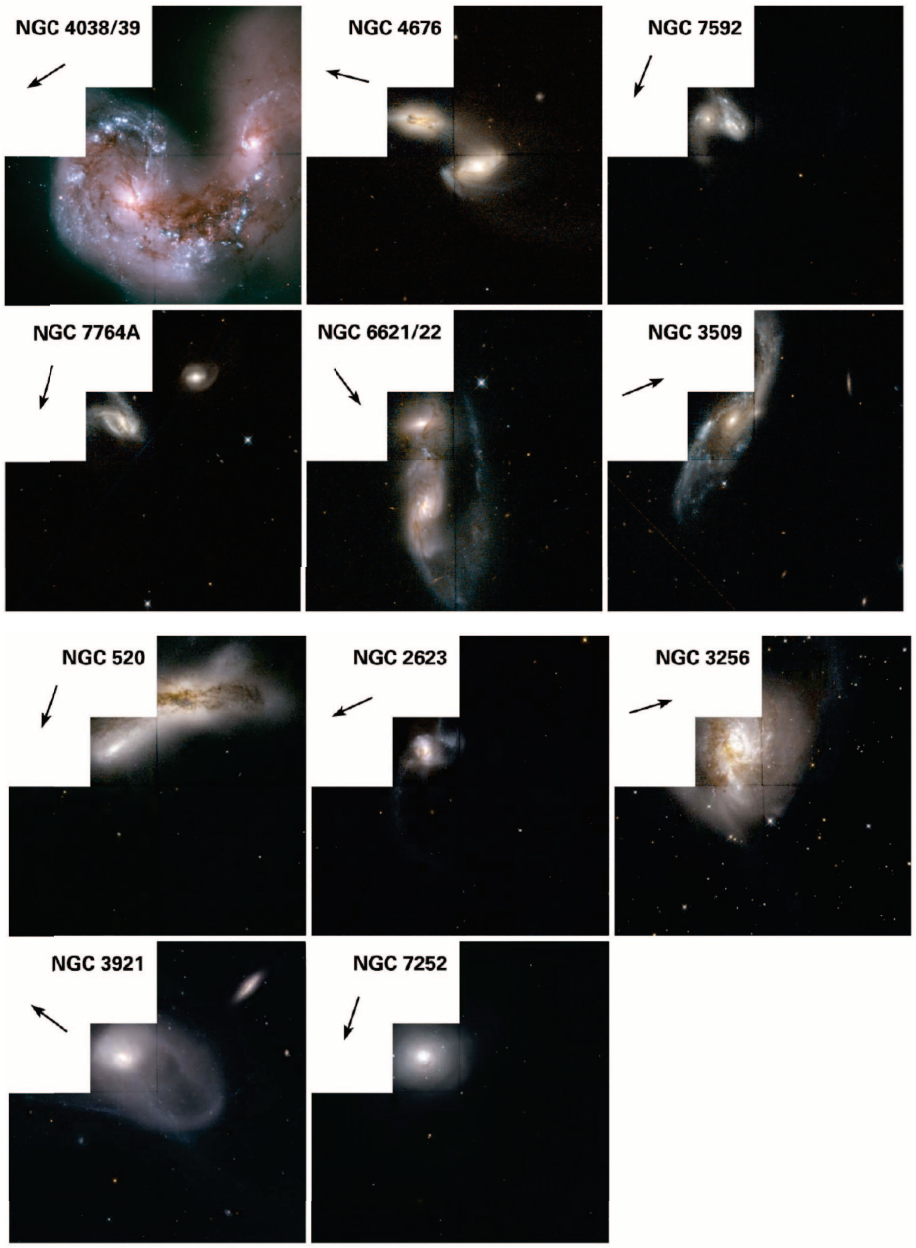


Figure 1.2: Color composite of The Toomre Sequence of merging galaxies observed in the *Hubble Space Telescope*. Image taken from Laine et al. (2003).

an eventually merge of the system. In this process of merging and strong fluctuation of the gravitational field, material will lead suffer a violent relaxation, where the gravitational potential of begins changing so quickly that star orbits are greatly affected, and lose any memory of their previous orbit. This relaxation would yield a distribution of the stellar component reassembling those observed in elliptical galaxies. These simulations suggest to them an evolutionary path: by sorting observed galaxies according to their numerical simulations for different stages of the dynamical evolution,

the authors introduce the Toomre sequence (Toomre 1977, see Fig. 1.2). As a historical note, it is interesting to note that despite the clear evidence for interactions as a key process in the evolutions of galaxies, it took almost a decade for the astronomical community to accept this scenario (see details in Kennicutt et al. 1996).

During the last forty years, our understanding of the merging process has been greatly improved. On the one hand, with much more computational power than early studies, numerical simulations now take into account the stars and the interstellar medium (ISM) as well as the associated phenomena occurring during the merger (see, Duc & Renaud 2013, for an updated review on numerical methods). On the other hand, the improvement of observational techniques has revealed much more information regarding the merging process (although slightly outdated, for a comprehensive review see Kennicutt et al. 1996). As we present in the next chapters of this dissertation, Toomre sequence lies at the core of many observational and numerical studies (including this study) aimed to understand how the properties of galaxies evolve as the interaction unfolds.

### 1.2.1 Internal and orbital parameters

As we pointed out above, the details of how interactions can affect the internal structure of galaxies depend on parameters related to their gravitational potential. In this section we present a brief overview of these parameters.

**(a) Morphology of the progenitors.** As we noted in Section 1.1, when a galaxy moves in a gravitational potential produced by another galaxy, different regions of the galaxy experience different gravitational forces. As a result, the galaxy can suffer strong distortions from its original shape resulting in large and well defined tails and bridges. However, this could depend on the initial distribution of the material in the progenitor. Assuming that the galaxy is composed only of point-like particles, if the material in the progenitor is distributed nearly randomly (e.g. stars in a elliptical galaxy) the net tidal effect from the companion would not translate into strong morphological signatures of distortion. On the other hand, if the progenitor shows a common velocity pattern (e.g., stars in a disk) the tidal field will have a similar impact in those elements sharing the same patterns allowing a more visible effect of the interaction. In other words, tidal features during a merger will be easier to detect when the matter in the progenitor is well organized, as in a disk galaxy than in systems with isotropic structures such as an elliptical galaxy (see Fig.1.3).

**(b) Spin-orbit coupling.** Using a small number of test particles in their simulations, Toomre & Toomre (1972) readily realized that spin-orbit coupling plays an important role in inducing large tidal structures. To easily understand its relevance we follow the description by Duc & Renaud (2013). Let's assume two disk galaxies A and B separated by a distance $r_{AB}$ lying in their orbital plane. The norm of the velocity of an element of mass of the galaxy A located at a radius r relative to the galaxy B is $r_{AB}\Omega \mp r\omega$, where $\Omega$ represents the orbital velocity and $\omega$ the (internal) rotation speed of the galaxy A. The sign in the second term depends on the alignment between $\Omega$ and $\omega$. In alignment (i.e., prograde encounter), the relative velocity ($r_{AB}\Omega - r\omega$)is lower than for a retrograde encounter ($r_{AB}\Omega + r\omega$). This means that for a prograde encounter the net effect of tides can be observed for a longer period of time than a retrograde one, making the structures formed in such encounter easily to observed. When the orbits are inclined, the response is less evident than planar orbits.

**(c) Mass ratio** The impact of merging between two galaxies strongly depends on the mass ratio between the progenitors. It has become common to distinguish major mergers (mass ratios smaller than 3:1, this is almost equal-mass galaxies) from minor mergers (ratios larger than 10:1). In

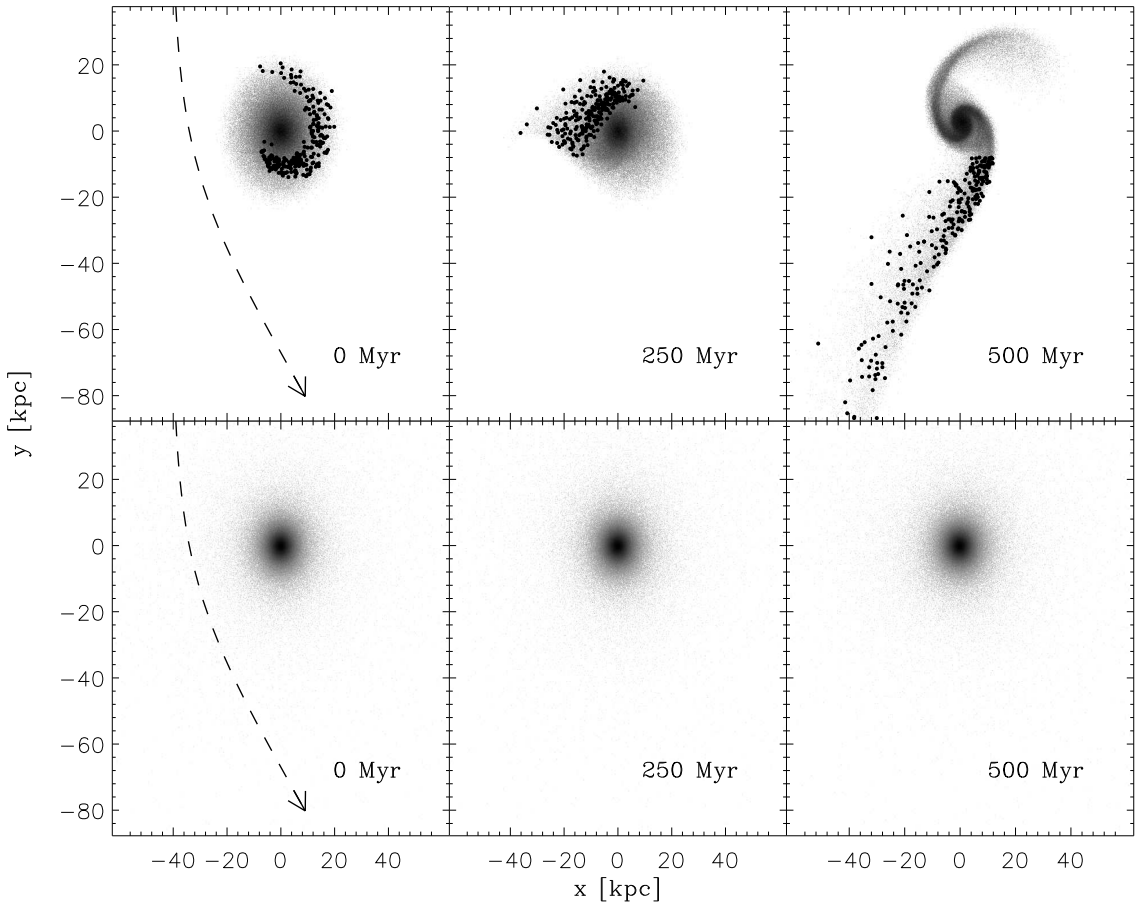


Figure 1.3: Top: morphology of a disk galaxy, seen face-on, during its interaction with a point-mass (mass ratio = 1), before the interaction (left), at pericenter (middle) and after (right). The dashed line indicates the trajectory of the point-mass (from top to bottom). The black dots tag a subset of particles that are situated in one of the tidal tails at t = 500 Myr. Bottom: same but for an elliptical galaxy. No tidal structures are visible. Image taken from Duc & Renaud (2013).

major simulated mergers the extension and duration of the tidal features is larger in comparison to those in minor mergers (Namboodiri & Kochhar 1985; Duc & Renaud 2013). It is also important to mention that internal structure and kinematics of merger remnants resulting from a major merger differ from those involved in a minor merger. Numerical simulations suggest that equal-mass merger remnants tend to show both disky and boxy shapes and slow rotation, this is, galaxies supported by anisotropic velocity dispersions. Minor merger remnants, show diverse morphological types but in most of the cases these galaxies are supported by rotation (e.g., Naab & Burkert 2003).

**(d) Impact Parameter** Although indirectly, the impact parameter can affect the morphology of the interacting galaxies. A close encounter will force one galaxy to pass through dense regions of the other resulting in a higher dynamical friction (Bertin et al. 2003, e.g.,). A close passage will also causes a significant tidal stripping (Ibata et al. 2001, e.g.,). Denser satellites can survive the disruption while less compact objects would be converted into stellar streams.

## 1.3 Spatially Resolved Kinematics

Most of the galaxies appear as extended sources on the sky. Depending on their morphology, the surface brightness of these galaxies is distributed in different ways. For objects with regular morphology, for instance ellipticals, their isophotes come in either round, disky or boxy shapes. On the other hand, the variety of shapes for the spiral galaxies is wider. Most of these galaxies show in their central region round isophotes which are normally considered to show spheroidal bulges, while at larger galactocentric radii the surface brightness is well represented by a disk-like structure. Whose isophotes are elliptical, their ellipticity varying with inclination to the line of sight. These observed two dimensional shapes correspond to three dimensional structures which in turn translate into different internal motions of the galactic components.

From basic assumptions we show the features we expect to find in a spatially-resolved kinematic map of a disk galaxy which is a fair (yet simplistic) representation of the velocity field observed in most spiral galaxies (and a majority of early-type galaxies, see Krajnović et al. 2011). Since we pursue a characterization of velocity fields from morphologically distorted objects (interacting and merging objects), we should also describe the methods frequently used to characterize the kinematics of galaxies. We will see that those methods rely on assumptions of regular internal motions of the galaxies, making it difficult to use these methodologies for a large sample of interacting and merging galaxies where it is not obvious the motions of their components are not regular. Using our methodology, we propose a technique to characterize velocity fields that makes no assumption on the possible internal motions (see Sec. 2.4.3). After this, we highlight some of the relatively scarce observations (in the optical and near infrared) of spatially resolved kinematics of merging systems in the nearby Universe. Finally, we present an overview of the different surveys aimed at studying the spatially resolved kinematics in merging galaxies at early epochs of the Universe.

### 1.3.1 Characterizing galactic velocity fields

The basic fact that galaxies, in particular spirals, rotate was discovered in 1914 by Wolf (1914) from the shape of the long slit spectra of M81 and M104. Later in 1918, Pease (1918) derived the first rotational curve in the central region of the Andromeda nebula. Depending on the spectral feature under study, it is possible to trace different components of the disk galaxies. Submilimiter and millimetric information provides information of the hydrogen either in its atomic or molecular form. A complete overview of in spatially resolved kinematics of spiral galaxies is presented by Beckman et al. (2004), in this section we will give a brief review.

To first order the material in disk galaxies is in concentric circular motion within a thin plane. The velocity of this rotation varies at different galactocentric radii and it is determined from the distribution of mass within a given radius. The plot of the observed velocity versus radius called the rotation curve shows two different regimes: a rapidly rising regime from the center out to a certain radius, followed by an almost constant velocity for a large range of radii (see Fig. 1.4). These two features are common in almost every rotational curve are characterized in the inner region as a rigid rotator and in the external region a dark matter halo has to be included to explain the why the velocity curve does not declinewith radius.

We recall that spatially resolved velocity fields are projections into the sky of the three dimensional motions of the galactic components. As a results, we observed only the radial component of the velocity in our direction. Then the observed velocity field in any point of galaxy plane projected into the sky plane can be expressed as:

$$v_{\rm obs} = v_{\rm sys} + v_\theta \sin i \cos\theta + v_R \sin i \sin\theta \tag{1.1}$$

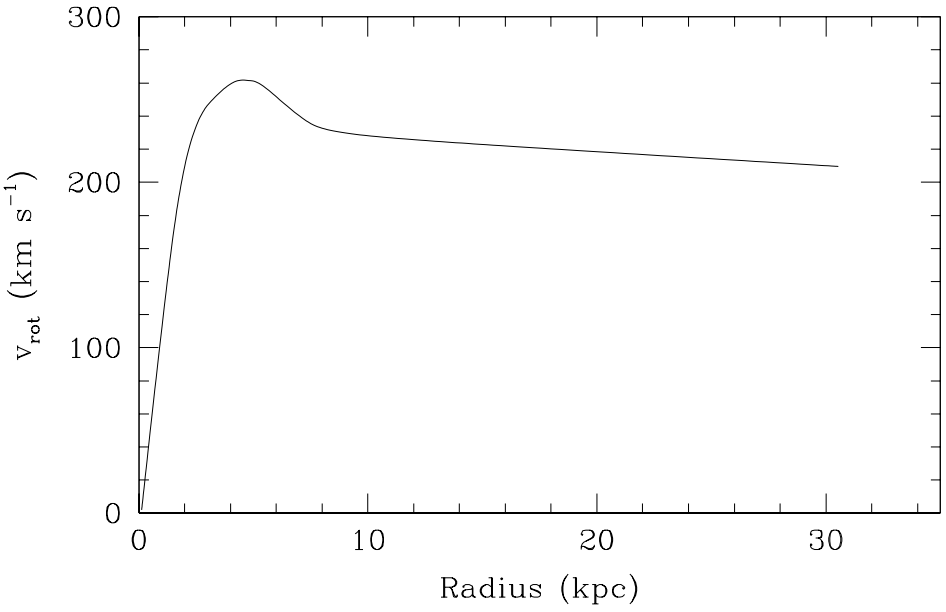


Figure 1.4: . Example of a velocity rotation curve from a disk galaxy. It shows the change from the inner "solid body" regime to larger galactocentric radii where the velocity reach almost a flat maximum. Figure taken from Beckman et al. (2004).

where $v_{\rm sys}$ is the systemic velocity of the entire galaxy, $v_\theta$, the tangential velocity component in the plane of the galaxy, and $v_R$ the radial component (with the initial assumption that material is confined within a thin disk); $i$ is the angle of inclination between the galaxy and sky plans. The coordinates $R$ and $\theta$ correspond to the point $P'(R,\theta)$ in the plane of the galaxy which is related to the point $P'(r,\phi)$ on the plane of the sky by:

$$\tan\theta = \tan(\phi - \phi_0)/\cos i \tag{1.2}$$

$$R = r\cos(\phi - \phi_0)/\cos\theta \tag{1.3}$$

where $\phi_0$ is the position angle of the galaxy major axis measured from north through east. For an ideal pure rotating velocity field the radial component is set to zero. In this ideal case the distribution of velocities with respect to the observer will have the form of the left panel of Fig. 1.5, where the regions with the same colors are denoted as "radial isovels". The axis of symmetry of this distribution corresponds to the locations of the maximum velocities in absolute value. In this ideal rotating velocity field, this axis coincides with the major axis of an ellipse which defines the projected disk position angle in the sky plane. Thus for a "well behaved" galaxy the location of these two axes should coincide. However, this is not always the case and radial (or vertical) motions are present in galaxies. Different kinematic strategies have been developed to characterize the two-dimensional distribution of velocities in galaxies. Here we describe some of the most relevant ones.

In general, there are three different strategies for characterizing a velocity field: (a) to subtract a pure circular velocity field and study the residuals map, (b) to decompose the velocity field into its Fourier components and (c) to generate a model of the velocity field assuming a particular symmetry

in the inner motion and minimize the residuals between the observed and modeled velocity fields. The last method is similar to method (a), but adding complexity to the modeled field. The first method is very straightforward. The parameters of the modeled rotational velocity field are derived partially from the rotation curve. These parameters include the systematic velocity, the maximum velocity (in absolute value) and the kinematic centre. However as Beckman et al. (2004) pointed out, it is necessary to take precautions in order to reduced as much as possible the systematic errors in other kinematic parameters such as the inclination and kinematic major position angle. Once these parameters are determined, the subtracted velocity field may indicate non-circular motions. In high spectral resolution velocity fields this method is able in some cases to determine signatures of flows in barred galaxies (e.g. Rozas et al. 2002).

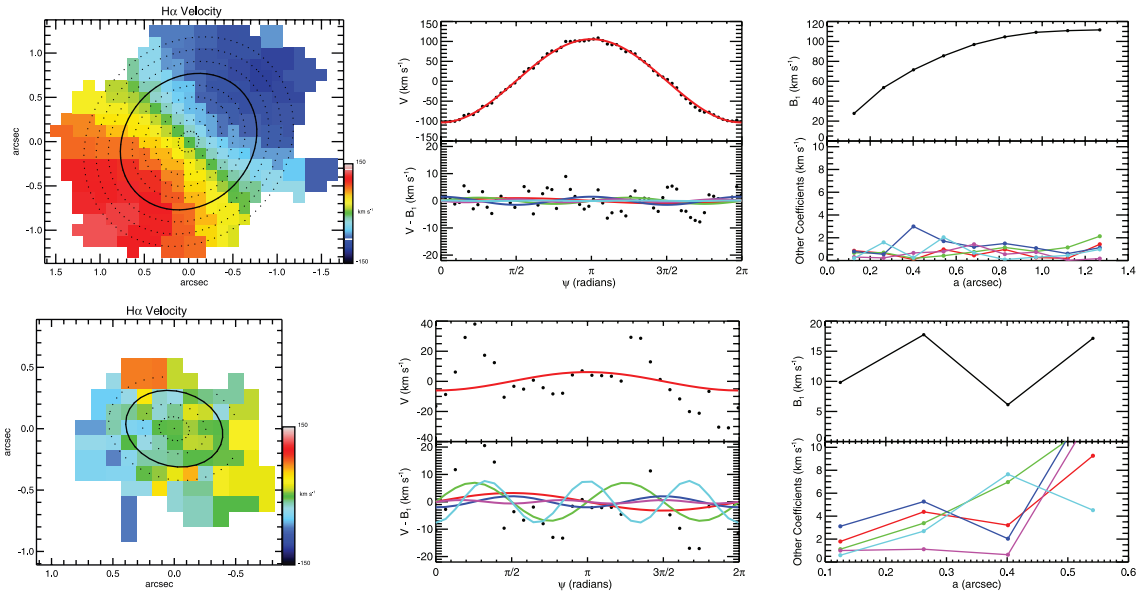


Figure 1.5: . Comparison of the velocity field of a toy thin-disk model (*top*) and a simulated field from a local luminous infra-red galaxy at redshift $z \sim 2$ (*bottom*). *From left to right:* Velocity field from model, in each ring (represented by the dotted lines) the *kinemetry* software analyzes the Fourier components of the line-of-sight velocities included in it. Best fitting of the Fourier moments of the velocity around the solid ellipse. Best parameters as function of the semimajor axis length $a$. Figure taken from Shapiro et al. (2008).

In previous years, other techniques have emerged in order to characterize the stellar or ionized gas velocity fields. One of the most used method decompose the velocity profile along a given elliptical ring in its Fourier components. The Fourier analysis is the most straightforward to characterize any periodic phenomenon. This method has been used previously in disk galaxies, assuming kinematic distributions of a thin disk (Begeman 1987). In some cases this method also allows the rings to have different inclinations (e.g., Rogstad et al. 1974). A generalization of this method has been introduced by Krajnović et al. (2006) by means of the software called *kinemetry*. This software devides the velocity field $K(a, \phi)$ into concentric elliptical rings that can be described by a given number (N+1) of the harmonic terms,

$$K(a,\phi) = A_0(a) + \sum_{n=1}^{N} A_n(a)\sin(n\phi) + B_n(a)\cos(n\phi) \tag{1.4}$$

where $\phi$ is the azimuthal coordinate and $a$ is the length of the semimajor axis of the ring in

the plane of the galaxy. If the inclination of the galaxy is well known, and the stars (or gas) are confined in a thin disk the circular motion of one element is represented by an ellipse in the plane of the sky. The velocity profile around a given ring is represented by the equation (1.1) without the last left hand-side term. The best position angle and inclination for each elliptical ring are derived by minimizing the expansion coefficients. Figure 1.5 shows an example of this method applied for velocity field of a thin disk toy model as well as a simulated galaxy at redshift $z$=2. The thin-disk toy model shows higher-order coefficients (than the magnitude of the velocity) smaller in comparison to those derived from the simulated high-redshift galaxy. This is used as an indicator of the degree of kinematic distortions produced by interaction (e.g., Shapiro et al. 2008).

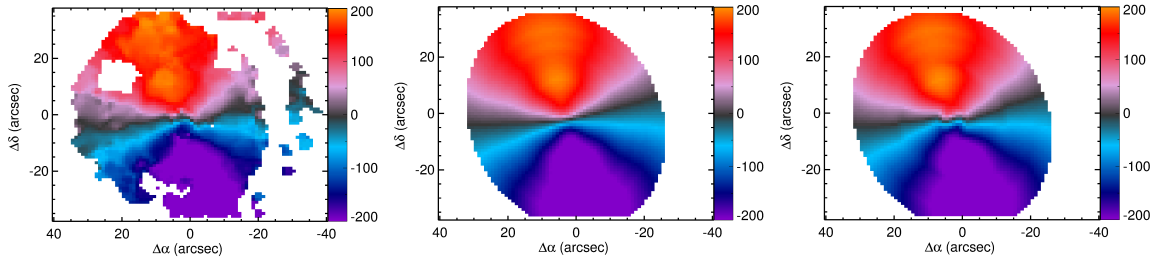


Figure 1.6: . Models of the ionized gas velocity field of the barred galaxy NGC 7321 (*left*) using the *Diskfit* software. Best fitting rotation only model (*middle*). Best fitting bisymmetric model *right*. Figure taken from Holmes et al. (submitted).

Finally, another methodology consist of fitting the observed velocity field with a velocity field with an intrinsic distortion. One example of this technique is the software *Diskfit* presented by Spekkens & Sellwood (2007). This software is designed to fit a bisymmetric distortion in a disk galaxy velocity field. This method is best suited to barred galaxies (see Fig. 1.6).

These methods have in common that in order to characterize the properties of the velocity fields, it is necessary to rely on an "a priori" parametrization of the intrinsic motions of the elements in the galaxies. As we have show in this section, these methods provided robust characterization on symmetric (or slightly distorted) velocity fields from galaxies with no companions nor any signature of interaction. However, by assuming an internal velocity fields, these methods may not provide a reliable characterization of the velocity fields for interacting and merging objects. Since we are aiming at characterizing the kinematic properties (in particular the kinematic position angle) of interacting and merging galaxies, we propose in this thesis an alternative method to determine the kinematic position angle with no assumptions about the internal motion of galaxies.

### 1.3.2 Velocity fields of nearby interacting and merger galaxies

Due to the complexity of the observational technique, the observation of optical or infrared velocity fields from merging galaxies in the nearby universe has been carry out for individual systems in a given interaction stage (e.g., Wild et al. 2014; Engel et al. 2010, see Fig.1.7 for an example of the Mice galaxies). In some cases the field of view covers only the central region of one of the companions in the binary system. There are no observational studies in the literature characterizing the velocity fields in a large sample of galaxies covering different stages of the interaction in the nearby Universe.

In recent years the study of modest samples of velocity fields from interacting galaxies at intermediate redshifts ($z < 0.09$) using integral field spectroscopy has become feasible. Westmoquette et al. (2012) present the characterization of 18 southern ionized gas velocity fields from (ultra) luminous

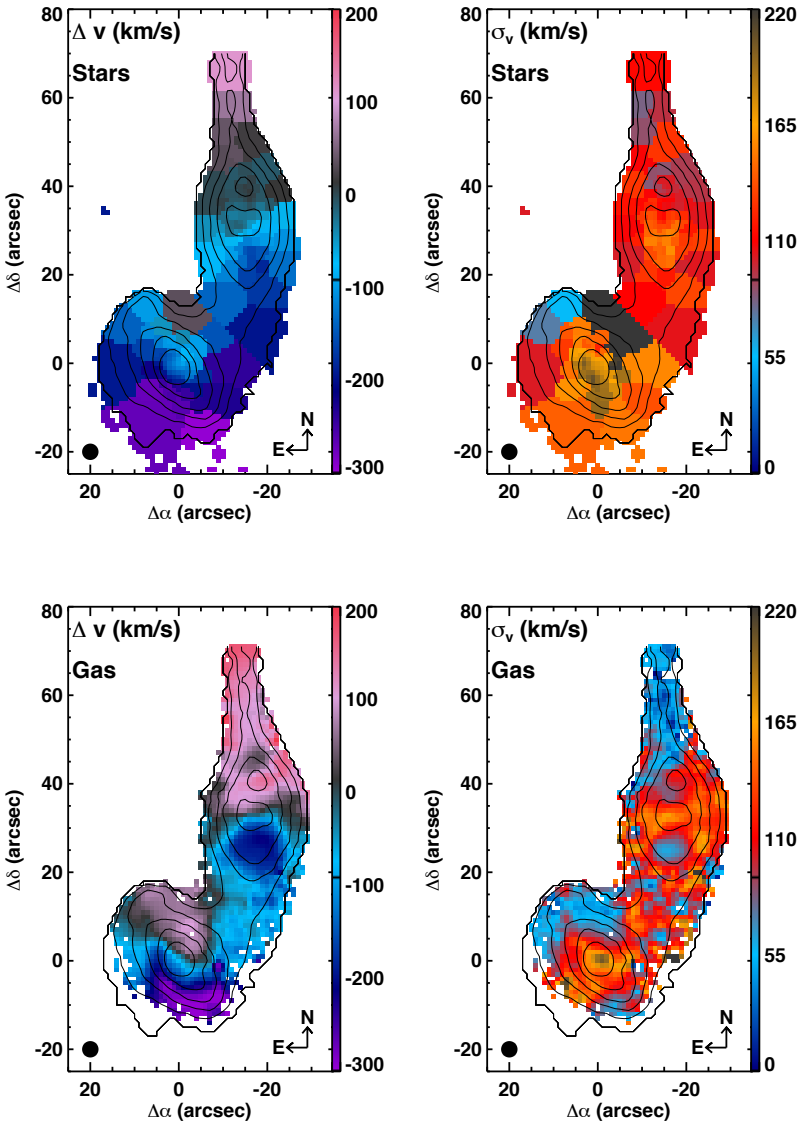


Figure 1.7: . Stellar (top) and ionised gas (bottom) velocity field (left) and velocity dispersion (right). The ionised gas maps are measured from the H$\alpha$ emission line in the V500 grating. Velocities are relative to the heliocentric velocity of NGC 4676A. The velocity dispersion maps have been corrected for instrumental resolution. The black circle shows the effective spatial resolution of the CALIFA observations before Voronoi binning of the data. This is one of the few case study where both galaxies in the system has velocity maps from their stellar and ionized gas component. The barred spiral NGC 4676B exhibits a strong twist in both its stellar and ionised gas disk. In NGC 4676A the high gas velocity dispersion indicate a powerful outflow. Figure taken from Wild et al. (2014).

infrared galaxies (U)LIRGs. Using a decomposition of the H$\alpha$ emission line profile, they found that 11 out of 18 galaxies present signatures of outflows in some cases associated with AGN activity. In addition, half of their sample have clear rotating gaseous disks. These integral field spectroscopic observations reveal the importance of studying the spatially resolved kinematic information in these complex systems. Bellocchi et al. (2012) characterize the ionized gas velocity field of a sample of

38 (U)LIRGs in a similar redshift range to Westmoquette et al. (2012). Their analysis a different kinematically distinct components suggest that a significant fraction of merging galaxies present pure rotating disk (29%), kinematically perturbed disks (47%) or complex velocity fields in their *narrow or systemic* component while a *broad* component is generally found in the central region of the galaxies blueshifted with respect to the systemic velocity. This suggest that a large fraction of LIRGS are supported by rotation in their systemic component. Using a morphological classification from isolated, interacting systems and mergers, they found a correlation between the merger stage and the mean kinematic properties inferred from the velocity fields. As the merger evolves (from isolated to merger galaxies) the mean velocity dispersion increases. Other studies gives study the spatially resolved velocity fields of the ionized gas (and stars) in the central region of mergers and merger remnants (e.g., Medling et al. 2014; Rupke et al. 2008).

Although these studies has provided insights in the impact of interactions in the internal motion of galaxies, they rely in methods that are not robust to characterize the kinematic properties where the internal motions are unknown and could strongly depart from symmetric velocity fields, which could be the case of morphological distorted objects like interacting and merging galaxies. The majority of these studies also lack of a representative sample for different stages of the merger event. Most of them study only one component of the interacting system. Finally, these studies lack comparison samples of galaxies of non-interacting galaxies.

### 1.3.3 Kinematic surveys at high redshift

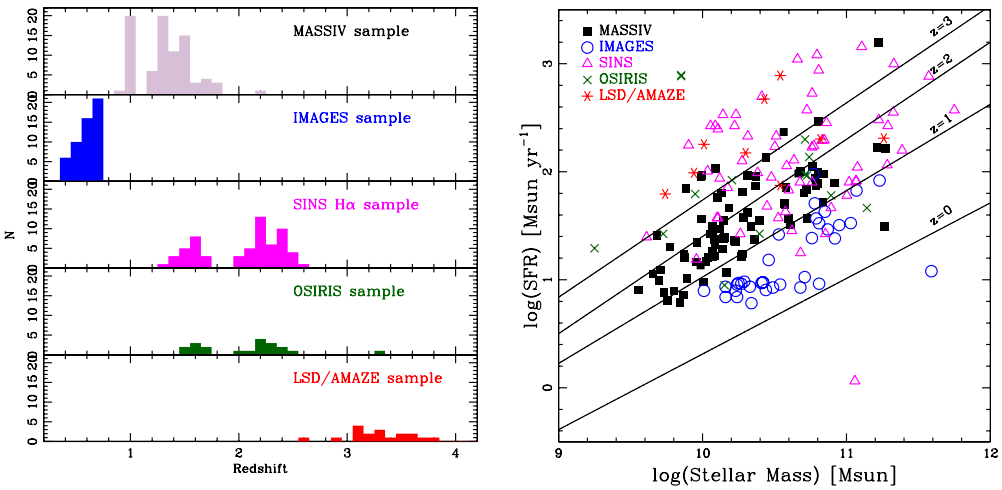


Figure 1.8: . *Left:* Distribution of the surveys with velocity field observations at high redshift. *Right:* Location for each of the targets in each survey in the star formation-stellar mass plane. Figure taken from Glazebrook (2013).

In the last 10 years most kinematic surveys have focused on the study of the spatially resolved properties of the galaxies at early epochs of the Universe. In particular, these studies have been designed to estimate the fraction of thick disk galaxies from those in an merger at high redshift (for a detailed overview see Glazebrook 2013). Here we present a list of the most relevant surveys carried out: The Spectroscopic Imaging survey in the Near infrared with SINFONI at VLT (the SINS survey, Förster Schreiber et al. 2009; Gnerucci et al. 2011); the OSIRIS UV-selected survey at Keck telescope (Law et al. 2009); FLAMES- GIRAFFE multi-object integral field facility at VLT

(Flores et al. 2006). The MASSIV survey (Contini et al. 2012). Fig. 1.8 shows a summary of the most important features of each survey. In Fig. 1.9 we present an example of the observed velocity field in from the FLAMES/GIRAFFE data (Flores et al. 2006).

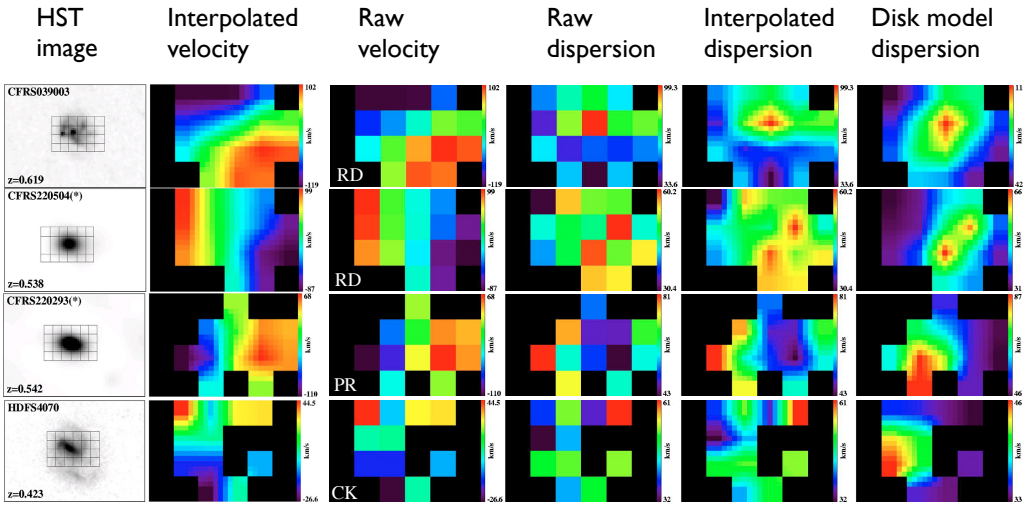


Figure 1.9: . Examples of the velocity fields at high redshift from sample FLAMES/GIRAFFE data. Each object represent one item of the classification presented by Flores et al. (2006): rotating disk (top), perturbed rotators (middle panels) and distorted field (bottom panel). Figure taken from Flores et al. (2006).

Despite the major efforts in order to characterize the velocity fields of merging galaxies from disk at high redshift, there has no been to date a comparison between the morphological position angle and the kinematic position angle derived in a sample of interacting galaxies in the nearby universe. This comparison is quite important since it allow us to establish whether the same physical processes are occurring at the precent epoch and the early Universe. It is also important to note that in the near future the next generation of telescopes and instruments will allow us to study galaxies at high redshift with the similar spatial resolution as the one we currently achieve for nearby galaxies (for instance the HARMONI instrument at the European Extreme Large Telescope, E-ELT[1])

## 1.4 Star Formation in Galaxies

The rate of the formation of new stars in a galaxy, along with its stellar mass, is one of the most fundamental parameters that dictates its structure, so the measurement of the star formation rate (SFR) is of capital importance in order to understand galactic evolution. After present the most common methods used to determine the SFR, we describe the main results obtained for normal galaxies in previous studies(i.e., non-interacting targets) including spatially resolved data. We also present previous studies of the SFR derived from interacting galaxies. The basic idea behind these studies is that interactions are responsible for triggering strong star formation episodes.

Theoretically, the SFR in a galaxy can be obtained by counting the young stars in a given mass range. However this is only possible for the closest galaxies. In practice, more than one methods should to be applied in order to get a reliable estimation of the SFR in galaxies. Most of these methods rely on integrated spectroscopy. From the spectral energy distribution (SED) of galaxies

[1]http://www.eso.org/sci/facilities/eelt/instrumentation/

at different Hubble types, there is a clear transition in the spectral continuum (Kennicutt 1992, see Fig. 1.10). Elliptical and lenticular galaxies spectra are dominated by red emission produced by old stars (G and K-type) while the spiral and irregular galaxies spectra show an enhancement in their blue region produced by A-type in the stars (Kennicutt et al. 1987b). There are indicators that are used to trace the SFR in galaxies here we list some of them:

**(a) Young *vs* old stellar population:** A very straightforward way to estimate the SFR would be to derived the ratio between young and old stellar components. For this method stellar evolution models are used to determine the luminosity in a given band and then compare with observed color or SED from a given galaxy (e.g. Larson & Tinsley 1978). This method assumes a set of parameters (e.g an initial mass function and SFR time evolution) that can lead to a large uncertainties in the derived SFR.

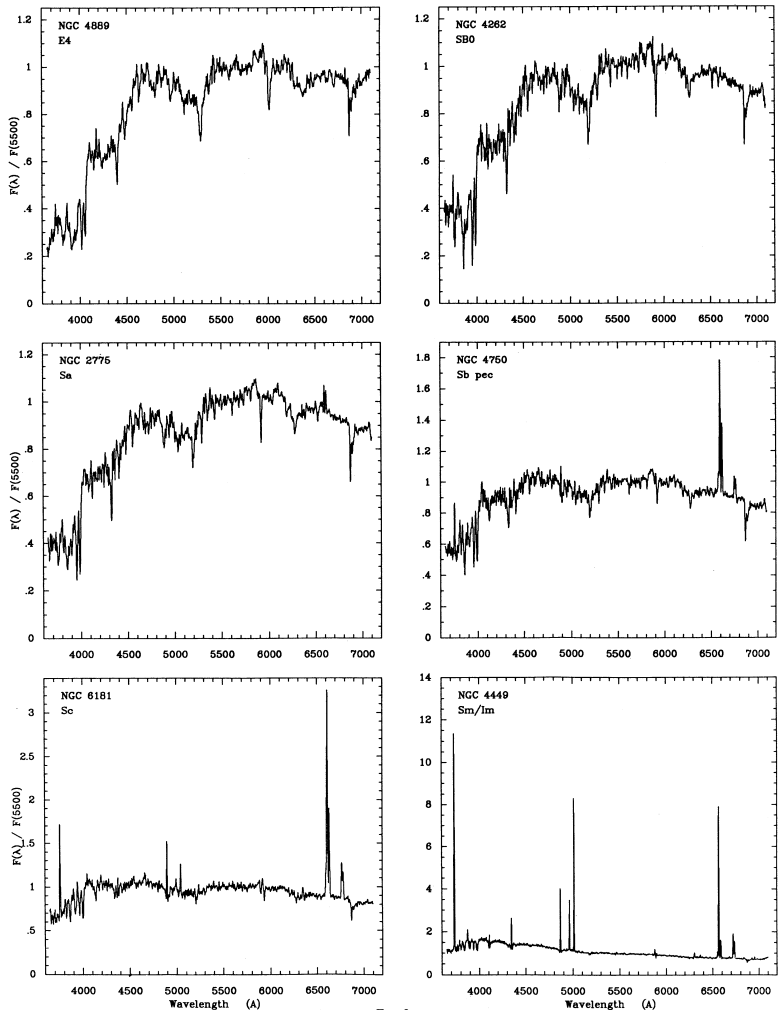


Figure 1.10: . Examples of integrated spectra for different morphologies in the Hubble sequence. Figure taken from Kennicutt (1992).

**(b) Ultraviolet continuum:** the ultraviolet continuum is produced mainly from young stars. Therefore the flux observed in this regime is related linearly with the SFR. The caveat of this tech-

nique for nearby galaxies is the large interstellar extinction at this spectral regime (for a review on the topic see Calzetti et al. 1994).

**(c) Far-infrared continuum:** another tracer of the SFR is provided by the far-infrared (FIR) continuum. Interstellar dust is responsible for absorbing a large fraction of the bolometric luminosity of the galaxy which is re-emited in the FIR regime (10-300 $\mu$m). Since the dust is prone absorb the ultraviolet radiation, its continuum emission can be used as an indirect tracer of the SFR (for a review on the topic see Calzetti et al. 1994). However, the dust can absorb radiation from different stellar populations including young and old stars. Isolating the contribution of the young stars responsible for the observed FIR emission is a difficult task. The situation changes in star-forming galaxies where the stellar population responsible of heating the dust is dominated by young stars.

**(d) Emission lines:** as can be observed in Fig. 1.10, the most dramatic change between SED occurs due to the presence and strength of emission lines. Elliptical galaxies have no emission lines while spirals and irregulars present a clear increment in the strength of the emission lines. It is well known that hydrogen recombination lines are directly related to the ultraviolet ionizing flux (e.g., Osterbrock 1989). Therefore, these lines provide direct measurements of the SFR of massive newly born stars. In particular, the H$\alpha$ emission line has become a powerful tool to determine the star formation in nearby galaxies. The H$\alpha$ integrated flux is converted into SFR by means of modeled stellar clusters (Kennicutt 1983). Extintion can affect H$\alpha$ integrated flux and consequently the determination of the SFR. This effect is particularly evident in central regions of galaxies with large lanes of dust where the integrated flux can be strongly diminished even in the order of 1 mag. Typical values of SFR for normal galaxies range from $\sim$ 0.001 - 10 $M_\odot$ yr$^{-1}$ (e.g., Kennicutt et al. 1994).

Another related method measures of the H$\alpha$ equivalent width. This parameter is defined as the ratio between the emission line luminosity and the adjacent continuum flux. This proxy gives an indication of the current star-formation activity compared to previous activity (it is also called the specific SFR, sSFR). If the luminosity is dominated by old stars, this provides an SFR per unit galaxy stellar mass. To summarize, as Kennicutt et al. (1996) pointed out, one has to be aware of the caveats for each of the proxy to determine the SFR, in some cases several estimators of the SFR at different spectral regimes have to be used to determine a robust estimate of this parameter.

### 1.4.1 Star formation in non-interacting galaxies

One of the goals of this thesis is to determine the real impact of interactions and mergers on the change of the SFR (is it incremented or decreased compared to isolated galaxies?) and to quantify the spatial extension of that change (where does it happen? does the sSFR change in the central or in the extended regions?). In order to answer these questions, we use sSFR maps of a large sample of isolated galaxies. Therefore we provide here an overview of previous studies on the determination of sSFR in nearby (normal) galaxies.

Most of the efforts to determine the sSFR use the equivalent width of the combined H$\alpha$+[N II] emission lines (Kennicutt & Kent 1983, see Fig.1.11). These studies already show a clear difference between different morphological types. Ellipticals and lenticulars show small (almost non-existent) equivalent widths while the disk and irregular objects display larger equivalent widths. Recently, studies in large samples of galaxies (using the Sloan Digital Sky Survey) suggest that sSFR is related to the stellar mass and oxygen abundance (e.g., Ellison et al. 2008a; Mannucci et al. 2010). For large stellar masses the sSFR seems to decrease. These authors also found that there seems to be a threshold in the sSFR at about $10^{-10}$ yr$^{-1}$ . We should note that there are some limitations for

these techniques. For a nearby galaxy, only a fraction of the galaxy can be observed implying that we determine the properties only in a specific region of the galaxy. Also a fixed size aperture in the sky covers different portions of objects at different redshifts.

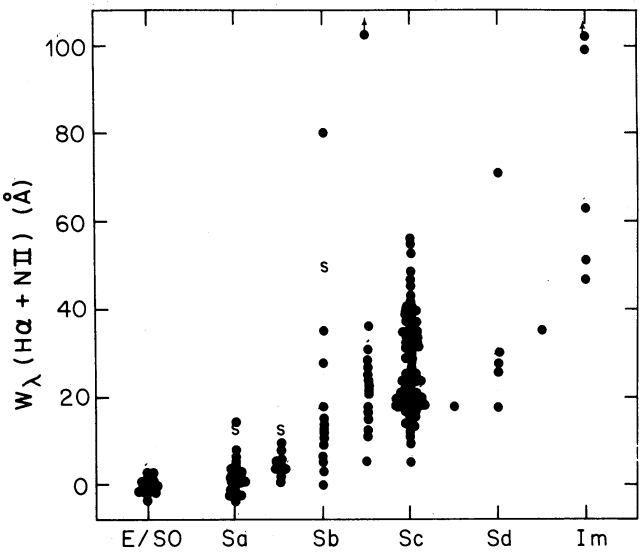


Figure 1.11: Hα+[N II] emission lines combined equivalent width for a sample distributed according their Hubble type. Figure taken from Kennicutt & Kent (1983).

With the advance of integral field spectroscopy, it has been possible to measure the physical properties of the galaxies in a spatially resolved way, particularly the equivalent with of the H$\alpha$ emission line. One of the most important results from these studies reveals that the radial distribution of the H$\alpha$ equivalent width shows a positive gradient. Once it is normalized to the effective radius, the slope of this gradient does not depend on the individual galaxy (Sánchez et al. 2012b, see left panel of Fig.1.12). Rosales-Ortega et al. (2012) found a mild relation between the local mass surface density and the H$\alpha$ equivalent width suggesting an "inside-out" grow scenario for disk galaxies (see right panel of Fig.1.12). This result contradicts the scenario proposed by Mannucci et al. (2010), in which the strong correlation between the stellar mass, the SFR and metallicity suggests an interplay of infall pristine gas and outflow of enriched material. Rosales-Ortega et al. (2012) indicated that the possible discrepancy between these studies could be attributed to aperture effects from the single-fiber observed sample.

### 1.4.2 Star formation in interacting galaxies

In this section we present some of the most relevant studies in the literature comparing the star formation in interacting and merging galaxies against isolated or control samples. In a seminal paper, Larson & Tinsley (1978) provided the first quantitative evidence of how interaction affects the properties of galaxies, in particular their star formation. They analyzed the UBV colors of a sample of non-interacting galaxies from the Hubble Atlas and a sample of interacting objects from the Arp atlas (see left panel in Fig.1.13). They found that interacting galaxies show bluer colors than the non-interacting sample. By modeling these colors using synthetic stellar populations, they suggested that the colors of interacting galaxies could be explained only by adding to the stellar

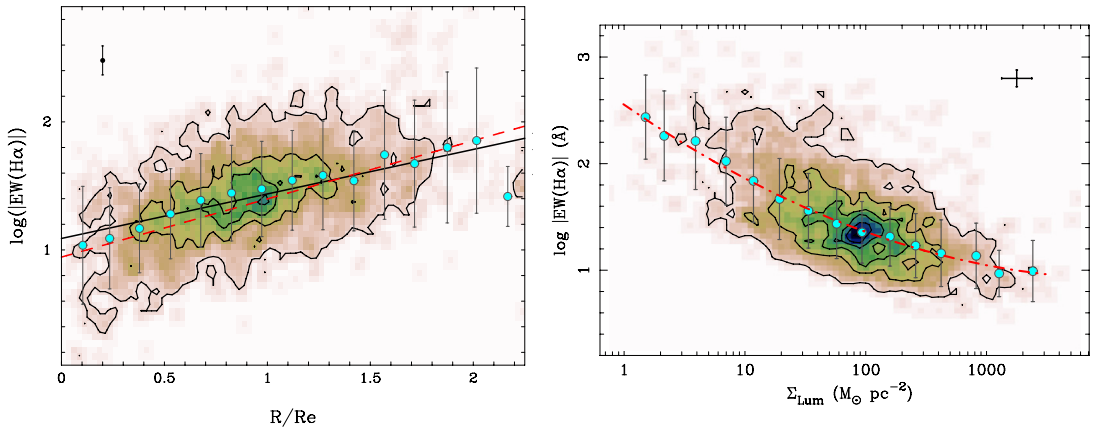


Figure 1.12: . *Left panel:* Radial distribution of the equivalent width of Hα (on a logarithmic scale of its absolute value), once scaled to the average value at the effective radius for each galaxy in a sample of 38 star-forming galaxies. The light-blue solid-circles indicate the mean value for each consecutive radial bin of ∼0.15 Re. The solid line shows the average linear regression found for each individual galaxy. The red dashed line shows the actual regression found for all the H ii regions detected for all the galaxies. Figure taken from Sánchez et al. (2012b). *Right panel:* Relation between Hα equivalent width and surface mass density. Figure taken from Rosales-Ortega et al. (2012).

population strong starburst with ages of $10^7$-$10^8$ yr. Their results provide observational and theoretical background on how we currently understand the star formation in interacting galaxies. Later, other studies presented detailed color analysis in larger samples of interacting galaxies confirming the above results (e.g., Carlberg et al. 1994; Hibbard & van Gorkom 1996; Patton et al. 1997, 2005).

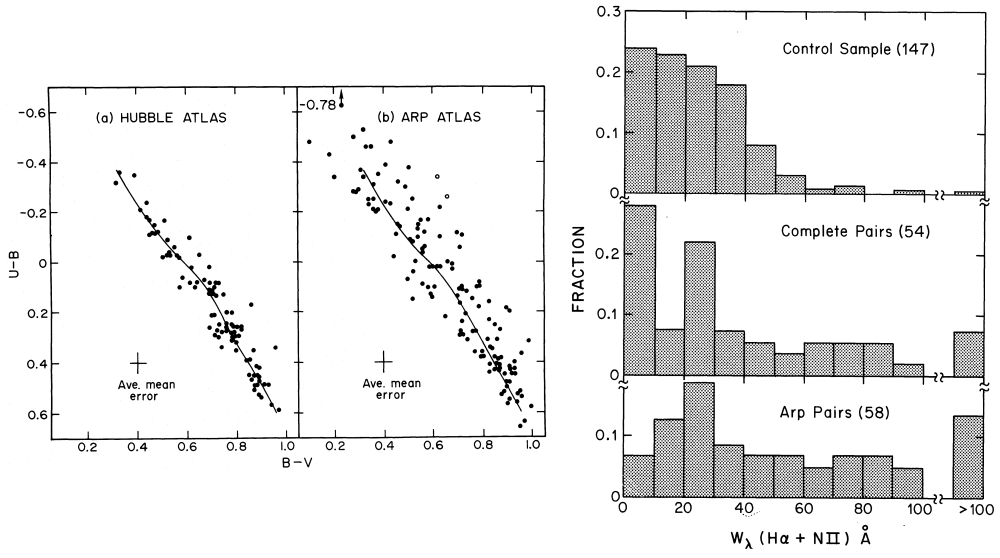


Figure 1.13: . Examples of early comparative studies between normal galaxies and interacting or merging galaxies *Left panel:* Comparison of the UBV colors of interacting and non-interacting galaxies in the Arp atlas. Figure taken from Larson & Tinsley (1978). *Right panel:* Comparison for different Hα+[N II] emission-line equivalent width distributions from non-interacting galaxies (*top*), pairs of galaxies (*middle*) and objects from the Arp atlas (*bottom*). Figure taken from Kennicutt et al. (1987a).

Early studies comparing the distribution of H$\alpha$+[N II] emission-line equivalent width from interacting and control galaxies already reveal differences between these two samples (see right panels of Fig.1.13; Bushouse 1987; Kennicutt et al. 1987a). The median equivalent width for interacting galaxies is larger than the median of the control sample. The large dispersion of the equivalent width distributions for the interacting and merging samples reveals objects that can reach SFR of $\sim 100$ M$_\odot$ yr$^{-1}$. Studies with larger samples support the hypothesis that interactions and mergers enhances the stellar formation activity (Barton et al. 2000; Lambas et al. 2003; Alonso et al. 2004; Nikolic et al. 2004). Note also that Far IR emission of interacting galaxies is enhanced in interacting and merger galaxies (for a review see, Sanders & Mirabel 1996)

Using data from the Sloan Digital Sky Survey, Ellison et al. (2008b) compare the star formation of a large sample of interacting galaxies with a matched sample of non-interacting galaxies in stellar mass and redshift. Pairs in their interacting sample has mass ratios close to unity covering different parameters of the interaction (such as projected distance between the pairs, $r_p < 30$ kpc, and stellar masses). They found a systematic enhanced star formation for the interacting sample up to a maximum projected distance. For small projected distances between the pairs the enhancement in the star formation is larger compared to control galaxies (see left panel in Fig. 1.14). In a further study, they found that considering pairs of galaxies with larger projected separations also yield a net enhancement in the SFR comparing with isolated galaxies ($r_p < 180$ kpc, Patton et al. 2013). Post-merger galaxies also present a larger SFR than non-interacting galaxies (see right panel of Fig. 1.14 Ellison et al. 2013b).

Despite these analysis of interacting galaxies, there been no up to date spatially resolved studies of the star formation in large samples of interacting and merger galaxies. Furthermore, it has not been possible to compare the star formation in these objects with a control sample on the same physical scale (e.g., the effective radius). Integral field spectroscopic observations for a large sample of galaxies allows us to compare the sSFR in a sample of interacting galaxies (with objects in the course of merger events) with the sSFR of a control sample of isolated galaxies in the same physical region. This will give us important clues about the enhancement of the star formation in interacting galaxies and if there is such enhancement, how extended is this SFR across the interacting galaxies.

## 1.5 Gas-phase metallicity in normal galaxies

The metallicity of the interstellar medium is strongly linked to the stellar content of the galaxies and the regulation of new born stars. Therefore this quantity is expected to correlate with the stellar mass and the SFR. Several studies on this subject found indeed the nowadays well-known luminosity - metallicity (Skillman 1989; Zaritsky et al. 1994; Salzer et al. 2005; Lee et al. 2006) and the stellar mass - metallicity relation (M-Z relation, Lequeux et al. 1979; Skillman 1992). Tremonti et al. (2004) found a tight relation between the stellar mass and the gas-phase oxygen abundance over three orders of magnitude in stellar mass using single fiber aperture spectra from a large sample of star-forming galaxies (see Fig.1.15). This relation has been confirmed also in different epochs of the Universe (Savaglio et al. 2005; Erb 2006; Maiolino et al. 2008). There are several scenarios to explain this tight relation: Loss of enriched gas by outflows (Tremonti et al. 2004; Kobayashi et al. 2007); the accretion of metal poor gas (Finlator & Davé 2008); variation of the initial mass function with the stellar mass (Köppen et al. 2007); selective star-formation efficiency or downsizing (Brooks et al. 2007; Ellison et al. 2008a; Calura et al. 2009; Vale Asari et al. 2009).

More recently, with the technical advance of integral field spectroscopy, it has been possible to study whether this tight relation holds locally in galaxies. One of the most important results from

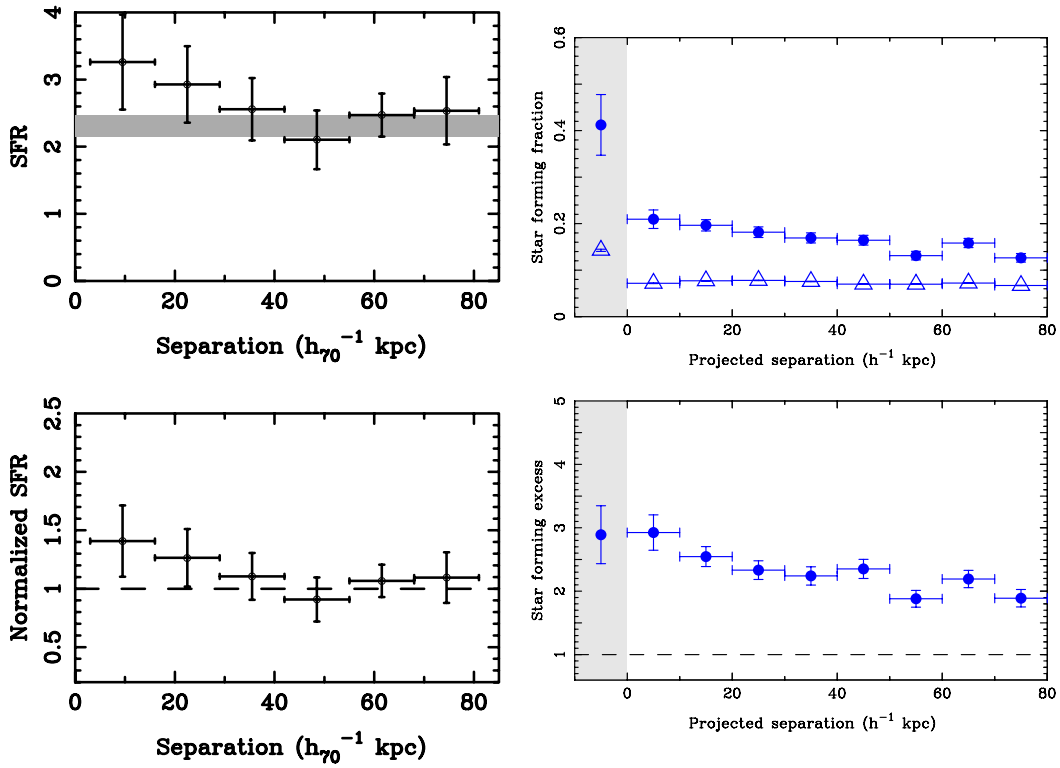


Figure 1.14: . Examples of recent comparative studies between normal galaxies and interacting or merging systems using a large sample of galaxies (Sloan Digital Sky Survey). *Left panel:* SFR for galaxies with a companion as a function of pair separation. Top panel: SFRs binned by separation. The gray region shows the field median for galaxies with a matched mass distribution. Bottom panel: SFRs normalized to the median control value. Figure taken from Ellison et al. (2008b). *Right panel:* The fraction of galaxies classified as star-forming as a function of projected separation. In the upper panel, filled points represent pairs and (in the grey shaded box) post mergers and open triangles show the star-forming fraction in the control sample. Figure taken from Ellison et al. (2013b).

spatially resolved studies of H II regions for a large samples of disk galaxies reveals that the radial distribution of the oxygen abundance shows a negative gradient. Once this gradient is normalize to the effective radius, the slope does not depend on the individual galaxies, suggesting that this gradient is an intrinsic property common in all the star-forming galaxies (Sánchez et al. 2012b). (Rosales-Ortega et al. 2012) found that the global M-Z relation determined from single fiber observations (e.g., Tremonti et al. 2004) also holds at local scales (i.e.,H II-regions scales). Their results suggest a scenario in which gas is been recycled in galaxies, both locally and globally. This process is much faster than other processes, such as that of gas accretion by inflow and/or metal loss due to outflows (Sánchez et al. 2012b). These results have been confirmed by means of a larger sample of integral field spectroscopic data (see Fig.1.16, Sánchez et al. 2013, 2014).

## 1.6 Gas-phase metallicity in interacting galaxies

As we note in Sec. 1.4.1, interactions and mergers are identified as key mechanisms in increasing the star formation rate (SFR) in galaxies (e.g., Sanders & Mirabel 1996; Borne et al. 1999). This enhancement is the result of tidally induced inflows of gas that favors the increment of star forma-

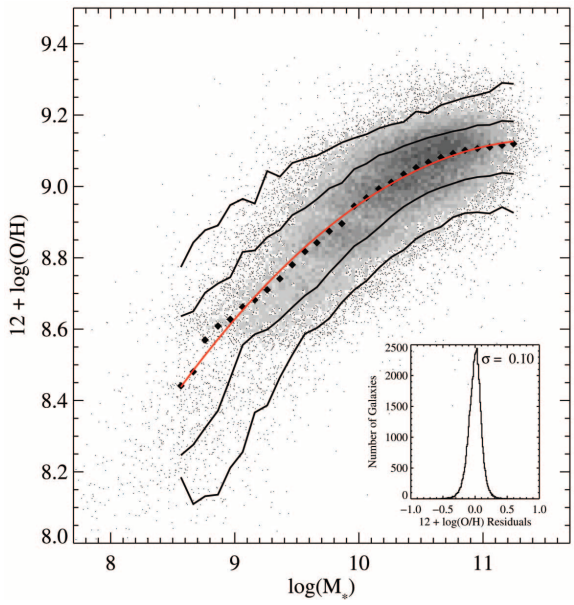


Figure 1.15: . Relation between stellar mass, in units of solar masses, and gas-phase oxygen abundance for $\sim$ 53,400 star-forming galaxies in the SDSS. The large black filled diamonds represent the median in bins of 0.1 dex in mass that include at least 100 data points. The solid lines are the contours that enclose 68% and 95% of the data. The red line shows a polynomial fit to the data. The inset plot shows the residuals of the fit. Figure taken from Tremonti et al. (2004).

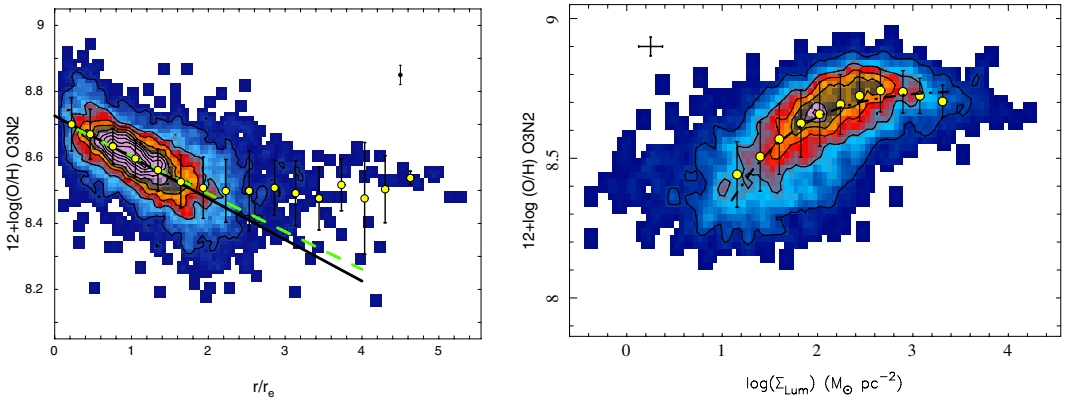


Figure 1.16: Global galactic properties of the oxygen abundance derived from local properties of a sample of $\sim$ 3000 H II regions. *Left panel:* Radial distribution of the oxygen abundance. after scaling to the average value at the disk effective radius for each galaxy. The image and contours show the density distribution of H II regions in this parameter space. The solid yellow points represent the average oxygen abundances, with their corresponding standard deviations indicated as error bars for consecutive bins of 0.3 galactocentric distances per disk effective radius.The dashed green line shows the result of the best linear regression to the data. The solid black lines in both panels represent the linear relation corresponding to the mean values of the zero points and slopes of the individual regressions derived for distribution of each individual galaxy. Figure taken from Sánchez et al. (2014). *Right panel:* distribution of the oxygen abundances for the 3000 individual H II regions extracted from the CALIFA data as a function of the surface mass density, represented with a density contour-plot. The dot-dashed line represents the best-fitted curve for these points. Figure taken from Sánchez et al. (2013).

tion activity in the central region of interacting and merging galaxies. In the above picture, these metal-poor gas inflows decrease the central metallicity in comparison to non-interacting galaxies (e.g., Kewley et al. 2006; Ellison et al. 2008b). As a consequence, merging galaxies are thought to contribute to the scatter in the mass-metallicity relation of star-forming galaxies.

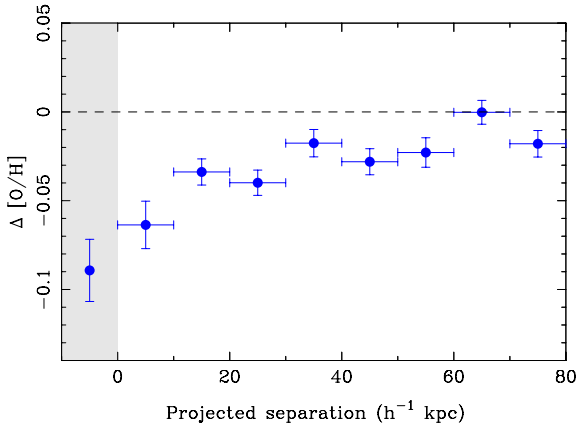


Figure 1.17: The change in metallicity for close pairs of galaxies relative to their control sample. The point in the grey shaded box shows the metallicity offset for galaxies in the SDSS post-merger sample. Figure taken from Ellison et al. (2013a).

Using data from the sample of pairs provided by the Sloan Digital Sky Survey, Ellison et al. (2008b) compare the oxygen abundance of a large sample of pair galaxies with a matched sample of non-interacting galaxies in stellar mass and redshift. They found that paired galaxies presented a lower metallicity in comparison to the control sample of $\sim 0.05$ dex. In another further study, Ellison et al. (2013a) found that post merger galaxies present a diluter metallicity than pair galaxies ($\sim 0.1$ dex) compared to a control sample of galaxies (see Fig. 1.17). Although, Sánchez et al. (2013) present the largest sample of H II regions, there is no up to date studies regard the impact of the metallicity at different scales of interacting galaxies. To test the hypothesis of diluted metallicity in interacting galaxies it is mandatory to perform a homogeneous comparison of the oxygen abundance for a sample of interacting and isolated galaxies using the same physical scale to avoid aperture effects in those measurements.

## 1.7 Thesis Project

In this chapter we have reviewed some aspects of the characterization of the velocity fields, the star formation and metallicity in nearby galaxies. In particular, we have focused on the main properties for normal (non-interacting) galaxies and those for interacting and merging objects. In this framework, and in order to gain a better understanding and assess the impact of interactions/mergers in galaxy evolution, there are a few key studies that can be now performed with the currently regular use of integral field spectroscopy for a large number of objects. Spatially-resolved data for such large sample of objects allows us to: (a) select a statistically significant number of objects at different stages of the merger, from pairs, interacting and merger remnant galaxies; (b) from the same survey we can select a well-matched control sample in order to differentiate those phenomena produced solely by the interaction from those due to secular processes; (c) we will have a unique set of spatially resolved data, which in turn provide a much better quantification of the properties in both samples

(e.g., no bias by aperture effects); (d) all the data set is observed, reduced, and analyzed homogeneously. In this context, we have developed this thesis project aimed at achieving the following goals:

- To obtain a homogeneous set of data. This means that the entire sample has to be observed with the same instrument, reduced with the same pipeline and analyzed using the same methodology.
- To extract from a large set of datacubes spatially resolved maps of physical properties such as kinematic maps, fluxes and equivalent widths.
- To develop a methodology able to determine parameters derived from two-dimensional data from isolated and interacting galaxies.
- To characterize the stellar and ionized gas velocity field of our control and interacting samples by means of an assumption-free method.
- To compare statistically and discuss the kinematic properties derived above from isolated galaxies with those derived in the sample of interacting and merging galaxies.
- To quantify statistically the extent of the star formation enhancement produced by interactions as well as test the real impact of mergers on the dilution of the central metallicity in nearby galaxies.

Specifically, two-dimensional kinematics provides significant insights into the impact of the interaction on the internal motion of nearby galaxies. To quantify the distortion presented by the interacting galaxies, it is required to use a method with no assumptions of the internal motions of the target. We present such methodology which we used to characterize statistically the kinematic of the stellar and ionized gas components of a large sample of isolated galaxies. Using this method we characterize a sample of interacting and merging galaxies. Then we study another property of nearby galaxies where interactions are expected to have a large impact: the star formation rate. Using the same samples presented above, we show that this enhancement of star formation is produced only in the central region of interacting galaxies.

The structure of this thesis is as follows: In Chapter 2 we present the sample selection as well as a detailed description of the methodology used to determine the kinematic properties of our samples. We also present the procedure to extract the flux maps and H$\alpha$ equivalent width necessary to determine the specific star formation rate as well as the metallicity proxies. In Chapter 3 we present the characterization of the stellar and ionized gas velocity fields for a large sample of isolated galaxies. We show that non-interacting galaxies present a tight alignment between the stellar and ionized gas principal orientation. Then in Chapter 4, we contrast the properties of this sample of isolated galaxies with the sample of interacting galaxies. This allows us to quantify the impact of interactions and mergers in the internal motion of galaxies. In Chapter 5 we study the star formation and the metallicity of interacting galaxies. In Chapter 6 we present future prospects for a large survey of spatially resolved surveys in particular for merging galaxies. Finally, in Chapter 7 we present a summary and the main conclusions derived from this thesis.

Chapter 2

# Data and Methodology

*In order to carry out a comprehensive study that allows us to understand the impact of interaction and mergers in galaxy evolution, it is necessary to have a representative sample of galaxies in the local Universe. For this reason we make use of the CALIFA survey, which is the first large sample of nearby galaxies observed using spatially-resolved spectroscopy. In Sec. 2.1 we describe the main properties, observational strategy and data reduction of this survey. Then, we describe the selection of specific targets in different environments included in the CALIFA survey namely, isolation (see Sec. 2.2) and interaction (see Sec. 2.3). Finally in Sec. 2.4.1 we describe the methodology we use to extract and to study homogeneously the stellar, ionized gas kinematics and the physical properties of the ionized gas.*

## 2.1 The CALIFA Survey

The Calar Alto Legacy Integral Field Area Survey (CALIFA, Sánchez et al. 2012a) is a statistically well-defined sample of $\sim$600 galaxies in the local universe using 250 observing nights with the PMAS/PPAK integral field spectrophotometer mounted at the Calar Alto 3.5 m telescope. This survey will provide the largest and most comprehensive wide-field IFU survey of nearby galaxies carried out to date. CALIFA provides a valuable bridge between large single-aperture surveys (e.g., SDSS) and moderate-sample studies with 3D instrumentation (e.g, PPAK, SAURON, VIRUS-P). Observations started in summer 2010 and the final run is scheduled for summer 2015. The defining scientific drivers for the observational setup of the project are: (a)to create maps covering the entire luminous extent of the galaxies in this sample for a wide range of parameters, (b) to derive the stellar population content both in age and metallicity, (c) to trace the distribution of ionized gas and estimate chemical abundances for the gas phase, (d) to measure the kinematic properties, both from emission and absorption lines. Thus, CALIFA maps entire galaxies in their emission- and absorption-line properties in an unprecedented way.

### 2.1.1 Target Selection: The CALIFA Mother-Sample

The objects observed in CALIFA (approximately 600 galaxies) are selected from a large sample of 939 galaxies (CALIFA Mother-Sample, CALIFA MS hereafter). The targets for this mother sample were selected from the photometric catalog of the Sloan Digital Sky Survey (SDSS, Abazajian et al. 2009). A detailed description of the selection and photometric properties of these galaxies is presented by Walcher et al. (2014). In this Section we outline the main selection criteria and properties of the CALIFA MS.

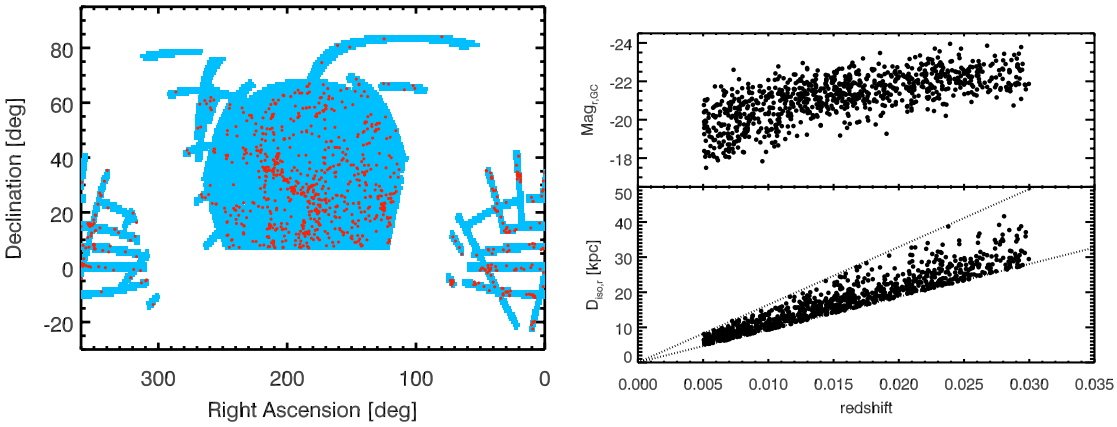


Figure 2.1: *Left:* Distribution of the CALIFA MS across the sky (red circles) over the footprint of the SDSS DR7 CAS (light blue). *Right:* redshift against Absolute magnitudes (*top*) and r-band isophotal size (*bottom*). Dotted lines represent the size selection limits. Figures taken from Walcher et al. (2014).

• **Size Selection.** The CALIFA MS was selected to include near and bright objects. These galaxies are drawn from the SDSS DR7 (Abazajian et al. 2009). Figure. 2.1 shows the location on the sky of the CALIFA MS over the SDSS footprints. The first selection criteria is objects within the range of sizes of $45'' < A_r < 79.2''$, where $A_r$ represents the isophote major axis at 25 mag per square arcsec in the $r$ band.

• **Quality assurance cuts.** To avoid photometric problems another thresholds were applied: exclude the Galactic plane ($b > 20$ ° or $b < -20°$); a selection on a number of SDSS flags to exclude objects with detection problems and the exclusion of very faint objects. This yields 1495 objects as an initial sample.

• **Redshifts.** The redshifts for these objects were obtained from the SIMBAD database. To have a comprehensive wavelength coverage the sample was restricted to the redshift range of $0.005 < z < 0.03$. This selection discard stars and galaxies without redshift measurements in either the SIMBAD or SDSS databases.

• **Visibility.** To avoid problems caused by atmospheric refraction, the declination was limited to $\delta > 7°$ and the Right Ascension to 5 h $< \alpha <$ 20 h.

• **Final adjustments.** By visual inspection five objects were rejected with sizes larger than those provided by the SDSS pipeline. For the final subsample two more objects were added: the companion in the Mice galaxies (NGC 4676B) and NGC 5947. In total, 939 make up the CALIFA MS (see left panels in Fig. 2.1).

The selection criteria yield a complete sample representative of the entire nearby galaxy population within a large range of stellar masses and sizes (Walcher et al. 2014). In the MS the spatial coverage of the integral field unit is very generous (see Sec. 2.1.2): 97% of the galaxies are covered to more than 2 $\times$ $r_{50}$, where $r_{50}$ represents the petrosian radius provided by the SDSS in the r-band. Given the spatial resolution of the instrument, the average spatial resolution is of $\sim$ 1 kpc (see Sec. 2.1.2). This allows us to resolved structures in individual objects (e.g., bulge, disc, arms, and in some cases tidal features such bridges and tidal tails).

Walcher et al. (2014) performed several tests on the completeness of the MS, desmostrating that a subsample of galaxies included in the CALIFA mother sample will be representative of the galaxy population in the nearby Universe. Figure 2.2 shows the ranges where the CALIFA MS is complete. Then, the observed subsample is a reliable set to infer properties of the galaxies at

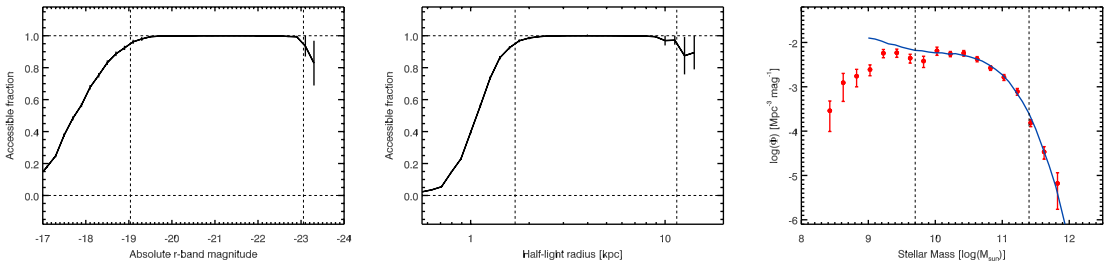


Figure 2.2: Fraction of SDSS galaxies with the CALIFA accessible range of $D_{iso}$ as function of the absolute magnitude (*left*) and half-light radius (*right*). Dotted vertial lines represent the range where the fraction is 95 %. *Left*: Mass function of the CALIFA MS (orange dots) compared with the function from (Moustakas et al. 2013, solid-blue line). Figures taken from Walcher et al. (2014).

different environments like the studies propose in this Thesis.

### 2.1.2 Observing Strategy

Here we present a brief overview of the technical aspects of the CALIFA survey in particular the main features of the instrument, the observing strategy and the main steps of the reduction. For a detailed description the reader is refer to Sánchez et al. (2012a), with improvements in the reduction presented by Husemann et al. (2013) and García-Benito et al. (2014). The CALIFA survey makes maximal use of the unique capabilities of the Postdam Multi Aperture Spectrograph, PMAS (Roth et al. 2005) in the PPAK mode. The PPAK fiber bundle consists of 382 fibers of 2.7 arcsec diameter each (see left panel of Fig. 2.3). From these fibers, 331 form a bundle in a hexagon configuration covering a FoV of $74'' \times 64''$, with a filling factor of $\sim$ 60%. 36 additional fibers sample the sky background, distributed in 6 bundles of 6 fibers each, along a circle $\sim$95 arcsec from the center of the instrument FoV.

A dithering scheme of three pointings is used to cover the complete field of view incrementing the spatial resolution. Three offsets are performed, corresponding to a shift of one fiber to its adjacent blank space. ($0''$, $0''$; -5.22$''$, -4.84$''$; -5.22$''$, +4.84$''$ in declination and right ascension with respect to the nominal coordinates). The reduction pipeline includes a spatial interpolation algorithm from the dithering scheme which yield a final spaxel size of $\sim$ 1 arcsec. The current median spatial resolution is $2\farcs7$ (García-Benito et al. 2014).

The CALIFA survey has been designed to observed in two complementary spectroscopic setups namely, the V500 and V1200 setups. The low-resolution V500 setup gives a nominal spectral resolution of 6 Å (FWHM) with a wavelength range 3745-7500 Å. This spectral regime allows studies of both the stellar population (continuum and absortion lines) and ionized gas (emission lines) using a large set of spectral features and emission lines. It covers from [O II]$\lambda$3727 to [S II]$\lambda$6731 in all the galaxies of the survey (see right panel of Fig. 2.3). The medium-resolution V1200 setup has a nominal resolution of 2.3 Å (FWHM). Its wavelength range covers the blue region of the spectrum (3650-4840 Å) including [O II]$\lambda$3727, Balmer break at $\sim$4000–4400 Å, H$\delta$, H$\gamma$ and [O III]$\lambda$4363. This setup is aimed to provided accurate measurements of both the stellar and the ionized gas kinematics from the H+K absorption features and the emission lines, respectively. Based on previous experiences with the instrument, exposure times were fixed for each of the setups: for the V500 setup the exposure time is 900 s per each of the three pointings in the dithering scheme while for V1200 setup three exposures of 600 s were taking per pointing. Selection of the exposure time is derived from previous studies using this instrument.

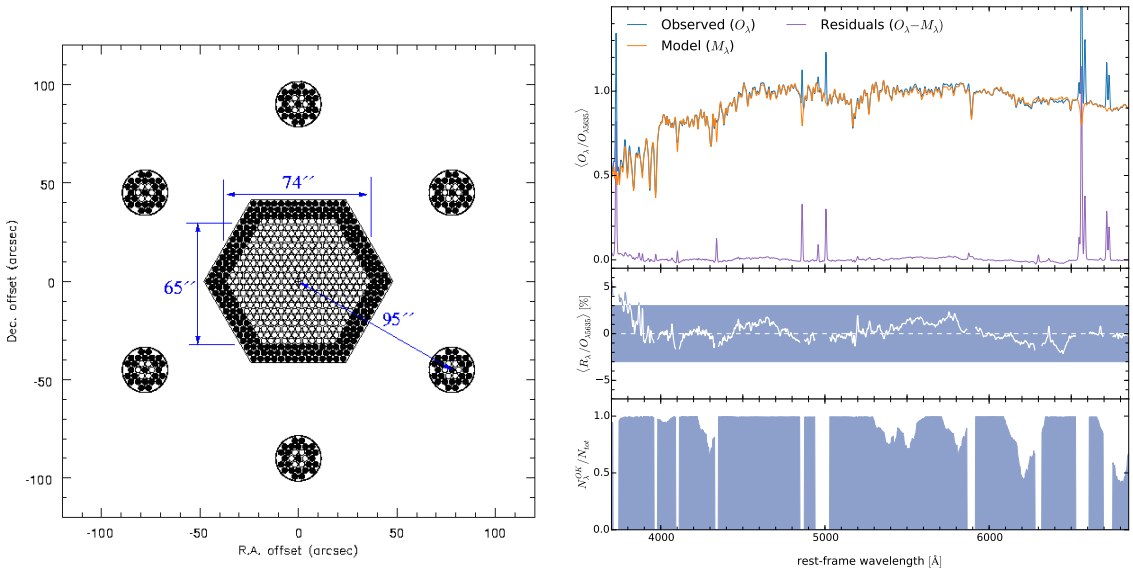


Figure 2.3: *Left:* Distribution of the fibers in the PMAS/PPAK instrument (Roth et al. 2005). The figure shows the central hexagonal bundle and the 6 bundles of 6 fibers each employed in sky background measurements. *Right:* Mean normalized spectrum of 170670 bins from 200 galaxies showing the wavelength coverage of the V500 setup (*top*) . After subtracting a modeled continuum from the observed spectrum, the residual reveals several emission lines. A zoom into the residual spectrum reveals that the subtracted residual level does not exceed the 6% (*middle*). The fraction of bins contributing in the median for each $\lambda$ is almost constant to unity (*bottom*). Figure taken from García-Benito et al. (2014).

### 2.1.3 Data Reduction

The data reduction for the CALIFA survey is performed with a dedicated pipeline. The current reduction pipeline (v1.5) is based on Python (Husemann et al. 2013, since v1.3c). Detailed description of this pipeline is presented by Sánchez et al. (2012a). Here we outline its main steps.

• **Removal of electronic signatures and realignment of the frames**: The CCD read-out software generates four different FITS files corresponding to each of the amplifiers in the detector. These files are combined in a single frame after subtracting the bias level and converting to counts from electrons. A master bias flat is created by averaging those observed during the night. Prior to combining the different exposures at the same position of the sky it is important to take into account the flexure, which causes possible offsets of the projected spectrum on the CCD. To mitigate this, the science and calibration frames are taken at most within 1.5 hours of each other. This yields a similar flexure pattern in both frames making it possible to extract the observed spectrum from the projected one in the CCD.

• **Spectral extraction and wavelength calibration**: The location of the spectrum on the CCD is determined using a continuum-illuminated exposure taken before the science exposures. To reduced the effects of cross-talk a Gaussian suppression is adopted. Then the extracted flux is stored in a row-stacked-spectrum file. Wavelength calibration is performed using HeHgCd lamp with exposures obtained before and after each pointing. Fiber-to-fiber corrections are performed by comparing the wavelength-calibrated row-stacked-spectra science frames with the corresponding frames derived from sky exposures taken during the twilight.

• **Sky subtraction:** The sky flux is obtained from the 36 fibers located at a distance of 95 arcsec from the center of the FoV (see left panel of Fig. 2.3). Little contamination from the science target is expected to affect the sky flux measurements in these fibers. The sky spectrum is obtained by combining the spectra from the 36 fibers. Contamination from close galaxies is also taken into account. Then this sky spectrum is subtracted from all the spectra in the corresponding science frame.

•**Flux calibration:** Flux calibration is performed by comparing spectrophotometric standard stars from the Oke Catalogue (Oke 1990), with the corresponding flux calibrated spectra. The pipeline also includes a transformation function from counts to intensity taking into account the extinction in both the standard star and the science target. The procedure ensures a good flux calibration throughout the wavelength range if the weather conditions are optimal. Offsets in the real and calibrated flux are expected if weather conditions are not suitable. Typically the relative flux calibration shows a dispersion of $\sim$ 2-3% ($\sim$ 0.025 mag) for wavelengths redder than 3850 Å. At shorter wavelengths the error becomes worse $\sim$ 8% ($\sim$ 0.08 mag). Note that these are also the typical values found in long-slit spectroscopy.

• **Data Cube reconstruction:** Once reduced, the science spectra from each pointing are combined in a single frame of 993 spectra. This is done by rescaling the different images to a common intensity by comparing the integrated spectra in an aperture of 30 arcsec diameter. Then the data is spatially resampled to a datacube with a regular grid using a flux-conserving interpolation method (for details see Sánchez et al. 2012a).

• **Differential atmospheric refraction (DAR):** The DAR is corrected once the data cube with a regular grid has been created. The pipeline performs a re-centering of the peak of the intensity spatial distribution at a given wavelength. Although there is a theoretical offset, the above method guarantees the homogeneity ofthe treatment of DAR corrections in all data sets.

• **Absolute flux re-calibration:** For the absolute calibration, the pipeline uses the SDSS photometry which is provided (by construction) for all the objects in the mother sample. Specifically, it makes use of the $g$ and $r$ SDSS images to perform a preliminary absolute recalibration. First the flux within a 30 arcsec aperture is measured in the SDSS images of these two filters (the SDSS counts-to-magnitudes is used). From the V500 data cube, the integrated spectra in an aperture of the same sizes is derived by adding contributions of individual spaxels and convolving this spectrum with the $g$ and $r$ filter passbands. From these two pairs of fluxes, a scaling factor is derived. For the V1200 data cube a scaling factor with respect to the V500 re-calibrated data cube is derived in a 5 arcsec central aperture. This is performed in the common wavelength range.

## 2.2 Control Sample: Non-interacting Galaxies

The sample of non-interacting galaxies is drawn from the CALIFA mother sample (see Sec.2.1.1) observed until November 2013. Using the SDSS $r$-band images of the observed galaxies, we selected 80 galaxies without evident signatures of interaction such as tidal tails, bridges, rings, shells or any other morphological distortion caused by a merging. Moreover, we considered galaxies isolated from companions within a physical radius of 250 kpc, a systemic velocity difference smaller than 1000 km s$^{-1}$, and a difference in magnitude in the SDSS r-band images larger than 2 mag (position and systemic velocities were taken from NED[1] ). We used a conservative physical radius for rejecting close companions with respect to pair-survey criteria (e.g., Ellison et al. 2008b). The systemic velocity selection criteria is supported by recent cosmological simulations (Moreno et al. 2013). Finally, we selected those galaxies for which stellar and ionized gas signal-to-noise ratios (S/N) allow reliable estimation of their kinematic properties (see Secs. 2.4.1 and 2.4.2).

[1]NASA/IPAC Extragalactic database. http://ned.ipac.caltech.edu/

It is important to note that these selection criteria do not exclude from the control sample galaxies with minor companions or galaxies located in the outskirts of groups. However, we estimated the perturbation caused by tidal forces induced by companions by means of the f-value (Varela et al. 2004). Values grater than -2 are required to produce sizable effects on a disc galaxy. We were able to measure the f-value in 71 objects. We found that 95% of these galaxies have f-values lower than -2 with a mean value of -4.0. This suggests that our sample is a fairly good representation of isolated galaxies. In fact, ten galaxies from our sample are also part of the AMIGA sample (Analysis of the interstellar Medium of Isolated GAlaxies, Verdes-Montenegro et al. 2005, CALIFA id: 2, 30, 131, 152, 275, 743, 748, 777, 779, 856). AMIGA sample is defined by strict isolation criteria, and shows it different physical properties at all wavelengths studied so far from galaxies in denser environments (even field galaxies). These ten galaxies are located in the region of lower tidal forces and number density of AMIGA full sample (Fig. 6 in Verley et al. 2007).

Our non-interacting sample includes different morphological types, bar strengths, and a relatively wide range of luminosities ($-24 \lesssim M_{r,p} \lesssim -19$). Morphological types and bar strengths were obtained by visual inspection of the SDSS $r$-band images by different members of the collaboration (Walcher et al. 2014, see also Table A.2). The sample is dominated by Sbs and Sc morphological types, which are also the dominant population of the AMIGA sample, hence characteristic of isolated galaxies. Finally, from a visual inspection of the velocity maps we excluded the early-type galaxy NGC 5623 from our sample. This galaxy presents a stellar counter-rotating disc, presumably originating in an early encounter, and it will be thus included in the sample of interacting galaxies (see Sec. 2.3).

## 2.3 Interacting and Merging Sample

### 2.3.1 Evolutionary scheme of galactic merging

Our aim is to study the physical properties of the interacting and merging galaxies evolve in the course of the merging event. Therefore, we need to set an evolutionary scheme for the merger. For this study we used a morphological classification introduced by Veilleux et al. (2002), based on n-body simulations of the merger of two spiral disk galaxies (Surace 1998, and references therein). It was introduced to analyse a sample of (U)LIRGs and it is still used for studies related to these objects (e.g., Arribas et al. 2008; Yuan et al. 2010; Haan et al. 2011). This classification cannot be used as a strict time sequence but rather as an indicator of the interaction/merging stage.

In Fig. 2.4 we show an example of this evolutionary scheme using the r-band Sloan Digital Sky Survey (SDSS) images as well as the stellar and ionised gas velocity fields. The main features of each stage are highlighted as follows:

• **Pre-merger stage:** the morphology in both galaxies of the pair remains unperturbed and separated. There is no clear evidence of tidal tails or any other visual feature of interaction. Note that this stage also includes systems where the galactic disks overlap in the line-of-sight (e.g., VV488 in Appendix A.3).

• **Merger stage:** two nuclei are identifiable and well-defined tidal tails and other merging structures such as bridges or plumes are readily seen in the optical images. While the pure morphological data do not guarantee that nuclei will necessary merge, the presence of these strong interacting features indicate an eventual merger.

• **Post-merger stage:** occurs after the nuclei have apparently coalesced. These systems have prominent tidal features, but only one nucleus can be clearly seen in the optical images. Moreover, the nuclear emission can be extended and cut by dust lanes.

• **Merger remnant stage:** galaxies display faint tidal features or evidence of previous interaction. Any possible tidal feature is close to the detection limit and the main brightness profile is

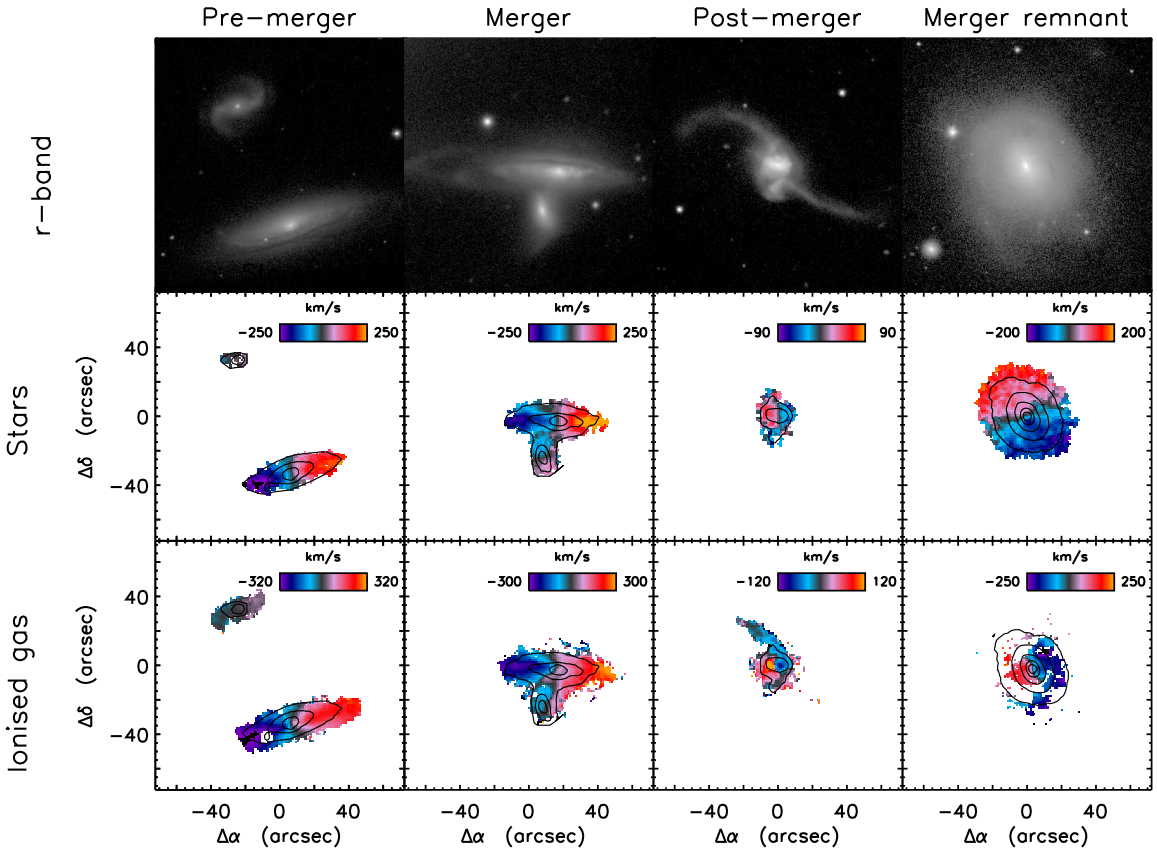


Figure 2.4: Example of the evolutionary scheme for interacting and merging galaxies described in Sec.2.3.1. Top: SDSS r-band images of galaxies included in the CALIFA survey, from left to right: Pre-merger stage, well-defined separation between the galaxies, no evident interaction signatures (IC 0944 and KUG 1349+143); Merger stage: two defined nuclei with evident interaction features (NGC 169 and NGC 169A); Post-merger stage, single extended nucleus in optical with prominent tidal features (NGC 2623). Merger remnant stage, possible tidal debris (NGC 5739). Middle: stellar velocity fields. Bottom: H$\alpha$+[NII] velocity field for each galaxy example. Contours represent the continuum obtained from the data cubes. Note that for these objects the velocity field distributions are extracted from a single IFU data cube, except for the pairs of galaxies in the pre-merger stage, where each galaxy has its own IFU data cube. Size of each box is 2 arcmin. Top is north and left is east.

given by a relaxed system such as that for an elliptical galaxy.

Several remarks have to be taken into account for this evolutionary scheme. First, from numerical simulations, Lotz et al. (2008) found similar trends in the evolution of the morphology of equal-mass gas rich mergers. However, they note that morphologies are specially disturbed at the first passage of the galaxies and right after the nuclei coalesced. Then, by visual inspection one may classify interacting galaxies after the first passage as a pair of galaxies prior to this event. Second, even though this scheme is drawn from numerical simulations of two disk spiral galaxies, we used it also for galaxies of different morphology (e.g., early- and late-type binary systems), we stress that the scheme has to be taken only as a broad indicator of the merger event. Third, the structure of the merger remnants can vary in a wide range of morphologies, depending primarily on the mass-ratios and the gas fraction of the progenitors (Hopkins et al. 2009a,b). For modest gas fractions, the merger remnants are likely to resemble spheroidal-like galaxies (e.g., Naab et al. 2006; Duc & Renaud 2013) while for gas-rich equal-mass merger remnants their morphology can be similar to disk-like galaxies (Lotz et al. 2008). We attempt to include both of these morphological types in the merger remnant stage (see Sect. 2.3.2).

By construction of the CALIFA sample, we are able to distinguish tidal features down to a certain surface-brightness limit. In our case this limit is $\sim 25$ mag arcsec$^{-2}$ (see Sec. 2.3.2). With this limit we will focus mainly on a major merger event that probably occured at $\sim 2.5$ Gyr ago (Ji et al. 2014). The lack of deeper imaging for the morphological selection of interacting galaxies can bias our selection. In particular, for the merger remnant stage, we select objects with long lasting tidal features. To detect merger remnants caused by a collision leaving weaker tidal features deep optical imaging is required (e.g., Atkinson et al. 2013; Duc et al. 2015). Although tidal-features can be caused by major mergers, they can also be the result of a minor merger event (e.g., Ebrova 2013). Numerical simulations as well as observational data suggest that morphological signatures such as shells in early-type galaxies can be caused by minor mergers (for instance in NGC 3923, Bílek et al. 2013).

### 2.3.2 Selection and Properties

The interacting sample was selected from 256 objects observed before March 2013[2]. Most of these galaxies are included in the CALIFA mother sample. As we explain below some other companions that were not included in this sample have also been observed.

We consider as objects in pairs those objects with companions within a projected distance of 160 kpc, systemic velocity difference smaller than 300 km s$^{-1}$ and difference in $r$-band magnitude smaller than 2 mag[3] (relative distances, systemic velocities and magnitudes were taken from NED [4]). The above selection parameters were taken as thresholds from previous galaxy-pair studies. The projected distance is motivated by pair studies suggesting tidal effects of companion's properties such as star formation rates up to 150 kpc (Patton et al. 2013). For the systemic velocity difference criterion, we use the threshold defined in large surveys of galaxy pairs (e.g., Ellison et al. 2008b, 2013a). These criteria yield 66 objects located in the pre-merger and merger stages. In 16 objects, more than one companion of the CALIFA object satisfies the criteria (i.e. triplets). In these cases, we selected as the companion object either the closest (or the brightest) object to the CALIFA source. Since our primary aim is to study properties of galaxies during a major merger we avoid to

[2]it also includes two galaxies observed in June and October of the same year: $NGC5623$ and $NGC7711$

[3]except for the systems Arp 178 (NGC 5614 / NGC 5615) and UGC 10695 where the differences in magnitude is of the order of 3 mag, however, signatures of interaction are evident.

[4]NASA/IPAC Extragalactic database. http://ned.ipac.caltech.edu/

select objects located in compact groups.

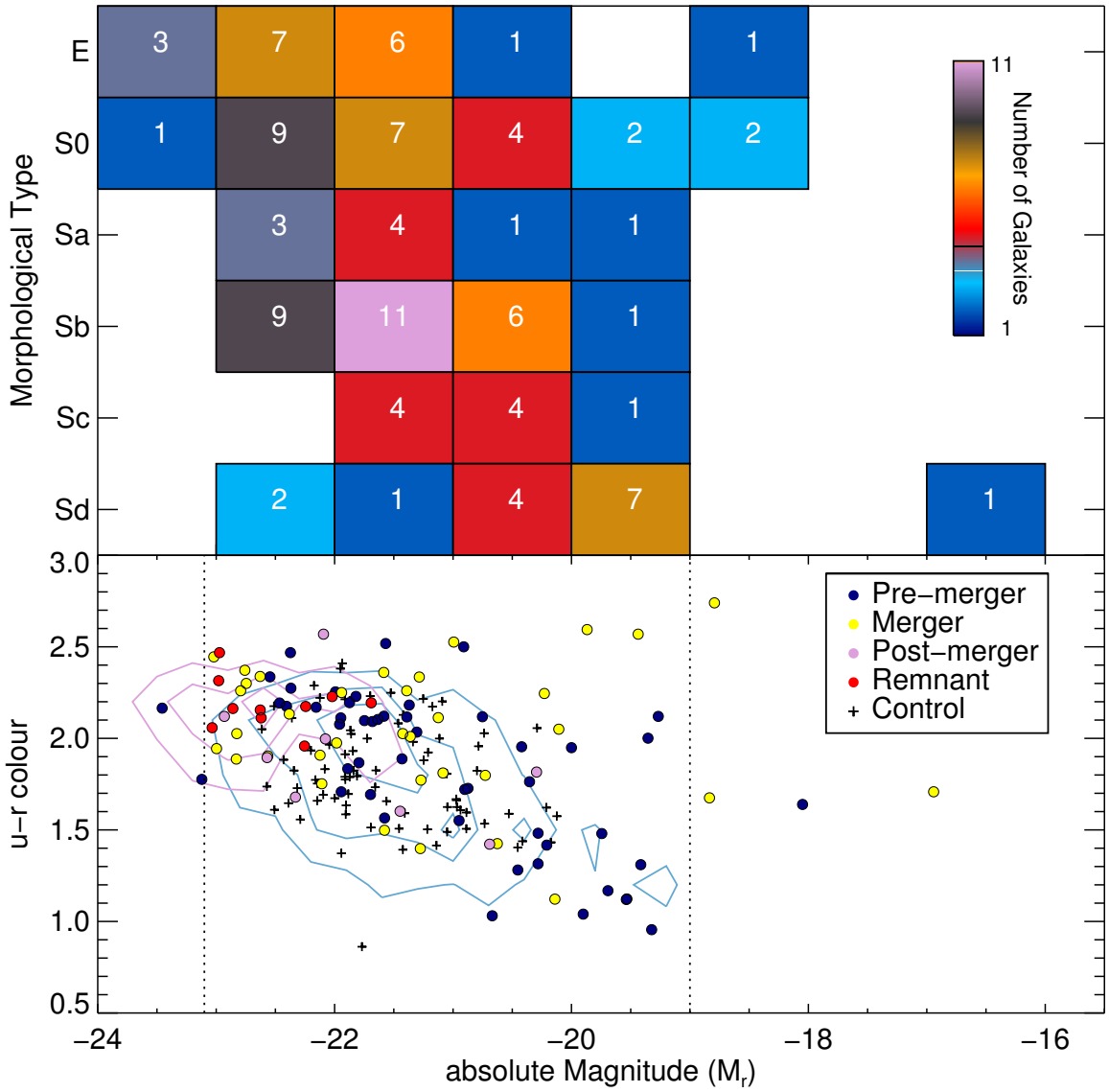


Figure 2.5: Top: Morphological type distribution against SDSS $r$-band absolute magnitude distribution of the interacting sample. The number in each bin represents the sources included on it. Bottom: Colour Magnitude Diagram for the CALIFA MS, control and interacting samples. Morphologies and absolute magnitudes are taken from Walcher et al. (2014). Blue, yellow, pink and red represent pre-merger, merger, post-merger and merger remnants stages, respectively. Plus symbols represent the control sample. For comparison we plot the density contours of the CALIFA MS. Red and blue contours represent the early- and late- type galaxies. Each of the contours represent the 25 %, 50% and 75% of the mother sample. Dotted vertical lines represent the range in absolute magnitudes where the CALIFA MS is representative of the overall galaxy population (Walcher et al. 2014).

From the objects in early interaction stages (pre- and merger) only 12 binary systems have both companions observed. In 6 pairs both companions are included in the CALIFA sample, and in 6 pairs the field-of-view (FoV) of the IFU is large enough to observe both galaxies. To alleviate this lack of complete pairs, we observed in a CALIFA complementary project those companions not included in

the mother sample (P.Is J.K. Barrera-Ballesteros and G. van de Ven). For this study we include 13 additional companions observed and reduced with a similar procedure to the CALIFA galaxies (see Secs. 2.1.2 and 2.1.3). In total there are 19 additional objects. The final number of objects between the pre-merger and merger stage is 85 (see Table 2.1). Note that despite our attempts to observe both companions of the binary systems, some of them have IFU data available only for one of the galaxies.

From the remaining sample of galaxies (i.e., those objects with no close companions of similar brightness) we select the post-merger subsample. We used their SDSS r-band images to classify by visual inspection objects with tidal features like those described above in Sect. 2.3.1. In particular, for the post-merger stage we did not include "normal" irregular galaxies [5] (i.e., those objects that even though they are irregular do not seem to be the result of a merger event, but rather clumpy disks, for an example see Fig. 2 in Ellison et al. 2013a). We include in our sample the object NGC 5623: even tough it does not present any signature of interaction nor close companions, its kinematics in both components does not resample the kinematic expected for a non-interacting object (see Sec. 2.2). It shows signatures of a stellar kinematic decouple core (KDC). The complete sample of interacting galaxies included in this study consists of 103 objects. In Table 2.1 we present the number of individual objects in each interaction stage while in Table A.2 we summarize the main properties of our interacting sample.

In the top panel of Fig. 2.5 we plot the distribution of the interacting sample according to their morphological type and SDSS $r$-band absolute magnitude. The sample covers a wide range of morphologies and luminosities. Morphologies were obtained by visual inspection from five members of the collaboration (Walcher et al. 2014). Note that they assigned regular morphological types to the sample of interacting galaxies. Pre-merger galaxies are expected to have a clear position in the Hubble sequence. For merger objects with evident signatures of interaction, they assigned a Hubble type to the central part of the companions. Post-merger objects with distorted morphologies (e.g., NGC 2623) were tagged as very late type spirals (Sc-Sd) owning a wide range of classifications from irregular to elliptical. We use the classification by Walcher et al. (2014) noting that for this particular objects there is a large uncertainty in the morphological classification. Absolute magnitudes and stellar masses for the CALIFA objects are obtained using a growth curve analysis based on SDSS-DR7 *ugriz* images (see details in Walcher et al. 2014). The estimates of these quantities for the CALIFA companions in binary systems were derived using a mask to obtain only the flux of individual target. For companions not included in the CALIFA MS, absolute magnitudes and stellar masses were derived using petrosian magnitudes from the SDSS-DR7 corrected to obtain similar magnitudes as those derived in the CALIFA MS (Walcher et al. 2014, see their Fig. 13).

| | | Interaction Stage | | | |
|---|---|---|---|---|---|
| | Total | pre merger | merger | post merger | remnant |
| Individual objects | 103 | 49 | 36 | 8 | 10 |
| Stellar Kinematics | 85 | 36 | 32 | 7 | 10 |
| Ionised gas Kinematics | 82 | 37 | 28 | 8 | 9 |

Table 2.1: Summary of the available kinematic data for the sample of interacting galaxies presented in this study. First row shows the number of individual objects in each interaction stage. The second and third rows present the available stellar and ionised gas velocity fields.

[5] UGC 4722, and NGC 7800

### 2.3.3 Interacting *vs* Mother and Control samples

Both, isolated and interacting samples are drawn from the CALIFA MS. As we pointed out in Sec. 2.1.1, the CALIFA MS is representative for the general galaxy population within the following limits: -19.0 to -23.1 in r-band absolute magnitude, 1.7 to 11.5 kpc in half light radii, and 9.7 to 11.4 in log(stellar mass $/M_{\odot}$). In the bottom panel of Fig. 2.5, we compare the CALIFA MS, control and interacting samples in the colour-magnitude diagram. We also mark the range of absolute magnitudes where the CALIFA MS is representative of the galaxy population. A large fraction of the objects from both control and interacting samples are within this range. In general, the galaxies at different interaction stages spread homogeneously across the colour-magnitud diagram except for the late merger remnants. Note that galaxies at this stage tend to lie in the red sequence rather than the blue cloud. The control sample also shares similar colors to the interacting sample.

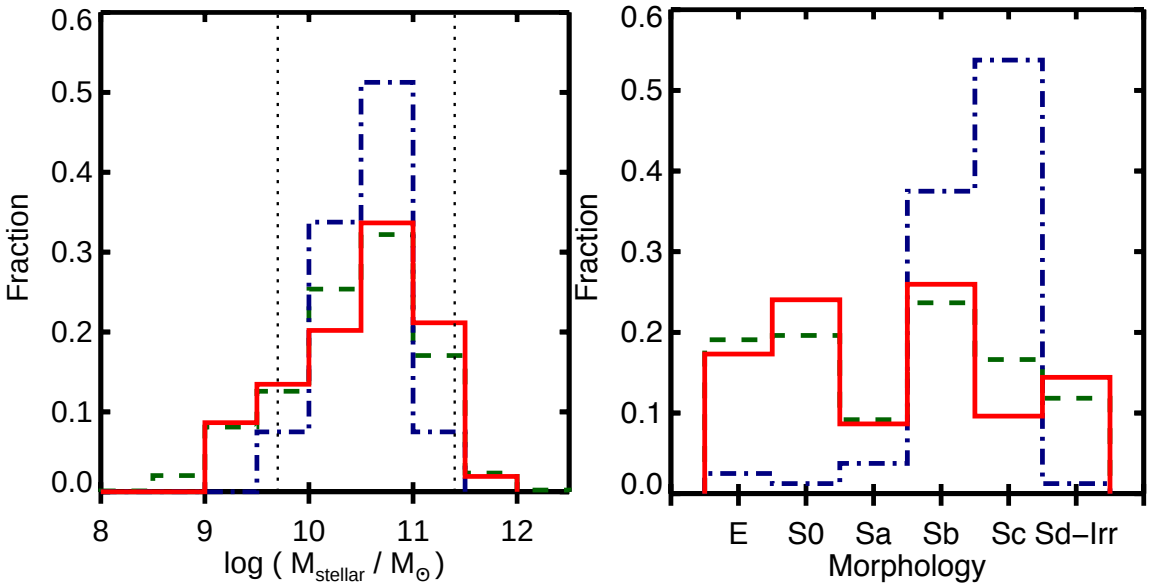


Figure 2.6: Comparison between CALIFA MS (green-dashed lines), control sample (blue-dotted-dashed lines) and interacting samples (red-solid lines). *Left:* Stellar mass distributions for these samples. Stellar mass for each galaxy is taken from Walcher et al. (2014). Vertical lines represent the stellar mass range where CALIFA MS is considered as representative of the nearby-galaxy population. *Right:* Morphological distributions of the three samples.

In top panel of Fig. 2.6 we show the stellar mass distribution of the CALIFA MS, control and interacting samples. Control and interacting distributions peak at similar stellar masses ($M_{stellar} \sim 10^{10.8}$ $M_{\odot}$ ). Most of the objects in both samples have their stellar masses within the range where the CALIFA MS is representative for the general galaxy population. However, a Kolmogorov-Schmirnoff test (KS-test, hereafter) reveals that these distributions are not probably drawn from the same distribution ($p_{KS} = 0.005$). Similarly, it is unlikely that control and CALIFA MS stellar mass distributions are drawn from the same distribution ($p_{KS} = 0.02$). The distribution of the control sample is narrower in comparison to the interacting one. On the one hand, the observations of interacting galaxies not included in the CALIFA MS allow low-mass galaxies to be part of this sample. Excess in the high-mass tail of this sample is caused by early-type galaxies not present in the isolated sample. On the other hand, isolated galaxies usually display narrow distributions in their physical properties with respect to other samples in different environments (e.g., Espada et al. 2011; Fernández Lorenzo et al. 2012). The latter is also evident when we compare the morphological type of these three different samples (see bottom panel of Fig. 2.6). The morphological

type selection of the control sample is restricted basically to late-type spiral galaxies with a clear lack of elliptical, lenticular and irregular galaxies, while the CALIFA MS and interacting samples spread over a wide range of morphologies. We consider that larger samples, in particular for the isolated galaxies, would be required to probe the kinematic in low/high stellar masses regimes of the interacting sample.

## 2.4 Methodologies

As we described above, to compare the spatially resolved properties of the interacting galaxies with those derived in the isolated sample it is necessary to use a unique method to extracting these properties from the data cubes in both samples as well as homogenous strategy to measure physical parameters. In this section we provide a brief description of the techniques used to extract the stellar and ionized gas velocity fields. We also introduces a method to measure kinematic properties from those velocity fields without assuming any intrinsic velocity pattern. Finally, we explain the techniques to extract the flux maps from several emission lines as well as the equivalent width of H$\alpha$ which we uses as a surrogate of the specific star formation rate.

### 2.4.1 Stellar Kinematic Extraction

The stellar kinematic extraction method for the CALIFA survey will be presented in Falcón-Barroso et al. (in prep.). Here we highlight the main steps. Spaxels with continuum S/N $< 3$ in the original V500 cube were unreliable and therefore not considered in further analysis. To achieve a minimum S/N of 20, we used a Voronoi-binning scheme for optical IFS data implemented by Cappellari & Copin (2003). We will refer to these Voronoi bins as "voxels". From this selection in the continuum S/N, a large fraction of the voxels ($\sim$80%) have the same size as the spaxels of the cube. The remaining fraction of the voxels are located in the outer regions of the galaxies and include a range between three or five spaxels.

To derive the line-of-sight velocity maps, for each data cube, a non-linear combination of a subset of stellar templates from the Indo-U.S. library (Valdes et al. 2004) is fit to each voxel using the penalized pixel-fitting method (pPXF, Cappellari & Emsellem 2004, see Fig. 2.7). Errors for each voxel, determined via Monte Carlo simulations, range from 5 to 20 km s$^{-1}$ for inner to outer voxels, respectively. Note that these uncertainties are smaller than the spectral sampling per spaxels from the data cubes. Since each spaxel offers a wide range of absorption lines to fit its line-of-sight velocity, the spectral location of these absorption features can be determine even at scales smaller than the spectral sampling. Figure 2.4 (middle panels) shows an example of stellar velocity fields for different galaxies at different stages of the merging sequence.

### 2.4.2 Ionized Gas Kinematic Extraction

The detailed description of the ionised-gas kinematic extraction method for the CALIFA survey is provided by García-Lorenzo et al. (2015). To obtain the ionised-gas emission in each spaxel we subtracted the stellar continuum spectra derived from the best stellar pPXF fit in its corresponding voxel (see left panels in Fig 2.8). No binning was done for the ionized gas. We assumed that the distribution of the stellar populations in each voxel is rather smooth and do not change from spaxel to spaxel within each voxel. A cross-correlation (CC) method is used to measure the velocity of the ionised-gas (see García-Lorenzo 2013, for details of the procedure). The method compares the spectrum in each spaxel in a given wavelength range with a template that includes the H$\alpha$+[NII]$\lambda\lambda$6548,6584 emission lines (6508$-$6623Å). The template corresponds to a Gaussian

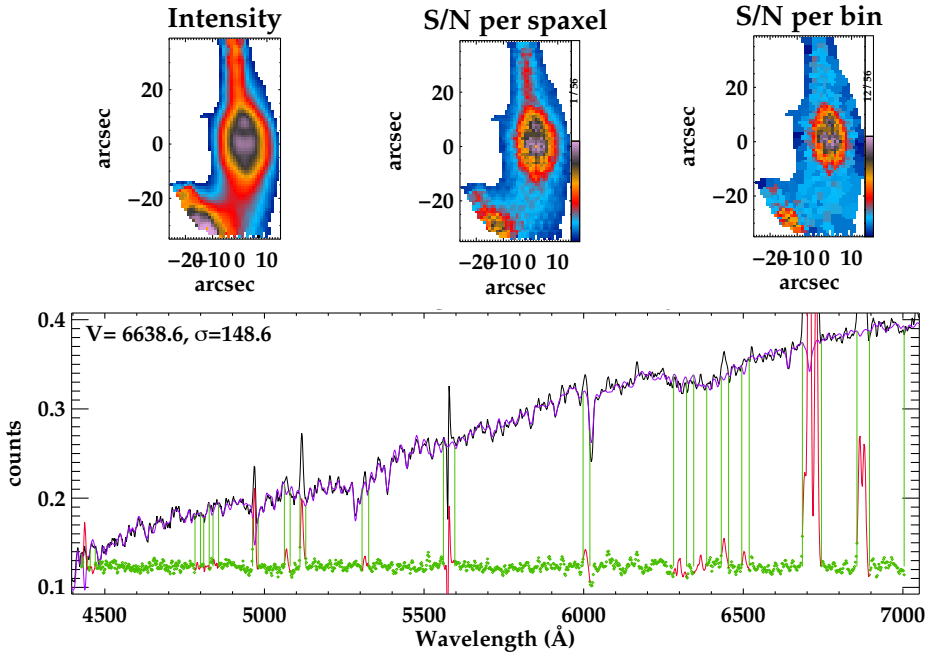


Figure 2.7: *Top:* Example of the data extracted from the ppxf-based CALIFA kinematic pipeline for NGC 4676 data cube. Besides the stellar velocity and velocity dispersion this pipeline also provides an estimate of the continuum intensity (*left*), signal-to-noise per spaxel (*middle*) and per bin (*right*) for the target. *Bottom.* Example of the fitted continuum. Black line shows the observed spectrum which includes the continuum (stellar) and emission lines (ionized gas) components. Purple line shows the best continuum spectra provided by ppxf. Vertical windows show the masked regions in the spectra. These regions are masked either to avoid emission lines or telluric lines (red lines) during the continuum fitting.

model for each emission line in the given wavelength range, shifted to the systemic velocity reported in NED and assuming a velocity dispersion equal to the instrumental resolution ($\sigma \sim 90\,\mathrm{km\,s^{-1}}$ at the H$\alpha$ emission line). We selected spaxels with S/N $>$ 8 in this emission line for the ionised gas velocity maps. Note that this method allows the measurement of the systemic velocity from different ionized species (see right panels in Fig 2.8). García-Lorenzo et al. (2015) present examples of the kinematic fitting per spaxel and the extraction of the ionized gas component. Figure 2.4 (bottom panels) show examples of an ionised-gas velocity fields. Estimated uncertainties in the location of the maximum of the CC function are $\sim$10 $\mathrm{km\,s^{-1}}$. As the pPXF method, the CC is also able to determine the velocity dispersion maps however, due to the low spectra resolution of the V500 data we did not attempt any further analysis of these maps.

### 2.4.3 Direct Estimation of the Kinematic Parameters

Qualitatively, a large fraction of galaxies in the CALIFA survey shows a global receding-approaching velocity field resembling that of rotating systems or, at least, ordered motions. Nevertheless, departures from circular/ordered motions are evident in many objects in the form of clear kinematic distortions in the velocity fields. For the sake of uniformity in the kinematic analysis of both the isolated and interacting samples, a simple approach has been adopted to estimate the kinematic parameters observed in the plane of the sky directly from the measured radial velocities.

In the past years, several analytic methods have been developed to determine kinematic pa-

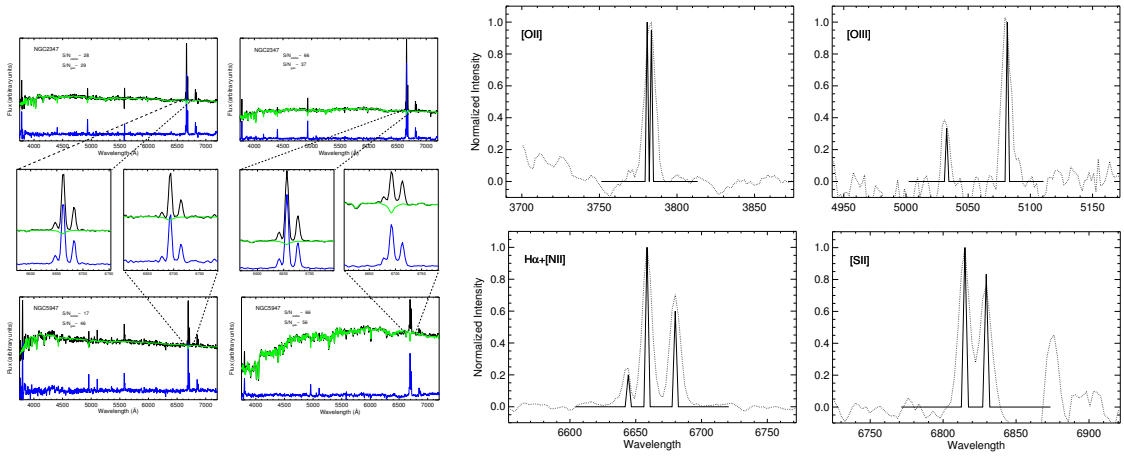


Figure 2.8: *Left:* Spectra of different signal-to-noise ratio in both the stellar and the ionized gas component of the galaxies NGC 2347 and NGC 5947. The panels show the full spectra (black lines), the continuum spectral fitting derived from the ppxf pipeline (green lines) and the residual spectra (blue lines). Middle panels show zoom frames at the H$\alpha$+[NII] region. *Right:* Templates (solid lines) generated from gaussian functions to simulate the emission in four ranges of the spectra (dotted lines). Figures taken from García-Lorenzo et al. (2015).

rameters from two-dimensional velocity distributions. For late-type galaxies, these models often consider a symmetric velocity distribution, either by assuming a thin disc geometry (e.g., Barnes & Sellwood 2003; Epinat et al. 2008) or symmetrical radial distortions with respect to some axis (Spekkens & Sellwood 2007). An alternative approach is a generalization of the isophote fitting (i.e. the standard task ellipse of IRAF) to higher-moments of the LOSVD, which assumes that along a best fitting ellipse the odd moments (such as velocity) follow a simple cosine law (Krajnović et al. 2006). Since our wish is to measure kinematic position angles separately on both the approaching and the receding sides of the galaxy, we use here a different approach.

We want to establish the observed (i.e., projected) typical ranges of kinematic parameters expected for isolated and interacting galaxies. From those kinematic values, we will be able to shed some light on the possible kinematic distortions induced by an interaction. Below we provide a quantitative characterization of the kinematics of galaxies through parameters derived directly from their stellar and ionized gas velocity distributions. No assumption about the behavior of the galactic components is made. We use the same method on our sample of interacting galaxies in order to make a consistent comparison. A rotational velocity field can be characterized by several parameters: kinematic centre, systemic velocity, global orientation of the field (i.e., kinematic PA), and its inclination with respect to the sky's plane. We restrict ourselves only to projected kinematic parameters of our samples. We consider that an estimate of the inclination via the velocity distribution would require assuming intrinsic behavior of the kinematic component (e.g., tilted-ring modeling, Józsa et al. 2007). Although this could be the case for some of the non-interacting galaxies presented in this study (but restricted only to the ionized gas component), it might not be the case for highly asymmetric velocity fields, such as those exhibited by interacting/merging galaxies. In this work, we focus mainly on characterizing the velocity fields via the kinematic PAs of their different components.

**Kinematic Centre:** To determine the global orientation of the velocity maps, it is first necessary to set the kinematic centre. For an ideal rotating disc the kinematic centres should be at the position with the largest velocity gradient (or gradient peak, GP hereafter), it also should be coincident with the optical nucleus. Based on this idea and in order to estimate the location of the

kinematic centre of our galaxies, the average directional derivative of both the stellar and ionized gas velocity fields were computed by calculating the average absolute difference of the velocity for each spectrum with the velocity of the surrounding regions. The resulting image (velocity gradient image hereafter) emphasizes those regions in the velocity field where the data are changing rapidly. Therefore, for galaxies showing regular motions, the peak of the average directional derivative image (velocity gradient peak, GP hereafter) should indicate the kinematic centre (Kutdemir et al. 2008; Arribas et al. 1997).

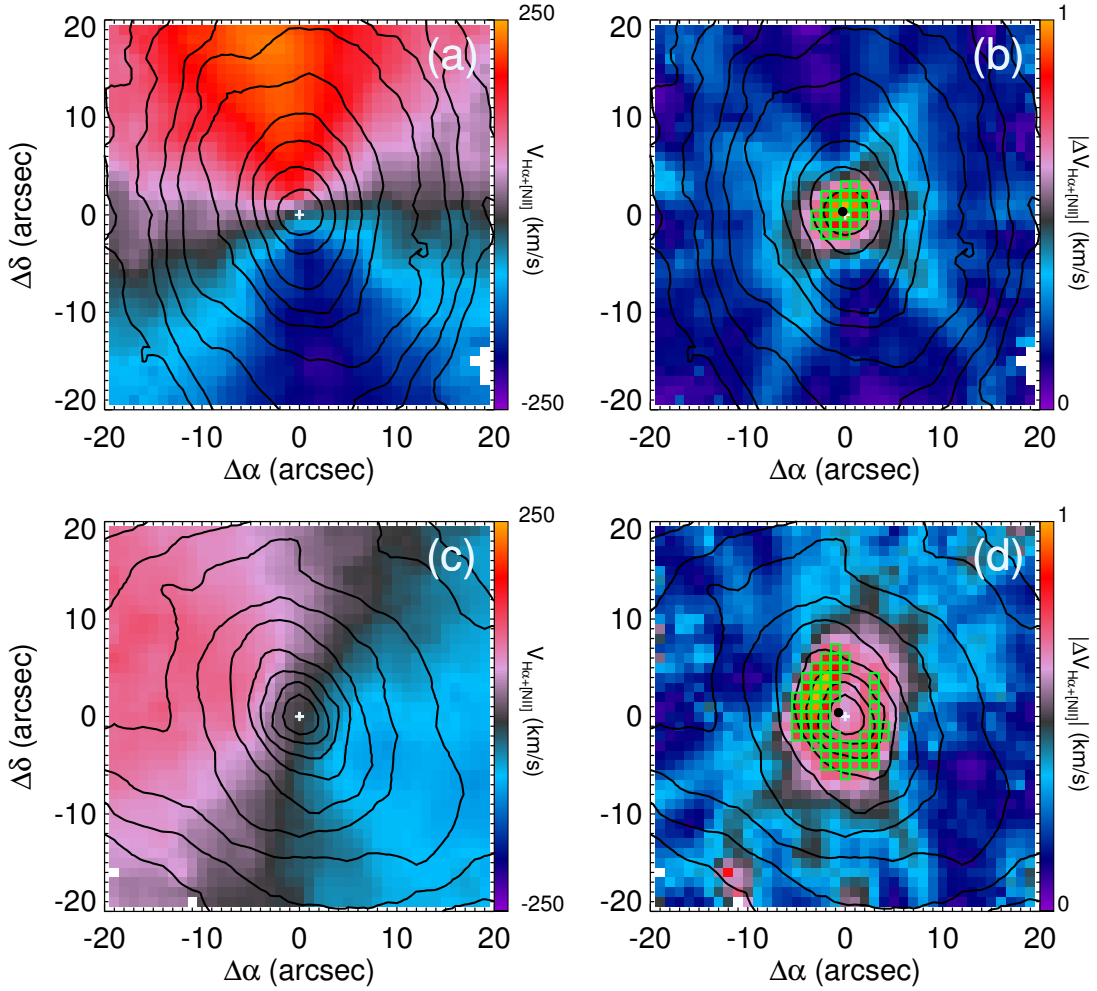


Figure 2.9: Example of the estimation of the kinematic center position for a galaxy with a single gradient peak (NGC 2347,panels a and b) and an object with a ring-like structure in its velocity gradient map (NGC 5947). Left panels show the ionized gas velocity field (determined using the CC in the H$\alpha$+[NII] region). Right panels show the velocity gradient maps. Green open squares indicate the velocity gradient pixels used to estimate the location of the gradient peak through the average of their positions weigthed by their gradient values. Contours from the stellar continuum are overlapped. The white plus sign marks the location of the optical nucleus (peak of the stellar continuum) and the black circle indicates the estimated KC position. Figures taken from García-Lorenzo et al. (2015)

To obtain the GP, in a region of $10'' \times 10''$ centered on the optical nuclei we determine the velocity gradient in each spaxel with respect to the surrounding spaxels. Then, we select the positions where

the velocity gradient is larger than its average inside this box. The presence of several velocity gradient peaks in the velocity field of a galaxy is then identified as a clear departure from pure rotation. We note that in many cases the velocity gradient distribution shows the optical nucleus surrounded by a ring-like or a bar-like structure of large velocity gradient values. Then, the GP is estimated from the weighted average location of the selected positions, using the velocity gradient at each location as weights (see Fig. 2.9). Finally, as kinematic centre we chose either optical nucleus ON or GP, depending on the best symmetry of the rotational curve (see details below).

**Position Angle of Kinematic Axes:** The major (projected) kinematic axis ($PA_{kin}$, hereafter) provides a measurement of the global kinematic orientation. It can be determined directly from the positions of the spaxels defining the kinematic lines of nodes (Nicholson et al. 1992). In practice, we plot the radial velocity for all the spaxels up to a given radius in a position-velocity diagram centered in the kinematic centre previously assigned (see right panel of Fig. 2.10). We then choose those spaxels with the maximum (minimum) projected velocity at the receding (approaching) side at different radii. Finally, for each side, we identify the selected spaxels in the velocity map. The average of their polar coordinates provides an estimation of $PA_{kin}$ and their standard deviation ($\delta PA_{kin}$) measures the scatter of these points around the straight line defining the kinematic PA. Following a similar procedure, we also determine the minor (receding and approaching) kinematic PA by selecting the spaxels with the lowest velocity differences respect to the kinematic center.

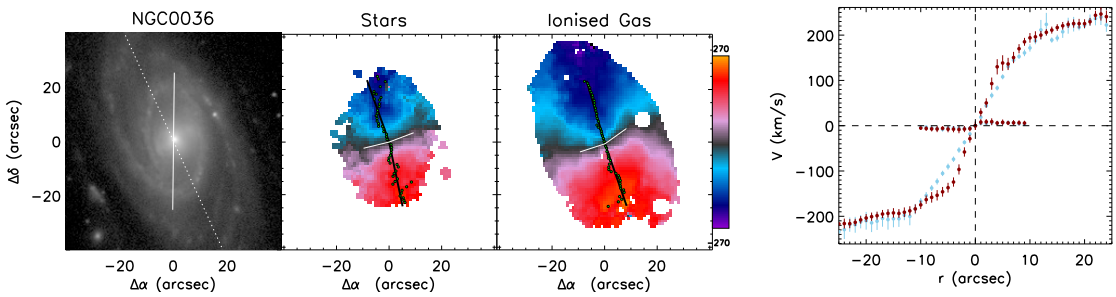


Figure 2.10: Example of the method used to determine projected kinematic position angles (PAs) from the velocity maps of the galaxy NGC 36. Left most panel shows the SDSS $r$-band image of the galaxy. White solid line represents the photometric PA measured at the same galactocentric distance as the kinematic PA ($PA_{morph}$, measured from the $r$-band image; see section 2.4.3). Dashed line represents the photometric PA measured at the outermost isophotes of the image ($PA^{out}_{morph}$, see section 3.2.6). Middle-left and middle-right panels show the stellar and ionised gas velocity maps, respectively. Green points highlight the locations where the maximum velocity is located at given radius, determined from the position-velocity diagram. Black lines for each kinematic side represent the average kinematic PA ($PA_{kin}$), while white thin lines along the zero-velocity curve show the average minor kinematic PA. Right panel shows the distance from the galactic centre versus the maximum for the stellar (blue points) and ionised gas (red points) components. The curve along $0\,km\,s^{-1}$ represent the velocities along the zero-velocity curve. The error bars represent the uncertainty in velocity determined from Monte Carlo simulations.

To compare the stellar and the ionized gas kinematic PA we pick the common maximum radius where both components can be measured. Although $PA_{kin}$ is usually defined as the angle between the north and the receding side of the velocity field (e.g., Schoenmakers et al. 1997), for the sake of homogeneity, we report the approaching and receding kinematic PAs independently ($PA_{kin,app}$ and $PA_{kin,rec}$) between 0 and 180 degrees from North to East. Typical errors in $PA_{kin}$ and $\delta PA_{kin}$ are of the order of 7 ° obtained from Monte Carlo simulations. We have also investigated the uncertainties introduced by the Voronoi binning in the stellar velocity maps (by artificially increasing the level of binning in a few of our galaxies) and established that they could bias the determination of $PA_{kin}$ at most 4°.

### 2.4.4 Ionized Gas Fluxes and H$\alpha$ Equivalent Width Extraction

Besides the kinematic properties of the isolated and interacting samples we also compare the properties of the ionized gas between these two samples. To extract the flux from the ionized gas emission lines we use the FIT3D package (Sánchez et al. 2006, 2011). Basically, this software is aimed at disentangling in the spatially resolved spectra the light coming from the stellar population and the emission from the ionized gas. The continuum and absorption features are modeled with a linear combination of synthetic stellar population (SSP) spectra while the emission lines are assumed to be single gaussian functions.

A basic step in the stellar population fitting method is to assign weights or eigenvalues to each spectra in a library of SSP. Note that in order to make the fitting it is also necessary to determine a velocity distribution function which is convolved to the SSP spectra. If the weights turn out to be negative during the fitting, this SSP spectrum is rejected and the fitting is performed once again. This approach provides a reliable subtraction of the contribution of the stellar population in the observed spectra. In the current version of the package, it uses a Monte-Carlo (MC) approach which fits a randomized version of the spectrum by means of the error vector. The final modeled stellar spectrum is the linear combination of the SSP using the average weights from the Monte-Carlo approach. To model the continuum FIT3D masks some regions of the spectrum such as: strong variable night sky emission line residuals, regions affected by instrumental signatures such as defects in the CCD, regions affected by telluric absorptions which were not completely removed during the flux calibration process and regions containing strong emission lines.

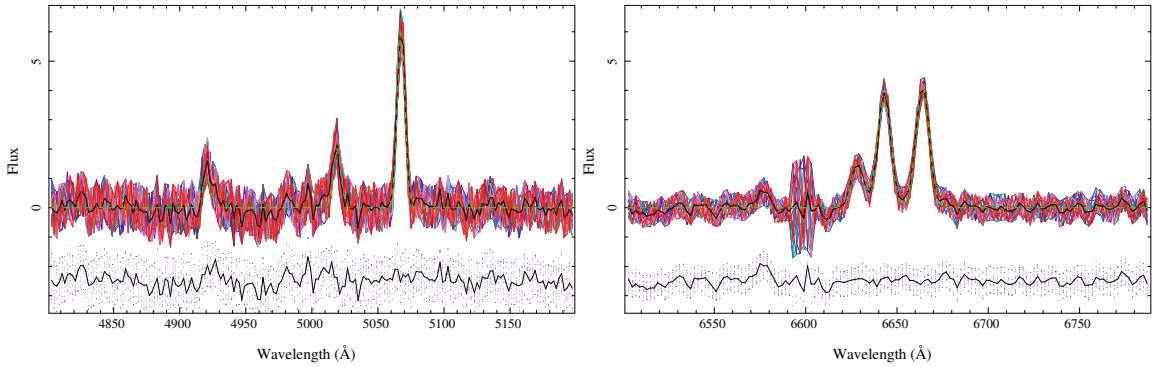


Figure 2.11: Examples of the FIT3D fitting technique used in two spectral regions with emission lines: H$\beta$ and [O III]$\lambda\lambda$4959,5007 (*left*) and H$\alpha$ and [N II]$\lambda\lambda$6548,6583 (*right*). Both panels show the central spectra (integrated in a 5 arcsec aperture) of NGC 2916 with continuum light removed (black line). Different MC realizations of the spectrum are overploted (color-coded points). Best fitted model to the emission lines is shown in green dashed lines. The residual for each MC realization are showed with the same color code and -2.5 flux units offset for clarity.

Once the contribution of the modeled stellar spectrum is subtracted from the original spectrum, it is possible to determine the properties of the ionized gas emission lines. The intensity of each emission line is fitted to a single gaussian function. These emission lines are fitted splitting the non- and linear components. As for the stellar population, the non-linear components includes the velocity and velocity dispersion while the linear component is the intensity. The fitting procedures perform an exploration of the non-linear parameters within a range of values, using an initial guess for the systemic velocity and velocity dispersion. In each step of this exploration a least-square fitting is performed to determine the linear parameter (i.e., the intensity). The reduced $\chi^2$ is stored in each iteration and the final combination of non-linear and linear parameters is chosen based on the minimization of this parameter. The errors in the determination of the parameter for each

emission line takes into account the error vector as well as the error derived in the derivation of the modeled continuum. We obtain the fluxes for the following lines: H$\alpha$, H$\beta$, [O III] $\lambda\lambda$ 4959, 5007, and [N II] $\lambda\lambda$5755, 6584. The analysis, including errors, was performed in a spaxel-by-spaxel basis which allows us to create flux maps for each of these emission lines, once subtracted the underlaying stellar population as explained above (see an example of emission-line maps in Fig. 2.12). We derive the EW(H$\alpha$) in each spectrum by dividing the H$\alpha$ flux by the average of the continuum emission adjacent to H$\alpha$ emission line. This average continuum was derived by measuring the mean flux of the continuum in spectral windows of 30 Å centered at blue-shifted and redshifted 100Å away from the H$\alpha$ emission line.

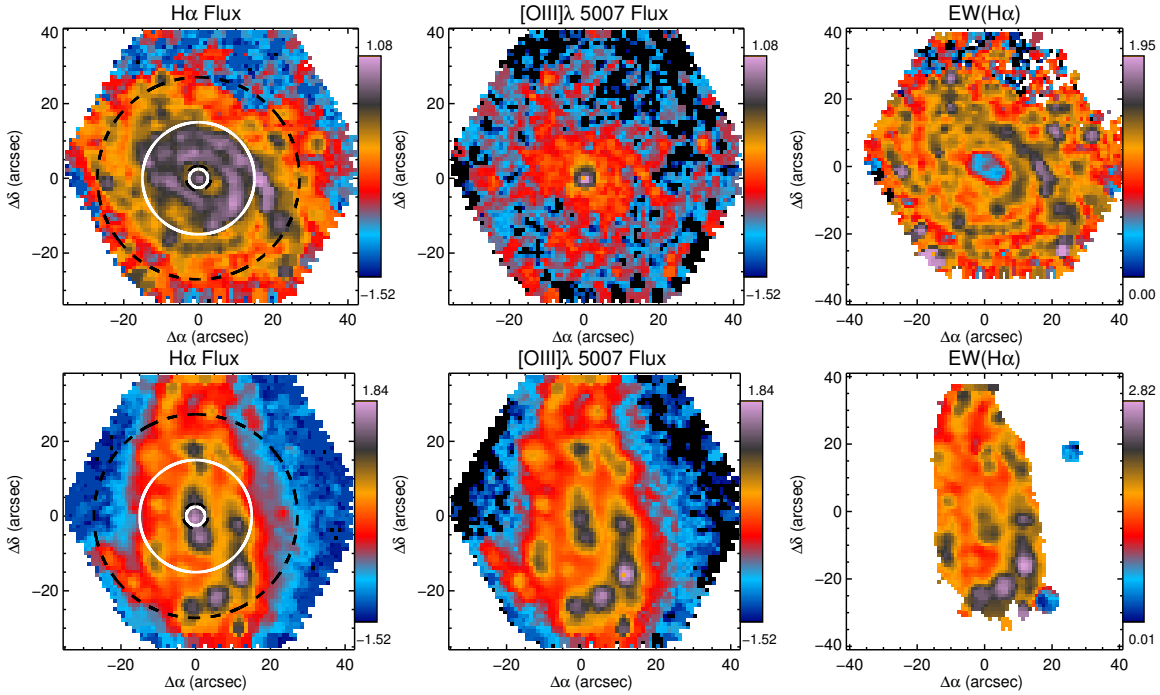


Figure 2.12: Emission line maps of a galaxy in the control sample (top panels, NGC 0214) and in the interacting sample (left panels, UGC 312). Left panels show the H$\alpha$ flux. White-solid and black-dashed circles represent the central and extended apertures in arcsecs and effective radius units, respectively. Middle panel shows the [O III]$\lambda$ 5007, emission line flux. The units in both flux maps are (log10) $10^{-16}$ erg s$^{-1}$ cm$^{-2}$ arcsec$^{-2}$. Right panels show the logarithm of the absolute values of EW(H$\alpha$) in units of Å.

### 2.4.5 EW(H$\alpha$) and oxygen abundance measurements in 2D maps

Figure 2.12 shows an example of the wealthy of the data provided by the data cubes. Even for a single galaxy, several structures can be observed in the emission line maps and the EW(H$\alpha$) which is a proxy for the specific star formation rate. However, in this study we constrain ourselves to integrated properties for each galaxy. Studies exploring the star formation and ionized gas two dimensional distributions in interacting galaxies will be lead for future works. Thus from the emission line flux maps we obtain the integrated properties for each galaxy. We select those spaxels with error smaller than 10% of their flux within two apertures centered in the optical nucleus: a central and extended apertures.

To study the impact of the scale used to derived the properties of the ionized gas, we select two different scales for the diameter of the central and extended apertures: a projected (5 and 30 arcsecs) and the effective radius (0.3 and 2.5 $R_{eff}$). We derive the effective radius for each galaxy using the same methodology outlined in the Appendix A of Sánchez et al. (2014). For the projected scale, we choose the size of the central aperture to be approximately twice the size of the spatial PSF in the survey (FWHM $\sim$ 2.5 arcsec). The central region in both samples covers between $\sim$ 0.6 and $\sim$ 3 kpc. The extended aperture was chosen to cover a wide portion of the galaxies. In terms of the petrosian radius we cover a generous portion of the galaxies (i.e, $1.5 \lesssim r_P \lesssim 8$). The central aperture in units of $R_{eff}$ is, in most of the cases, larger than the spatial PSF. It is also comparable to the central projected aperture. In most of the galaxies the extended aperture in units of $R_{eff}$ covers the entire FoV (see Fig. 2.12). In a few cases where the two companions in a binary system are covered by a single FoV, this aperture includes both galaxies (e.g., NGC 169).

To obtain the EW(H$\alpha$) for each galaxy, we average individual spaxel absolute values included within each of the apertures. In the case of the observed oxygen abundance in each aperture we use the empirical calibration O3N2 derived in Marino et al. (2013), which make use of the logarithm of the fluxes ratios $\log$ ([O III] $\lambda$5007/H$\beta$) and $\log$ ([N II] $\lambda$6584/H$\alpha$). The O3N2 empirical calibrator has been proven to be a robust estimator of the metallicity when it is no possible to have its direct estimation by auroral lines (López-Sánchez & Esteban 2010). In Sec. 5.5.1 we study the impact of this oxygen abundance calibrator by contrasting our measurements using the above calibrator with the one presented by Pettini & Pagel (2004).

Chapter 3

# Kinematic Alignment of Non-interacting CALIFA Galaxies

*In this chapter we study the stellar and ionized gas velocity field of 80 non-interacting galaxies presented in Sec. 2.2. The analysis of the velocity fields is done through the measurement of their global kinematic orientation (see Sec. 2.4.3). The study of galaxies in isolation is a key step towards understanding how fast-external processes, such as major mergers, affect global kinematic properties of galaxies. When compare to the photometric orientation, we find that morpho-kinematic differences are smaller than 22 degrees in 90% of the sample for both stellar and ionized gas components. Moreover, internal kinematic misalignments are generally smaller than 16 degrees. We find a tight relation between the global stellar and ionized gas kinematic orientation consistent with circular-flow pattern motions in both components (90% of the sample has differences smaller than 16 degrees). This relation also holds, generally in barred galaxies on the bar and galaxy disc scales. Our findings suggest that even in the presence of strong bars, both the stellar and the gaseous components tend to follow the gravitational potential of the disk. As a result, global kinematic orientations can be used to assess the degree of external distortions in interacting galaxies.*

*The results and conclusion of this chapter has been presented in Barrera-Ballesteros et al. 2014, A&A, 568, 70*

## 3.1 Introduction

To first order, disk galaxies are rotationally-supported systems (for a historical review see e.g., Sofue & Rubin 2001). The observed line-of-sight velocity distributions are expected to show a regular rotation pattern in the form of the so-called "spider diagram", with the position angle (PA) of the minimum and maximum aligned with the optical major axis. However, several physical processes can disturb this regular behavior. On the one hand, kinematic perturbations can be induced by external factors such as ram-pressure stripping (e.g., Kronberger et al. 2008) or galactic merger (e.g., Naab & Burkert 2003). On the other hand, kinematic departures from regular rotation can be due to internal instabilities such as spiral arms or bars (e.g., Binney & Tremaine 2008; Sellwood 2013). To disentangle the perturbations due to interactions and mergers, it is necessary first to study the possible global kinematic perturbations due to internal processes in the stars and ionized gas components across the galaxies.

In contrast to long-slit, integral-field spectroscopy (IFS) is a unique tool to study kinematic

properties across the entire galaxies (see Chapter 1). Even though 3D spectroscopic surveys are now feasible for a large set of galaxies (e.g.: GHASP, GH$\alpha$FaS, ATLAS$^{3D}$, SAMI; Epinat et al. 2008; Hernandez et al. 2008; Cappellari et al. 2011; Croom et al. 2012), these surveys have usually focused on the study of the kinematics of early-type systems (e.g.: SAURON, ATLAS$^{3D}$; Emsellem et al. 2004; Krajnović et al. 2011) or a specific wavelength range with high spectral resolution such as the H$\alpha$ range in spiral galaxies in different environments (e.g., GHASP, and GH$\alpha$FaS Fathi et al. 2009; Epinat et al. 2008).

As we already pointed out in Sec. 2.1, the CALIFA survey (Sánchez et al. 2012a) provides a unique opportunity to study simultaneously the stellar and ionized gas global kinematics in a sample of galaxies that covers a wide range of morphological types, stellar masses and environments. In this chapter we want to characterize the stellar and the ionized gas kinematics for a sample of non-interacting galaxies by means of their global orientation. In the next chapter we will use these results to quantify how much the kinematic of a sample of interacting galaxies differentiates with respect to the kinematics of isolated ones. In other words, the result from this work will yield a yardstick describing kinematic distortions due to internal processes with which to compare to kinematic disturbances induced by major merger events.

The spatial coverage provided by the CALIFA IFS data allow us to study the effect of structures such as bars in non-interacting galaxies on the global kinematics. Bars are elongated structures frequently present in disk galaxies. About 40−50 % of nearby disk galaxies observed in optical wavelengths show bars features (e.g., Marinova et al. 2007; Barazza et al. 2008; Aguerri et al. 2009). This fraction is even higher (about 60−70 %) for near-infrared observations (e.g., Eskridge et al. 2000; Knapen et al. 2000; Menéndez-Delmestre et al. 2007). Hydrodynamical simulations of these systems show that the bar component contributes only between 10 and 20 % to the disk potential (e.g., Scannapieco et al. 2010), and yet it can produce important changes in the gas dynamics. Bars are efficient in redistributing angular momentum, energy and mass in both luminous and dark matter components (e.g., Weinberg 1985; Debattista & Sellwood 1998, 2000; Athanassoula 2003; Martinez-Valpuesta et al. 2006; Sellwood 2006; Sellwood & Debattista 2006; Villa-Vargas et al. 2009). The effects of this angular momentum redistribution is different on gas and stars due to their different properties (e.g., Thielheim & Wolff 1982). For example, flows are observed within the co-rotation radius towards the galaxy centre only in the gas component (e.g., Rozas et al. 2002). In the following sections we present the kinematic characterization of the non-interacting galaxies: morpho-kinematic and kinematic misalignments are compared against different bar strengths as well as at different radii of barred galaxies. The impact of bars on the velocity field is also discussed. Finally we present our main findings and conclusions.

## 3.2 Kinematic Alignment of non-Interacting Galaxies

### 3.2.1 Kinematic Centre

As we pointed out in Sec. 2.4.3, in order to determine the major kinematic orientation, first it is necessary to define a kinematic centre. For this we used the velocity gradient peak. We recall that for a pure rotating disk the gradient peak should coincide with both the optical nucleus and the kinematic centre. We present our results of the comparison between the position of the gradient peak (GP) and the optical nucleus (ON). The original size of the fibre was taken as the minimum distance to report an offset between the GP and ON (i.e., 2.7″). We find that a large fraction of galaxies in the sample do not present a significant offset between these two positions (69/80) in the stellar component. The mean offset for the GP in this component is 1.5 arcsec and its standard deviation is 1.1 arcsec, respectively. In the rest of the stellar velocity fields this offset is due to possible SNe

in the central region (e.g., NGC 7478) or the possibility in barred galaxies that the GP is located at the end of bar (e.g. NGC 6004). The ionized gas presents similar offsets (mean offset of 1.3 and standard deviation of 0.9 arcsecs). However, the fraction of galaxies with small offsets is larger (74/80) in comparison to the stellar component. The galaxies with large offsets are either edge on galaxies (e.g., UGC 841) or patchy in emission (e.g., NGC 4956). As we explain in Sec. 2.4.3, for the kinematic centre we choose either ON or GP, depending on the symmetry of the rotational curve. In all the cases with large offset in the GP (in both components) the ON yields a more symmetric velocity curve than the GP suggesting that this shift in location is influenced by some morphological structure such as bars, arms, etc . This gave the result that in 21/80 and 5/80 velocity fields the ON was selected as the kinematic centre for the stellar and ionized gas components, respectively. As we note above most of the offsets are smaller than the formal spatial resolution of the instrument, in particular, for the stellar component where we perform spatial binning (although small for the nuclear region), this yield a larger number of fields where the ON was selected as kinematic centre. In tables A.2 and A.3 we list the gradient peak location with respect to the optical centre when the choice for the kinematic centre was the GP, and the systemic velocity derived for both components as the mean value within a 2.7″ radius of the selected kinematic centre.

### 3.2.2 Global morpho-kinematic misalignments

Once we have set the kinematic centre, we determine the major kinematic position angle by averaging the locations of the maximum and minimum velocities at different distances from the kinematic center (following the procedure explained in Sec. 2.4.3). Alignment between the major morphological major and kinematic position angles has been used to quantify the degree of distortion in a galaxy, in particular for merger and interacting galaxies (e.g., Epinat et al. 2008). To determine the impact of interactions and mergers in this particular parameter, first we need to determine the alignment in isolated galaxies as reference.

In Fig. 3.1 we show the morpho-kinematic PA misalignment (i.e., $PA_{morph} - PA_{kin}$) for the stellar and ionized-gas components (top and middle panels, respectively) against the total stellar mass of the galaxies (stellar masses were taken from Walcher et al. 2014, ). Since there is no preference between the kinematic approaching and receding PA, both of them were compared with respect to $PA_{morph}$. Note that similar results are obtained if only the maximum morpho-kinematic misalignment is compared. We do not find any trend between the stellar mass and the morpho-kinematic PA misalignment, in any component, for our sample of galaxies. There seems to be an enhancement in the misalignment of morpho-kinematic misalignment at stellar mass of $M_{stellar} \sim 10^{10.3}$ $M_{\odot}$, this enhancement in the misalignment is not well contraint, further studies are required to verify such misalignment.

About 90% of the galaxies have morpho-kinematic misalignments smaller than 21(stellar)/ 22 (ionized gas) degrees. The mean misalignment and standard deviation are $\sim 0^{\circ}$ and $\sim 10^{\circ}$, respectively in both components. This indicates a global agreement between the morphological and kinematic orientations in non-interacting galaxies regardless of the morphological type or bar strength. Barred galaxies tend to have larger morpho-kinematic differences and the larger error bars (see tags in Fig. 3.1). Larger differences in the stellar component are observed in IC 1683, NGC 5735, and NGC 171. For the two former galaxies the kinematic PA is similar to $PA^{out}_{morph}$ rather than $PA_{morph}$. However $PA_{kin}$ of NGC 171 is not similar to any of the photometric PA presented here (see Fig. 3.4). For the ionized gas component, NGC 3687 and NGC 5735 present disagreements between the photometric and kinematic PA. In Sec. 3.2.6, we study the impact of deriving the kinematic PA at different radius, in particular for barred galaxies.

Krajnović et al. (2011) found that 90% of the ATLAS$^{3D}$ galaxies displayed stellar morpho-

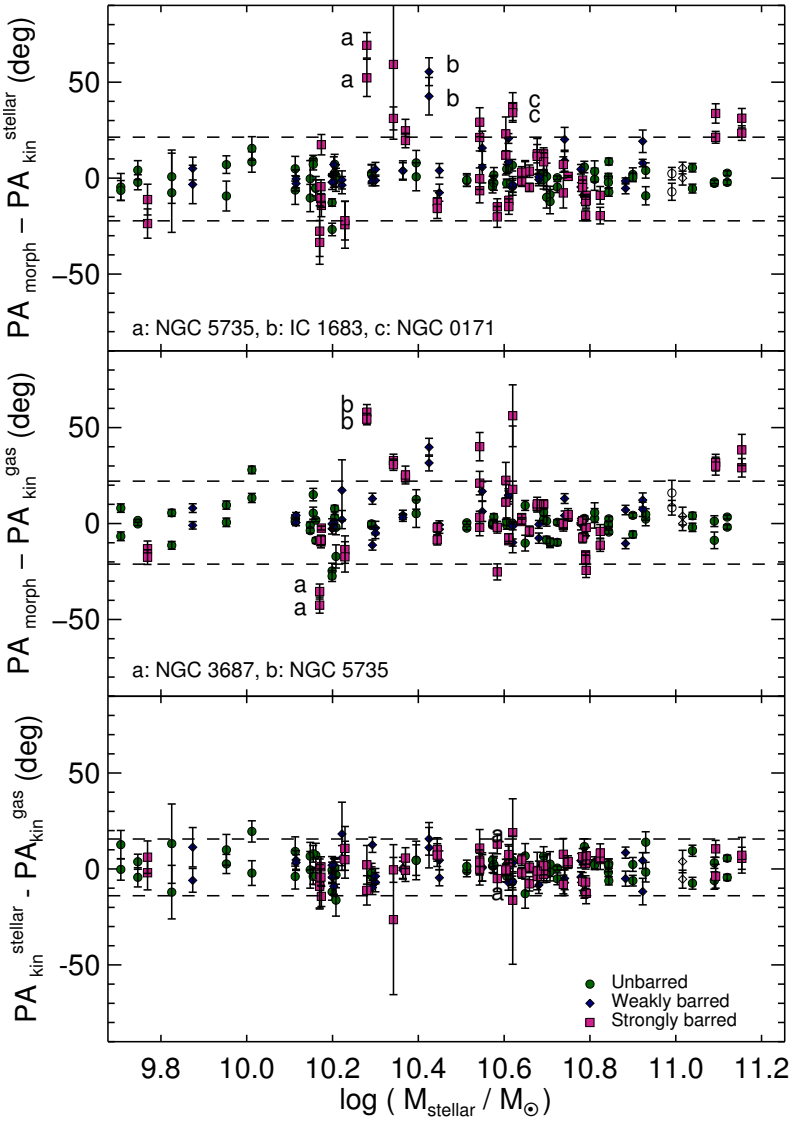


Figure 3.1: Difference between the morphological PA ($PA_{morph}$) and kinematic PA ($PA_{kin}$) against the total stellar mass for the stellar (top) and the ionized gas (middle), as well as the stellar versus ionized-gas kinematic PA (bottom). Both kinematic sides of the velocity maps were compared with $PA_{morph}$ (top panels) and between each component (bottom panel). In each panel, the green-filled circles represent the non-barred galaxies, blue diamonds are weakly-barred galaxies and violet squares correspond to barred galaxies. For early-type galaxies we use open circles. Dashed lines represent the $2\sigma$ dispersion of the sample. Labels indicate the $3\sigma$ outliers. Error bars are determined from Monte Carlo simulations.

kinematic misalignments smaller than 16° in their stellar component. From a sample of 24 early-type bulges, Falcón-Barroso et al. (2006) found that 80% showed stellar morpho-kinematic differences smaller than 20°. Our results, based on a sample of non-interacting galaxies with a wide range of morphological types, are consistent with those findings. For the ionized-gas, the Fabry-Perot survey of late-type spirals and irregular galaxies, GHASP (Epinat et al. 2008), reported 85% of the objects

with morpho-kinematic misalignments smaller than 15°. These results are also in agreement with our findings. Similar results have also been found for smaller samples (e.g. Kutdemir et al. 2008).

Although we present here projected kinematic properties of non-interacting galaxies, in Sec. A.1 we study the possible impact of the inclination for the determination of kinematic properties. In Fig. A.2 we plot the previous morpho-kinematic misalignments with respect to the photometric ellipticity as a proxy for the inclination ($\epsilon$, see Sec. 2.4.3). As is expected, larger misalignments are found at low ellipticities whereas at high ellipticities the morpho-kinematic misalignments are reduced due to the projection effects. However, at larger radii we suggest that even at low ellipticities these misalignments reduced significantly (see Sec. 3.2.6).

Our results suggest that for a non-interacting galaxy the misalignment between the photometric and global (stellar- and/or ionized gas-) kinematic orientation is small for a wide range of morphologies and stellar masses (smaller than 20°, with a mean value of $\sim 0°$). This also holds for galaxies with strict isolation critera (i.e., AMIGA subsample), where the average misalignment for these galaxies is $\sim$1° with a standard deviation of 8° and 5° for the stellar and ionized gas component, respectively.

### 3.2.3 Stellar-gas kinematic misalignments

The datacubes from the CALIFA survey allow us to perform a homogeneous comparison of the major kinematic orientation between the stellar and ionized gas components. As in the case of the morpho-kinematic misalignment, this parameter will gauge what is the typical (mis)alignment expected for non-interacting galaxies which allows us to quantifiy how interactions and mergers affect the kinematics of both components. In the bottom panel of Fig. 3.1 we show the difference between the stellar and ionized gas kinematic PA (i.e.$\mathrm{PA}_{\mathrm{kin}}^{\mathrm{stellar}} - \mathrm{PA}_{\mathrm{kin}}^{\mathrm{gas}}$). As in previous plots, we separate our sample according to bar strength. In this stellar mass range, we do not find any trend. Barred and non-barred galaxies present similar alignments between their components. In fact, the mean difference between orientations of these two components is $\sim$1° with a standard deviation of $\sim$7°. For 90% of the galaxies, the global orientation of the stellar and the ionized gas velocity fields agrees, with differences smaller than 16°. The only galaxy that seems to present large kinematic misalignment between the two components is the late-type barred galaxy NGC 171. The large uncertainties in the ionized gas component as well as the fact that the locations of maximum velocity present a significant deviation from a straight line in the gas component, suggest that the strong bar is the driver that distort the ionized gas velocity field. From the SDSS $r$-band image, this object presents a bar as large as the FoV of the instrument with an extended ring. This is the only galaxy with these features in the sample presented here. In Fig. A.4 we plot these misalignments with respect to the ellipticity. For a wide range of inclinations, the alignment between the two components is consistent. Summarizing, our measurements reveal small morpho-kinematic misalignments for the two components as well as small stellar versus gas kinematic misalignments for barred galaxies, comparable to those for non-barred galaxies. At the spatial and spectral resolution of the CALIFA survey, both components in our sample of non-interacting galaxies seem to follow a similar kinematic pattern even in the presence of bars.

### 3.2.4 Internal kinematic PA misalignments

As García-Lorenzo et al. (2015) suggest, another parameter useful for tracing possible deviations in a velocity field from a pure rotation is the (mis)alignment between the approaching and receding kinematic sides for each component. In Sec. 2.4.3 we estimated the kinematic PA from the approaching and receding sides as well as their departures from a straight line ($\mathrm{PA}_{\mathrm{kin,rec}}$, $\mathrm{PA}_{\mathrm{kin,app}}$,

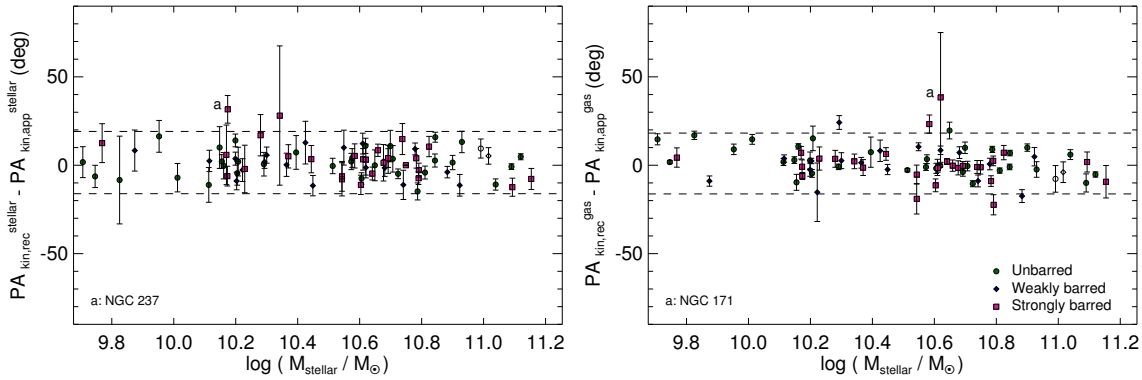


Figure 3.2: Internal kinematic misalignment between the receding PA ($PA_{kin,rec}$) and approaching ($PA_{kin,app}$) kinematic position angle against the stellar mass. In each panel the green-filled circles represent the non-barred galaxies, blue diamonds correspond to weakly-barred galaxies and violet squares represent the barred galaxies. Open circles represent the early-type galaxies. Dashed lines represent the $2\sigma$ dispersion of the sample ($\sim$15°). Labels indicate the $3\sigma$ outliers. Error bars at the left-top of each panel represent the typical error determined from Monte Carlo simulations.

$\delta PA_{kin,rec}$, $\delta PA_{kin,app}$). This allows us to study the internal kinematic misalignment, defined as $|PA_{kin,rec} - PA_{kin,app}| - 180°$, which should be zero for a regular rotational pattern. Figure 3.2 presents these misalignments for the stellar (left) and the ionized gas (right) components.

We find that $\sim 92\%$ of the objects have internal kinematic misalignment smaller than 15° for both the stellar and the ionized gas components. This is hold for different stellar masses and ellipticities (see Fig. A.3). Assuming that our objects are a representative sample of isolated galaxies (see Walcher et al. 2014), we suggest that any distortion in the line-of-sight velocity distribution that produces a kinematic misalignment larger than those values is not caused by internal processes.

### 3.2.5 Kinematic PA deviation from a straight line

The method presented in this study uses directly the measured radial velocities allowing us to determine by how much the major kinematic position angle deviates from a straight line. For a pure rotational velocity field, $PA_{kin}$ should be a straight line across the galaxy. These kinematic deviations $\delta PA_{kin}$ range from 5° to 40° between the two components for a large fraction of these galaxies ($\sim 90\%$). The mean value of these deviations is twice as big as the stellar component as for the ionized gas ($\sim$ 15° and $\sim$ 7°, respectively). The standard deviation of $\delta PA_{kin}$ is also twice as big for stars as for the ionized gas component ($\sim$ 8° and 4°, respectively). In Fig. 3.3 (top-panel) we plot the distribution of $\delta PA_{kin}$ for different bar strengths. The fact that the mean deviation of the stellar component is almost twice that of the ionized gas could be explained by several factors. Although we can determine the stellar velocity in each spaxel with relatively small uncertainty, the change of velocity for neighboring spaxels could be smaller than the spectral resolution leading to a higher scatter in the positions of maximum velocity. However, the method used here to derive kinematic properties is based entirely on the symmetry that a pure rotational velocity field should display. Therefore, any deviation translates to a perturbation in the parameters we are using to quantify our velocity fields. A small $\delta PA_{kin}$ in the ionized gas indicates that the gas lies in a thin disk, while the stellar component presents 'dynamical-heated' structures (e.g., dynamical heated disk, pressure-supported bulge, etc).

As we mention above, the barred galaxy NGC 171 is the object for which it most difficult to

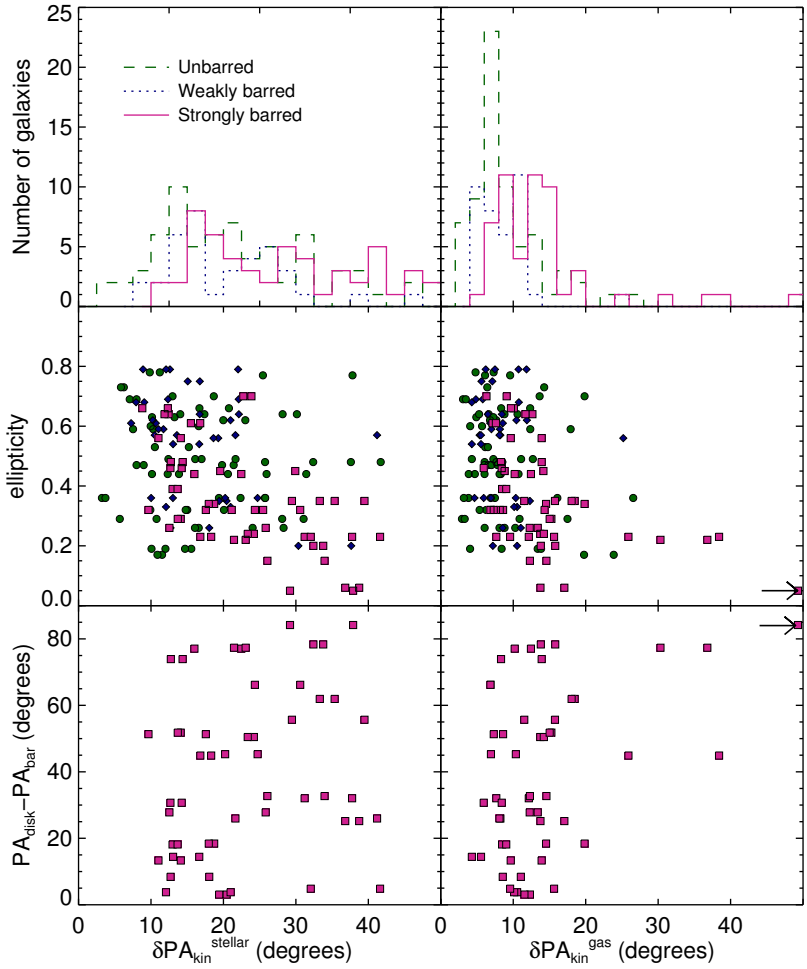


Figure 3.3: Top: Histograms of the kinematic departure from a straight line in the velocity maps measured via $\delta PA_{kin}^{stellar}$ (left) and $\delta PA_{kin}^{gas}$ (right) separated by different bar strengths. Dashed-lines represent the non-barred galaxies, dotted-lines correspond to the weakly-barred galaxies and solid-lines shows the distribution of strong barred galaxies. Middle: Apparent flattening of the galaxies via the ellipticity, as in previous figures, the green-filled circles represent the non-barred galaxies, blue diamonds correspond to weakly-barred galaxies and violet squares represent the barred galaxies. Bottom: Difference between the PA of the disk ($PA_{disk}$) and the PA of the bar ($PA_{bar}$) for strongly-barred galaxies only. Arrows in middle and bottom gas panels indicate the galaxy NGC 171 ($\delta PA_{kin}^{gas} \sim 90$ ° )

trace a symmetric velocity field in its ionized gas component (see Appendix A.3), the deviation of the maximum-velocity positions from a straight line is of the order of $\delta PA_{kin}$ ∼90°. In Sec. 3.3, we discuss the possible relation of $\delta PA_{kin}$ to the bar strength of the non-interacting galaxies.

### 3.2.6 Dependence on the measuring radius

In previous sections, to compare the $PA_{kin}$ of both components, we used the same distance to average the polar coordinates of positions defined by the lines of nodes (see Sec. 2.4.3). In our sample of

non-interacting galaxies, usually the stellar velocity map limits the range of this distance where the average is taken. For barred galaxies, it is similar (and a occasionally smaller) than half the length of the bar (see $r_{bar}$ in table A.2 and r in tables A.2 and A.3). For the majority of the galaxies, the ionized gas extends further out. Our results could therefore be biased because of measuring the average kinematic orientation in a range similar or close to the bar length.

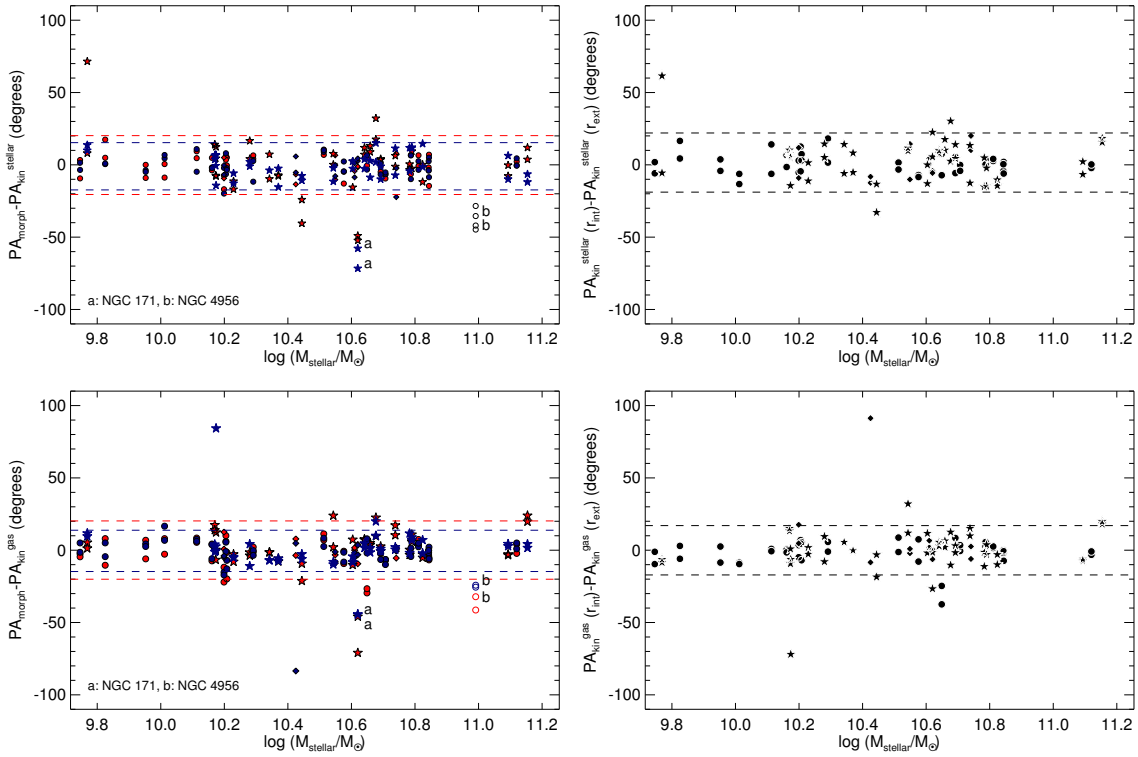


Figure 3.4: Left panels: Morpho-kinematic PA misalignments at different regions of the galaxy against the stellar mass for both the stellar (top panel) and the ionized gas (bottom panel) components in a subsample of low-inclined galaxies. In each of these panels, the red points represent the morpho-kinematic PA misalignment between $PA^{out}_{morph}$ (see table A.2) and $PA_{kin}$ at $r_{in}$. Blue points represent the morpho-kinematic misalignment between $PA^{out}_{morph}$ and $PA_{kin}$ up to $r_{out}$ (see section 3.2.6 for details). Filled circles, squares and stars represent non-barred, weakly-barred and strongly-barred galaxies, respectively. Right panels: Difference between the kinematic PA derived at $r_{in}$ and $r_{out}$ against the stellar mass for both the stellar (top panel) and the ionized gas (bottom panel) components. In the panels we highlight those objects with larger misalignments.

To study the impact on this distance range in the global orientation of the galaxies, we calculated the morpho-kinematic misalignments at different radii in a sub-sample of 49 low-inclined galaxies ($\epsilon < 0.5$ ). $PA_{kin}$ is computed out two different radii, $r_{out}$ and $r_{in}$ (see table A.4). The former defines the largest extension of the velocity map in any component. For barred galaxies, $r_{in}$ defines the bar length, for non-barred galaxies we define it as half of the $r_{out}$. $PA_{kin}(r_{out})$ is the average of the polar coordinates from $r_{in}$ to $r_{out}$, while $PA_{kin}(r_{in})$ is the average from the kinematic centre up to $r_{in}$.

Left panels of Fig. 3.4 show, for both components, the morpho-kinematic misalignment with respect to the orientation of an ellipse at the outermost region of each galaxy ($PA^{out}_{morph}$ ). Red symbols correspond to misalignments with $PA_{kin}(r_{in})$, while blue ones represent misalignments for $PA_{kin}(r_{out}$ ). Note that in most of the cases $PA^{out}_{morph}$ is measured at larger radii than $PA_{kin}(r_{out})$. Right panels compare the difference between $PA_{kin}(r_{in})$ and $PA_{kin}(r_{out})$. Figure 3.4 shows the sim-

ilar alignment of the kinematic PA for different morphologies at the different measuring radius, $r_{in}$ and $r_{out}$, in particular for barred galaxies. The comparison of kinematic PAs and $PA^{out}_{morph}$ (left panels) reveals that 90% of the objects have differences smaller than 16° (20°) for the outer (inner) region in the stellar component. The differences are smaller for the ionized gas (13° and 20° for outer and inner regions, respectively). When we compare $PA_{kin}$ at the inner and outer radii (right panels), we find that 90% of the galaxies have differences smaller than 20° (16°) for the stellar (ionized gas) component. These plots quantify what we observed in velocity fields; at different radii the orientation of the major kinematic PA remains rather constant. Moreover at different radii, $PA_{kin}$ seems to be aligned with the orientation of the major photometric axis rather than other readily observable morphological features such as bars. We find one outlier in both components: the strongly barred late-type galaxy (NGC 171). This galaxy presents the smallest ellipticity in the sample (see Fig. A.2), making it difficult to determine a reliable estimate of $PA^{out}_{morph}$. From these morpho-kinematic differences as well as the differences presented in Sections 3.2.2 and 3.2.4 we suggest that for this sample of non-interacting galaxies, the stars and the ionized gas follow the potential of the disk.

## 3.3 The impact of bars in velocity maps

Throughout this chapter, we find that the global kinematic orientation (measured by the major-axis kinematic PA) for the stellar and the ionized gas are aligned for non-interacting objects in the CALIFA survey (see Figs. 3.1 and 3.2). Simultaneous comparisons of the stellar and ionized gas resolved kinematics in barred galaxies are rather scarce. Falcón-Barroso et al. (2006) studied the velocity distributions of 24 spiral bulges. This sample included nine barred galaxies. Kinematic misalignments between the two components for these galaxies ranged from 1° to 38°. A subsequent detailed study of the galaxy NGC 5448 (Fathi et al. 2005) revealed a kinematic misalignment between these two components of 25°. These larger differences are explained by the fact that the morphological PA of the galaxies was measured within the same FoV probed by their kinematics (i.e., the inner regions of those galaxies). The $PA_{morph}$ in those cases are thus biased due to the bar.

This alignment between the two components seems to hold at different galacto-centric radii of the galaxies (Fig. 3.4), even for barred galaxies. To quantify the departures from perfect axisymmetry in the global kinematic orientation, we plot histograms in top panels of Fig. 3.3 showing the deviations from a perfect straight line observed in the stellar and ionized-gas kinematic maps ($\delta PA^{stellar}_{kin}$, $\delta PA^{gas}_{kin}$). As already noted in Sec. 3.2.4, the mean value of these deviations is higher for the stellar component than for the ionized gas. For both components, the strongly barred galaxies present slightly higher values than the unbarred galaxies. In particular, the ionized gas component presents a difference between the distribution of barred and unbarred galaxies. This suggests that although the global kinematic orientation is stable in non-interacting galaxies, in particular for barred galaxies, some kinematic parameters, such as $\delta PA^{gas}_{kin}$ (at higher spatial and spectral resolution as the present velocity fields), can be sensitive to the presence of strong bars.

It is important to note that there is still a fair fraction of strongly barred systems with $\delta PA_{kin}$ consistent with those observed in unbarred galaxies. We have investigated whether this effect is caused by the flattening of the galaxy, or by the relative orientation of the bar with respect to the disc major axis. This is shown in the middle and lower panels of Fig. 3.3. The projected deviation of the kinematic PA ($\delta PA_{kin}$) seems to grow at lower apparent flattening of the galaxy (as a surrogate for inclination). This trend is particular clear for barred galaxies and may be induced by projections effects. Using the method presented in this study, any kinematic deviation from a straight line would be more easily quantified in a nearly face-on velocity field than in the same field viewed edge-on. For highly inclined galaxies with large kinematic deviations, we may even trace vertical motions rather

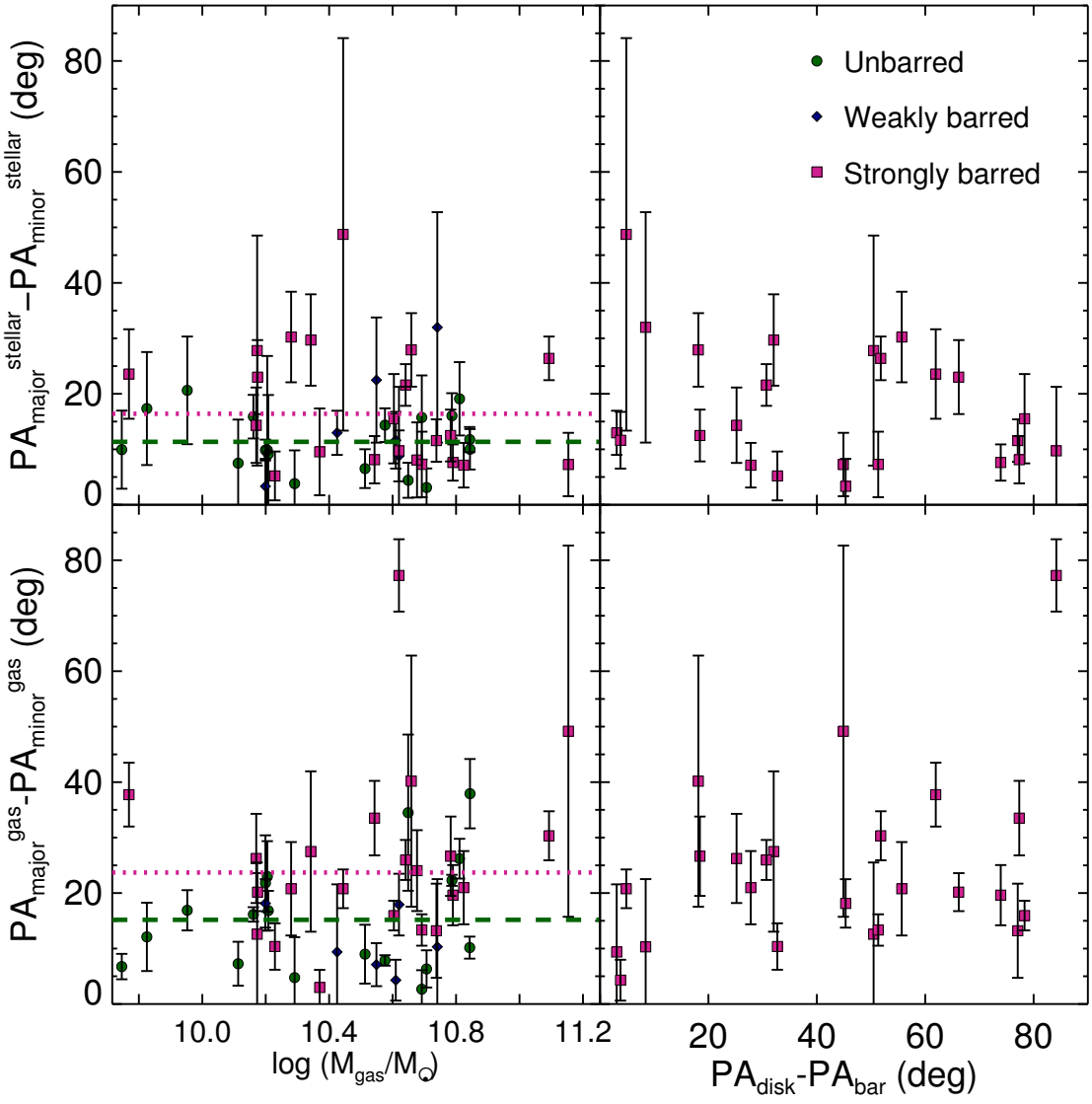


Figure 3.5: Misalignment between the major and minor kinematic PA for a subsample of low-inclined galaxies($\epsilon$ ¡ 0.5). 0° represents perpendicularity between major and minor axes (see Sec. 3.3 for details). Left panels show these misalignments as function of the stellar mass for the stellar (top) and the ionized gas (bottom) components. Right panels present these kinematic misalignment as function of the morphological alignment of the bar with respect to the disc for barred galaxies. As in previous figures, the green-filled circles represent the unbarred galaxies, blue diamonds correspond to weakly barred galaxies and violet squares represent the barred galaxies. Dotted violet lines represent the mean value for the barred galaxies, while dashed-green lines represent the mean value for the unbarred galaxies.

than radial deviation from a circular velocity field, however, other kinematic indicators, such as the intrinsic kinematic misalignment do not present a clear trend in ellipticity (see Appendix A.1). As for the orientation of the bar with respect to the disc major axis, the kinematic deviations covers a wide range of values for a given alignment between the bar and disc orientations, indicating that for barred galaxies, the orientation of the bar with respect to the disc may not affect drastically the scatter in the location of maximum velocities.

The velocity maps of barred galaxies often show, however, clear signatures of perturbations from a symmetric velocity field (e.g., Hernandez et al. 2005; Fathi et al. 2009). A characteristic "S"-shape in the zero-velocity curve is observed in several of these ionized gas kinematic maps (e.g., Peterson & Huntley 1980; García-Barreto & Rosado 2001; Emsellem et al. 2006). For a rotating disc galaxy, the major and minor axes are perpendicular everywhere (Binney & Merrifield 1998). To account for the distortion in the zero-curve velocity, we estimate the difference between the above kinematic PAs. For each galaxy with low-inclination ($\epsilon < 0.5$), we estimate the largest departure among the four kinematic PAs (approaching and receding major PAs and their corresponding minor PAs), where 0° represents perpendicularity between major and minor axes. In Fig. 3.5 we represent these departures against the stellar mass (left panels) and the photometric alignment of the bar with respect to the disc for barred galaxies (right panels), for the stellar (top panels), and ionized gas components (bottom panels). For the stellar component, almost all the slightly inclined galaxies present differences smaller than ∼30° except for the barred galaxy NGC 6155. Furthermore, strongly-barred galaxies spread homogeneously in this range as the unbarred objects.

The average departure between strongly and unbarred galaxies is similar (∼11° and ∼15°, respectively). The ionized gas component displays a wide range of differences between the major and minor kinematic PAs. In particular, strongly barred galaxies present a wider range of differences than the unbarred sample. The average of this difference for the barred galaxies is larger (∼24°) than the unbarred galaxies (∼15°). According to numerical simulations, the difference between the major and minor kinematic PAs is best seen in velocity fields where the bar makes an angle of 45° with the major axis of the galaxy (e.g., Athanassoula 1984; Scannapieco & Athanassoula 2012). Due to the moderate sub-sample of barred galaxies in this study and the rather large uncertainty in determining the minor kinematic PA, it is not clear whether larger differences in the kinematic PAs are observed at this specific angle between the bar and the disc PA. For the stellar component, however, an increment in this difference seems to be present at $PA_{disc}$ - $PA_{bar} \sim 50°$. In the ionized gas, for a given morphological alignment between the bar and the disc we find a broad range of differences between the major and minor kinematic PAs. Given the spectral and spatial resolution in our velocities distributions, we consider that the difference between the major and minor kinematic PAs is a sensitive indicator of the presence of a bar in particular for the ionized gas component.

Detailed individual studies are required in order to explain the shape and length of the distortion in this velocity curve, as well as to determine if the ionized gas is a more sensitive component to the bar potential. These issues are beyond the scope of this study; however, our results can motivate numerical simulations to address the nature of the kinematics in non-interacting galaxies (e.g., Holmes et al., in prep.). As opposed to previous indicators (see Figs. 3.1 and 3.2), this indicator of kinematic distortion varies significantly for non-interacting galaxies, making difficult to use it as a discriminator for distinguishing the kinematic distortion produced by the merging event or a secular process.

## 3.4 Summary and Conclusions

We have studied the stellar and ionized gas kinematics for a sample of 80 non-interacting galaxies in the CALIFA survey. A quantification of the kinematic properties in this sample is a first step towards the understanding of the impact of interactions and mergers and secular process in the kinematics of galaxies. The fraction of barred and unbarred objects in this sample is similar. We find that for 90% of the sample, the global orientation of the stellar and ionized gas is fairly well aligned (misalignment smaller than $\sim 20°$) with respect to the global photometric orientation of the galaxy, including barred and unbarred objects. From the method used to measure the major kinematic PA,

we studied the internal kinematic PA misalignments namely, the difference between the receding and approaching kinematic PA. We found intrinsic aligned velocity fields in both components for a large fraction of the sample (intrinsic misalignments smaller than 15° degrees for the stellar and the ionized gas components).

We also compared the derived kinematic PA for the stellar and the ionized gas components. We observe a tight alignment (16° degrees of difference) between the two components for the majority of this non-interacting sample. This result holds in barred galaxies when the comparison is carried out either at the radius of the bar or further out. From these results we suggest that the global kinematics in non-interacting galaxies in both the stellar and the ionized gas components (measured by the major kinematic position angle) seems to be dominated by the mass of the disc, rather than other morphological components that can induce non-circular patterns in the observed velocity fields, such as bars. Even though bars can locally redistribute the angular momentum, energy, and mass, the kinematic pattern that seems to dominate across the galactic disc -including the bar- is consistent with a regular rotational pattern.

We will use the results presented in this chapter to gauge the kinematic distortions caused by external forces in galaxies that undergo a merger event in the next chapter.

Chapter 4

# Kinematic (mis)Alignments in CALIFA Merging Galaxies

*In this chapter we present spatially resolved stellar and/or ionized gas kinematic properties for a sample of 103 interacting galaxies previously selected in Sec. 2.3. This sample was tailored to trace different merger stages, from close companions, pairs with morphological signatures of interaction to coalesced merger remnants. In order to distinguish global kinematic signatures caused by a merger event from those driven by internal processes, we compare our galaxies with a control sample of 80 non-interacting galaxies studied in the previous chapter. As explained in Sec. 2.4.3, we measure for both the stellar and the ionized gas components the major kinematic position angles ($PA_{\rm kin}$, approaching and receding) directly from the velocity distributions with no assumptions about the internal motions. This method also allows us to derive the deviations of the kinematic PAs from a straight line ($\delta PA_{\rm kin}$). We find that around half of the interacting objects show morpho-kinematic PA misalignments that cannot be found in the control sample. In particular, we observe those misalignments in galaxies with evident signatures of interaction. On the other hand, the level of alignment between the approaching and receding sides for both samples is similar, with most of the galaxies displaying small misalignments. Radial deviations of the kinematic PA orientation from a straight line in the stellar component measured by $\delta PA_{\rm kin}$ are large for both samples. However, for a large fraction of interacting galaxies, the ionized gas $\delta PA_{\rm kin}$ is larger than the typical values derived from isolated galaxies (48%), indicating that this parameter is a good indicator to trace the impact of interaction and mergers in the internal motions of galaxies. By comparing the stellar and ionized gas kinematic PA, we find that 42% (28/66) of the interacting galaxies have misalignments larger than 16°, compared to 10% from the control sample. Our results show the impact of interactions in the global motion of stellar and ionized gas as well as the wide variety of their spatially resolved kinematic distributions. This study also constitutes a local Universe benchmark for kinematic studies in merging galaxies at high redshift.*

*The results and conclusion of this chapter has been presented in an article published in the journal Astronomy and Astrophysics (Barrera-Ballesteros et al., in press)*

## 4.1 Introduction

Galaxy mergers play a crucial role in the (co-)evolution of stars and ionized gas in galaxies, in particular their kinematics. As we discuss in Chapter 1, from a morphological perspective only, the single-merger event is associated with close pairs, companions with clear signatures of interaction

and/or galaxies with signatures of a previous merger. Since gravitational forces shape the morphology of the galaxies as the merger evolves, kinematic departures from a pure rotational disk are expected in these systems (Kronberger et al. 2007).

Over the past 50 years, the understanding of the galactic merger process has evolved considerably (see and extended overview in Secs. 1.1 and 1.2). Early studies were based on observations of galaxies with peculiar features (Arp 1966) and the seminal work by Toomre & Toomre (1972) attempted to understand those peculiar features with rudimentary computational power. Nowadays, computational capability and a better understanding of the interstellar medium have provided a deeper understanding of the evolution of different galactic components across the merger event (e.g., Springel 2005; Hopkins et al. 2006; Di Matteo et al. 2007; Hopkins et al. 2008; Barnes & Hibbard 2009; Barnes 2011). Even though it is possible to study the kinematic properties of the entire merging sequence, numerical simulations in general focus on a given stage of the merger event (e.g., Naab & Burkert 2003; Cox et al. 2006a; Jesseit et al. 2009; Karl et al. 2010; Privon et al. 2013). This is the case in order to compare with the available heterogeneous set of observational data. Studies of simulated line-of-sight velocity distributions or 2D velocity fields are becoming standard in the study of the velocity field distortions induced by merging (e.g., Kronberger et al. 2007; Jesseit et al. 2007; Bois et al. 2012; Porter et al. 2012).

On the observational side, spatially resolved kinematics of merging galaxies have been analyzed in high and low redshift regimes. At high redshift ($z \gtrsim 0.5$), several surveys have studied the ionized gas velocity fields of star-forming galaxies, most of them showing strong interaction signatures. These surveys find that a large fraction of galaxies are rotating discs ($\gtrsim 60\%$; for a review see Glazebrook 2013). In the nearby Universe, several IFU studies have been devoted analyzing in detail individual systems in a given interaction stage (e.g., Engel et al. 2010; Alonso-Herrero et al. 2012; Wild et al. 2014). Some merging objects have been included in large observational samples devoted to study specific science cases for local galaxies. For instance, the stellar kinematics in early type galaxies (e.g., NGC 5953 included in the SAURON project Falcón-Barroso et al. 2006) or ionized gas kinematics for spiral or irregular galaxies (GHASP, Epinat et al. 2008). More recently, significant number of studies focus in the characterization of the ionized gas velocity fields of (Ultra)-Luminous IR Galaxies ([U]LIRGs) with morphological tidal features or merging remnants (e.g., Colina et al. 2005; Dasyra et al. 2006; Arribas et al. 2008; Piqueras López et al. 2012). For a large sample of these galaxies Bellocchi et al. (2013) showed that their ionized gas velocity fields are dominated by rotation. Despite these efforts, usually these studies lack the comparison between the stellar and ionized gas components at different stages of the merging event. Since these components could react differently during the merger, it is crucial to understand how the kinematic of these components evolve during a galactic encounter. To distinguish the possible distortions or imprints due to secular processes from those related to the merger, a homogeneous control sample matched in stellar mass is also required.

In this chapter we aboard to analyze the stellar and ionized gas velocity distributions as the merger event evolves by studying several galaxies at different stages of this event, also we compare the kinematic properties of these galaxies with those derived from a set of non-interacting objects. An observational study of this nature requires a homogeneous method and analysis procedures. Moreover, we have to be able to depict kinematics from stellar and ionized gas components not for a single merging stage but during the entire merging sequence. The CALIFA survey (Sánchez et al. 2012a) allows us to carry out this kind of studies (see Sec. 2.1). All the interacting/merging galaxies, as well as the non-interacting objects, are observed with the same observational setup. It also includes a large variety of non-interacting objects allowing us to use them as a control sample (see Sec. 2.2).

## 4.2 Kinematic (mis)alignments as tracer of the interaction

In order to have reliable measurement of the kinematic parameters described in Sec. 2.4, we avoid deriving kinematic parameters in objects where the velocity range was smaller than 50 km $s^{-1}$, and the extension in any component was smaller than 5 arcsec. In Table 2.1, we list the number of sources where we are able to determine stellar and ionized gas kinematic parameters. Even though, both the pPXF and the CC methods are able to determine velocity dispersion maps (see Secs. 2.4.1 and 2.4.2) due to the low spectra resolution of the V500 data we did not attempt any further analysis of these maps (nor in the sample of non-interacting galaxies).

Before we present the kinematic properties of the interacting sample and contrast them with those from isolated galaxies we want to stress the difference between these two samples. Even though their absolute magnitudes, stellar masses and colors are similar (see Figs. 2.5 and 2.6), there is a clear lack of ellipticals and lenticular galaxies in the control sample compared with the interacting and CALIFA MS (see bottom panel Fig. 2.6). As we noted in Sec. 2.3.3 the distributions of physical properties of samples of isolated galaxies tend to by narrower than those observed for interacting and merger galaxies. Nevertheless, kinematic parameters derived for ellipticals and lenticular included in the control sample are within the typical values of this sample (see Chapter 3). For the sake of comparison, we assume that trends found for the galaxies in the control sample are representative of the entire sample regardless their morphology.

There are some velocity fields where it is not possible to determine any kinematic feature [1]. For these objects, the kinematic perturbations across the velocity fields are large enough to prevent any measurement of the kinematic PA. It could be that observations with better spatial and spectral resolution could provide a determination of the kinematic PA using the above methods. To account for such galaxies in our statistics, we assign them the largest misalignment plus 10 ° for each considered parameter. We include these objects in our analysis to represent those objects where measurements of the kinematic PA cannot be performed using the methodology and data presented in this study.

### 4.2.1 Kinematic centre in interacting galaxies

As for the control sample, we gauge the kinematic centre in the interacting sample using either their gradient peak from the velocity gradient maps or the optical nucleus (see Sec. 3.2.1). We use the size of the fibre as threshold to determine an offset between these two locations (2.7″). For the stellar component a small fraction of interacting galaxies, similar to the control sample, displays an offset in their kinematic centre (17/85). In the case of the ionized gas, a large portion of the interacting sample displays an offset between the GP and ON (30/82). This fraction is almost five times larger than that of the control sample. We note that the orientation of the kinematic PA in not strongly affected by the deviation either of the ON or GP as kinematic centre. In particular, for the ionized gas velocity fields only 9/82 galaxies present large differences in their kinematic orientation if one of the two positions is chosen. As kinematic centre we choose either ON or GP, depending on the best symmetry of the rotational curve. As complementary information, in Tables A.6 and A.7, we list the systemic velocity derived for both the stellar and the ionized gas components, respectively, as the mean velocity within a 2.7 arcsec aperture centered at the kinematic centre.

[1] NGC5394, IC1079, and UGC11958 for the stellar component; UGC10650, NGC3303NED01 for the ionized gas component; and NGC5615 for both components.

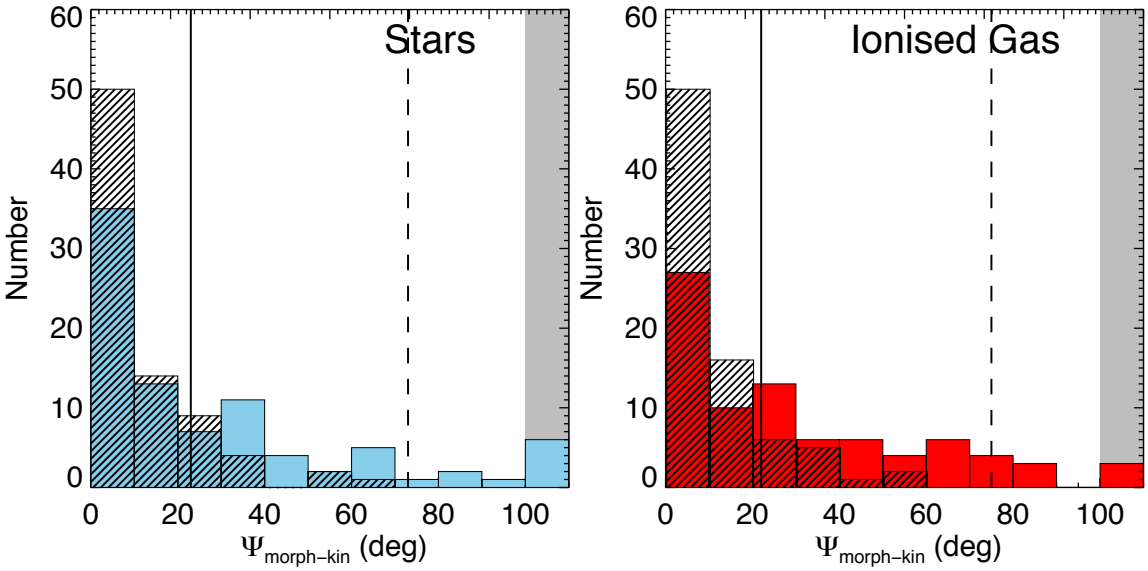


Figure 4.1: Distribution of the misalignment between the photometric and kinematic position angle $\Psi_{\rm morph-kin}$ for the stellar (left, blue histogram) and the ionized gas (right, red histogram). In each plot line-filled histograms represent the distribution of $\Psi_{\rm morph-kin}$ for the control sample. Solid lines represent the misalignment for 90% of the control sample. Dashed lines represent the same value for the interacting galaxies. The bin located in the gray areas in both components represent the misalignment for those galaxies where is not possible to determine $\rm PA_{kin}$

### 4.2.2 Morpho-Kinematic misalignments

Following the same methodology as for the control sample, to study the stellar and the ionized gas $\rm PA_{kin}$, we pick the common maximum radius where both components can be measured (see r value in Tables A.6 and A.7). Note that for some strongly interacting systems the radius r covers each companion, rather than the entire binary system (e.g., NGC 0169/ NGC 0169A, NGC 4841A/ NGC 4841B). Typical errors for both the stellar and ionized gas components for $\rm PA_{kin}$ and $\delta \rm PA_{kin}$ are $\sim 5^\circ$ (see individual values in Tables A.6 and A.7 for the stellar and the ionized gas, respectively). As we described in Sec. 2.4.3, these errors are derived from Monte Carlo simulations.

In Fig. 4.1 we present the distributions of the misalignment between $\rm PA_{kin}$ and $\rm PA_{morph}$ ($\Psi_{\rm morph-kin}$) for the stars (left panel) and the ionized gas (right panel). To include 90% of the stellar morpho-kinematic PA misalignment in the control sample, we need to set a limiting value of $21^\circ$ . We find that 43 % (37/85) of the interacting sample has morpho-kinematic misalignments larger than $21^\circ$ for this component. To include 90% of the stellar morpho-kinematic misalignments in the interacting sample, we need to set a limit of $72^\circ$. The interacting and control stellar morpho-kinematic misalignments are not likely to be drawn from the same parent distribution ($p_{KS} < 0.001$). The interacting sample shows a larger median $\Psi_{\rm morph-kin}$ misalignment and a wider distribution with respect to the control sample (see Table 4.1).

Similarly to the stellar component, 90% of the control sample has morpho-kinematic misalignments up to $22^\circ$ in the ionized gas component. We find that 52 % (43/82) of the interacting sample has morpho-kinematic misalignments larger than $22^\circ$. Ionised gas morpho-kinematic misalignments for a large portion of interacting galaxies (90%) reach values up to $75^\circ$. Just as in the stellar component, ionized gas $\Psi_{\rm morph-kin}$ for the interacting sample, shows a larger median misalignment and a wider distribution than the control galaxies (see Table 4.1).

The variety of radial velocity distributions is great. Some galaxies present kinematic PAs that clearly differ from the morphological ones. Although the scope of this particular study is to present statistical results of the kinematic (mis)alignments of a merging sample in comparison to an isolated sample, for the sake of illustration let us highlight one object with large morpho-kinematic misalignments, the early-type galaxy NGC 5623. This galaxy does not present any close companion, or any other readily observable signature of interaction from the images, but its stellar velocity distribution reveals a clear kinematically decoupled core (KDC). This KDC is aligned with the morphological PA of the galaxy. However, the ionized gas kinematic PA (which extends $\sim$ 10 arcsec), is nearly perpendicular to the KDC orientation. Simulations suggest that mergers in a given configuration can lead to such a KDC feature. Note that this is not the only case of a KDC in our sample (e.g., NGC 5953 Falcón-Barroso et al. 2006, 2007). These cases are examples of how different the kinematic structure of a galaxy can be to that expected from its morphology. Due to he misalignments between its star and gas kinematic orientations, we classify this object as a merger remnant.

In the left panels of Fig. 4.2 we plot the control and interacting morpho-kinematic misalignments with respect to their stellar masses for the stellar (top panel) and ionized gas (bottom panel) components. As we already pointed out in Sec. 3.2.2, the morpho-kinematic misalignments in the control sample (for any component) do not seem to vary strongly at different stellar mass ranges. This is not the case for the interacting sample. For the stellar component, we find an increment in the morpho-kinematic misalignment at the mass range of $10 < \log(\mathrm{M_{stellar}}/\mathrm{M_{\odot}}) < 10.5$. The interacting and control sample in this mass range do not seem to be drawn from the same parent distribution ($\mathrm{p}_{KS} < 0.02$). The explanation of this increment in the misalignment at this mass range is non-trivial. It can be due to the distribution of stellar masses of interacting galaxies. Most of the galaxies in this mass bin are pairs of galaxies. According to cosmological simulations, the stellar mass distribution function of galaxy pairs peaks in a similar mass range (Moreno et al. 2013). However, note that a significant fraction of interacting galaxies have their stellar mass within this mass bin (see Fig. 2.6). A larger samples of interacting galaxies at different mass bins would be required to confirm this difference.

At the same mass bin, ionized gas $\Psi_{\mathrm{morph-kin}}$ misalignment shows an enhancement over the control one. In each stellar mass bin, the median $\Psi_{\mathrm{morph-kin}}$ of the interacting sample is larger compared to the median derived from the control sample. This suggests that ionized gas has a strong reaction to interactions and mergers. In the less massive bin, the median $\Psi_{\mathrm{morph-kin}}$ misalignment is larger in comparison to median misalignments at massive bins in the interacting sample (except for the above mass bin). This could indicate that lighter companions are prone to show difference in their physical properties with respect to massive galaxies induced by their heavy companions (e.g., Alonso-Herrero et al. 2012). We stress that in this particular mass bin there is no galaxies in the control sample to compare with. A detailed study of low-mass interacting galaxies would be required to further test this scenario.

We study whether $\Psi_{\mathrm{morph-kin}}$ misalignments are related to a particular stage of the merger event. In right panels of Fig. 4.2 we plot the morpho-kinematic misalignments of the interacting sample according to their interaction stages for both, the stellar (upper panel) and ionized gas (bottom panel) components. For the stellar component we find that the merger stage shows the largest median value (and wider distribution) of $\Psi_{\mathrm{morph-kin}}$ with respect to the other interaction stages. In fact, the distribution of the morpho-kinematic misalignments from this stage and the distribution of the control sample misalignments do not seem to be drawn from the same parent distribution ($p_{KS} \sim 0$).

Although the spread for the misalignments in each stage is rather large, the median value per stage follows a trend across the merger event. Pre-mergers (i.e., pairs of galaxies), present median misalignment slightly larger than median $\Psi_{\mathrm{morph-kin}}$ from the control sample. In the merger stage,

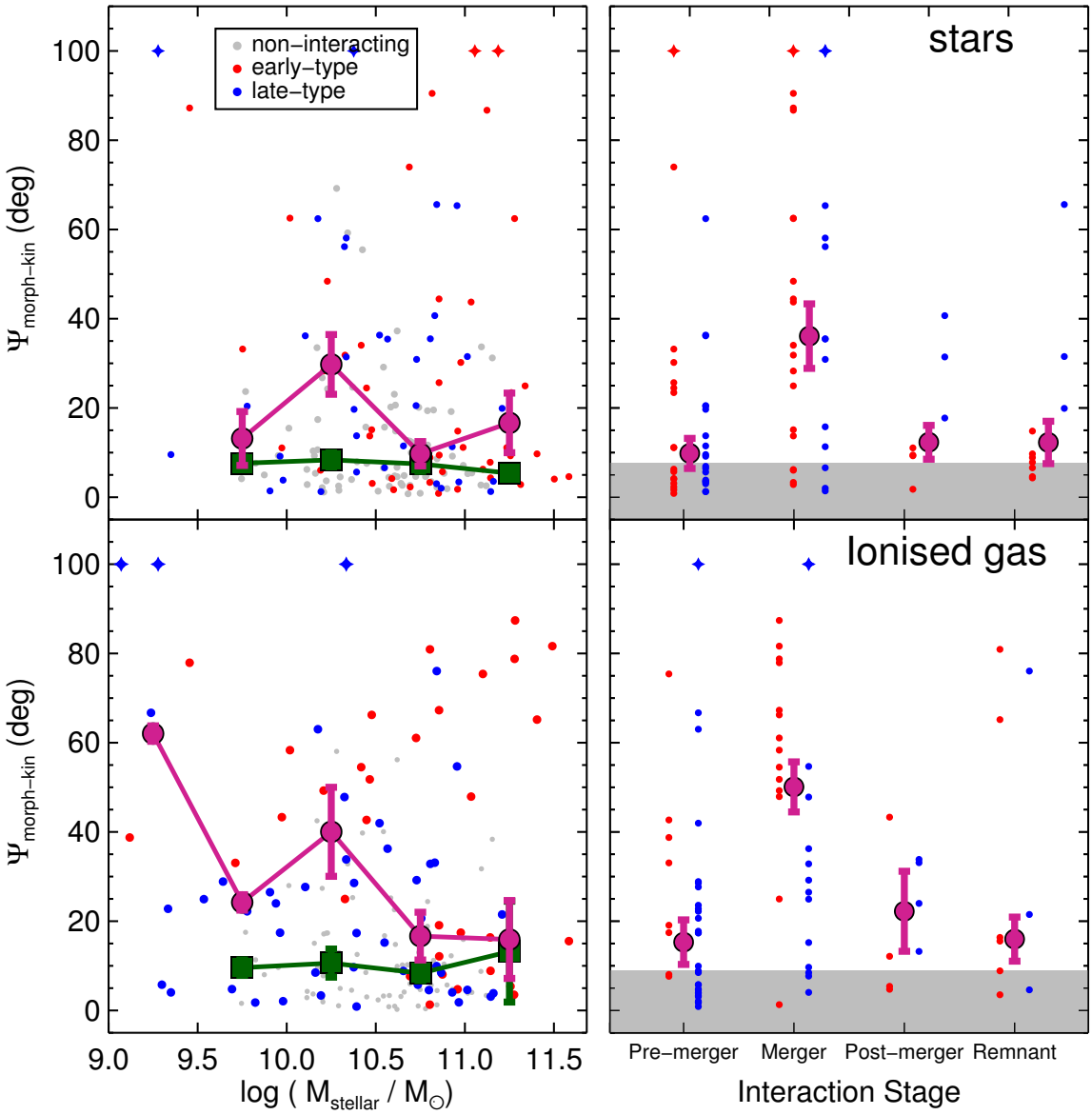


Figure 4.2: Morpho-kinematic misalignment ($\Psi_{\rm morph-kin}$) for the stellar (top) and ionized gas (bottom) components against the stellar mass (left) and the interacting stage (right). In each of the panels, the red symbols represent early-type galaxies (i.e., E, S0 and Sa) and late-type are shown by blue symbols (i.e., Sb, Sc, Sd). Star-symbols represent those objects where was not possible to determine $\Psi_{\rm morph-kin}$. For the left panels, gray dots represent the control sample, green squares and pink circles represent the median of $\Psi_{\rm morph-kin}$ in mass bins of 0.5 in units of $\log({\rm M_{stellar}/M_{\odot}}$ for the control and interacting samples, respectively. For the right panels, the pink circles represent the median of $\Psi_{\rm morph-kin}$ in each interaction stage bin. Gray regions shows the median morpho-kinematic misalignment obtained from the control sample. In each panel the error-bars for each median value in each bin are obtained from bootstrapping.

its median misalignment is clearly larger than control sample median as well as those from other interaction stage bins. Note also that post-merger and remnant stages present slightly larger median values than the control sample one.

Ionised gas morpho-kinematic median misalignments at different interaction stages follow a similar trend as those derived from the stellar component. Note that in each interaction bin the median misalignment from the ionized gas is larger than for the stellar component.

The fact that in both components the median $\Psi_{\rm morph-kin}$ in all the interaction stages is systematically larger than the median misalignment for isolated galaxies indicates that interactions and mergers do have an impact altering the internal structure of galaxies. Even more, morpho-kinematic misalignments during different merging stages suggest that as the companions merge the velocity distribution of the components departs significantly from that observed in isolated galaxies. After coalescing, remnants tend to show slightly larger morpho-kinematic alignments as those found in isolated galaxies. Note also that comparison of $\Psi_{\rm morph-kin}$ misalignments for the different components suggest that ionized gas reacts more easily to interactions and mergers than the stellar component.

Finally, we note that a significant fraction of objects with kinematic misalignment larger than the control sample are early type galaxies (elliptical and lenticular galaxies). This became evident for the ionized gas in the merger stage (see red points in bottom right panel of Fig. 4.2). To identify whether this is a signature of the current or a previous interaction in this type of galaxies, it is required individual detailed studies in each interacting system which is beyond the scope of the present study.

### 4.2.3 Internal Kinematic misalignments

As we described in Sec. 2.4.3, we are able to determine independently the approaching and receding kinematic PA from the velocity field distributions. Any misalignment between these two sides indicates possible departures from a pattern of ordered motions. In Fig. 4.3, we present for both samples the distributions of these misalignments ($\Psi_{\rm kin-kin}$) for the stellar (left panel) and ionized gas (right panel) components. To include 90% of the stellar internal kinematic misalignments in the control sample, we need to set a limiting value of 13 °. We find that 21 % (18/85) of the interacting sample has internal kinematic misalignments larger than 13 °. To include 90% of the stellar internal kinematic misalignments in the interacting sample, we need to set a limit of 22 °. Medians and standard deviations are similar between these two samples (see Table 4.1).

As we observed in Sec. 3.2.4, the galaxies in the control sample also have small $\Psi_{\rm kin-kin}$ values for the ionized gas. To include 90% of the ionized gas internal kinematic misalignments in the control sample, we need to set a limiting value of 15 °. The interacting sample covers a wider range of $\Psi_{\rm kin-kin}$ than the control sample in this component (see right panel in Fig. 4.3). We find that 20% (16/82) of the interacting sample has kinematic misalignments larger than 15 °. To include 90% of the ionized gas internal kinematic misalignments in the interacting sample, we need to set a limit of 30 °. This suggest that ionized gas could react more easily to mergers than the stellar component (as we already pointed out in Sec. 4.2.2). However, note that median and standard deviations are similar for both samples (see Table 4.1).

These results indicate that interactions and mergers have an impact on the internal kinematic alignment of galaxies, in particular for the ionized gas component. However, we note that the fraction and median values of these misalignments are smaller than those we find in the morpho-kinematic indicator (see Sec. 4.2.2). A KS-test suggests that control and interacting internal kinematic misalignments can share the same parent distribution.

We also study the dependence of internal kinematic misalignments with respect to the stellar mass. We find that interacting and control samples share similar median internal kinematic align-

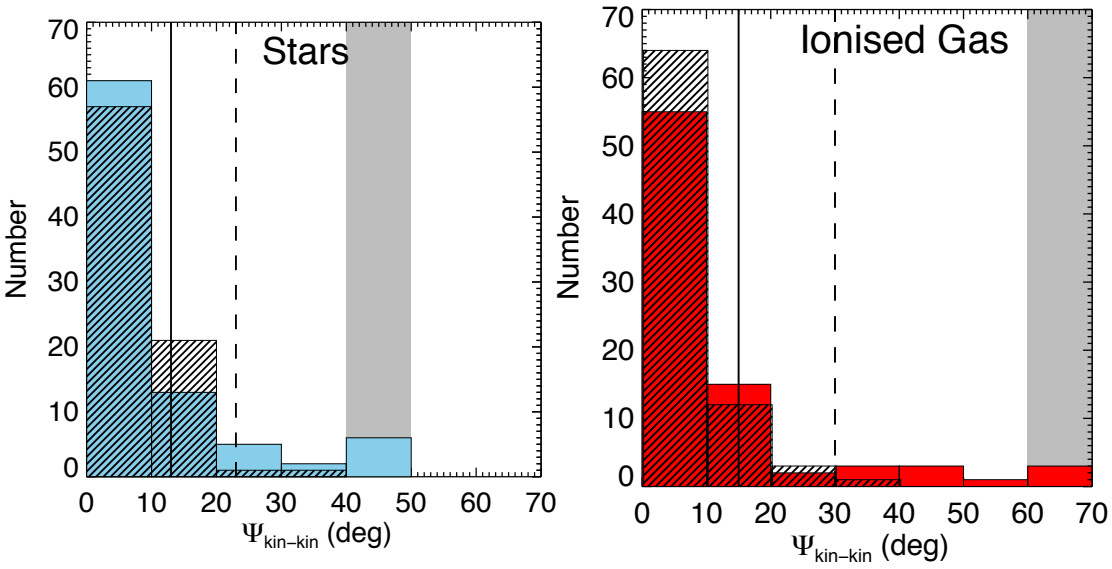


Figure 4.3: Distribution of the kinematic misalignment between the receding and approaching position angles $\Psi_{kin-kin}$ for the stellar (left, blue histogram) and the ionized gas (right, red histogram) components of the interacting sample. In each plot line-filled histograms represent the distribution of $\Psi_{kin-kin}$ for the control sample. Solid lines represent the misalignment for 90% of the control sample. Dashed lines represent the same value for the interacting sample. The bins locate in the gray areas represent those galaxies where is not possible to determine $\Psi_{kin-kin}$.

ments in the stellar component at different mass bins (see top left in Fig. 4.4). This is also the case for the ionized gas, except for the stellar mass bin $9 < \log(M_{stellar}/M_{\odot}) < 9.5$ (see bottom left panel in Fig. 4.4). As for the morpho-kinematic misalignments, ionized gas in interacting galaxies at this mass bin seem to be more kinematically disturbed than more massive galaxies. When we compare the median values of $\Psi_{kin-kin}$ for different interaction stages (see right panels in Fig. 4.4), we find that these misalignments are slightly larger than the median from the control sample. Our results indicate that the signatures of the merger are more subtle in this kinematic tracer than other such as the morpho-kinematic misalignment (see Sec. 4.2.2).

To illustrate the above scenario, we highlight here the well-studied merger remnant NGC 2623 (e.g., Evans et al. 2008). Although its stellar velocity gradient is small ($\sim$ 50 km/s), this velocity field has well defined approaching and receding sides within the radius we estimate $PA_{kin}$. However, these sides are misaligned to each other by $\Psi_{kin-kin} \sim 35\,^{\circ}$. The orientation of the ionized gas velocity field is similar to the stellar field. It is worth mentioning that IFU observations in the nuclear region ($\sim$ 600 pc) in the mid-infrared reveal that in the ionized gas (Br$\gamma$) the orientation of the nuclear disc is consistent with that we found in our velocity distributions (Medling et al. 2014).

These results indicate that motions of interacting galaxies, probed by the alignment between the receding and approaching kinematic sides, do not show significant differences from those observed in isolated galaxies. This holds for different interacting stages and a significant range of stellar masses. This suggests that in those interacting systems showing highly distorted morphologies (e.g., post-merger galaxies) the internal kinematic misalignment may not be a good tracer of the effect on the motion of the galactic components due to interactions and mergers. Dedicated set of numerical simulations would be required to determine whether the results obtained from this kinematic indicator are representative of the actual motions as the merger evolves.

It is important to note that a small fraction of interacting galaxies displays small misalignments

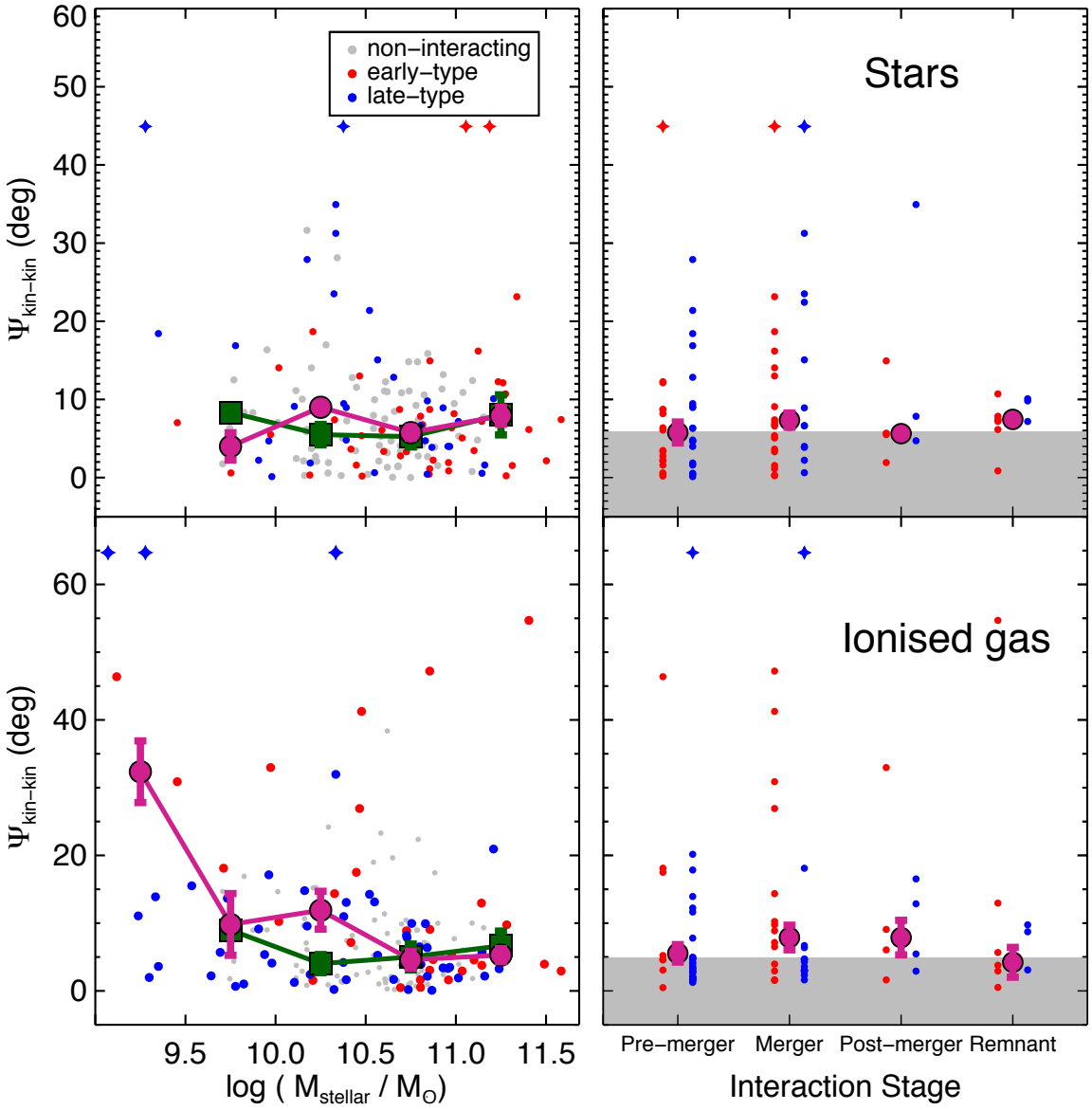


Figure 4.4: Internal kinematic misalignment ($\Psi_{\rm kin-kin}$) for the stellar (top) and ionized gas (bottom) components against the stellar mass (left) and interaction stage (right). As in Fig. 4.2, the red symbols represent early-type galaxies (i.e., E, S0 and Sa) and late-type are shown by blue symbols (i.e., Sb, Sc, Sd). For the left panels, gray dots represent the control sample. Green squares and pink circles represent the median of $\Psi_{\rm kin-kin}$ in each stellar mass and interaction stage bin for left and right panels, respectively.

between their kinematic sides although their velocity distributions do not resemble a symmetric velocity field. For instance, the interacting galaxy NGC 3991 displays an ionized gas velocity field where its sides seem to be aligned ($\Psi_{\rm kin-kin} = 15 \pm 6\,^{\circ}$). However, this object does not show the flattening in the velocity curve expected for a disc-like velocity field (see Appendix A.3). Other galaxies also display velocity fields with similar features: for the stellar component as is the case for Arp 220, NGC 3406NED01, and NGC 3406NED02; while for the ionized gas, NGC 3303, NGC 5394

and NGC 5614. In the following sections we will study other kinematic parameter to characterize as much as possible our sample of interacting galaxies.

Table 4.1: Summary of the kinematic misalignments of the interacting galaxies compared with the control galaxies.

| | | $\Psi_{\rm morph-kin}$ (°) | | $\Psi_{\rm kin-kin}$(°) | | $\delta_{\rm kin}$(°) | |
|---|---|---|---|---|---|---|---|
| | | control | interacting | control | interacting | control | interacting |
| Stellar kinematics | 90% of sample | 21 | 72 | 13 | 22 | 37 | 41 |
| | median | 7 | 14 | 6 | 6 | 20 | 19 |
| | standard deviation | 8 | 21 | 5 | 6 | 9 | 9 |
| Ionised gas kinematics | 90% of sample | 22 | 75 | 15 | 30 | 18 | 42 |
| | median | 8 | 23 | 5 | 6 | 10 | 18 |
| | standard deviation | 8 | 28 | 5 | 6 | 4 | 13 |

### 4.2.4 Kinematic PA deviations

Besides the measurement of $\rm PA_{kin}$, the spatially resolved data also allow us to measure how it changes across the velocity field by means of its deviation at different radii ($\delta\rm PA_{kin}$, see Sec. 2.4.3). This parameter quantifies by how much locations of maximum velocities deviate from a straight line. In a rotational only velocity field this value is zero: all the positions are aligned with the line of nodes for both kinematic sides.

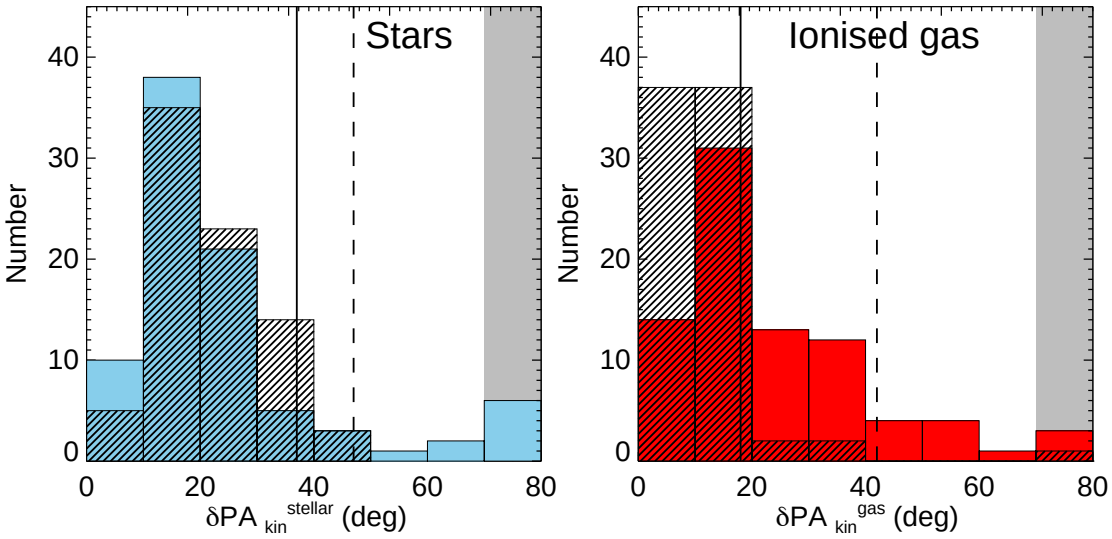


Figure 4.5: Distribution of the deviation of the kinematic PA from a straight line ($\delta\rm PA_{kin}$) for the stellar (left, blue histogram) and the ionized gas components (right, red histogram). Similar to Figs. 4.1 and 4.3, in each plot line-filled histograms represent the distribution of $\delta\rm PA_{kin}$ for the control sample. Solid lines represent the misalignment for 90% of the control sample. Dashed lines represent the same value for the interacting galaxies. The bins locate in the gray areas represent those galaxies where is not possible to determine $\delta\rm PA_{kin}$.

In Fig. 4.5 we present for both samples the $\delta\rm PA_{kin}$ distributions for the stellar (left panel) and the ionized gas (right panel) components. To include 90% of the stellar kinematic PA deviations in

the control sample, we need to set a limiting value of 37 °. We find that 15% (11/85) of the interacting sample has stellar $\delta PA_{kin}$ deviations larger than 37 °. To include 90% of the stellar kinematic PA deviations in the interacting sample, we need to set a limiting value of 41 °. The control and interacting $\delta PA_{kin}$ distributions are likely to be drawn from the same parent distribution ($p_{KS} = 0.7$). The similarities in both distributions suggests that processes responsible to deviate kinematic axes from a straight line are similar in isolated and interacting objects (see medians and standard deviations for each sample in Table 4.1).

For the control sample, the ionized gas kinematic PA deviations are smaller than stellar ones. To include 90% of the ionized gas kinematic PA deviations in the control sample, we need to set a limiting value of 18 °. On the other hand, interacting sample covers a wider range of ionized gas kinematic PA deviations than the control ones (see right panel of Fig. 4.5 and Table 4.1). We find that 48% (41/82) of the objects in this sample has $\delta PA_{kin}$ deviations larger than 18 °. To include 90% of the ionized gas kinematic PA deviations in the interacting sample, we need to set a limiting value of 42 °. Contrary to the stellar component, the interacting and control $\delta PA_{kin}$ distributions for the ionized gas, are not drawn from the same parent distribution ($p_{KS} \sim 0$). The kinematic PA deviations for both components support the results from Sec.4.2.2 namely, interactions and mergers have a larger impact on the ionized gas than in the stellar component.

As in previous sections, we study the dependence of the kinematic PA deviations with stellar mass. We find that these deviations in the stellar component are similar for both the control and interacting samples at different mass bins. Moreover, they tend to decrease for high-mass galaxies (see top left panel of Fig. 4.6). The origin for this trend is not evident. Since we observe this trend in both samples, we suggest that it can be produce by an internal process related to the stellar mass of the galaxy rather than external process such as merger event. Further studies with larger samples are required to confirm and further explain this possible trend. On the other hand, $\delta PA_{kin}$ of the ionized gas remains constant in different stellar mass bins for both samples (see middle left panel of Fig. 4.6). For this component, the median of $\delta PA_{kin}$ at the different mass bins of the interacting sample is systematically larger than the values from the control sample.

In an attempt to quantify the impact of the merger on both components, we plot in the bottom left panel of Fig. 4.6 the ratio between the ionized gas and stellar $\delta PA_{kin}$ deviation. We find that at low and intermediate stellar mass bins the interacting sample has larger ratios than control galaxies. While median values for the interacting sample in these mass bins are large or close to unity, the control sample medians are close to or lower than 0.5. In the highest mass bin, ratios for both samples are similar within the uncertainties. These results suggest that lighter companions in interacting systems react faster than the heavier ones. In fact, similar results have been found for previous observations (e.g., NGC 7771+NGC 7770, Alonso-Herrero et al. 2012) and numerical simulations (e.g., Naab & Burkert 2003) of minor mergers. It is still necessary to explore, with samples covering a wide range in pair parameter space, their impact in the internal motion of interacting galaxies such as the mass ratio.

In the right panels of Fig. 4.6, we separate $\delta PA_{kin}$ deviations according to their interaction stage. Except for the post-merger stage, stellar $\delta PA_{kin}$ deviations remain rather constant for different stages of the merger. Furthermore, they are similar to the median deviations of the control sample. For the ionized gas, the medians from the interacting sample are larger than the median $\delta PA_{kin}$ from the control sample (9 °). In particular, the median deviation of the post-merger stage is larger than other interaction stages (see middle right panel of Fig. 4.6). This suggests that both components display enhanced kinematic PA deviations after the two nuclei coalesced. We have to note that our sample in this particular interaction bin is small, and therefore a large sample of post-merger galaxies is required to confirm this trend. Ratios between ionized gas and stellar $\delta PA_{kin}$ are similar

to the unity at different interaction stages and larger than the median ratio of the control sample (see bottom right panel of Fig. 4.6).

In some objects showing similar $PA_{kin}$ at both kinematic sides, we found large $\delta PA_{kin}$ values. These are the cases of the merging galaxies NGC 3303, NGC 5394, or NGC 5614. Therefore, it is necessary to take into account different kinematic parameters to characterize the velocity field of interacting galaxies. In Sec. 4.3 we discuss the fraction of interacting galaxies that present deviations in more than one kinematic parameter in comparison to the control sample.

### 4.2.5 Ionized gas vs stellar kinematics

Comparisons between spatially-resolved stellar and ionized gas kinematics in the nearby universe for interacting galaxies are rather scarce.They have been performed for a few individual interacting systems (e.g., NGC 6240 [Engel et al. 2010], the Mice [Wild et al. 2014]). Thanks to the wavelength coverage of the CALIFA sample, we can study the motions of both the stellar and ionized gas components. In addition, we can also contrast the parameters we measure in a control sample ($\Psi_{morph-kin}$, $\Psi_{kin-kin}$, and $\delta PA_{kin}$) with those observed in a sample of interacting galaxies.

In Fig. 4.7 we plot the distribution of these differences for the control (80 objects) and interacting samples (where possible, 66 objects). It shows that 90% of the control sample have $\Psi_{gas-stars}$ differences smaller than 16 °. We find that 42% (28/66) of the interacting sample has kinematic differences larger than 16 °. In fact, $\Psi_{gas-stars}$ for the interacting sample can reach values up to 75 °. The distributions of the interacting and control of $\Psi_{gas-stars}$ are not likely to be drawn from the same parent distribution ($p_{KS} = 0$). We also note that the fraction of interacting galaxies with strong kinematic misalignments (i.e., $\Psi_{gas-stars} < 30$ °) reduces to 18% (12/66).

The left panels of Fig. 4.8 show $\Psi_{gas-stars}$ for the interacting and control samples with respect to their stellar masses. The interacting and control samples share similar trends in their median values for different mass bins (see left panel of Fig. 4.8). However, median misalignments are systematically larger for interacting galaxies.

In the right panels of Fig. 4.8 we separate $\Psi_{gas-stars}$ of each galaxy according to its interaction stage. On the pre-merger stage, only a few objects shows misalignments larger than the median value for isolated galaxies. On the contrary, median misalignment for merging pairs is significantly larger than $\Psi_{gas-stars}$ median for the control sample. Indeed, objects in this stage present a wide range of misalignments and also the larger measured misalignment (e.g., NGC 3303, NGC 5929, NGC 5216, UGC 335NED02). However, in the same stage, more than half of the galaxies present alignments similar as those observed in isolated galaxies. Post-merger galaxies present a median misalignment similar to the control sample, albeit the large uncertainty and small size of the subsample. Merger remnants show the largest median misalignment. Most of these objects present large misalignments (e.g., NGC 5739, NGC 5623). We also note that all objects with (measured) strong kinematic PA misalignment between the stellar and ionized gas are early-type objects. The galaxy that shows the strongest distortion is the merging galaxy NGC 3303 (and its companion NGC 3303 NED01). It reaches the counter-rotating case ($\Psi_{gas-stars} \sim 180°$), as we already mention in Sect. 4.2.4, this system present a distorted ionized gas velocity field. Although this system is classified morphologically as a pair of early-type galaxies, the close projected separation between the nuclei ($\sim 5$ kpc) and the fact that they are rather embedded in a single disc-like structure with large tidal features suggest that this system is caught right before the two nuclei coalesced (Georgakakis et al. 2000; Mezcua et al. 2014).

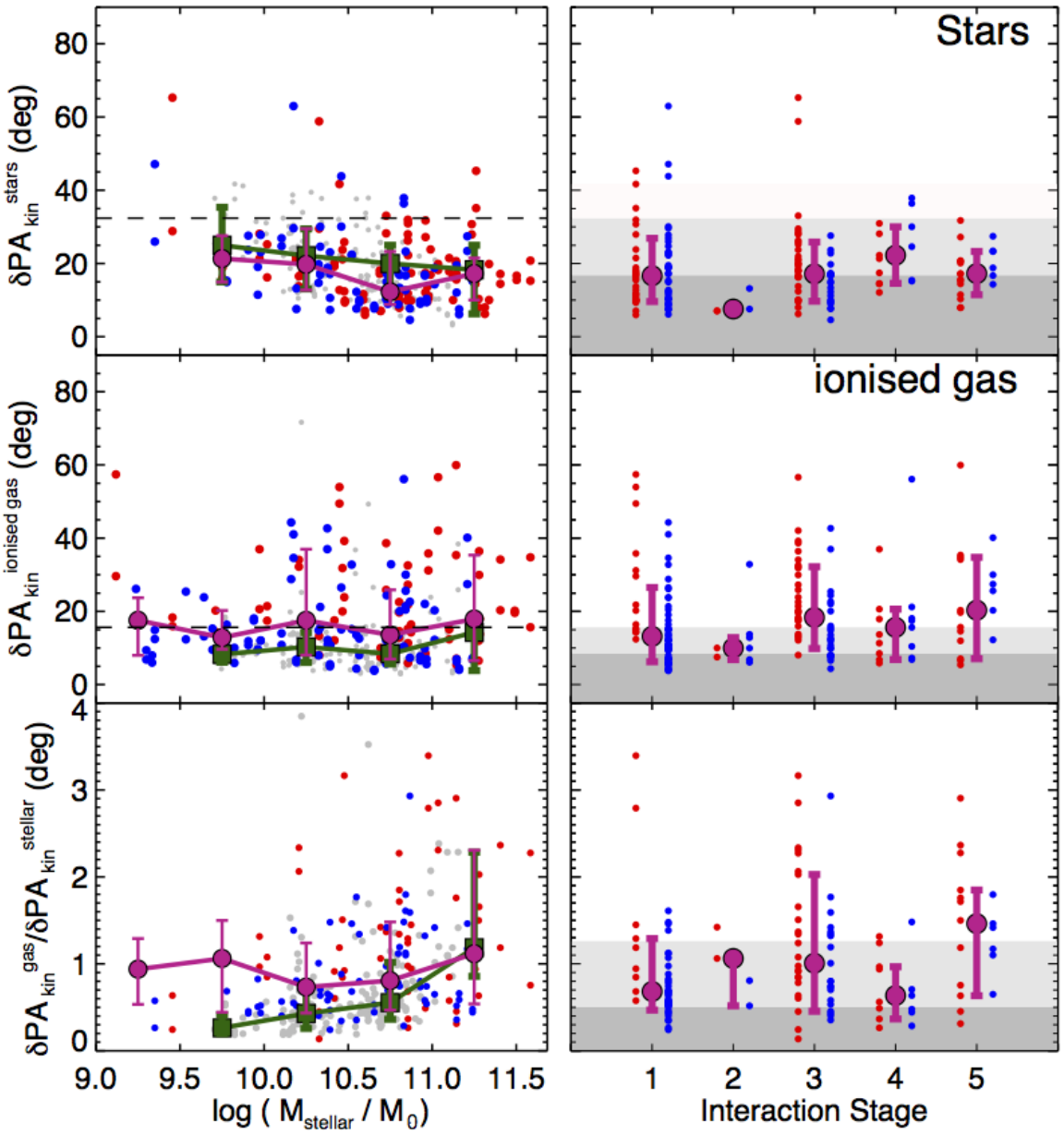


Figure 4.6: Top and middle panels: Kinematic PA deviation from a straight line ($\delta PA_{kin}$) for the stellar and ionized gas components with respect to the stellar mass (left panels) and interaction stage (right panels), respectively. Bottom panels: Ratio between the kinematic PA deviation of the stellar and the ionized gas component. As in Fig. 4.2, the red symbols represent early-type galaxies (i.e., E, S0 and Sa) and late-type are shown by blue symbols (i.e., Sb, Sc, Sd). For the left panels, gray dots represent the control sample while green squares and pink circles represent the median of $\delta_{kin}$ in mass bins of 0.5 in units of $\log(M_{stellar}/M_{\odot})$ for the control and interacting sample, respectively. For the right panels, the pink circles represent the median of $\Psi_{morph-kin}$ in each interaction stage bin while gray regions shows the median $\delta PA_{kin}$ obtained from the control sample. In each panel the error-bars for each median value are obtained from bootstrapping.

## 4.3 Impact of the interactions on internal motions of galaxies

Throughout this study we aim to quantify the impact of the merging in galactic kinematics at different stages of merging process by comparing different parameters from a sample of interacting

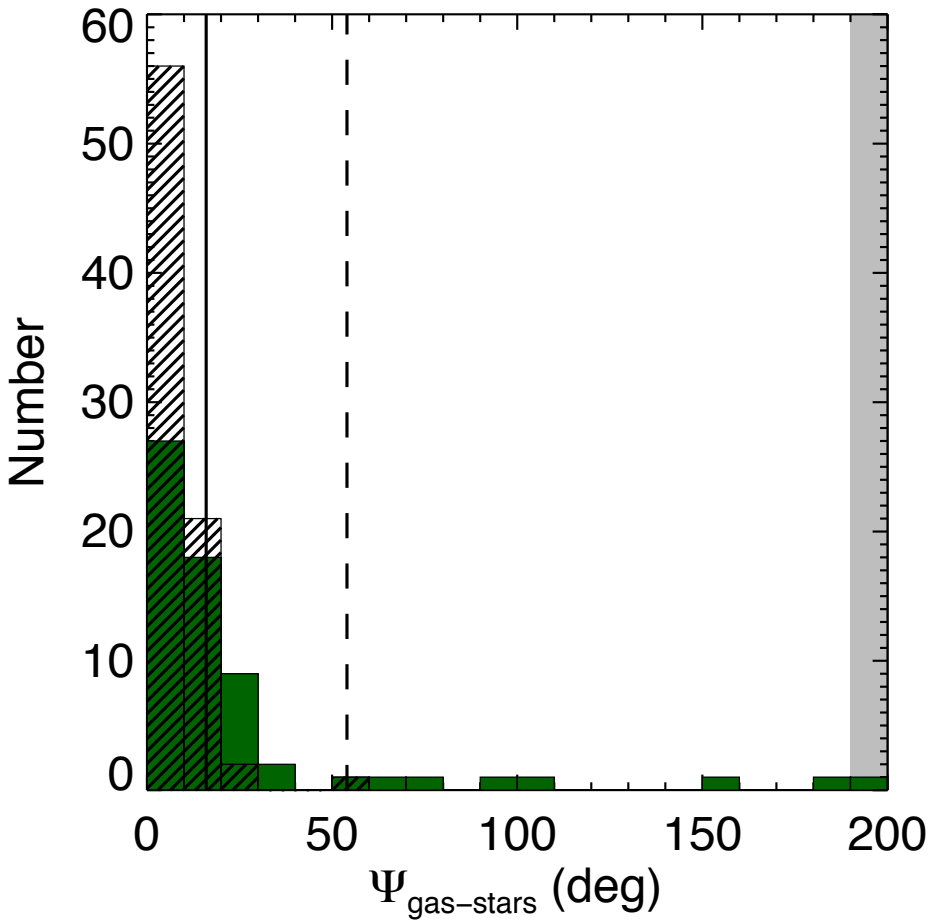


Figure 4.7: Distribution of the kinematic misalignment between the stellar and ionized gas components ($\Psi PA_{gas-stars}$). Line-filled histograms represent the distribution of $\Psi PA_{gas-stars}$ for the control sample while green histrogram show the distribution of these misalignments for the interacting sample. Solid line represents the largest deviation for 90% measured in the control sample. Dashed line represents the same value for the interacting galaxies.

galaxies with a sample of isolated objects. Based only in the morpho-kinematic PA misalignments, we find that a significant fraction of interacting galaxies presents large misalignments (see Sec. 4.2.2). Moreover, most of these misalignments are found in pairs with evident signatures of interaction (see Fig. 4.2), making the morpho-kinematic misalignment a good indicator to gauge the effect of interaction at this stage of interaction. When we explore the kinematic alignments between the receding and approaching sides ($\Psi_{kin-kin}$), we find that their distributions for the interacting sample resemble those from the control sample in both components (see Table 4.1 and Fig. 4.3). In general, median $\Psi_{kin-kin}$ values for different interaction stages are similar to those derived from the control sample (see Sec. 4.2.3) indicating that the impact of interactions and subsequent merger is more subtle for this kinematic indicator than others presented in this study. We note that velocity fields cover, in most of the cases, the central region of the interacting galaxies. It can be that at larger scales the misalignment between the kinematic sides of galaxies increases. However, detail kinematic modeling for interacting galaxies is required to understand the cause of the little impact of interactions on this parameter.

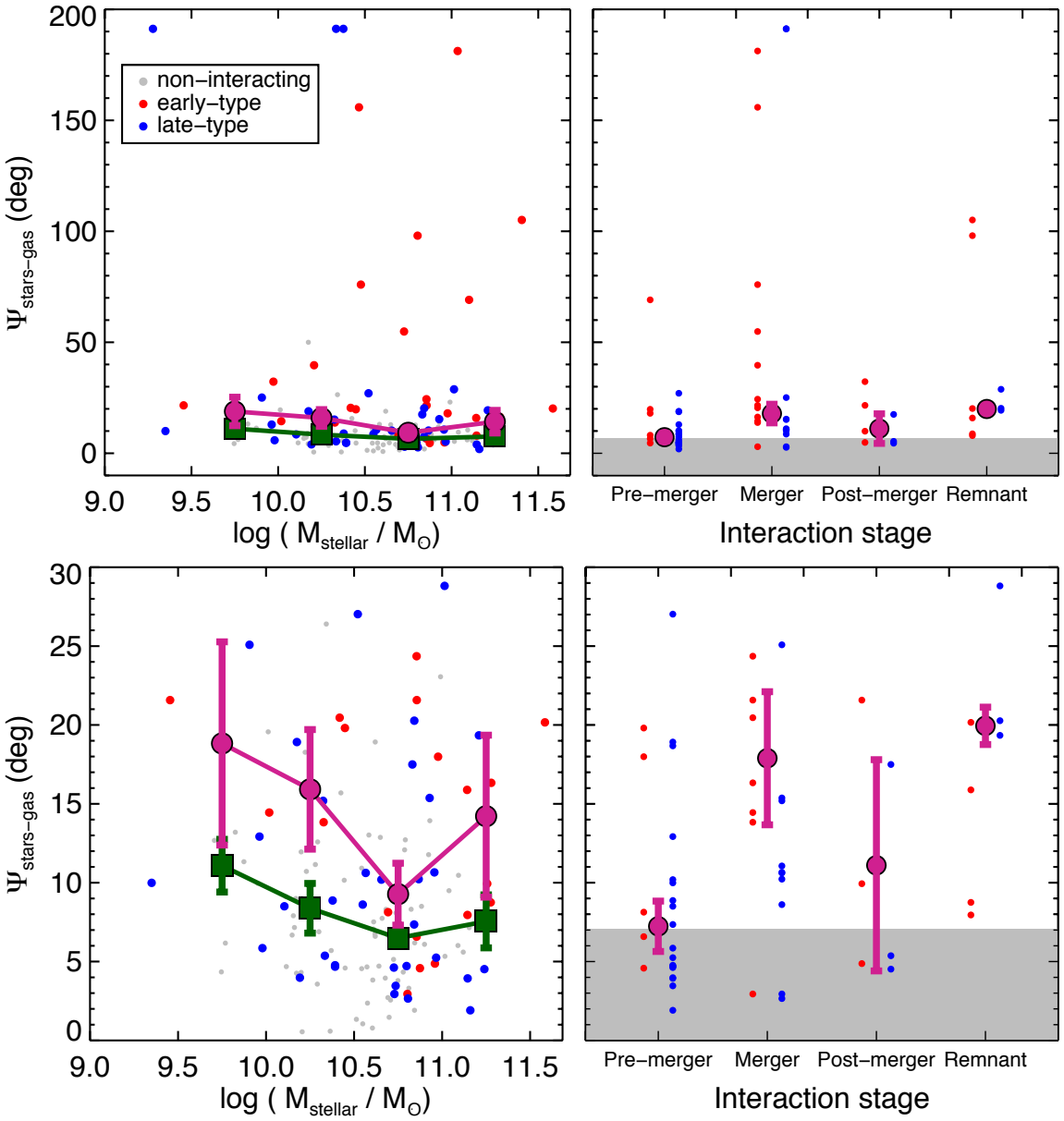


Figure 4.8: Kinematic misalignment between the stellar and the ionized gas component ($\Psi_{\rm stars-gas}$) against the stellar mass (left) and the interacting stage (right). Top panels show the entire range of $\Psi_{\rm stars-gas}$ while bottom panels show a zoom to highlight median values. In all the panels the red symbols represent early-type galaxies (i.e., E, S0 and Sa) and late-type are shown by blue symbols (i.e., Sb, Sc, Sd).For the left panels, gray dots represent the control sample while green squares and pink circles represent the median in each stellar mass bins for the control and interacting samples, respectively. For the right panels, the pink circles represent the median of $\Psi_{\rm stars-gas}$ in each interaction stage bin while gray regions shows the median $\Psi_{\rm stars-gas}$ obtained from the control sample. Error bars are dominated by the uncertainty in the kinematic orientations, which are derived from Monte Carlo simulations.

Further similarities between the interacting and the control sample are present in the stellar kinematic PA deviations ($\delta{\rm PA_{kin}}$, see left panels of Fig.4.5). In both samples we find large stellar $\delta{\rm PA_{kin}}$ medians (see Sec. 4.2.4). This suggest that the mechanisms responsible to produce these large values could be similar. Such mechanisms could include radial motions or dynamical heating.

We note that ionized gas kinematic deviations in nearly half of the interacting sample are larger than those obtained from the control sample. This indicates that ionized gas has a proned reaction to the interaction/merger. Ionized gas kinematic deviations are also systematically larger at different interaction stages than those found in the control sample, in particular for the post-merger stage where its median deviation is the largest among the interaction stages (see Fig.4.5).

Comparing the stellar and the ionized gas kinematic PAs we find that nearly half of the interacting galaxies show misalignments larger than those observed in the sample of isolated galaxies (see Fig. 4.7). This suggest that merging event does have an impact in the kinematic of the galaxies. At different interaction stages these median values change significantly. For pre-merger galaxies, median misalignment is similar as the one derived from the control sample,suggesting that interactions have a similar impact in the kinematics of both components than secular processes in isolated galaxies. As the merger evolves the systems in the merging phase show a larger median misalignment between the two components in comparison to the median from the control sample. This indicates that at this phase, tidal effects do have a differential impact in the kinematic orientation of the components. Detailed numerical studies will be required to explore the initial parameters that lead to observed kinematic configuration of the stars and the ionized gas major kinematic PA. Due to its large error bar the median kinematic misalignment from the post-merger stage ranges from the one obtained from the control sample to the one derived from the merger stage. Studies on numerical simulated mergers suggest that velocity fields should present strong distortions after the two nuclei have coalesced (e.g., Kronberger et al. 2007). However, spatially resolved observations of central regions of ULIRGs including post-merger galaxies, find that at these scales the kinematic orientation of both the stellar and the ionized gas components are very similar to each other (Medling et al. 2014). In this scenario, young stars formed in situ, follow the kinematics of the ionized gas rather than the kinematics of those stars from the progenitor galaxies. A detailed study of the resolved stellar population in our sample is required to constraint the ages of the stellar population in these merger remnants. In addition, a larger sample of post-merger galaxies is required to understand which type of motions predominate between these two components.

In the remnant subsample we find the largest median misalignment between the stars and the ionized gas. 6 out of 9 galaxies are early-type objects. Assuming that these galaxies are the remnants of a merger event, the kinematic orientation of the stars and ionized gas components is not likely to change significantly (Lagos et al. 2015). Several factors can explain this apparent dichotomy. As for the post-merger sample, the size of the remnant sample is rather modest in comparison to the pre-merger and merger ones. Although this is expected (Darg et al. 2010; Ellison et al. 2013a), our sub-samples may not cover homogeneously the space parameters of the merging. On the other hand as we note in Sec. 2.3.1 our ability to determine weather a galaxy is a merger remnant is based only in the observation of low-surface brightness tidal features. This features could be the result of a recent minor merger or a newly supply of gas (Davis et al. 2011; Lagos et al. 2015) leading to the observed strong difference between the kinematic orientation of the stars and the ionized gas in these galaxies.

The wealthy of the data allow us to compile the different kinematic parameters presented in this study to quantify the impact of interactions and mergers in the global galactic kinematics. We find that 63% (65/103) of the interacting sample has a kinematic misalignment larger than 90% of the control sample in at least one of the parameters for any component. We also estimate the fraction of interacting galaxies with differences in at least two kinematic indicators larger than the control sample in each component. For the stellar and ionized gas components we find that these fractions correspond to 21% (18/85) and 39% (32/82), respectively. These fractions reveal that interactions and mergers have a significant impact in the motions of the galaxy's components in particular for the ionized gas. Furthermore, from the objects in the interacting sample with $\Psi_{\rm gas-stars}$ larger than the control sample we explore the fraction of these objects with large misalignments in any other

kinematic parameters presented (i.e., $\Psi_{\rm morph-kin}$, $\Psi_{\rm kin-kin}$, and $\delta{\rm PA}_{\rm kin}$) including both components. We find that 16/66 (23%) objects show misalignments larger than the values expected for isolated galaxies. Although this fraction is not as large as those derive from some individual kinematic parameters, it reveals that in general the interaction has a noteworthy impact in the motion of galaxies.

Most of the statistical studies of spatially-resolved kinematic in merging galaxies have been carry out at high redshift ($z < 0.5$, for a review see Glazebrook 2013). Usually mergers at high redshift are identify by their morphology (e.g., Conselice et al. 2003, 2008; Bluck et al. 2012). Most of these studies found a significant fraction of high-redshift galaxies with regular kinematic patterns despite their irregular morphology, suggesting the presence of gas-rich discs at early stages of the Universe. Kinematic studies are useful to distinguish between a rotating disc or distorted motions due to a merging. Indeed one criteria used to distinguish rotating discs at high redshift is the alignment between (modeled) kinematic and morphological PA (e.g., Epinat et al. 2012). Although it is beyond the scope of the present study, this statistical characterization and model-free methodology can be used as a high resolution benchmark for kinematic properties of merging galaxies that can be compare with those at high redshift.

Finally let us note that although studies of large samples of velocity fields of interacting and mergers galaxies in the local Universe are rather scarce, Bellocchi et al. (2013) found that a significant portion of ULIRGs are dominated by rotation (76%). Their sample covers different stages from interacting to mergers galaxies. Even though, we cannot confirm with the kinematic properties presented here that our sample of interacting galaxies are supported by rotation, by comparing with a control sample that is expected to be supported by rotation, we find evidence that this could be the case in some objects in our sample of interacting galaxies.

Note however that not always the alignment in the kinematic parameters presented in this study represent rotational support. For instance, Engel et al. (2010) found that even though circular-kinematic signatures are present in the velocity distributions of the binary system NGC 6240, the interacting galaxies are not necessarily dynamically supported by rotation. In a future work we will explore the dynamical support of our interaction sample through better spectral resolution data from CALIFA (V1200 configuration, Husemann et al. 2013).

## 4.4 Summary and Conclusions

In this study we analyze the stellar and ionized gas velocity fields of 103 interacting galaxies covering different stages of the merger event – from close pairs to merger remnants. To differentiate the kinematic signatures due to internal processes from those triggered by the interaction, we measured homogeneously the same kinematic properties in a sample of isolated galaxies (Barrera-Ballesteros et al. 2014). We measure the major kinematic position angles from both receding and approaching sides directly from the velocity maps in both components, making no assumptions on the internal kinematics of the interacting systems. This method provides: the morpho-kinematic misalignment for both sides, the internal (mis)alignment between both kinematic sides, the deviation of the kinematic PA from a straight line, and when stellar and ionized gas kinematics are measurable, the (mis)alignment between these two components.

We find that 43% (37/85) and 52% (43/82) of the interacting sample has stellar and ionized gas morpho-kinematic misalignments larger than those found in the control sample. In particular, we find a large fraction of these morpho-kinematic misalignments in galaxies included in binary systems with evident signatures of interaction. The median internal kinematic misalignment for

interacting galaxies is slightly larger than the one derived from the control galaxies at different stellar masses and interaction stages. Comparison between the stellar and the ionized gas kinematic PA (66 objects) reveals that 42% (28/66) of the interacting sample has misalignments larger than those presented by the control sample. In particular, median misalignments of mergers and remnants are significantly larger than median provided by isolated galaxies. Distributions of the stellar kinematic PA deviations are similar in both samples. However, 48% (41/82) of the interacting galaxies have ionized gas kinematic PA deviations larger than control sample, in particular in the post-merger stage. This suggests that kinematic PA deviations in the ionized gas can be used as a tracer to determine whether a galaxy is or has been under an interaction or recent merger.

Our study indicates that interactions have a significant impact in the motion of stars and ionized gas in galaxies. Even more, our results probe the wide range of kinematic stages observed in galaxies under different phases of merger. From velocity fields with similar properties as those found in isolated galaxies to very distorted velocity fields with large kinematic misalignments.

The CALIFA survey allow us to characterize the spatially resolved properties of galaxies at different stages of interaction. In particular, this study provides a nearby Universe benchmark for kinematic comparisons with high redshift galaxies. Further studies with simulated high redshift observations using the current spatially resolved data will allow us to quantify the fraction of rotating disks and compare with the fraction observed at high redshift. Such simulations for the ionized gas in CALIFA galaxies have been already carried out (Mast et al. 2014).

Our findings encourage the comparison of observational velocity fields with those obtained from numerical simulations. Exploring different configurations of the merging galaxies with different properties of the progenitors will give significant insight to reveal which are the relevant parameters that yield the variety of observed velocity fields in merging galaxies.

Chapter 5

# Star Formation and Metallicity in Merging Galaxies

*In this chapter we study the impact of the interaction in the star formation and oxygen abundance at different galactic scales. To disentangle the effect of the interaction and merger from internal processes we contrast our results with a control sample introduced in Sec. 2.2. We confirm the moderate enhancement (× 2-3 times) of specific star formation rate (sSFR) for interacting galaxies in central regions as reported by previous studies, however, star formation is comparable when observed in extended regions. We find that control and interacting star forming galaxies share similar oxygen abundances in their central regions, when normalize to their stellar masses. Oxygen abundances of these interacting galaxies seem to decrease respect to the control objects at large aperture sizes measured in effective radius. Although the enhancement in central star formation and lower metallicities for interacting galaxies have been attributed to tidal induced inflows, our results suggest that other processes such as stellar feedback can contributed to the metal enrichment in interacting galaxies. The results and conclusions of this chapter has been presented in an article published in the journal Astronomy and Astrophysics (Barrera-Ballesteros et al. 2015)*

## 5.1 Introduction

Interactions and mergers are identified as key mechanisms in increasing the star formation rate (SFR) in galaxies (e.g., Sanders & Mirabel 1996; Borne et al. 1999). In particular, luminous infrared galaxies (LIRGs), which are associated almost exclusively to merger events, present strong episodes of star formation (e.g., Ellison et al. 2013b). The scenario proposed by these studies and hydrodynamical numerical simulations (e.g., Mihos & Hernquist 1996; Barnes & Hernquist 1996) suggests that this enhancement is the result of tidally induced inflows of gas that favors the increment of star formation activity in the central region of interacting and merging galaxies. Large samples of interacting and merging galaxies in the Sloan Digital Sky Survey (SDSS, e.g., Ellison et al. 2008b, 2013a; Scudder et al. 2012; Patton et al. 2013) indicate that although central SFR is enhanced in these objects compared with non-interacting galaxies of similar stellar mass, on average this increment is rather moderate. This indicates that the triggering of starburst episodes depends on more parameters than the mere fact of galaxies being in interaction (orbital configuration and intrinsic properties of the progenitors; e.g., Cox et al. 2006b; Di Matteo et al. 2008).

It is also worthwhile noting that statistical spectroscopic studies like the one above are performed by observing a fixed projected portion of the galaxies (e.g., SDSS or GAMA fiber sizes; Casteels

et al. 2014; Robotham et al. 2014). This yields measurements on different galactic scales, making it difficult to assess the extension of star formation. In this regard, IFS observations of interacting galaxies are crucial for understanding whether the enhancement in the SFR is a global or a localized process. An example of the usefulness of such observations has been demonstrated by Wild et al. (2014) considering a single interacting system NGC4676A/B . From a detailed study of the Mice galaxies, they found that there is a moderate increment in the central SFR and no net enhancement in the global SFR. Statistical studies of spatially resolved star formation in interacting galaxies are therefore required. Even more, to make a fair comparison, a homogeneously observed sample of non-interacting galaxies is also required. Recently, numerical simulations are starting to explore the extend of star formation induced by the interaction. Moreno et al. (2015) find enhancement in the star formation on the central kpc scales and moderately suppressed activity at larger galacto-centric radii.

In the above picture, these metal-poor gas inflows decrease the central metallicity in comparison to non-interacting galaxies (e.g., Kewley et al. 2006). As a consequence, merging galaxies are thought to contribute to the scatter in the mass-metallicity relation (hereafter M-Z relation) of star forming galaxies. However, recent numerical simulations that included feedback processes have suggested that nuclear metallicity depends on more factors than the dynamics of the gas, such as the chemical enrichment due to the ongoing star formation, the stellar (and possible AGN) feedback, and returned material by evolved stars into the interstellar medium (ISM) of the entire galaxy (Torrey et al. 2012). The result of the interplay between these different processes in these simulations could lead, in some cases, to a depression in the central metallicity or even an enhancement with respect to isolated galaxies. Spatially resolved observational studies are then required to shade some light on the chemical evolution of interacting/merging galaxies.

Recently, IFS studies have been carried out aimed at understanding the properties of the ionized gas in individual H II regions for a large sample of galaxies. The radial gradient of oxygen abundance in galactic disks has been characterized, with an observed flattening in this gradient caused by interactions and mergers (Sánchez et al. 2014). These authors also confirmed the global and local nature of the M-Z relation (Sánchez et al. 2013). These studies have been possible due to the IFS data provided by the CALIFA survey (Sánchez et al. 2012a, see Sec. 2.1). This dataset allows us to study, for the first time spatially resolved properties of the ionized gas in a significant sample of interacting and merging galaxies to unveil the effect of interactions at different spatial scales and at different stages of the interaction. It also allow us to compare these properties with a sample of homogeneous observations of non-interacting galaxies.

In this study we aim to investigate the impact of interactions on the star formation and oxygen abundance on different galactic scales. To accomplish this, we study the emission-line flux maps extracted from the data cubes of interacting and post-merger galaxies as explained in Sec.2.4.4. From these maps we derived integrated properties such as the H$\alpha$ equivalent width [hereafter, EW(H$\alpha$)] and flux ratios essential to derive oxygen abundances. In Section 5.2 we use these flux ratios to classify each of the two samples into star-forming and non-star-forming galaxies. Using this classification, we compare in Section 5.3 the EW(H$\alpha$) of the interacting and control sample for the star-forming and non-star-forming galaxies. In Section 5.4 we compare the scatter of the metallicity between star forming control and interacting galaxies in their central region. In Section 5.5 we study the change of the metallicity scatter at different aperture sizes. Finally, we summarize our results in Section 5.6.

## 5.2 BPT diagrams

As we described in Sec. 2.4, from the flux maps of the interacting and control samples we measured the integrated fluxes in two different apertures: a central and extended apertures. For each of these two apertures sizes we used two different scales, in arcsec (30 and 5 arcsec, for the extended and central apertures, respectively) and $R_{eff}$ units (2.5 and 0.5 $R_{eff}$). We chose the size of the central aperture to be approximately twice the size of the PSF in the survey (FWHM $\sim$ 2.5 arcsec). The extended aperture was chosen to cover a wide portion of the galaxies. In terms of the Petrosian radius we covered a generous portion of the galaxies (i.e., $1.5 < r_p < 8$). We plot in Fig. 5.1 for each aperture and scale described in Sec. 2.4 the classical diagnostic diagram using the line ratios log ([O III] $\lambda$5007/H$\beta$) vs log ([N II] $\lambda$5755/H$\alpha$) (Baldwin et al. 1981, BPT diagram hereafter) in order to determine the fraction of star-forming galaxies in each of the two samples for a given aperture size. We also included the demarcation line described by Kewley et al. (2001). Star-forming objects lie below this line while AGN-powered sources are mostly located above it. On both size scales the trends in each aperture are similar. For the central apertures (see left panels of Fig. 5.1) in both samples, a large fraction of galaxies spread in the right side of the BPT diagram, covering from the star forming to the AGN zone. However, some interacting objects lie in the so-called left branch (i.e., log ([N II]$\lambda$6583)/H$\alpha$) $\lesssim$ - 0.6), associated with star-forming galaxies. In the extended apertures (right panels of Fig. 5.1) a large fraction of galaxies from both samples lie in the star-forming zone indicating that the integrated flux includes a large fraction of H II regions in both samples than in the central aperture.

We note that for both aperture sizes in these BPT diagrams there is a non-negligible fraction of interacting galaxies located in the left-branch whereas none of the control sample galaxies is located in this zone. As explained in Sánchez et al. (2014), objects located in this branch are correlated with a large fraction of young stellar population. For the central aperture, these galaxies are included in pairs or interacting systems (10 objects in both aperture scales). This also holds for the extended aperture (13 and 12 objects for the 30 arcsec and 2.5 effective radius apertures, respectively). Since these galaxies are expected to have a large fraction of young stellar population, these results suggest an increment in the SFR in interacting galaxies with respect to the control sample, particularly in binary systems. In the following section we study the impact on the change of the sSFR by the interaction/merger across the galaxies by means of the spatially resolved EW(H$\alpha$).

## 5.3 Central and extended EW(H$\alpha$)

Once we discriminated in both the control and interacting samples between star and non-star forming galaxies for each aperture size, we explore how the EW(H$\alpha$) changes at different scales of these galaxies. The subsample of star forming galaxies is selected in the interacting and control samples following the criteria used by Sánchez et al. (2014): objects with line ratios below the Kewley demarcation line in the BPT diagnostic diagram in Fig. 5.1 and EW(H$\alpha$) larger than 6 Å. These criteria assure that the selected galaxies are indeed star forming galaxies. Our spatially resolved data allow us to study the distribution of the EW(H$\alpha$) at different aperture sizes in galaxies classified as star and non-star forming galaxies depending on the ionized gas fluxes in each aperture. From Fig. 5.1 we note that the non-star forming sample includes mostly AGN-like objects suggesting that the fraction of objects with a LINER-like spectrum is negligible.

In Fig. 5.2 we plot the log(EW(H$\alpha$)) distributions of star and non-star forming galaxies for both samples at the 5 and 30 arcsec apertures ($EW_{central}$ and $EW_{extended}$, respectively) for galaxies classified as star and non-star forming galaxies in the 5 arcsec aperture (see Sec. 5.1). In Fig. 5.3 we plot the same distributions using as classification the integrated fluxes within the 30 arcsec aperture.

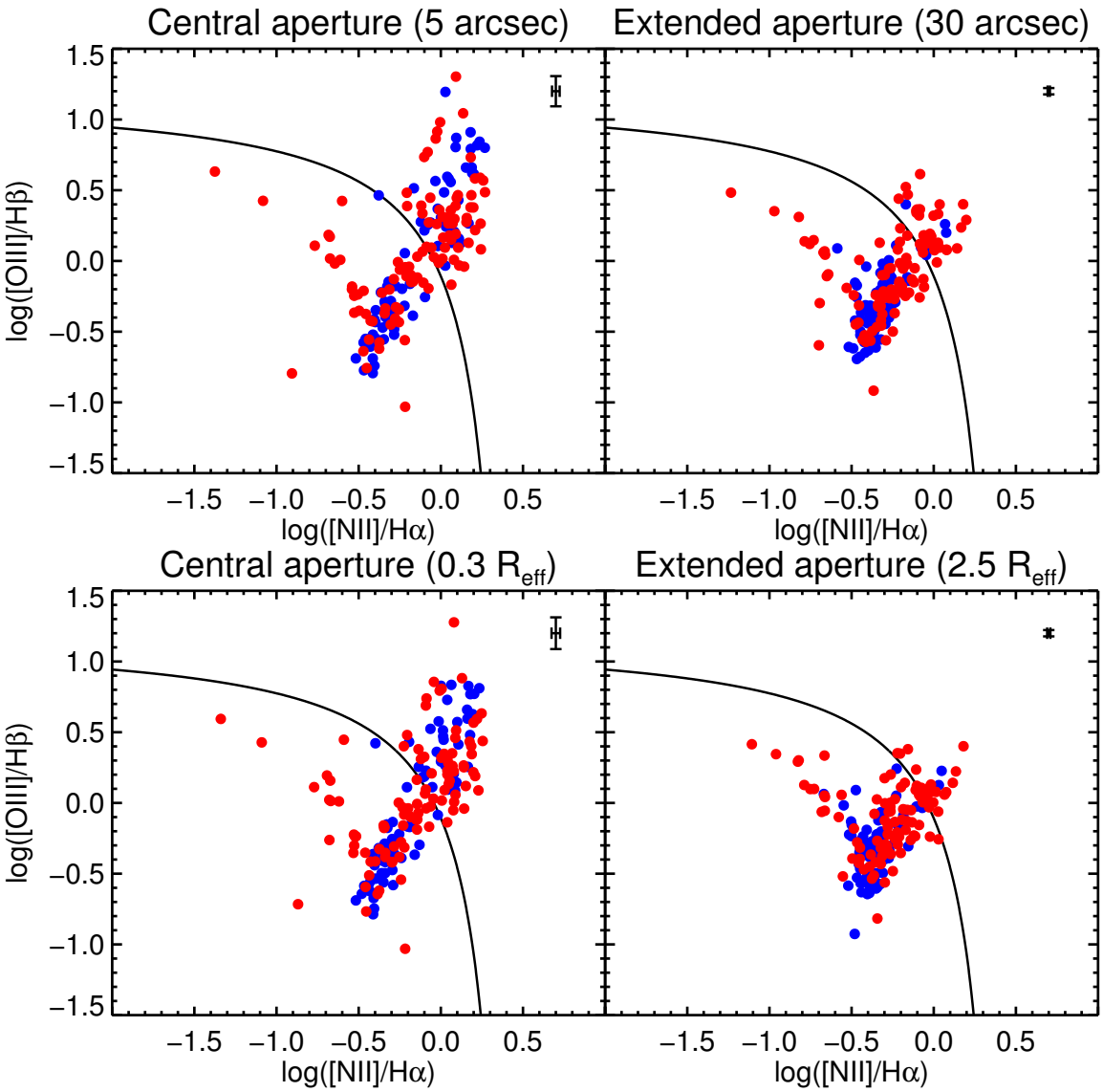


Figure 5.1: BPT diagnostic diagrams for the control (blue points) and interacting (red points) samples measured within a central (left panels) and extended (right panels) apertures centered in the optical nucleus. Fluxes in top panels are derived using apertures in a arcsec scale while fluxes in bottom panel are obtained using an effective radius scale. The solid lines in each panel represent the division between star forming and non-star forming galaxies presented in Kewley et. al (2001). Typical uncertainty is plotted at the top of each panel.

We repeat the same exercise using the 0.3 and 2.5 $R_{eff}$ aperture sizes. (see Figs. 5.4 and 5.5). We note that the EW(H$\alpha$) distributions in both samples using either the arcsec or effective radii scales are similar for the central and extended aperture sizes, respectively. In order to make a reasonable comparison with previous results using single-fiber spectroscopic, we will focus our analysis in the EW(H$\alpha$) derived from the arcsec apertures.

Although the fraction of galaxies selected in the central aperture as star forming is similar for control and interacting samples (33 and 35 objects, respectively), when we compare their $EW_{central}$ distributions we find that a significant fraction of interacting galaxies (10/35) present larger values

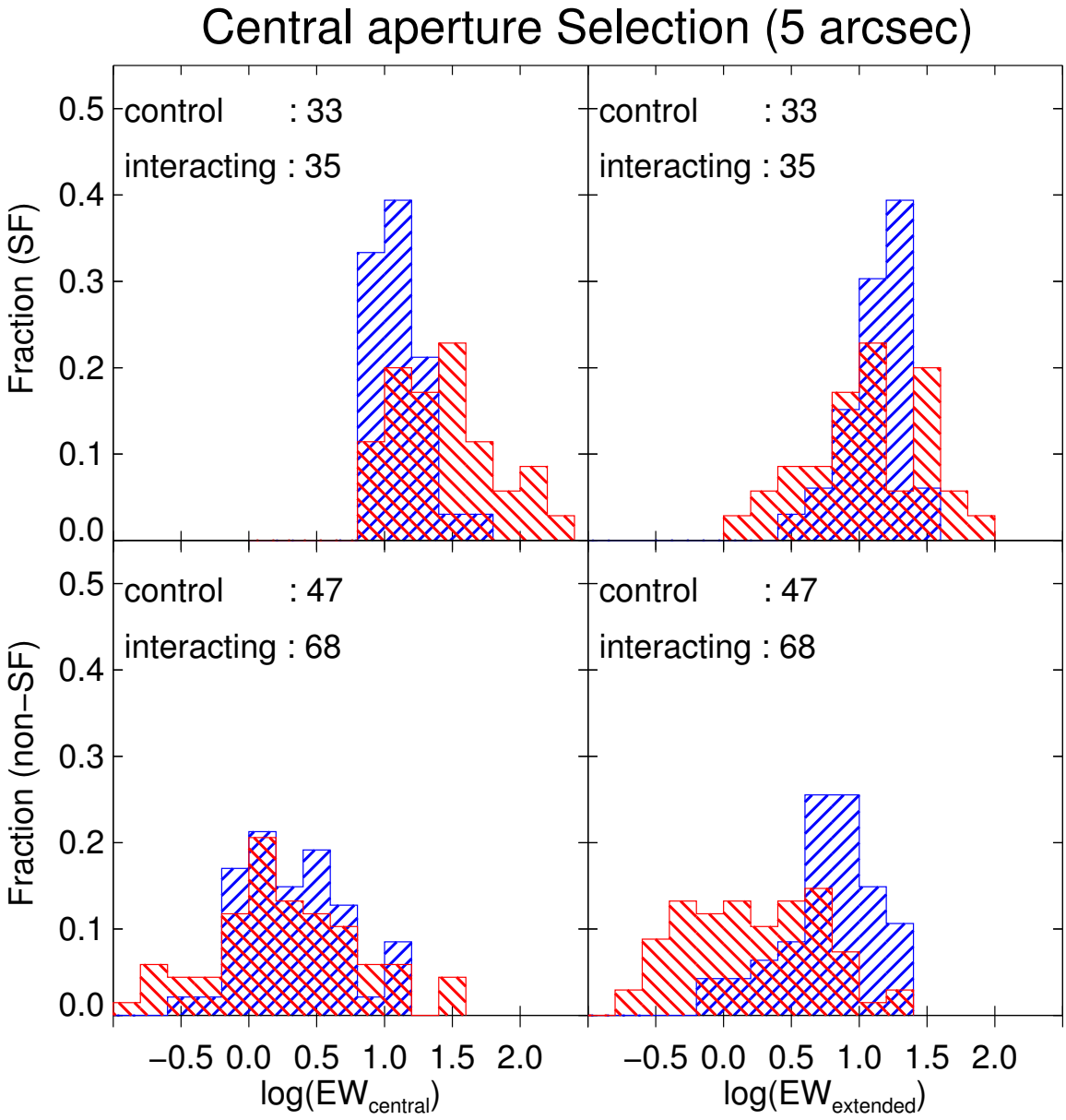


Figure 5.2: Distributions of the integrated EW(H$\alpha$) for the interacting (red) and control (blue) samples using an aperture size of 5 arcsec. Top and bottom panels show the distributions of the star-forming and non-star-forming galaxies, respectively. Left and right panels show the EW(H$\alpha$) distributions measured using the 5 ($EW_{central}$) and 30 ($EW_{extended}$) arcsec apertures, respectively. For this classification we use the integrated emission line fluxes ratios presented in Sec. 5.1 using the same selecting aperture size.

in comparison to the entire control sample (see top left panel of Fig. 5.2). Most of these objects are either in close pairs or in binary systems with evident signatures of interaction (33/35). A large fraction of these interacting galaxies are late-type (28/35). We also find clear statistical differences between these two samples. The median $\log(EW_{central})$ of the star forming interacting subsample is larger than the median of the control sample ([1.41 $\pm$ 0.07] log(Å) and [1.09 $\pm$ 0.03] log(Å),

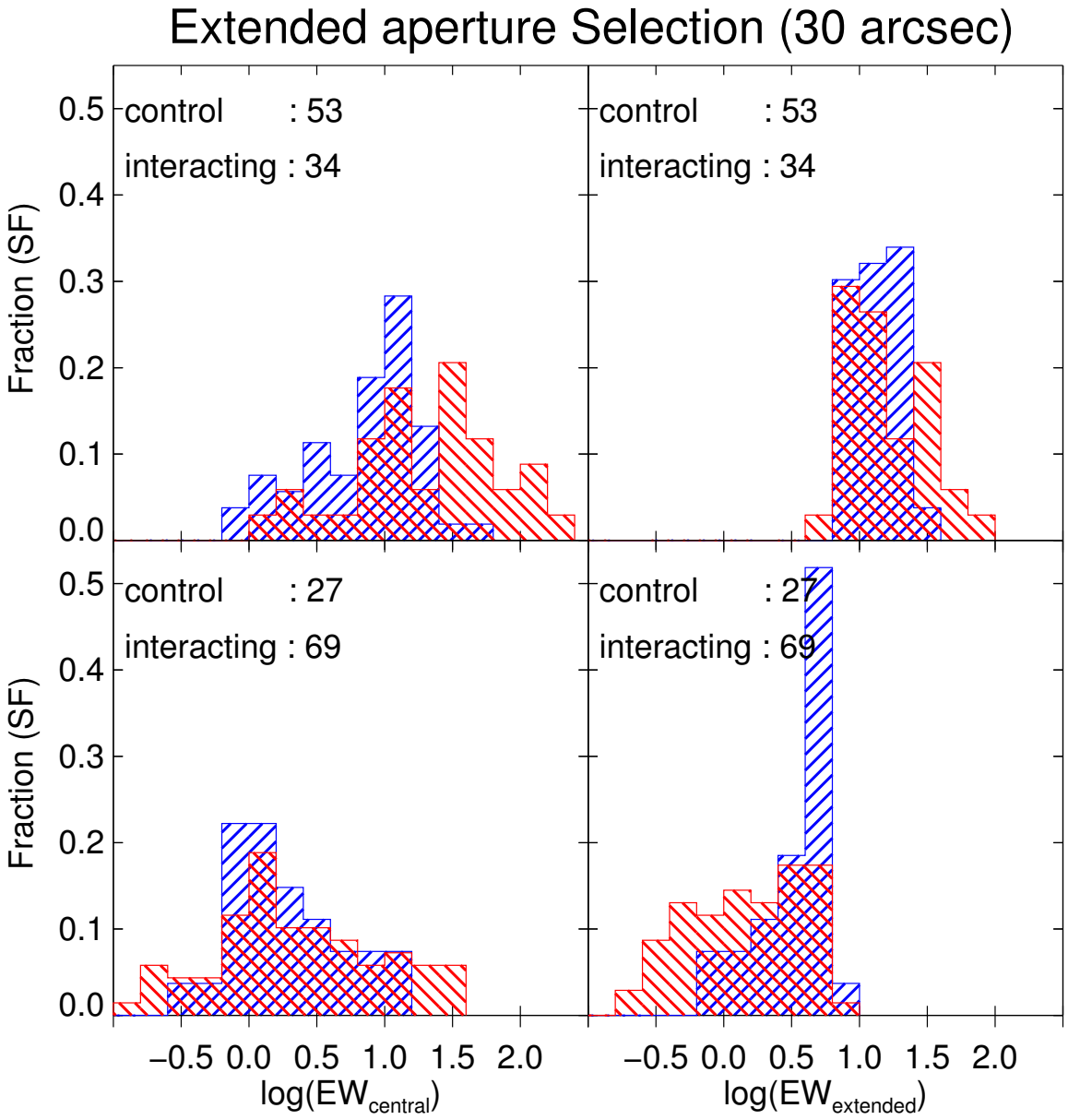


Figure 5.3: Distributions of the integrated EW(H$\alpha$) using an aperture size of 30 arcsec. As in Fig. 5.2 blue and red histograms represent control and interacting EW(H$\alpha$) distributions, respectively. Top and bottom panels show the distributions star and non-star forming galaxies, respectively.

respectively) [1]. These interacting galaxies cover a wide range of logEW(H$\alpha$) in comparison to the control sample (standard deviations of [0.38 $\pm$ 0.07] log(Å) and [0.39 $\pm$ 0.07] log(Å), respectively). Moreover, a Kolmogorov-Smirnoff test (KS-test, hereafter) reveals that these two samples are not likely to be drawn from the same parent sample ($p_{KS} = 0.001$). We transform the EW(H$\alpha$) to sSFR by means of the empirical relation presented by Sánchez et al. (2013). For the interacting star forming galaxies the median sSFR is (2.3 $\pm$ 0.2) $\times$ $10^{-10}$ yr$^{-1}$ while the median sSFR for the control subsample is approximately half the interacting value ([9.3 $\pm$ 0.9] $\times$ $10^{-11}$ yr$^{-1}$).

[1]Errors in the medians and standard deviations are obtained from a bootstrapping method.

The distributions of $EW_{extended}$ for galaxies selected as star forming in the central aperture are rather similar (see top right panel of Fig. 5.2), median values are of the same order in both samples ([1.07 ± 0.01] log(Å) and [1.18 ± 0.02] log(Å), respectively). The moderate sSFR enhancement we observe in central regions of interacting galaxies (∼ 2.5 times) has been reported by previous statistical studies (e.g., Kewley et al. 2006; Ellison et al. 2008b; Knapen & James 2009; Patton et al. 2013). However, we point out that those studies covered a portion larger than the central region. In fact, their aperture sizes are similar to our extended aperture where we find a moderate reduction of the sSFR compared to isolated galaxies (∼ 0.74 times).

In comparison to the star forming galaxies, the non-star forming galaxies selected by the central aperture in both samples present a rather similar distribution towards small $EW_{central}$ values (see bottom lef panel of Fig. 5.2). We remark here that these subsamples include objects located in the AGN zone in the BPT diagram or those with EW(H$\alpha$) smaller than 6Å. Although it is beyond the scope of this study, the similarity between these distributions calls the attention to further studies in order to understand the real impact of the interaction in triggering the nuclear activity of galaxies. We find however, a clear difference between the distributions of $EW_{extended}$ for the same sample of galaxies (see bottom right panel of Fig. 5.2). The median $EW_{extended}$ of the interacting sample is four times smaller than the control one ([0.20 ± 0.08] log(Å) and [0.82 ± 0.05] log(Å), respectively).

The control star forming galaxies selected using the extended aperture almost doubles the interacting ones (see top left panel of Fig. 5.3). The median $\log(EW_{central})$ for the interacting subsample is almost three times larger than the median of the control sample ([1.41 ± 0.1]log(Å) and [0.99 ± 0.03] log(Å), respectively). For the same subsample of star forming galaxies, $EW_{extended}$ is very similar for the interacting and control sample ([1.11 ± 0.02] log(Å), see top right panel in Fig. 5.3). A KS-test reveals that these two samples could be drawn from the same parent sample ($p_{KS}$ = 0.3). This suggests that the net enhancement of the SFR occurs mainly in the central region of the interacting galaxies rather than in the outer regions.

In the extended aperture, the selection of non-star forming galaxies yields almost three times more interacting objects than control ones. The distribution as well as the median of $EW_{central}$ is similar for both samples ([0.18 ± 0.07] log(Å), see bottom left panel in Fig. 5.3). On the other hand, $EW_{extended}$ present significant differences between the interacting and control samples (see bottom right panel in Fig. 5.3). Median $EW_{extended}$ for interacting sample is three times smaller than the control one ([0.17 ± 0.06] log(Å) and [0.64 ± 0.03] log(Å), respectively). In fact, a KS-test indicates that these two distributions are not likely to be drawn from the same parent sample ($p_{KS} = 0.001$).

Our analysis shows that regardless the criteria we use to select star forming galaxies the interacting sample has a consistent moderate enhancement in the central sSFR when compare with isolated star forming objects. At extended scales both samples present similar distributions of $EW_{extended}$ and, depending on the aperture used to classify the star-forming galaxies, similar or moderately suppressed total sSFR. Most of these interacting objects are late-type galaxies in pairs or merging systems. These results suggest that moderate enhancement (∼ 2-3 times larger) in the specific star formation rate occurs only in the central region of interacting galaxies. This scenario is consistent with gas been funneled to the central region of galaxies due to the interaction: large amounts of gas (subsequently enhanced sSFR) is found in the central region of interacting galaxies, whereas integrated sSFR remains similar or moderately suppressed. Our spatially-resolved study agrees with the numerical simulations presented by Moreno et al. (2015). They found that increment of star formation in merging galaxies are observed within the central kpc, while in outer galacto-centric radii the activity is moderately suppressed. Our results also agree with studies of supernovae radial distributions (e.g., Habergham et al. 2012; Herrero-Illana et al. 2012) that found type Ibc

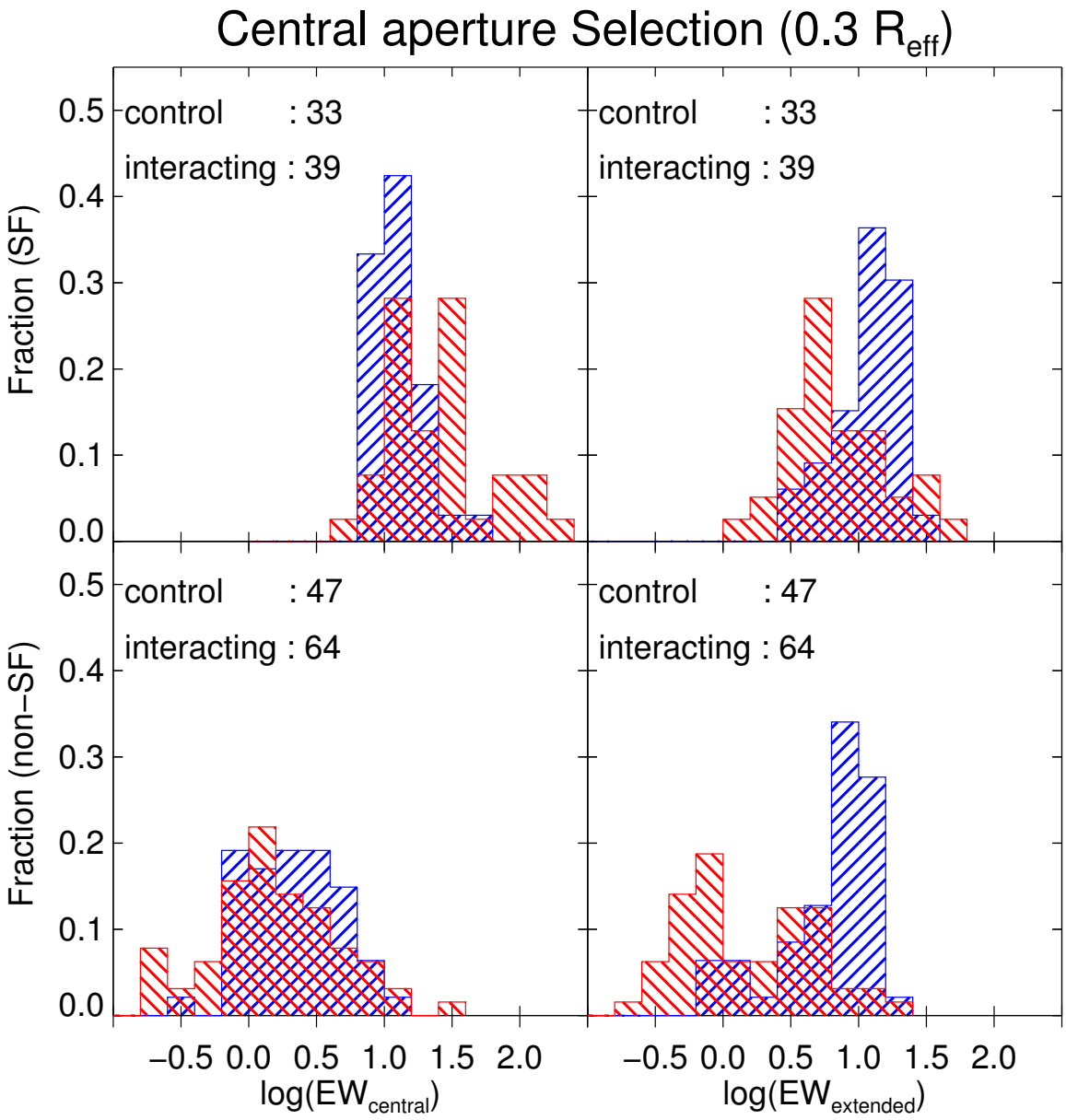


Figure 5.4: Distributions of integrated EW(H$\alpha$) for the interacting (red) and control (blue) galaxies. The distribution of the panels is similar to Fig. 5.2. For these histograms we use an aperture size of 0.3 $R_{eff}$.

supernovae, those more correlated to the on-going star-formation (Galbany et al. 2014), are more centrally concentrated in disturbed/interacting galaxies.

In galaxies considered as non-star forming the central EW(H$\alpha$) distribution is similar between interacting and isolated objects whereas the extended EW(H$\alpha$) is systematically smaller for the interacting sample. This points out that the process responsible for the observed central EW(H$\alpha$) in non-star forming galaxies for both samples could be similar. From the BPT diagrams (see Fig. 5.1), this process could involve only AGN activity. On the other hand, small values of the extended EW(H$\alpha$) for interacting galaxies could imply either a low budget of gas available to be ionized or

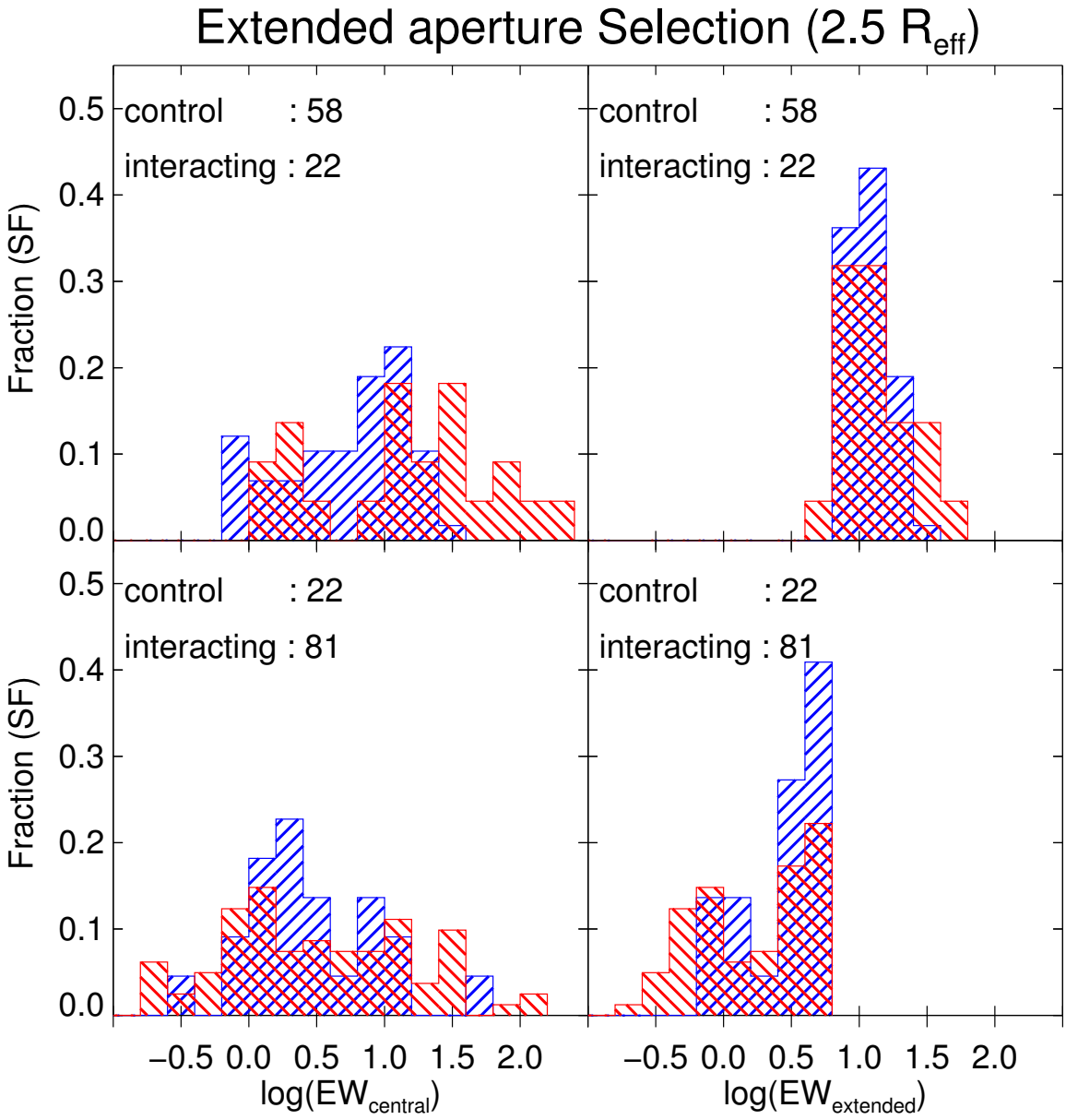


Figure 5.5: Distributions of integrated EW(H$\alpha$) for the interacting (red) and control (blue) galaxies using an aperture size of 2.5 $R_{eff}$. The distribution of the panels is similar to Fig. 5.4.

a weak radiation field across the merging galaxies. Since these galaxies are the complement of the star forming subsample, they cover a wide range of interaction stages and morphological types. A further division of the non-star forming galaxies EW(H$\alpha$) in the above properties lead a few objects in each bin, making difficult to derive reliable results. We will require a large sample of merging galaxies in particular in the post-merger and remnant stages to derive statistical meaningful conclusions regards the mechanisms responsible for the observed trends in the central and extended EW(H$\alpha$) in non-star forming merging galaxies.

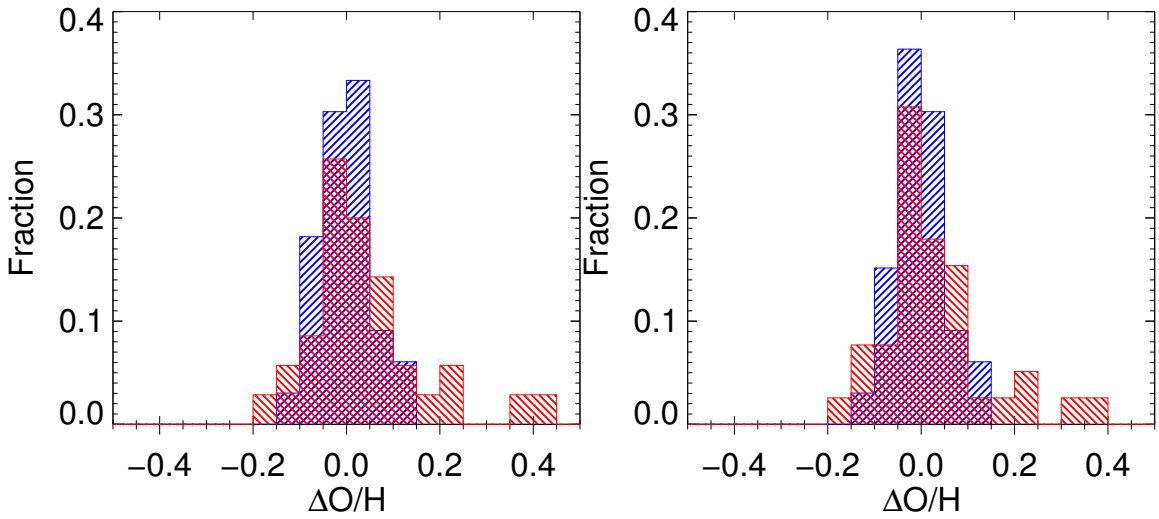


Figure 5.6: *Left:* Distributions of ΔO/H in the central (5 arcsec) aperture for the interacting (red) and the control (blue) star forming galaxies, see text for details. *Right:* Distributions of ΔO/H using a central aperture of 0.3 $R_{eff}$.

## 5.4 Central Oxygen Abundances

Observational studies suggest that the enhancement in the star formation activity in the central region of interacting galaxies is connected with a dilution of the oxygen abundance (e.g., Kewley et al. 2006; Ellison et al. 2008b; Sánchez Almeida et al. 2014a,b) which in turns contributes to the scatter of the M-Z relation. This decrement is associated with the supply of metal-poor gas to the central region via inflows. To test this scenario, we study the scatter between the observed metallicity and the M-Z relation for a given stellar mass in star forming galaxies. We derive from the emission line fluxes the oxygen abundance of each galaxy classified in Sec. 5.3 as star forming in the central aperture for both the interacting and control samples. Then, we provide the difference (or scatter) between the abundance determined from the flux ratios and the one expected from the M-Z relation (ΔO/H) derived by Sánchez et al. (2013). For the objects included in the CALIFA survey we use the stellar masses presented by Walcher et al. (2014). For the companions not included in the survey, stellar masses were derived in a similar fashion as for the CALIFA galaxies. As explained in (Sánchez et al. 2013), this empirical M-Z relation is derived for metallicities at one effective radius. Nevertheless, we can transform this abundance at different radii, in particular to the central aperture radius, by means of the metallicity gradient in disk galaxies (Sánchez et al. 2014).

In Fig. 5.6 we plot the distributions of ΔO/H for both, interacting and control samples in the central aperture (5 arcsec and 0.3 $R_{eff}$, left and right histograms, respectively). The distribution for the control sample in the 5 arcsec aperture is well centered around zero, with a median value of $(0.001 \pm 0.006)$ dex and a rather narrow distribution ($\sigma\Delta O/H_{control} = 0.056 \pm 0.006$ dex). On the other hand, the median of the distribution from the interacting sample is slightly larger than the one from the control sample ($0.03 \pm 0.01$ dex). However, the interacting sample owns a wider range of values in comparison with the control sample ($\sigma\Delta O/H_{merger} = 0.10 \pm 0.01$ dex). A KS-test indicates that these two samples are likely to be drawn from the same parent sample distribution ($p_{KS} = 0.32$). We find a similar distribution for the 0.3 $R_{eff}$ aperture with median values of $(-0.001 \pm 0.006)$ dex and $(0.021 \pm 0.02)$ dex for the control and interacting samples, respectively. The interacting sample is slightly metal rich than the control sample ($0.02 \pm 0.02$ dex). This indicates that in central regions, star forming merging galaxies have similar oxygen abundance than control sample. Despite

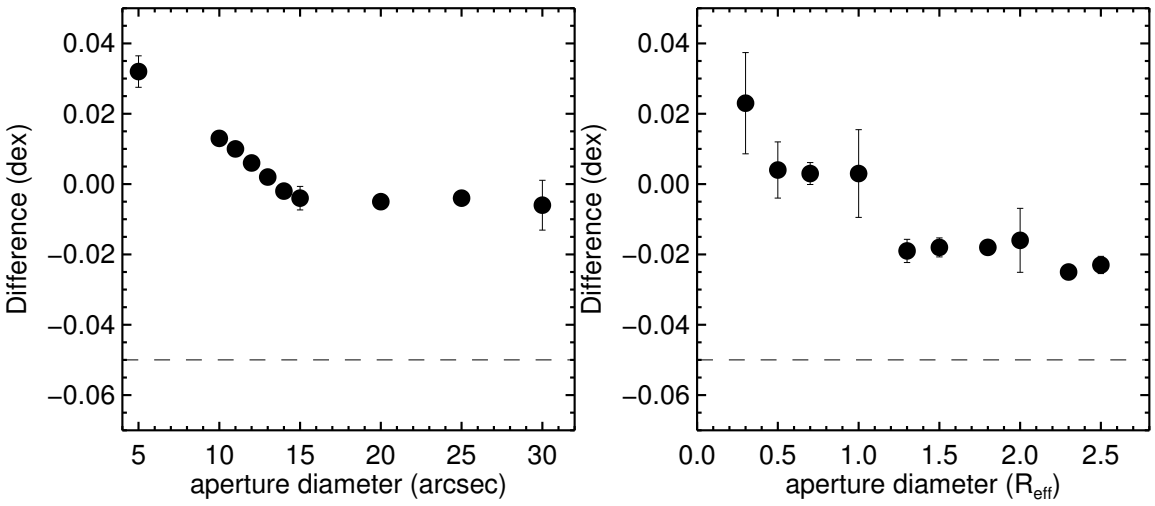


Figure 5.7: Differences in the median values of $\Delta$O/H between the interacting and control sample at different aperture sizes. *Left:* The aperture sizes are measured in arcsecs. *Right:* Aperture scales are measured in effective radius. Dashed line represent the difference reported by Ellison et al. (2008b). Errors bars are determined using bootstrapping in both samples. Note that in any of the scales the differences reach the values found in single-fiber spectrocopic studies.

that both apertures provide similar results, the most reliable one comes from the 0.3 $R_{eff}$ aperture size since it covers a similar physical region in all the galaxies in both samples. This first IFS census suggest that even though there is an enhancement of the sSFR in the central region of interacting galaxies the oxygen abundance remains similar to the one found in isolated galaxies. In other words, the scatter observed in the M-Z relation does not seem to be linked with the star formation rate of the galaxies presented in this study.

Our results differs from the single-fiber spectroscopic studies carry out within the SDSS galaxy-pair sample (Ellison et al. 2008b). They found a lower oxygen abundance of $\sim$ 0.05 - 0.1 dex between their galaxy-pair samples and control sample. One evident reason for the disparity between these two studies could be attributed to the number of objects in each sample. SDSS pairs and control samples included 1716 galaxies in binary systems and 40095 galaxies, respectively, whereas our samples of star forming galaxies include 33 and 35 objects in both interacting and control samples, respectively. Despite this difference in the size of the samples, we are able to account for the enhancement in the central SFR of interacting galaxies (see Figs. 5.2 and 5.4), in agreement with the SDSS studies, but not for the dilution in central metallicities. We note that our reported small variations in the metallicity in the central aperture may be bias by aperture effects or even the calibration used to derived the metallicity. In the following two sections we explore the possible bias in our results for these two factors.

## 5.5 Metallicity as function of the aperture size

Our IFS data allows to explore the effect of measuring the gas metallicity at different aperture sizes and scales. In particular, we can study whether the lower abundances presented in single-fiber studies for the star forming interacting galaxies (e.g., Ellison et al. 2008b) could be caused by aperture effects. More important, we will have an estimation on how the metallicity changes at different galactic scales. In Fig. 5.7 we plot the differences in the median metallicity value for the interacting and control star forming galaxies at different aperture sizes. We plot these differences

for two aperture scales, in arcsecs and in effective radius. The sample of galaxies selected for these plots are those classified as star forming galaxies in the central aperture of each scale.

For the aperture scale in arcsecs, we observe that the difference in metallicities between the two samples decreases as the aperture size increases, reaching a plateau at $\sim$ 15 arcsec. After this size the differences in metallicity are rather constant for different aperture sizes ($\sim$ -0.01 dex). On the other hand, using as aperture scale the effective radius of each galaxy, the difference in metallicity for the two samples decrease as the size of the aperture increases. For the largest aperture (2.5 $R_{eff}$), the interacting galaxies shows a lower metallicity of $\sim$ 0.02 dex respect to control galaxies. Although, there is a decrement in the metallicity of merging galaxies for large apertures, we do not observe the difference presented by previous spectroscopic studies (e.g., Kewley et al. 2006; Ellison et al. 2008b). Even more in the physical motivated aperture ($R_{eff}$), we find rather similar metallicities in the central regions with hints of a dilution of metallicities of the interacting galaxies at larger scales. This suggest that despite the inflows of ionized gas induce by the interaction, the metallicity in the central regions of interacting galaxies present similar properties as those for isolated galaxies. At large scales, there seems to be a dilution in the metallicity of interacting objects.

### 5.5.1 Metallicity as function of the abundance calibrator

In general, the variations in metallicity between the control and interacting galaxies are not larger in any case than 0.1 dex. This regime of small variations can be biased by several factor. In this section we explore and quantify the impact of these differences by the abundance calibrator. In Fig. 5.8 we plot the differences as function of aperture sizes in arcsec as in Sec. 5.5. As we note in Sec. 2.4, to derive these differences we use the improved empirical calibration for the O3N2 indicator given by Marino et al. (2013). We over plot these differences using a different calibration provided by Pettini & Pagel (2004). As we note above, using the improved calibrator, the differences between the interacting and control sample are very small, flattening out at $\sim$ 15 arcsecs to $\sim$ -0.01 dex. However, when we use the calibrator from Pettini & Pagel (2004), we find that in larger apertures the interacting galaxies have lower metallicities than control galaxies. Even more at $\sim$ 20 arcsec the differences in metallicity reach the value found by Ellison et al. (2008b).

To explain this apparent difference between our results and those using another calibrator, we note that our sample is in a closer vicinity than the sample presented by Ellison et al. (2008b). At the median redshift of the SDSS-pair sample ($z \sim 0.06$, see their Fig.2) an aperture of 3 arcsec is equivalent to central regions of $\sim$ 3.5 kpc. On the other hand, an aperture of 5 arcsec used to define the central region in this study covers a central portion of $\sim$ 1 kpc at the median redshift of our sample ($z \sim 0.01$). As consequence, the SDSS-pair single-fiber observations cover a wider region than the area covered by our central aperture. In fact, at the 20 arcsec aperture where the differences in metallicity (using the calibrator from Pettini & Pagel (2004)) are similar as those found by Ellison et al. (2008b) this aperture is covering a region of $\sim$ 3.5 kpc at the median redshift of our sample. Although we did not used the same indicators for metallicity as for the single-fiber spectroscopic survey studies, we suggest that using abundance calibrators presented in the literature it is possible to obtain the same lower metallicity in interacting galaxies. Finally we want to highlight that regardless the indicator used to derive the oxygen abundance, the metallicity in the central regions for interacting galaxies is similar as the one derived for the control sample.

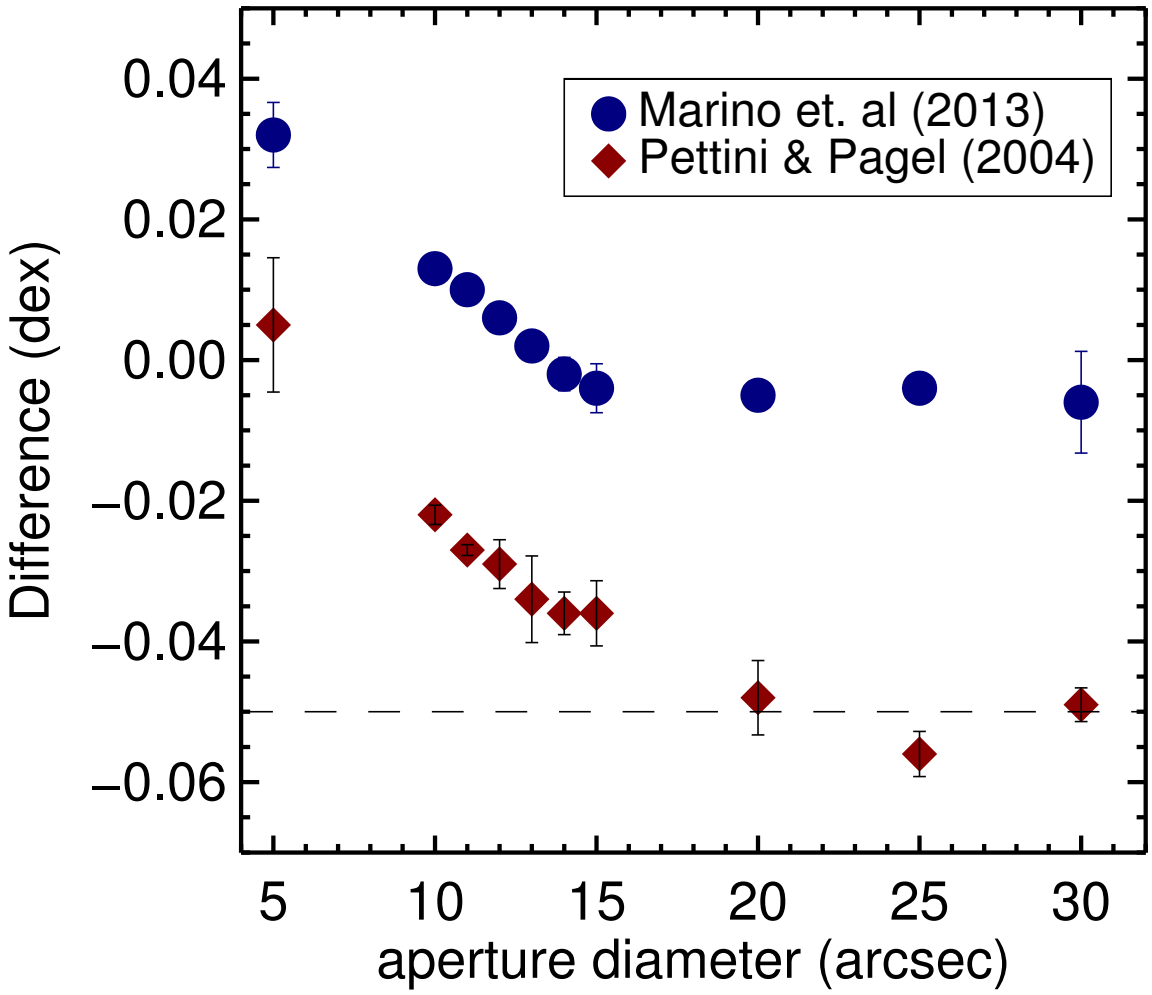


Figure 5.8: Similar as Fig. 5.7. Differences in the median values of $\Delta$O/H between the interacting and control sample at different aperture sizes. In this case we compare, using apertures in arcsec units, the differences in metallicity using different calibrators. Blue circles represent the differences obtained from the O3N2 revisited calibrator used in this study given in Marino et al. (2013). Red diamonds show the difference obtained from the calibrator presented by Pettini & Pagel (2004). Dashed line represent the difference reported by Ellison et al. (2008b).

## 5.6 Conclusions

We use the spatially-resolved information provided by the CALIFA survey to carry out the first statistical study of the impact of the merger event on the SFR and the oxygen abundance at different galactic scales for a sample over 100 galaxies at different stages of interaction. Moreover, this survey allows us to determine homogeneously the same properties in a control sample of 80 non-interacting galaxies. We separated the galaxies in both samples between star and non star forming galaxies (see Secs. 5.2 and 5.3). For the first subsample, we find a (moderate) enhancement in the SFR in the central region of interacting galaxies. However, in outer regions the SFR is similar or moderately suppressed in comparison to the control sample (see Sec. 5.3). This is in agreement with previous observational studies (e.g., Ellison et al. 2008b; Yuan et al. 2012) as well as numerical simulations (e.g., Hopkins et al. 2013; Moreno et al. 2015). These studies indicate that tidal induced star formation becomes evident in the central region of the galaxies as a consequence of gas inflows. In

this scenario, the new supply of low abundance gas to the central region produces a dilute metallicity. Contrary to this picture, we find similar metallicities in the central region of star forming interacting galaxies to those found in isolated galaxies (see Sec. 5.4). When we consider larger apertures (in effective radius units) we find hints of dilute metallicities in the interacting galaxies (see Sec. 5.5). Our results support the notion of a tight interplay between different physical processes in the central part of interacting galaxies. Although metal-poor gas inflows can be considered as the main process that affects the chemical evolution towards the center of interacting galaxies, there are some other processes to be taken into account that could enrich the ionized gas such as stellar (or AGN) feedback or returned material into the ISM. The results presented here encourage IFS studies in larger samples of interacting galaxies in order to understand the evolution of the galactic chemical content and to quantify how different merging configurations can affect the merger-induced metallicity dilution.

Chapter 6

# Future Work and Perspectives

*In this chapter we present preliminary results and analysis of future work and a brief introduction to the next generation of large IFU surveys in the nearby Universe: the MaNGA survey. The large sample offered by this survey will allow us to pursue further the physical phenomena in merging galaxies. In particular, the study of the ionized kinematics will help us to determined the role of interactions in triggering the activity observed in mergers, and specifically if and when the AGN's are switched on by interactions.*

## 6.1 Future CALIFA-related studies

In the different sections of this thesis we have noted that there are several studies that can be carried out as extensions of the topics presented here. In the following list we present some of these studies:

- To explore the dynamical support of the interacting galaxies at different merger stages. This has to be carried out with better spectral resolution than the one presented in this study (e.g., V1200 setup) in order to have a robust determination of the velocity dispersion. This data will also allows us to study radial change if any of the lambda parameter. This will give us hints regards the rotational or pressure dynamical support of the interacting galaxies.In turn, this will be very helpful to constrain the numerical simulations of merger galaxies.

- To compare our observed velocity fields from a set of numerical simulations with different merging parameters in order to constrain the most plausible orbital configurations and initial parameters of the progenitors.

- To compare the star formation and metallicity of merging galaxies with those derived for in non-interacting galaxies, we integrated those properties in different apertures sizes. However, we note a vast number of structures in the equivalent width as well as in the emission line flux maps. Recent numerical studies suggest that structures in the maps of star formation could give important clues about the formation scenario of a merger remnant (Moreno et al. 2015). More over, the flux ratio maps con provide important clues on the presence of inflows or outflows triggered by the interaction.

## 6.2 MaNGA: a natural step forward

Despite the numerous studies aimed at establish a connection between interactions/mergers and the trigger of the nuclear activity, there is still a large debate whether the interactions play a primary role in switching the AGN activity. To shade a light on this issue, and to obtain an answer for a representative population of nearby galaxies, it is necessary *a)* to explore extensively the parameters of the interaction. This implies a large sample of interacting galaxies covering homogeneously the parameter space, *b)* to have enough resolving spectral power to distinguish kinematic features in the velocity and velocity dispersion spatial distributions and *c)* to obtain a large wavelength coverage to measure several emission lines from the ionized gas. The integral field unit (IFU) survey *MaNGA* (Mapping the Nearby Galaxies at APO) provides these outstanding features.

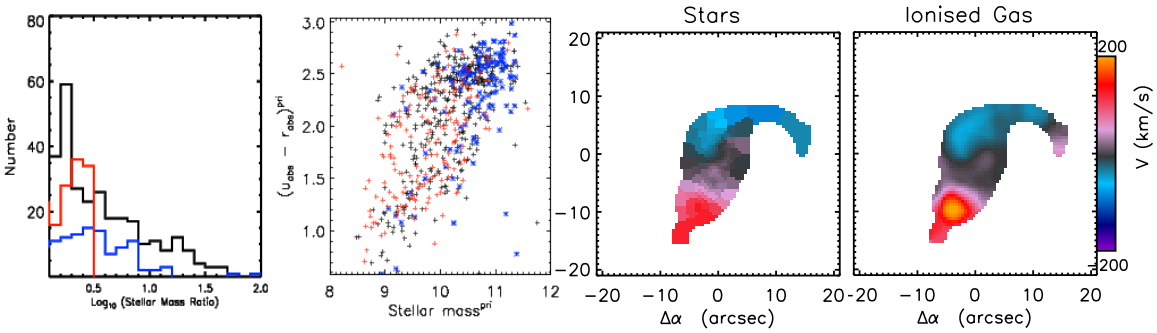


Figure 6.1: Statistical/spatial resolving power of the MaNGA survey. *Left panels:* range of parameters covered by interacting MaNGA systems (stellar mass ratio and stellar mass vs color of the primary companion) with both companions included in the MaNGA survey (black lines and points), ancillary candidates with one companion (blue lines and point) and both companions (red lines and points) in one bundle (taken from the ancillary MaNGA-mergers project, Lin and collaborators). *Right panels:* stellar and ionized gas velocity fields extracted from VV 705 MaNGA data cube using specific designed pipeline (Barrera-Ballesteros et al., 2014).

From the 10000 galaxies included in the MaNGA sample, 2978 objects are in pairs with at least one companion included in the MaNGA sample (projected separation $r_p < 50$ Kpc/h and separation in systemic velocity dV $< 500$ km/s, Yuan et al., Lin et al., 2014). Among these, 377 have both companions targeted by MaNGA (see black lines and dots in left panels of Fig. 6.1). In fact, there are 117 objects awarded as part of an ancillary MaNGA program, see blue and red dot in left panels of Fig. 3; Yuan et al. and Lin et al., 2014). MaNGA will allow us to identify kinematic structures in the velocity fields (see right panels of Fig. 6.1). The large spectral range (∼360-1000 nm) covers spectral lines for a large variety of ions (e.g., H$\alpha$, H$\beta$, H$\gamma$, H$\delta$; oxygen, nitrogen and sulfur forbidden lines).

**Revealing feeding and feedback mechanisms:** From the kinematic maps extracted from the MaNGA data cubes, we will be able to identify dynamical imprints caused by feeding and/or feedback mechanisms. Wild et al. (2014) found in the interacting pair the Mice (NGC4676A/B) that NGC4676A shows dynamical signatures of an outflow (i.e., zero-velocity curve has a V-shape along the minor axis and enhanced velocity dispersion along this axis, see Fig. 1.7). Kinematics from different emission lines will aid to spot inflows and/or outflows. For instance, distortions in the central region of the [OIII]$\lambda$5007 velocity field along with enhancement in velocity dispersions will suggest the presence of an outflow caused by an AGN. As a first step we will identify and characterize these dynamical features produced either by inflows or ionized gas been expelling by outflows. Then, we will study how these dynamical signatures relate to properties of the interacting

systems such as interaction stage, stellar mass, mass ratio. This is a fundamental step towards understanding where and when the above physical processes are taking place as the interaction evolves.

The parameters that can be taken into account include intrinsic properties of the companions (stellar masses, morphology, colors) and properties of the system (e.g., interaction stage, mass ratio). However, to explore the parameters of the ionized gas in interacting galaxies while the MaNGA observations are taking place, we will focus our analysis on: galaxies at different interaction stages from separate pairs, merging to remnants, a wide stellar mass range for the massive companion (mass bin of 0.5 $\log(M_*/M_\odot)$) and different mass ratios (bins of 0.2). We consider that at least five systems are required in each bin of the parameter space to have statistically meaningful results. Since observations are still in progress, the data set will be available by the end of this Thesis.

**Hunting the ionization sources in interacting galaxies:** The wavelength range coverage by the MaNGA survey allows us to extract the emission from a large set of atomic species. Emission line ratios are powerful tools to distinguish possible ionization mechanisms (e.g., HII regions, old stars, shocks or AGNs). Thanks to the MaNGA data cubes, we will be able to build emission-line ratio maps. Identifying structures in emission-line ratios maps will to traces the sources of ionization at different galactic scales. For instance, in Amanda del Olmo master's thesis we built such maps for the merging system Arp 91 (see left panels of Fig. 6.2). We found clear structures, for example the low [OIII]$\lambda$ 5007/H$\beta$ circumnuclear ring in NGC 5953. These structures indicate different sources of ionization in different regions of the galaxies.

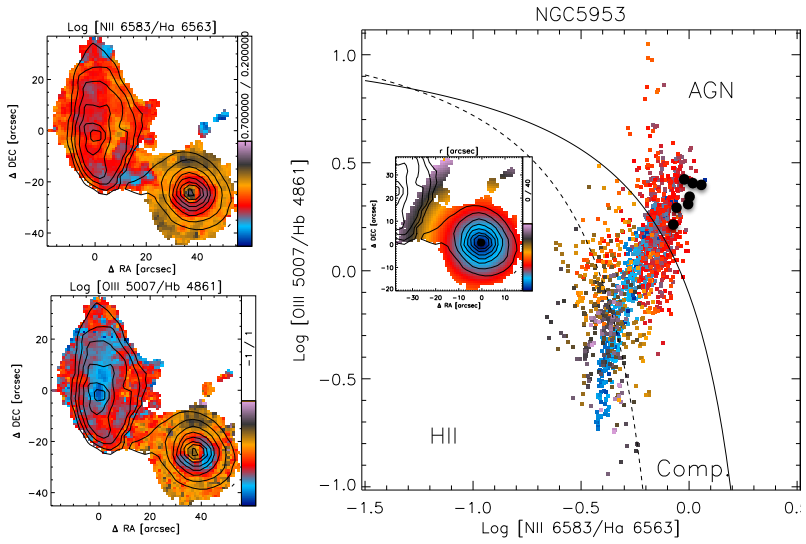


Figure 6.2: Tools to disentangle ionized sources across the merging galaxies *Left*: [NII]$\lambda$ 6583/H$\alpha$ and [OIII]$\lambda$ 5007/H$\beta$ emission-line ratio maps of Arp 91. *Right:* BPT diagnostic diagram for NGC 5953. Black dots represent nuclear spaxels. Inset shows in color code the distance from the center, used to plot the spaxels in the BPT diagram. While nuclear spectra is AGN-like, the surrounding regions present zones of star formation activity. This region coincides with the circumnuclear ring observed in left-hand emission line ratio maps. At larger galactocentric radii gas seem to be ionized by a different source most likely old stars.

These maps will provide insights in the physical properties of the ionized gas across the entire pair of interacting galaxies. Along with the kinematic maps, these two-dimensional distributions will trace the impact of the inflows or outflows in the ionized gas. Other important tools we will use

are diagnostic diagrams (e.g., BPT diagram). They will allow us to identify the ionization mechanisms at different galactocentric distances (see right panel of Fig. 6.2). We will be able to compare the ionization models in several diagnostic diagrams to differentiate the nature of ionization sources such as HII regions, shocks or AGNs (e.g., Allen et al. 2008, Luridiana et al. 2015) at different stages of interaction and mass ratios. Performing this statistical study will represent a major improvement in our understanding of the physical mechanisms that are trigger by inflows and outflows.

Numerical simulations suggest that onset (and timescales) of different physical phenomena such as starburst episodes, nuclear activity and quenching depend on the geometrical configuration and progenitor properties of a given interaction (e.g. Hopkins et al. 2008). Currently, the lack of the required observational information hampers our understanding of the specific evolutionary order of those phenomena as the merger unfolds.

The proposed study of spatially extended ionization conditions and dynamical properties in a statistically significant sample, covering a well defined sequence of interaction stages, will provide an observational framework to understand the role of mergers in triggering (or preventing) star-formation and AGN activity. This project will be essential to signal the timescales required for setting different phenomena cause by interaction: angular momentum loss, central starburst, AGN activity and eventual quenching. In summary, the ultimate goal of this project is to reveal the time sequence of these events as the merger evolves by studying the described data products.

Chapter 7

# Conclusions

In this work we present state-of-the-art spatially resolved observations provided by the CALIFA survey which allow us to study the properties of interacting and merging galaxies across their full optical extension and contrast them with a homogeneous control sample of non-interacting galaxies. In these Section we highlight the main conclusion that we have derived during this thesis.

**Stellar and ionized gas kinematics of non-interacting galaxies**

- From a sample of 80 non-interacting galaxies (used as control sample), we find that for 90% of the sample, the global orientation of the stellar and ionized gas kinematics is fairly well aligned (misalignment smaller than $\sim 20°$) with respect to the global photometric orientation of the galaxy, including barred and unbarred objects.

- We studied the internal kinematic PA misalignments namely, the difference between the receding and approaching kinematic PA. We found intrinsic aligned velocity fields in both components for a large fraction of the control sample (intrinsic misalignments smaller than $15°$ degrees for the stellar and the ionized gas components).

- We also compared the derived kinematic PA for the stellar and the ionized gas components. We observe a tight alignment ($16°$ degrees of difference) between both components for the majority of this non-interacting sample. This result holds in barred galaxies when the comparison is carried out either at the radius of the bar or further out. From these results we suggest that the global kinematics in non-interacting galaxies in both the stellar and the ionized gas components (measured by the major kinematic position angle) seems to be dominated by the mass of the disk, rather than other morphological components that can induce non-circular patterns in the observed velocity fields, such as bars.

**Stellar and ionized gas kinematics of interacting galaxies at every merger stage**

- From the 103 galaxies included in the interacting sample we find that 43% (37/85) and 52% (43/82) of the interacting sample has stellar and ionized gas morpho-kinematic misalignments larger than any of those found in the control sample. In particular, we find a large fraction of these morpho-kinematic misalignments in galaxies included in binary systems with evident signatures of interaction. In addition, median internal kinematic misalignment for interacting galaxies is slightly larger than the one derived from the control galaxies at different stellar masses and interaction stages.

- Comparison between the stellar and the ionized gas kinematic PA (66 objects) reveals that 42% (28/66) of the interacting sample has misalignments larger than those presented by the control sample. In particular, the median misalignments of mergers and remnants are significantly larger than median provided by isolated galaxies. Distributions of the stellar kinematic PA deviations are similar in both samples. However, 48% (41/82) of the interacting galaxies have ionized gas kinematic PA deviations larger than control sample, in particular in the post-merger stage. This suggests that kinematic PA deviations in the ionized gas can be used as a tracer to determine whether a galaxy is or has been under an interaction or recent merger.

- Our study indicates that interactions have a significant impact on the motion of stars and ionized gas in galaxies. Even more, our results probe the wide range of kinematic stages observed in galaxies under different phases of merger. From velocity fields with similar properties to those found in isolated galaxies to very distorted velocity fields with large kinematic misalignments.

- The CALIFA survey allows us to characterize the spatially resolved properties of galaxies at different stages of interaction. In particular, this study provides a nearby Universe benchmark for kinematic comparisons with high redshift galaxies. Further studies with simulated high redshift observations using the current spatially resolved data will allow us to quantify the fraction of rotating disks and compare with the fraction observed at high redshift. Such simulations for the ionized gas in CALIFA galaxies have been already carried out (Mast et al. 2014).

- Our findings encourage the comparison of observational velocity fields with those obtained from numerical simulations. Exploring different configurations of the merging galaxies with different properties of the progenitors will give significant insight to reveal which are the relevant parameters that yield the variety of observed velocity fields in merging galaxies.

**Spatial extent of the specific star formation rate enhancement and metallicity in interacting and merging galaxies**

- The CALIFA data allow us carry out the first statistical study on the impact of the merger event on the SFR and the oxygen abundance at different galactic scales for a sample over our sample of galaxies at different stages of interaction and the control sample. We find a (moderate) enhancement in the SFR in the central region of interacting galaxies. However, in outer regions the SFR is similar or moderately suppressed in comparison to the control sample (see Sec. 5.3), in agreement with previous observational studies as well as numerical simulations.

- Those studies suggest that tidally induced star formation becomes evident in the central region of the galaxies as a consequence of gas inflows. In this scenario, the new supply of low abundance gas to the central region produces a dilute metallicity. Contrary to this picture, we find similar metallicities in the central region of star forming interacting galaxies to those derived for isolated galaxies (see Sec. 5.4). When we consider larger apertures (in effective radius units) we find hints of dilute metallicities in the interacting galaxies (see Sec. 5.5).

- Our results support the notion of a tight interplay between different physical processes in the central part of interacting galaxies. Although metal-poor gas inflows can be considered as the main process that affects the chemical evolution towards the center of interacting galaxies, there are some other processes to be taken into account that could enrich the ionized gas such as stellar (or AGN) feedback or returned material into the ISM.

- The results presented here encourage IFS studies in larger samples of interacting galaxies in order to understand the evolution of the galactic chemical content and to quantify how different merging configurations can affect the merger-induced metallicity dilution.

Chapter 8

# Conclusiones

En esta tesis presentamos lo ultimo en observaciones espectroscopicas espacialmente resueltas usando los datos del estudio CALIFA. Gracias a su amplia muestra de galaxias pudimos estudiar estadísticamente las propiedades de galaxias en interacción en distintos estados de la fusion. Ademas de esto, esta muestra de galaxias nos permitió comparar las propiedades de estas galaxias con una muestra de galaxias aisladas. En esta sección presentamos los resultados mas importantes de esta tesis:

**Cinematica estalar y del gas ionizado en galaxias aisladas**

- De la muestra de galaxias aisladas (usadas luego como muestra de control), encontramos que el 90% de la muestra presenta mapas de velocidad con ángulos cinemáticos de posición bastantes alineados en ambas componentes (estelar y del gas ionizado) respecto al ángulo de posición definido por la fotometría de las galaxias (con desalineamientos menores a $\sim 20°$).

- Al estudiar los alineamientos de los ángulos de posición cinemática de la regiones que se alejan y se acercan en los mapas de velocidad de cada uno de los componentes, encontramos que la mayoría de estas galaxias (90%) presentan ambos bien alineados (dealineamientos menores que 15 degrees).

- Al comparar los ángulos de posición cinemáticos de las estrellas y el gas ionizado, encontramos que una gran parte de estas galaxias presentan un buen alineamiento entre estas dos componentes (desalinemientos menores que 16 °). Este resultado es valido tanto para galaxias de disco como para galaxias barradas, así mismo para distintos radios donde hacemos las medidas; en el caso de las galaxias barradas, dentro y fuera de la barra. De estos resultados, sugerimos que la cinemática global de la componente estelar y del gas ionizado esta dominada principalmente por la masa del disco de la galaxia en distintos regiones de las galaxias, incluso en la presencia de una barra.

**Cinematica estalar y del gas ionizado en galaxias a lo largo de la interacción**

- De nuestra muestra de 103 galaxias en interacción, encontramos que el 43% (37/85) en su componente estelar y 52% (43/82) en su componente del gas ionizado, presentan desalineamientos del ángulo de posición cinemático respecto al ángulo fotométrico mayores que los observados para la muestra de galaxias aisladas. En particular, encontramos que la mayoría de estos objetos que presentan este desalineamiento son galaxias que se encuentran en pares de galaxias claramente en interacción. Este desalineamiento es sistemáticamente mayor en la muestra de galaxias en interacción que para la muestra de control a distintas masas estelares.

- En aquellas galaxias donde era posible la comparación entre el ángulo de posición cinemáticos de la componente estelar y el gas ionizado (66 objetos), encontramos que 42% (28/66) de la muestra de galaxias en interacción tiene desalineamientos mayores que aquellos que encontramos en la muestra de galaxias aisladas. En particular, encontramos que estos dealineamientos son mas evidentes en galaxias en evidente estado de interacción y en remanentes de la fusion. Por otra parte, al estudiar las desviaciones radiales de la orientación del ángulo de posición cinemático de la componente estelar medidas mediante $\delta \mathrm{PA}_{\mathrm{kin}}$ encontramos que estas distribuciones son similares en ambas muestras. Sin embargo, este no es el caso para la componente del gas ionizado, donde el parámetro $\delta \mathrm{PA}_{\mathrm{kin}}$ en 48% (41/82) de la muestra de galaxias en interacción es mayor que los valores que encontramos en la muestra de galaxias aisladas. Particularmente, estos altos valores de $\delta \mathrm{PA}_{\mathrm{kin}}$ se observan en la muestra de galaxias fusionadas. En este trabajo sugerimos el uso de $\delta \mathrm{PA}_{\mathrm{kin}}$ como herramienta para determinar si una galaxia a sufrido o no un encuentro o fusion reciente.

- Este estudio muestra el impacto que tiene las interacciones en los movimientos internos de las galaxias. Mas aun, este estudio muestra el amplio rango de distribuciones de velocidades que se pueden encontrar en una muestra de galaxias en interaccion. Desde mapas de velocidades similares a aquellos que se observan en galaxias aisladas hasta mapas con fuertes distorsiones cinemáticas.

- La muestra de galaxias que provee CALIFA nos ha permitido estudiar la cinemáticas de galaxias en distintos estados de la fusion de galaxias. Así, este estudio se puede considerar como un punto de comparación para el estudio de las propiedades cinemáticas de resueltas de galaxias observadas en el universo temprano. Próximos estudios simulando la cinemáticas de galaxias a alto redshift usando nuestros datos, permitirán determinar la fracción de galaxias rotantes en el universo cercano para poder compararla con aquellos obtenidos en previos estudios de cinemática en galaxias con alto corrimiento al rojo.

- Finalmente, esperamos que nuestro trabajo motive otros estudios que ayuden a comprender mejor la evolución de las propiedades de las galaxias usando simulaciones numéricas. Estas simulaciones serian de gran ayuda para entender cuales parámetros de la interacción son los que mas impacto tienen en la evolucion de las componentes galácticas.

**Incremento de la taza de formación estelar especifica en la parte central de galaxias interactivas y su metalicidad**

- Los datos observados para la muestra de CALIFA nos permitió realizar el primer trabajo estadístico sobre el impacto de las interacciones en propiedades de las galaxias resueltas espacialmente como la taza de formación estelar especifica (sSFR, por sus siglas en ingles) y la abundancia de oxigeno. Nuestros resultados muestran un incremento (moderado) en la sSFR, específicamente en la parte central de las galaxias en interacción. Sin embargo, en las regiones exteriores los valores de la sSFR son similares a aquellos observados en galaxias aisladas (Sec. 5.3). Estas observaciones apoyan simulaciones numéricas llevas a cabo recientemente.

- Las simulaciones numéricas sugieren que la formación estelar inducida por las interacciones son consecuencia de flujos de material hacia el centro de dichas galaxias. En este escenario, el material proveniente de las regiones externas de las galaxias posee metalicidades mas bajas que las que se esperarían en el centro de una galaxias sin interacciones. Contrario a esta imagen, nuestros resultados sugieren metalicidades similares entre las galaxias en interacción y nuestra muestra de galaxias de control. Cuando analizamos la metalicidad en regiones mas amplias encontramos evidencias de metalicidades diluidas en galaxias en interacción, en comparación con las galaxias de control (Sec. 5.5). Nuestros resultados sugieren una fuerte correlación entre distintos procesos físicos en la parte central de las galaxias en interacción.

- Aunque los flujos de material metálicamente pobre hacia el centro de las galaxias intereactivas son considerados como el principal mecanismo que afecta la evolución de la metalicidad en estos objetos, nuestro trabajo demuestra que en las partes centrales de estas galaxias es necesario considerar otros procesos físicos tales como el enriquecimiento del medio interestelar por procesos como retroalimentación de material de las estrellas o del núcleo de la galaxia.
- Nuestro trabajo motiva a continuar con estudios de las propiedades de las galaxias en interacción de una manera resuelta usando una muestra mucho mas larga que permita determinar cuales son los parámetros mas importantes que afectan la formación estelar y la metalicidad así como la evolución de dichas propiedades a medida que las galaxias se fusionan.

# References


Abazajian, K. N., Adelman-McCarthy, J. K., Agüeros, M. A., et al. 2009, ApJS, 182, 543

Aguerri, J. A. L., Méndez-Abreu, J., & Corsini, E. M. 2009, A&A, 495, 491

Alonso, M. S., Tissera, P. B., Coldwell, G., & Lambas, D. G. 2004, MNRAS, 352, 1081

Alonso-Herrero, A., Rosales-Ortega, F. F., Sánchez, S. F., et al. 2012, MNRAS, 425, L46

Arp, H. 1966, ApJS, 14, 1

Arp, H. 1967, AJ, 72, 289

Arp, H. 1969, A&A, 3, 418

Arribas, S., Colina, L., Monreal-Ibero, A., et al. 2008, åp, 479, 687

Arribas, S., Mediavilla, E., García-Lorenzo, B., & del Burgo, C. 1997, ApJ, 490, 227

Athanassoula, E. 1984, Phys. Rep., 114, 319

Athanassoula, E. 2003, MNRAS, 341, 1179

Atkinson, A. M., Abraham, R. G., & Ferguson, A. M. N. 2013, ApJ, 765, 28

Baldwin, J. A., Phillips, M. M., & Terlevich, R. 1981, PASP, 93, 5

Barazza, F. D., Jogee, S., & Marinova, I. 2008, ApJ, 675, 1194

Barnes, E. I. & Sellwood, J. A. 2003, AJ, 125, 1164

Barnes, J. E. 2011, MNRAS, 413, 2860

Barnes, J. E. & Hernquist, L. 1996, ApJ, 471, 115

Barnes, J. E. & Hibbard, J. E. 2009, AJ, 137, 3071

Barrera-Ballesteros, J. K., Falcón-Barroso, J., García-Lorenzo, B., et al. 2014, A&A, 568, A70

Barrera-Ballesteros, J. K., Sánchez, S. F., García-Lorenzo, B., et al. 2015, ArXiv e-prints

Barton, E. J., Geller, M. J., & Kenyon, S. J. 2000, ApJ, 530, 660

Beckman, J. E., Zurita, A., & Vega Beltrán, J. C. 2004, Lecture Notes and Essays in Astrophysics, 1, 43

Begeman, K. G. 1987, PhD thesis, , Kapteyn Institute, (1987)

Bellocchi, E., Arribas, S., & Colina, L. 2012, A&A, 542, A54

Bellocchi, E., Arribas, S., Colina, L., & Miralles-Caballero, D. 2013, A&A, 557, A59

Bertin, G., Liseikina, T., & Pegoraro. 2003, A&A, 405, 73

Bílek, M., Jungwiert, B., Jílková, L., et al. 2013, A&A, 559, A110

Binney, J. & Merrifield, M. 1998, Galactic Astronomy

Binney, J. & Tremaine, S. 2008, Galactic Dynamics: Second Edition (Princeton University Press)

Bluck, A. F. L., Conselice, C. J., Buitrago, F., et al. 2012, ApJ, 747, 34

Bois, M., Emsellem, E., Bournaud, F., et al. 2012, ArXiv e-prints

Borne, K. D., Bushouse, H., Colina, L., et al. 1999, Ap&SS, 266, 137

Brooks, A. M., Governato, F., Booth, C. M., et al. 2007, ApJ, 655, L17

Bushouse, H. A. 1987, ApJ, 320, 49

Calura, F., Pipino, A., Chiappini, C., Matteucci, F., & Maiolino, R. 2009, A&A, 504, 373

Calzetti, D., Kinney, A. L., & Storchi-Bergmann, T. 1994, ApJ, 429, 582

Cappellari, M. & Copin, Y. 2003, MNRAS, 342, 345

Cappellari, M. & Emsellem, E. 2004, PASP, 116, 138

Cappellari, M., Emsellem, E., Krajnović, D., et al. 2011, MNRAS, 413, 813

Carlberg, R. G., Pritchet, C. J., & Infante, L. 1994, ApJ, 435, 540

Casteels, K. R. V., Conselice, C. J., Bamford, S. P., et al. 2014, MNRAS, 445, 1157

Colina, L., Arribas, S., & Monreal-Ibero, A. 2005, ApJ, 621, 725

Conselice, C. J., Bershady, M. A., Dickinson, M., & Papovich, C. 2003, AJ, 126, 1183

Conselice, C. J., Rajgor, S., & Myers, R. 2008, MNRAS, 386, 909

Contini, T., Garilli, B., Le Fèvre, O., et al. 2012, A&A, 539, A91

Cox, T. J., Dutta, S. N., Di Matteo, T., et al. 2006a, ApJ, 650, 791

Cox, T. J., Jonsson, P., Primack, J. R., & Somerville, R. S. 2006b, MNRAS, 373, 1013

Croom, S. M., Lawrence, J. S., Bland-Hawthorn, J., et al. 2012, MNRAS, 421, 872

Darg, D. W., Kaviraj, S., Lintott, C. J., et al. 2010, MNRAS, 401, 1043

Dasyra, K. M., Tacconi, L. J., Davies, R. I., et al. 2006, ApJ, 651, 835

Davis, T. A., Alatalo, K., Sarzi, M., et al. 2011, MNRAS, 417, 882

Debattista, V. P. & Sellwood, J. A. 1998, ApJ, 493, L5

Debattista, V. P. & Sellwood, J. A. 2000, ApJ, 543, 704

Di Matteo, P., Bournaud, F., Martig, M., et al. 2008, A&A, 492, 31

Di Matteo, P., Combes, F., Melchior, A.-L., & Semelin, B. 2007, A&A, 468, 61

Duc, P.-A., Cuillandre, J.-C., Karabal, E., et al. 2015, MNRAS, 446, 120

Duc, P.-A. & Renaud, F. 2013, in Lecture Notes in Physics, Berlin Springer Verlag, Vol. 861, Lecture Notes in Physics, Berlin Springer Verlag, ed. J. Souchay, S. Mathis, & T. Tokieda, 327

Duncan, J. C. 1923, ApJ, 57, 137

Ebrova, I. 2013, ArXiv e-prints

Eggen, O. J., Lynden-Bell, D., & Sandage, A. R. 1962, ApJ, 136, 748

Ellison, S. L., Mendel, J. T., Patton, D. R., & Scudder, J. M. 2013a, MNRAS, 435, 3627

Ellison, S. L., Mendel, J. T., Scudder, J. M., Patton, D. R., & Palmer, M. J. D. 2013b, MNRAS, 430, 3128

Ellison, S. L., Patton, D. R., Simard, L., & McConnachie, A. W. 2008a, ApJ, 672, L107

Ellison, S. L., Patton, D. R., Simard, L., & McConnachie, A. W. 2008b, AJ, 135, 1877

Emsellem, E., Cappellari, M., Peletier, R. F., et al. 2004, MNRAS, 352, 721

Emsellem, E., Fathi, K., Wozniak, H., et al. 2006, MNRAS, 365, 367

Engel, H., Davies, R. I., Genzel, R., et al. 2010, A&A, 524, A56

Epinat, B., Amram, P., Marcelin, M., et al. 2008, MNRAS, 388, 500

Epinat, B., Tasca, L., Amram, P., et al. 2012, A&A, 539, A92

Erb, D. 2006, in Bulletin of the American Astronomical Society, Vol. 38, American Astronomical Society Meeting Abstracts, 925

Eskridge, P. B., Frogel, J. A., Pogge, R. W., et al. 2000, AJ, 119, 536

Espada, D., Verdes-Montenegro, L., Huchtmeier, W. K., et al. 2011, A&A, 532, A117

Evans, A. S., Vavilkin, T., Pizagno, J., et al. 2008, ApJ, 675, L69

Falcón-Barroso, J., Bacon, R., Bureau, M., et al. 2006, MNRAS, 369, 529

Falcón-Barroso, J., Bacon, R., Bureau, M., et al. 2007, in Science Perspectives for 3D Spectroscopy, ed. M. Kissler-Patig, J. R. Walsh, & M. M. Roth, 111

Fathi, K., Beckman, J. E., Piñol-Ferrer, N., et al. 2009, ApJ, 704, 1657

Fathi, K., van de Ven, G., Peletier, R. F., et al. 2005, MNRAS, 364, 773

Fernández Lorenzo, M., Sulentic, J., Verdes-Montenegro, L., et al. 2012, A&A, 540, A47

Finlator, K. & Davé, R. 2008, MNRAS, 385, 2181

Flores, H., Hammer, F., Puech, M., Amram, P., & Balkowski, C. 2006, A&A, 455, 107

Förster Schreiber, N. M., Genzel, R., Bouché, N., et al. 2009, ApJ, 706, 1364

Galbany, L., Stanishev, V., Mourão, A. M., et al. 2014, A&A, 572, A38

García-Barreto, J. A. & Rosado, M. 2001, AJ, 121, 2540

García-Benito, R., Zibetti, S., Sánchez, S. F., et al. 2014, ArXiv e-prints

García-Lorenzo, B. 2013, MNRAS, 534

García-Lorenzo, B., Márquez, I., Barrera-Ballesteros, J. K., et al. 2015, A&A, 573, A59

Georgakakis, A., Forbes, D. A., & Norris, R. P. 2000, MNRAS, 318, 124

Glazebrook, K. 2013, ArXiv e-prints

Gnerucci, A., Marconi, A., Cresci, G., et al. 2011, A&A, 528, A88

Haan, S., Armus, L., Laine, S., et al. 2011, ApJS, 197, 27

Habergham, S. M., James, P. A., & Anderson, J. P. 2012, MNRAS, 424, 2841

Hernandez, O., Carignan, C., Amram, P., Chemin, L., & Daigle, O. 2005, MNRAS, 360, 1201

Hernandez, O., Fathi, K., Carignan, C., et al. 2008, PASP, 120, 665

Herrero-Illana, R., Pérez-Torres, M. Á., & Alberdi, A. 2012, A&A, 540, L5

Hibbard, J. E. & van Gorkom, J. H. 1996, AJ, 111, 655

Hopkins, P. F., Cox, T. J., Hernquist, L., et al. 2013, MNRAS, 430, 1901

Hopkins, P. F., Cox, T. J., Kereš, D., & Hernquist, L. 2008, ApJS, 175, 390

Hopkins, P. F., Cox, T. J., Younger, J. D., & Hernquist, L. 2009a, ApJ, 691, 1168

Hopkins, P. F., Hernquist, L., Cox, T. J., et al. 2006, ApJS, 163, 1

Hopkins, P. F., Somerville, R. S., Cox, T. J., et al. 2009b, MNRAS, 397, 802

Hubble, E. P. 1936, Realm of the Nebulae

Husemann, B., Jahnke, K., Sánchez, S. F., et al. 2013, A&A, 549, A87

Ibata, R., Irwin, M., Lewis, G., Ferguson, A. M. N., & Tanvir, N. 2001, Nature, 412, 49

Jesseit, R., Cappellari, M., Naab, T., Emsellem, E., & Burkert, A. 2009, MNRAS, 397, 1202

Jesseit, R., Naab, T., Peletier, R. F., & Burkert, A. 2007, MNRAS, 376, 997

Ji, I., Peirani, S., & Yi, S. K. 2014, ArXiv e-prints

Józsa, G. I. G., Kenn, F., Klein, U., & Oosterloo, T. A. 2007, A&A, 468, 731

Karl, S. J., Naab, T., Johansson, P. H., et al. 2010, ApJ, 715, L88

Keenan, P. C. 1935, ApJ, 81, 355

Kennicutt, R. C., Roettiger, K. A., Keel, W. C., van der Hulst, J. M., & Hummel, E. 1987a, in NASA Conference Publication, Vol. 2466, NASA Conference Publication, ed. C. J. Lonsdale Persson, 401–408

Kennicutt, Jr., R. C. 1983, ApJ, 272, 54

Kennicutt, Jr., R. C. 1992, ApJ, 388, 310

Kennicutt, Jr., R. C. & Kent, S. M. 1983, AJ, 88, 1094

Kennicutt, Jr., R. C., Roettiger, K. A., Keel, W. C., van der Hulst, J. M., & Hummel, E. 1987b, AJ, 93, 1011

Kennicutt, Jr., R. C., Schweizer, F., & Barnes, J. E. 1996, Galaxies: Interactions and Induced Star Formation

Kennicutt, Jr., R. C., Tamblyn, P., & Congdon, C. E. 1994, ApJ, 435, 22

Kewley, L. J., Dopita, M. A., Sutherland, R. S., Heisler, C. A., & Trevena, J. 2001, ApJ, 556, 121

Kewley, L. J., Geller, M. J., & Barton, E. J. 2006, AJ, 131, 2004

Knapen, J. H. & James, P. A. 2009, ApJ, 698, 1437

Knapen, J. H., Shlosman, I., & Peletier, R. F. 2000, ApJ, 529, 93

Kobayashi, C., Springel, V., & White, S. D. M. 2007, MNRAS, 376, 1465

Köppen, J., Weidner, C., & Kroupa, P. 2007, MNRAS, 375, 673

Krajnović, D., Cappellari, M., de Zeeuw, P. T., & Copin, Y. 2006, MNRAS, 366, 787

Krajnović, D., Emsellem, E., Cappellari, M., et al. 2011, MNRAS, 414, 2923

Kronberger, T., Kapferer, W., Schindler, S., & Ziegler, B. L. 2007, A&A, 473, 761

Kronberger, T., Kapferer, W., Unterguggenberger, S., Schindler, S., & Ziegler, B. L. 2008, A&A, 483, 783

Kutdemir, E., Ziegler, B. L., Peletier, R. F., et al. 2008, A&A, 488, 117

Lagos, C. d. P., Padilla, N. D., Davis, T. A., et al. 2015, MNRAS, 448, 1271

Laine, S., van der Marel, R. P., Rossa, J., et al. 2003, AJ, 126, 2717

Lambas, D. G., Tissera, P. B., Alonso, M. S., & Coldwell, G. 2003, MNRAS, 346, 1189

Larson, R. B. & Tinsley, B. M. 1978, ApJ, 219, 46

Law, D. R., Steidel, C. C., Erb, D. K., et al. 2009, ApJ, 697, 2057

Lee, H., Skillman, E. D., Cannon, J. M., et al. 2006, ApJ, 647, 970

Lequeux, J., Peimbert, M., Rayo, J. F., Serrano, A., & Torres-Peimbert, S. 1979, A&A, 80, 155

López-Sánchez, Á. R. & Esteban, C. 2010, A&A, 517, A85

Lotz, J. M., Jonsson, P., Cox, T. J., & Primack, J. R. 2008, MNRAS, 391, 1137

Maiolino, R., Nagao, T., Grazian, A., et al. 2008, A&A, 488, 463

Mannucci, F., Cresci, G., Maiolino, R., Marconi, A., & Gnerucci, A. 2010, MNRAS, 408, 2115

Marino, R. A., Rosales-Ortega, F. F., Sánchez, S. F., et al. 2013, A&A, 559, A114

Marinova, I., Jogee, S., Bacon, D., et al. 2007, in Bulletin of the American Astronomical Society, Vol. 39, American Astronomical Society Meeting Abstracts, 905

Martinez-Valpuesta, I., Shlosman, I., & Heller, C. 2006, ApJ, 637, 214

Mast, D., Rosales-Ortega, F. F., Sánchez, S. F., et al. 2014, A&A, 561, A129

Medling, A. M., U, V., Guedes, J., et al. 2014, ApJ, 784, 70

Menéndez-Delmestre, K., Sheth, K., Schinnerer, E., Jarrett, T. H., & Scoville, N. Z. 2007, ApJ, 657, 790

Mezcua, M., Lobanov, A. P., Mediavilla, E., & Karouzos, M. 2014, ApJ, 784, 16

Mihos, J. C. & Hernquist, L. 1996, ApJ, 464, 641

Moreno, J., Bluck, A. F. L., Ellison, S. L., et al. 2013, MNRAS

Moreno, J., Torrey, P., Ellison, S. L., et al. 2015, MNRAS, 448, 1107

Moustakas, J., Coil, A. L., Aird, J., et al. 2013, ApJ, 767, 50

Naab, T. & Burkert, A. 2003, ApJ, 597, 893

Naab, T., Jesseit, R., & Burkert, A. 2006, MNRAS, 372, 839

Namboodiri, P. M. S. & Kochhar, R. K. 1985, Bulletin of the Astronomical Society of India, 13, 363

Nicholson, R. A., Bland-Hawthorn, J., & Taylor, K. 1992, ApJ, 387, 503

Nikolic, B., Cullen, H., & Alexander, P. 2004, MNRAS, 355, 874

Oke, J. B. 1990, AJ, 99, 1621

Osterbrock, D. E. 1989, Astrophysics of gaseous nebulae and active galactic nuclei

Patton, D. R., Grant, J. K., Simard, L., et al. 2005, AJ, 130, 2043

Patton, D. R., Pritchet, C. J., Yee, H. K. C., Ellingson, E., & Carlberg, R. G. 1997, ApJ, 475, 29

Patton, D. R., Torrey, P., Ellison, S. L., Mendel, J. T., & Scudder, J. M. 2013, MNRAS, 433, L59

Pease, F. G. 1918, Proceedings of the National Academy of Science, 4, 21

Peterson, C. J. & Huntley, J. M. 1980, ApJ, 242, 913

Pettini, M. & Pagel, B. E. J. 2004, MNRAS, 348, L59

Pfleiderer, J. & Siedentopf, H. 1961, ZAp, 51, 201

Piqueras López, J., Colina, L., Arribas, S., Alonso-Herrero, A., & Bedregal, A. G. 2012, A&A, 546, A64

Porter, L. A., Somerville, R. S., Croton, D. J., et al. 2012, ArXiv e-prints

Privon, G. C., Barnes, J. E., Evans, A. S., Hibbard, J. E., & Mazzarella, J. M. 2013, in American Astronomical Society Meeting Abstracts, Vol. 221, American Astronomical Society Meeting Abstracts, 405

Robotham, A. S. G., Driver, S. P., Davies, L. J. M., et al. 2014, MNRAS, 444, 3986

Rogstad, D. H., Lockhart, I. A., & Wright, M. C. H. 1974, ApJ, 193, 309

Rosales-Ortega, F. F., Sánchez, S. F., Iglesias-Páramo, J., et al. 2012, ApJ, 756, L31

Roth, M. M., Kelz, A., Fechner, T., et al. 2005, PASP, 117, 620

Rozas, M., Relaño, M., Zurita, A., & Beckman, J. E. 2002, A&A, 386, 42

Rupke, D. S. N., Veilleux, S., & Baker, A. J. 2008, ApJ, 674, 172

Salzer, J. J., Lee, J. C., Melbourne, J., et al. 2005, ApJ, 624, 661

Sánchez, S. F., Kennicutt, R. C., Gil de Paz, A., et al. 2012a, A&A, 538, A8

Sánchez, S. F., Rosales-Ortega, F. F., Iglesias-Páramo, J., et al. 2014, A&A, 563, A49

Sánchez, S. F., Rosales-Ortega, F. F., Jungwiert, B., et al. 2013, A&A, 554, A58

Sánchez, S. F., Rosales-Ortega, F. F., Marino, R. A., et al. 2012b, A&A, 546, A2

Sánchez Almeida, J., Elmegreen, B. G., Muñoz-Tuñón, C., & Elmegreen, D. M. 2014a, A&A Rev., 22, 71

Sánchez Almeida, J., Morales-Luis, A. B., Muñoz-Tuñón, C., et al. 2014b, ApJ, 783, 45

Sanders, D. B. & Mirabel, I. F. 1996, ARA&A, 34, 749

Savaglio, S., Glazebrook, K., Le Borgne, D., et al. 2005, ApJ, 635, 260

Scannapieco, C. & Athanassoula, E. 2012, MNRAS, 425, L10

Scannapieco, C., Gadotti, D. A., Jonsson, P., & White, S. D. M. 2010, MNRAS, 407, L41

Schoenmakers, R. H. M., Franx, M., & de Zeeuw, P. T. 1997, MNRAS, 292, 349

Scudder, J. M., Ellison, S. L., Torrey, P., Patton, D. R., & Mendel, J. T. 2012, MNRAS, 426, 549

Sellwood, J. A. 2006, ApJ, 637, 567

Sellwood, J. A. 2013, Dynamics of Disks and Warps, ed. T. D. Oswalt & G. Gilmore, 923

Sellwood, J. A. & Debattista, V. P. 2006, ApJ, 639, 868

Shapiro, K. L., Genzel, R., Förster Schreiber, N. M., et al. 2008, ApJ, 682, 231

Skillman, E. D. 1989, ApJ, 347, 883

Skillman, E. D. 1992, in Elements and the Cosmos, ed. M. G. Edmunds & R. Terlevich, 246

Sofue, Y. & Rubin, V. 2001, ARA&A, 39, 137

Spekkens, K. & Sellwood, J. A. 2007, ApJ, 664, 204

Springel, V. 2005, MNRAS, 364, 1105

Surace, J. A. 1998, PhD thesis, Institute for Astronomy University of Hawaii 2680 Woodlawn Dr. Honolulu, HI 96822

Thielheim, K. O. & Wolff, H. 1982, MNRAS, 199, 151

Toomre, A. 1977, in Evolution of Galaxies and Stellar Populations, ed. B. M. Tinsley & R. B. G. Larson, D. Campbell, 401

Toomre, A. & Toomre, J. 1972, ApJ, 178, 623

Torrey, P., Cox, T. J., Kewley, L., & Hernquist, L. 2012, ApJ, 746, 108

Tremonti, C. A., Heckman, T. M., Kauffmann, G., et al. 2004, ApJ, 613, 898

Valdes, F., Gupta, R., Rose, J. A., Singh, H. P., & Bell, D. J. 2004, ApJS, 152, 251

Vale Asari, N., Stasińska, G., Cid Fernandes, R., et al. 2009, MNRAS, 396, L71

Varela, J., Moles, M., Márquez, I., et al. 2004, A&A, 420, 873

Veilleux, S., Kim, D.-C., & Sanders, D. B. 2002, ApJS, 143, 315

Verdes-Montenegro, L., Sulentic, J., Lisenfeld, U., et al. 2005, A&A, 436, 443

Verley, S., Leon, S., Verdes-Montenegro, L., et al. 2007, A&A, 472, 121

Villa-Vargas, J., Shlosman, I., & Heller, C. 2009, ApJ, 707, 218

Vorontsov-Velyaminov, B. A. 1959, in Atlas and catalog of interacting galaxies (1959), 0

Vorontsov-Vel'Yaminov, B. A. & Arkhipova, V. P. 1962, in Morphological catalogue of galaxies., 1 (1962), 0

Walcher, C. J., Wisotzki, L., Bekeraité, S., et al. 2014, A&A, 569, A1

Weinberg, M. D. 1985, MNRAS, 213, 451

Westmoquette, M. S., Clements, D. L., Bendo, G. J., & Khan, S. A. 2012, MNRAS, 424, 416

Wild, P. 1953, PASP, 65, 202

Wild, V., Rosales-Ortega, F., Falcón-Barroso, J., et al. 2014, A&A, 567, A132

Wolf, M. 1914, Astronomische Nachrichten, 199, 319

Yuan, F.-T., Takeuchi, T. T., Matsuoka, Y., et al. 2012, A&A, 548, A117

Yuan, T.-T., Kewley, L. J., & Sanders, D. B. 2010, ApJ, 709, 884

Zaritsky, D., Kennicutt, Jr., R. C., & Huchra, J. P. 1994, ApJ, 420, 87

Zwicky, F. 1956, Ergebnisse der exakten Naturwissenschaften, 29, 344

Zwicky, F. 1962, PASP, 74, 70

Appendix A

# Kinematic Properties of the interacting and control samples

## A.1 Kinematic alignments versus apparent ellipticity in non-interacting galaxies

All the kinematic parameters presented in this study are determined on the plane of the sky. Therefore, it is expected that any intrinsic kinematic property would be affected by the inclination of the galaxy with respect to the plane of the sky. In this appendix we show the same kinematic misalignments presented in section 3.2 with respect to the apparent ellipticity as proxy of the apparent inclination of the galaxies.

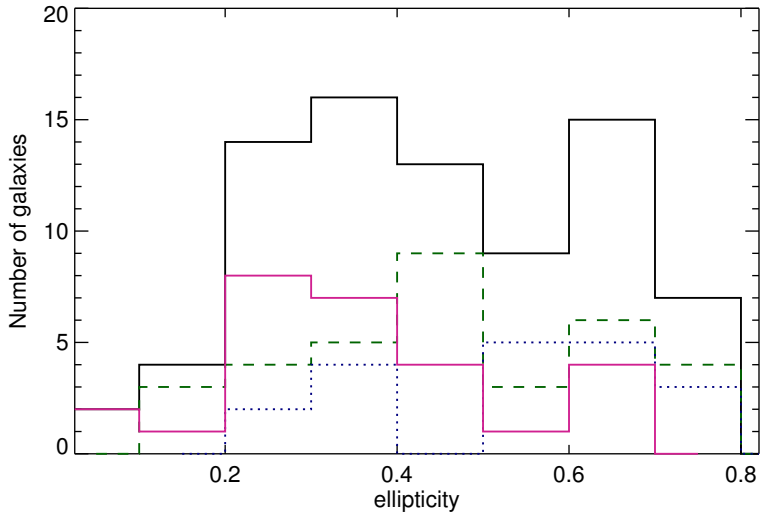


Figure A.1: Distribution of the ellipticity as proxy of the inclination for the galaxies used in this study. Dashed lines represent the unbarred galaxies, dotted-lines correspond to the weakly barred galaxies and solid lines shows the distribution of strong barred galaxies.

In Figure A.1 we plot the distribution of the non-interacting galaxies with respect to the ellip-

ticity. We have a fair coverage of galaxies at different inclinations, in particular for the low-inclined ones ($\epsilon < 0.5$). To have consistent results, we also try to have the same fraction of barred vs unbarred galaxies in different ellipticity bins.

In Figure A.2 we plot the morpho-kinematic misalignments explained in section 3.2.2 against the ellipticity for both components, as well as the internal kinematic misalignment in each component ( Fig. A.3) and the comparison of the kinematic PA between the stars and the gas (Fig. A.4). We find large morpho-kinematic misalignments in galaxies with low ellipticities ($\epsilon < 0.3$, see Fig. A.2).

For the kinematic parameters independent of the morphology (i.e., Figs. A.3 and A.4), we find rather similar values in different ellipticity bins. In each panel of these figures, we plot an estimation of the projections effects as function of the ellipticity assuming a face-on misalignment of 60° (see Fig. A.2) in any of the (morpho-) kinematic indicators. This value was chosen to approximately match the misalignments found at large ellipticities. Within uncertainties, all the galaxies display internal kinematic misalignments that are smaller than the ones expected for their inclinations. In other words, for these misalignments, we do not find large scatters at low ellipticities, as expected for a quantity heavily affected by projection effects.

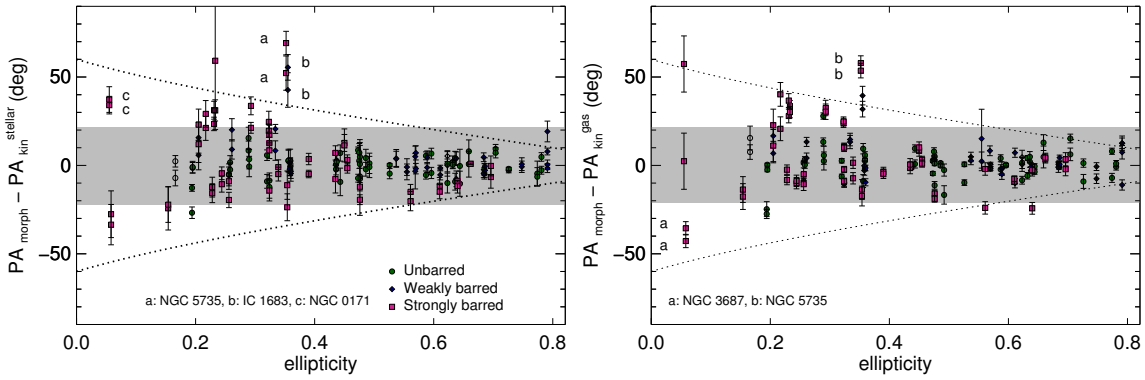


Figure A.2: Difference between the morphological PA ($PA_{morph}$) and the kinematic PA ($PA_{kin}$) against the ellipticity of the outermost isophote of the galaxy for the stars (left panel) and the ionised gas (right panel). Both kinematic sides of the velocity maps were compared with $PA_{morph}$. In each panel, the green filled circles represent the unbarred galaxies, blue diamonds are weakly barred galaxies, and violet squares correspond to barred galaxies. For early-type galaxies we use empty circles. Labels indicate the 3-$\sigma$ outliers. Dashed lines represent the projection effect of a morpho-kinematic misalignment of 60° measured in the plane of the galaxy. In each panel, the grey area represents the 2$\sigma$ dispersion of the sample.

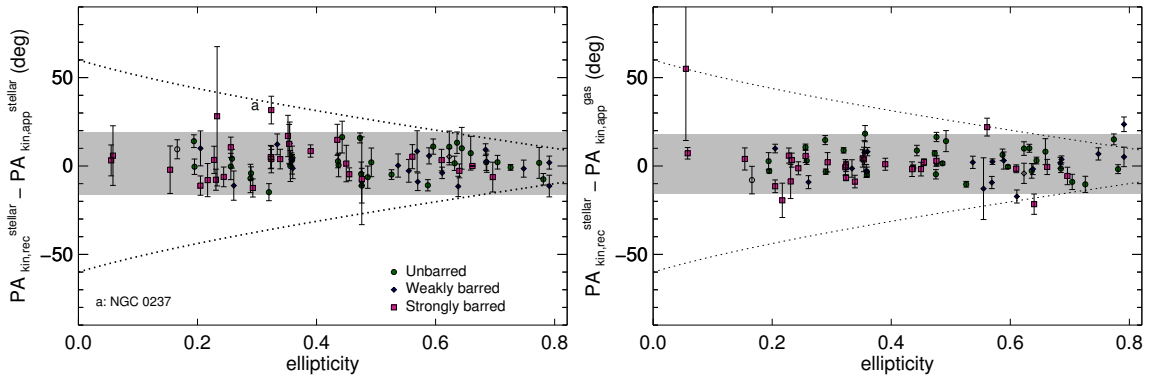


Figure A.3: Internal kinematic misalignment between the receding PA ($PA_{kin,rec}$) and approaching ($PA_{kin,app}$) kinematic position angle against the ellipticity. In each panel the green filled circles represent the unbarred galaxies, blue diamonds correspond to weakly barred galaxies, and violet squares represent the barred galaxies. Empty circles represent the early type galaxies. Labels indicate the 3-$\sigma$ outlier. Dashed lines represent the projection effect of a morpho-kinematic misalignment of 60° measured in the plane of the galaxy. In each panel, the grey area represents the 2$\sigma$ dispersion of the sample.

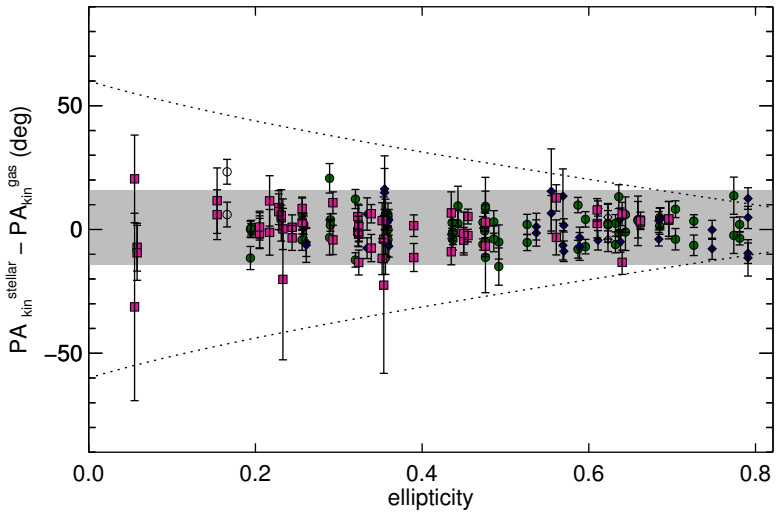


Figure A.4: Stellar and ionized gas difference respects the ellipticity. The green filled circles represent the unbarred galaxies, blue diamonds correspond to weakly barred galaxies, and violet squares represent the barred galaxies. Empty circles represent the early-type galaxies. Dashed lines represent the projection effect of a morpho-kinematic misalignment of 60° measured in the plane of the galaxy. In each panel, the grey area represents the 2$\sigma$ dispersion of the sample.

## A.2 Tables

Table A.1: Morphological parameters of the sample of non-interacting CALIFA galaxies used in this study.

| CALIFA id | Name | Morphological type | Bar strength | $\epsilon$ | $PA^{out}_{morph}$ ($^{o}$) | $PA_{bar}$ ($^{o}$) | $r_{bar}$ (arcsec) | Stellar mass log($M/M_{\odot}$) |
|---|---|---|---|---|---|---|---|---|
| (1) | (2) | (3) | (4) | (5) | (6) | (7) | (8) | (9) |
| 1 | $IC5376$ | Sb | A | 0.69 | 50 | ... | ... | 10.57 |
| 2 | $UGC00005$ | Sbc | A | 0.53 | 50 | ... | ... | 10.72 |
| 7 | $UGC00036$ | Sab | AB | 0.61 | 50 | ... | ... | 10.88 |
| 8 | $NGC0001$ | Sbc | A | 0.32 | 50 | ... | ... | 10.71 |
| 10 | $NGC0036$ | Sb | B | 0.48 | 50 | 128 | 12 | 10.79 |
| 23 | $NGC0171$ | Sb | B | 0.05 | 50 | 122 | 33 | 10.62 |
| 25 | $NGC0180$ | Sb | B | 0.34 | 50 | 147 | 22 | 10.78 |
| 28 | $NGC0214$ | Sbc | AB | 0.26 | 50 | 59 | 14 | 10.74 |
| 30 | $NGC0237$ | Sc | B | 0.32 | 50 | 40 | 7 | 10.17 |
| 31 | $NGC0234$ | Sc | AB | 0.20 | 50 | ... | ... | 10.55 |
| 33 | $NGC0257$ | Sc | A | 0.36 | 50 | ... | ... | 10.69 |
| 41 | $UGC00841$ | Sbc | A | 0.77 | 50 | ... | ... | 9.71 |
| 43 | $IC1683$ | Sb | AB | 0.35 | 50 | 168 | 8 | 10.43 |
| 53 | $UGC01057$ | Sc | AB | 0.69 | 50 | ... | ... | 10.11 |
| 108 | $NGC1093$ | Sbc | B | 0.39 | 50 | 117 | 10 | 10.66 |
| 116 | $UGC02405$ | Sbc | A | 0.66 | 50 | ... | ... | 10.40 |
| 131 | $NGC1542$ | Sab | AB | 0.59 | 50 | ... | ... | 10.30 |
| 147 | $NGC2253$ | Sbc | B | 0.32 | 50 | ... | ... | 10.37 |
| 149 | $NGC2347$ | Sbc | AB | 0.36 | 50 | ... | ... | 10.62 |
| 151 | $NGC2410$ | Sb | AB | 0.68 | 50 | ... | ... | 10.78 |
| 152 | $UGC03944$ | Sbc | AB | 0.57 | 50 | 94 | 5 | 9.87 |
| 153 | $UGC03969$ | Sb | A | 0.78 | 50 | ... | ... | 10.61 |
| 273 | $IC2487$ | Sc | AB | 0.79 | 50 | ... | ... | 10.29 |
| 275 | $NGC2906$ | Sbc | A | 0.44 | 50 | ... | ... | 10.29 |
| 277 | $NGC2916$ | Sbc | A | 0.36 | 50 | ... | ... | 10.65 |
| 307 | $UGC05359$ | Sb | B | 0.70 | 50 | ... | ... | 10.54 |
| 364 | $UGC06036$ | Sa | A | 0.73 | 50 | ... | ... | 11.09 |
| 386 | $UGC06312$ | Sab | A | 0.64 | 50 | ... | ... | 10.93 |
| 414 | $NGC3687$ | Sb | B | 0.06 | 50 | 174 | 14 | 10.17 |
| 436 | $NGC3811$ | Sbc | B | 0.23 | 50 | 22 | 24 | 10.34 |
| 489 | $NGC4047$ | Sbc | A | 0.26 | 50 | ... | ... | 10.58 |
| 515 | $NGC4185$ | Sbc | AB | 0.33 | 50 | 167 | 20 | 10.61 |
| 518 | $NGC4210$ | Sb | B | 0.24 | 50 | 47 | 17 | 10.17 |
| 580 | $NGC4711$ | Sbc | A | 0.47 | 50 | ... | ... | 10.20 |
| 602 | $NGC4956$ | E1 | A | 0.17 | 50 | ... | ... | 10.99 |
| 610 | $UGC08267$ | Sb | AB | 0.75 | 50 | ... | ... | 10.68 |
| 624 | $NGC5157$ | Sab | B | 0.23 | 50 | 138 | 21 | 11.15 |
| 630 | $NGC5205$ | Sbc | B | 0.35 | 50 | 108 | 12 | 9.77 |
| 664 | $UGC08778$ | Sb | A | 0.70 | 50 | ... | ... | 10.15 |
| 684 | $NGC5406$ | Sb | B | 0.29 | 50 | 56 | 20 | 11.09 |
| 714 | $UGC09067$ | Sbc | AB | 0.54 | 50 | 27 | 5 | 10.36 |
| 715 | $NGC5520$ | Sbc | A | 0.49 | 50 | ... | ... | 9.75 |
| 743 | $NGC5622$ | Sbc | A | 0.48 | 50 | ... | ... | 10.11 |
| 748 | $NGC5633$ | Sbc | A | 0.26 | 50 | ... | ... | 10.16 |
| 753 | $NGC5656$ | Sb | A | 0.19 | 50 | ... | ... | 10.51 |
| 764 | $NGC5720$ | Sbc | B | 0.44 | 50 | 60 | 7 | 10.74 |
| 768 | $NGC5732$ | Sbc | A | 0.48 | 50 | ... | ... | 9.83 |
| 771 | $NGC5735$ | Sbc | B | 0.35 | 50 | 94 | 20 | 10.28 |
| 777 | $NGC5772$ | Sab | A | 0.44 | 50 | ... | ... | 10.84 |
| 779 | $UGC09598$ | Sbc | AB | 0.64 | 50 | ... | ... | 10.45 |
| 782 | $UGC09629$ | E7 | AB | 0.62 | 50 | ... | ... | 11.02 |
| 790 | $UGC09777$ | Sbc | A | 0.49 | 50 | ... | ... | 10.21 |
| 791 | $NGC5908$ | Sa | A | 0.36 | 50 | ... | ... | 11.12 |
| 804 | $NGC5971$ | Sb | AB | 0.56 | 50 | ... | ... | 10.22 |
| 810 | $NGC5980$ | Sbc | A | 0.60 | 50 | ... | ... | 10.62 |
| 813 | $NGC6004$ | Sbc | B | 0.20 | 50 | 15 | 16 | 10.60 |
| 823 | $NGC6063$ | Sbc | A | 0.44 | 50 | ... | ... | 9.95 |
| 824 | $IC1199$ | Sb | AB | 0.57 | 50 | ... | ... | 10.20 |
| 826 | $NGC6081$ | S0a | A | 0.59 | 50 | ... | ... | 11.04 |
| 831 | $NGC6132$ | Sbc | A | 0.64 | 50 | ... | ... | 10.15 |
| 834 | $UGC10380$ | Sb | AB | 0.79 | 50 | ... | ... | 10.92 |
| 836 | $NGC6155$ | Sc | A | 0.29 | 50 | ... | ... | 10.01 |
| 842 | $NGC6186$ | Sb | B | 0.23 | 50 | 54 | 35 | 10.44 |
| 853 | $NGC6361$ | Sab | A | 0.29 | 50 | ... | ... | 10.81 |
| 854 | $UGC10811$ | Sb | B | 0.66 | 50 | ... | ... | 10.75 |
| 856 | $IC1256$ | Sb | AB | 0.36 | 50 | 130 | 7 | 10.20 |
| 857 | $NGC6394$ | Sbc | B | 0.64 | 50 | ... | ... | 10.79 |
| 862 | $NGC6478$ | Sc | A | 0.63 | 50 | ... | ... | 10.90 |
| 869 | $NGC6941$ | Sb | B | 0.26 | 50 | 108 | 16 | 10.82 |
| 872 | $UGC11649$ | Sab | B | 0.22 | 50 | 162 | 17 | 10.54 |
| 876 | $NGC7047$ | Sbc | B | 0.45 | 50 | 115 | 20 | 10.68 |
| 886 | $NGC7311$ | Sa | A | 0.47 | 50 | ... | ... | 10.84 |
| 887 | $NGC7321$ | Sbc | B | 0.32 | 50 | 62 | 10 | 10.69 |
| 889 | $NGC7364$ | Sab | A | 0.32 | 50 | ... | ... | 10.79 |
| 890 | $UGC12185$ | Sb | B | 0.56 | 50 | 139 | 22 | 10.58 |
| 896 | $NGC7466$ | Sbc | A | 0.62 | 50 | ... | ... | 10.70 |
| 904 | $NGC7591$ | Sbc | B | 0.46 | 50 | 1 | 11 | 10.64 |
| 924 | $NGC7716$ | Sb | A | 0.19 | 50 | ... | ... | 10.20 |
| 929 | $UGC12810$ | Sbc | B | 0.61 | 50 | ... | ... | 10.61 |
| 938 | $NGC5947$ | Sbc | B | 0.15 | 50 | 26 | 11 | 10.23 |

(1) CALIFA ID number. (2) name of the galaxy. (3) morphological type from visual clasification (see Walcher et. al 2014, submitted, for details). (4) bar strength of the galaxy from the same morphological visual clasification (see Walcher et. al 2014, submitted, for details). (5) and (6) ellipticity ($\epsilon$) and position angle ($PA^{out}_{morph}$) from an ellipse fitting at the largest scale isophote of the SDSS r-band image. Both measurements were inferred using the IRAF task *ellipse*. (7) and (8) position angle ($PA_{bar}$) and length of the bar ($r_{bar}$) derived from an ellipse fitting on the SDSS r-band image. (9) stellar masses (see Walcher et. al 2014, submitted, for details).

Table A.2: Stellar kinematic properties of the non-interacting sample selected for this study included in the CALIFA survey.

| id | $\Delta\alpha$ | $\Delta\delta$ | $V_{sys}$ | $r_{max}$ | $r_{min}$ | $PA_{morph}$ | PA approaching | | PA receding | |
|---|---|---|---|---|---|---|---|---|---|---|
| | | | | | | | $PA_{kin}$ | $\delta PA_{kin}$ | $PA_{kin}$ | $\delta PA_{kin}$ |
| | ($''$) | ($''$) | (km $s^{-1}$) | ($''$) | ($''$) | ($^\circ$) | ($^\circ$) | ($^\circ$) | ($^\circ$) | ($^\circ$) |
| (1) | (2) | (3) | (4) | (5) | (6) | (7) | (8) | (9) | (10) | (11) |
| 1 | 0.6 ± 0.6 | 1.7 ± 0.5 | 4963 ± 9 | 22 | – | 3.7 ± 0.4 | 6.0 ± 3.3 | 7.1 ± 2.2 | 8.2 ± 3.2 | 8.0 ± 1.8 |
| 2 | ... | ... | 7209 ± 1 | 22 | – | 45.2 ± 0.9 | 49.9 ± 2.7 | 10.5 ± 2.7 | 45.0 ± 0.2 | 15.2 ± 2.7 |
| 7 | ... | ... | 6238 ± 1 | 20 | – | 17.4 ± 0.2 | 22.7 ± 2.8 | 10.7 ± 2.3 | 18.8 ± 1.6 | 7.3 ± 1.8 |
| 8 | -0.6 ± 0.5 | -1.1 ± 0.6 | 4515 ± 9 | 20 | 7 | 106.0 ± 1.1 | 114.6 ± 4.2 | 15.0 ± 4.9 | 118.2 ± 6.2 | 20.1 ± 3.7 |
| 10 | ... | ... | 5939 ± 1 | 25 | 10 | 179.3 ± 0.6 | 19.4 ± 2.7 | 14.4 ± 2.1 | 12.0 ± 2.3 | 12.7 ± 2.4 |
| 23 | 0.4 ± 0.5 | -1.0 ± 0.6 | 3857 ± 1 | 20 | 10 | 126.0 ± 0.7 | 88.8 ± 7.2 | 29.2 ± 7.6 | 92.0 ± 4.9 | 37.9 ± 10.2 |
| 25 | 0.4 ± 0.5 | -0.7 ± 0.4 | 5204 ± 6 | 30 | 7 | 167.1 ± 1.0 | 168.1 ± 4.0 | 18.7 ± 3.0 | 172.0 ± 3.8 | 18.0 ± 3.4 |
| 28 | 0.2 ± 0.5 | 0.2 ± 0.7 | 4500 ± 12 | 12 | 5 | 60.4 ± 0.8 | 51.3 ± 5.4 | 12.7 ± 4.7 | 40.2 ± 6.3 | 18.0 ± 4.9 |
| 30 | ... | ... | 4142 ± 1 | 20 | 7 | 177.3 ± 0.8 | 17.0 ± 5.8 | 24.3 ± 5.8 | 165.3 ± 5.2 | 30.6 ± 7.4 |
| 31 | 1.9 ± 0.7 | -1.1 ± 0.8 | 4391 ± 6 | 30 | 5 | 82.2 ± 4.9 | 66.5 ± 7.3 | 37.6 ± 5.5 | 76.4 ± 6.7 | 30.3 ± 9.4 |
| 33 | -1.1 ± 0.7 | 1.2 ± 0.8 | 5183 ± 12 | 20 | 7 | 93.7 ± 1.5 | 91.0 ± 6.3 | 25.7 ± 5.6 | 94.4 ± 4.8 | 25.8 ± 7.6 |
| 41 | 1.3 ± 0.5 | -1.4 ± 0.6 | 5524 ± 9 | 15 | – | 53.9 ± 0.2 | 58.6 ± 7.1 | 37.8 ± 9.9 | 60.3 ± 5.1 | 25.4 ± 7.5 |
| 43 | ... | ... | 4839 ± 9 | 12 | 7 | 156.4 ± 1.0 | 19.0 ± 9.7 | 20.4 ± 8.1 | 31.8 ± 7.2 | 19.4 ± 6.4 |
| 53 | -0.8 ± 0.5 | 0.1 ± 0.6 | 6294 ± 12 | 20 | – | 152.2 ± 0.5 | 152.6 ± 4.7 | 22.1 ± 4.7 | 155.1 ± 3.8 | 12.4 ± 2.9 |
| 108 | ... | ... | 5224 ± 1 | 20 | 5 | 96.5 ± 1.2 | 92.9 ± 3.0 | 13.0 ± 5.0 | 101.4 ± 1.8 | 13.7 ± 4.2 |
| 116 | -0.8 ± 0.4 | 0.1 ± 0.8 | 7676 ± 21 | 10 | – | 172.4 ± 1.4 | 164.5 ± 6.3 | 20.8 ± 7.8 | 171.7 ± 7.2 | 16.7 ± 7.1 |
| 131 | 0.2 ± 0.5 | -1.8 ± 0.6 | 3689 ± 10 | 18 | – | 128.0 ± 0.4 | 123.4 ± 3.6 | 11.7 ± 2.6 | 129.2 ± 2.8 | 11.0 ± 2.7 |
| 147 | ... | ... | 3549 ± 0 | 25 | 7 | 141.7 ± 1.9 | 117.0 ± 5.7 | 25.5 ± 3.5 | 122.1 ± 3.3 | 21.1 ± 5.0 |
| 149 | -0.3 ± 0.5 | -0.0 ± 0.4 | 4396 ± 12 | 20 | 5 | 3.9 ± 0.8 | 8.5 ± 4.3 | 13.0 ± 3.1 | 7.2 ± 4.0 | 10.0 ± 3.7 |
| 151 | 1.4 ± 0.5 | 0.5 ± 0.5 | 4662 ± 9 | 29 | – | 37.0 ± 0.3 | 32.4 ± 2.5 | 9.1 ± 1.8 | 41.7 ± 2.3 | 7.9 ± 1.4 |
| 152 | 0.6 ± 0.6 | 1.3 ± 0.7 | 3881 ± 9 | 20 | – | 121.9 ± 0.5 | 116.9 ± 5.9 | 21.7 ± 5.3 | 125.2 ± 10.0 | 41.2 ± 14.8 |
| 153 | -3.1 ± 0.7 | -1.6 ± 0.8 | 7984 ± 18 | 20 | – | 134.9 ± 0.3 | 137.7 ± 2.2 | 11.2 ± 3.0 | 130.2 ± 2.4 | 9.8 ± 3.8 |
| 273 | 1.3 ± 0.7 | 1.9 ± 0.8 | 4326 ± 11 | 33 | – | 162.9 ± 0.2 | 162.6 ± 2.7 | 12.6 ± 2.1 | 164.5 ± 2.5 | 12.1 ± 2.3 |
| 275 | -1.0 ± 0.4 | -0.3 ± 0.4 | 2169 ± 5 | 27 | 5 | 82.1 ± 0.6 | 79.6 ± 4.6 | 13.9 ± 2.6 | 80.2 ± 4.9 | 20.6 ± 4.6 |
| 277 | -0.3 ± 0.4 | -0.8 ± 0.5 | 3690 ± 6 | 25 | 9 | 22.3 ± 0.7 | 19.7 ± 5.9 | 22.4 ± 3.4 | 19.6 ± 6.4 | 19.4 ± 2.9 |
| 307 | ... | ... | 8344 ± 16 | 15 | – | 95.2 ± 0.5 | 101.8 ± 6.3 | 23.9 ± 13.3 | 95.5 ± 5.6 | 22.7 ± 7.2 |
| 364 | ... | ... | 6474 ± 1 | 25 | – | 99.8 ± 0.4 | 102.6 ± 1.4 | 6.2 ± 0.8 | 101.8 ± 0.8 | 5.9 ± 1.0 |
| 386 | 0.5 ± 0.6 | 0.4 ± 0.5 | 6297 ± 10 | 17 | – | 48.9 ± 0.9 | 44.9 ± 3.9 | 14.0 ± 3.2 | 58.1 ± 4.7 | 17.4 ± 3.9 |
| 414 | ... | ... | 2521 ± 0 | 25 | 7 | 107.9 ± 3.2 | 135.6 ± 12.8 | 36.8 ± 7.8 | 141.5 ± 11.0 | 38.7 ± 6.4 |
| 436 | 0.3 ± 0.7 | 0.5 ± 0.7 | 3106 ± 9 | 20 | 5 | 24.3 ± 1.1 | 145.1 ± 39.0 | 31.2 ± 8.0 | 173.2 ± 5.9 | 37.8 ± 11.5 |
| 489 | -0.2 ± 0.4 | -0.9 ± 0.7 | 3392 ± 5 | 25 | 10 | 104.1 ± 1.0 | 102.4 ± 3.7 | 16.6 ± 3.9 | 106.6 ± 3.8 | 16.1 ± 3.4 |
| 515 | ... | ... | 3868 ± 1 | 25 | 10 | 0.2 ± 1.1 | 159.5 ± 2.3 | 12.1 ± 3.0 | 171.8 ± 5.4 | 21.0 ± 3.1 |
| 518 | ... | ... | 2712 ± 0 | 30 | 5 | 88.5 ± 1.0 | 99.2 ± 4.4 | 24.2 ± 3.5 | 93.0 ± 3.5 | 23.4 ± 4.4 |
| 580 | ... | ... | 4082 ± 1 | 23 | 5 | 43.3 ± 0.5 | 40.6 ± 4.4 | 21.4 ± 3.9 | 36.1 ± 5.1 | 19.8 ± 3.7 |
| 602 | -0.4 ± 0.2 | -1.0 ± 0.3 | 4737 ± 5 | 15 | – | 75.2 ± 0.8 | 72.9 ± 3.2 | 11.5 ± 3.0 | 82.4 ± 4.4 | 10.9 ± 4.7 |
| 610 | 1.4 ± 0.8 | -1.2 ± 1.0 | 7125 ± 19 | 20 | – | 39.4 ± 0.3 | 40.2 ± 3.2 | 16.7 ± 5.0 | 38.7 ± 3.6 | 15.1 ± 4.5 |
| 624 | 0.5 ± 0.4 | 0.5 ± 0.3 | 7255 ± 7 | 25 | 6 | 116.4 ± 1.5 | 92.9 ± 3.5 | 18.3 ± 2.8 | 85.2 ± 4.8 | 16.8 ± 3.2 |
| 630 | ... | ... | 1768 ± 1 | 20 | 9 | 146.4 ± 0.7 | 157.6 ± 8.0 | 35.3 ± 8.0 | 170.1 ± 7.6 | 33.3 ± 6.5 |
| 664 | ... | ... | 3220 ± 0 | 25 | – | 118.7 ± 0.2 | 109.4 ± 2.6 | 13.0 ± 2.0 | 111.5 ± 2.9 | 18.7 ± 2.7 |
| 684 | -1.5 ± 0.3 | -0.2 ± 0.3 | 5331 ± 6 | 27 | 7 | 141.2 ± 2.1 | 119.9 ± 2.3 | 14.1 ± 2.5 | 107.5 ± 4.6 | 13.7 ± 2.6 |
| 714 | 0.4 ± 0.7 | -0.4 ± 0.6 | 7793 ± 18 | 20 | – | 16.7 ± 0.5 | 12.7 ± 5.0 | 13.0 ± 2.9 | 13.0 ± 4.3 | 16.7 ± 4.1 |
| 715 | -0.7 ± 0.8 | 0.0 ± 0.7 | 1885 ± 9 | 30 | 7 | 66.5 ± 0.4 | 68.7 ± 3.9 | 17.0 ± 3.4 | 62.4 ± 5.0 | 21.7 ± 3.6 |
| 743 | -0.1 ± 0.6 | 1.3 ± 0.7 | 3868 ± 8 | 25 | 5 | 85.9 ± 0.5 | 92.1 ± 7.5 | 32.4 ± 5.2 | 81.0 ± 6.4 | 25.7 ± 6.5 |
| 748 | 0.3 ± 0.7 | -0.4 ± 0.4 | 2355 ± 4 | 25 | 10 | 192.5 ± 0.5 | 17.8 ± 6.2 | 24.0 ± 4.8 | 17.6 ± 4.1 | 28.3 ± 6.3 |
| 753 | -0.3 ± 0.4 | -0.5 ± 0.5 | 3175 ± 4 | 25 | 7 | 56.1 ± 0.6 | 57.4 ± 3.0 | 15.6 ± 2.8 | 57.0 ± 3.2 | 10.1 ± 1.8 |
| 764 | 1.0 ± 0.7 | -1.1 ± 0.8 | 7704 ± 11 | 20 | 7 | 128.4 ± 0.7 | 121.3 ± 4.0 | 16.0 ± 4.8 | 136.1 ± 7.8 | 22.5 ± 4.2 |
| 768 | -1.0 ± 0.5 | -0.2 ± 0.6 | 3735 ± 8 | 15 | 7 | 42.4 ± 0.9 | 50.0 ± 20.6 | 37.6 ± 12.1 | 41.7 ± 13.8 | 41.7 ± 7.4 |
| 771 | -1.1 ± 0.8 | -1.8 ± 0.9 | 3762 ± 9 | 20 | 7 | 98.7 ± 0.9 | 29.5 ± 6.6 | 29.5 ± 7.6 | 46.5 ± 9.7 | 39.5 ± 14.3 |
| 777 | 0.5 ± 0.4 | -1.0 ± 0.4 | 4836 ± 9 | 30 | 10 | 36.1 ± 0.4 | 35.7 ± 2.0 | 10.1 ± 1.6 | 38.4 ± 3.1 | 12.3 ± 1.9 |
| 779 | -1.8 ± 0.5 | -1.1 ± 0.6 | 5527 ± 8 | 23 | – | 121.8 ± 0.3 | 129.4 ± 4.4 | 22.1 ± 5.0 | 117.9 ± 3.7 | 16.7 ± 5.7 |
| 782 | 0.9 ± 0.3 | 0.9 ± 0.3 | 7803 ± 10 | 12 | – | 152.9 ± 0.5 | 147.6 ± 3.0 | 10.3 ± 3.3 | 152.9 ± 3.6 | 21.0 ± 8.2 |
| 790 | ... | ... | 4677 ± 1 | 12 | 5 | 143.6 ± 1.3 | 142.4 ± 5.6 | 16.1 ± 4.3 | 144.5 ± 5.9 | 12.4 ± 4.5 |
| 791 | 1.2 ± 0.3 | 0.4 ± 0.3 | 3316 ± 5 | 30 | – | 152.3 ± 0.3 | 149.7 ± 1.2 | 3.2 ± 0.7 | 154.5 ± 1.3 | 3.7 ± 0.6 |
| 804 | -2.2 ± 0.5 | -0.5 ± 0.5 | 3388 ± 7 | 15 | – | 126.8 ± 0.5 | 130.5 ± 4.4 | 19.3 ± 4.8 | 127.7 ± 4.7 | 18.6 ± 5.8 |
| 810 | -0.3 ± 0.5 | -0.1 ± 0.5 | 4117 ± 9 | 25 | – | 15.3 ± 0.5 | 8.6 ± 3.0 | 10.0 ± 2.4 | 19.6 ± 3.1 | 16.6 ± 3.0 |
| 813 | ... | ... | 3836 ± 1 | 28 | 7 | 113.1 ± 8.8 | 101.1 ± 5.5 | 33.8 ± 5.3 | 90.0 ± 4.4 | 32.4 ± 6.1 |
| 823 | ... | ... | 2838 ± 1 | 25 | 7 | 159.2 ± 0.6 | 152.2 ± 4.5 | 31.4 ± 6.5 | 168.5 ± 7.8 | 26.0 ± 4.3 |
| 824 | -0.4 ± 0.5 | -1.7 ± 0.6 | 4730 ± 14 | 27 | – | 159.8 ± 0.2 | 161.6 ± 3.0 | 10.5 ± 1.8 | 152.7 ± 4.0 | 13.6 ± 2.2 |
| 826 | -0.4 ± 0.5 | -1.2 ± 0.5 | 5070 ± 9 | 25 | – | 127.9 ± 0.3 | 133.4 ± 2.3 | 10.3 ± 2.2 | 122.5 ± 2.2 | 7.5 ± 1.3 |
| 831 | -0.3 ± 0.8 | 0.4 ± 0.7 | 4957 ± 12 | 15 | – | 123.4 ± 0.6 | 123.8 ± 9.4 | 30.1 ± 9.9 | 133.8 ± 7.1 | 28.2 ± 8.4 |
| 834 | ... | ... | 8694 ± 1 | 15 | – | 114.2 ± 0.5 | 106.3 ± 1.9 | 8.9 ± 2.6 | 95.0 ± 5.8 | 22.0 ± 3.4 |
| 836 | 0.6 ± 0.8 | 0.8 ± 0.8 | 2424 ± 4 | 29 | – | 148.9 ± 0.9 | 140.5 ± 5.3 | 28.1 ± 7.3 | 133.4 ± 6.1 | 31.1 ± 5.0 |
| 842 | 0.3 ± 0.5 | -2.2 ± 0.5 | 2970 ± 6 | 30 | 7 | 54.7 ± 0.4 | 66.9 ± 5.6 | 41.6 ± 4.5 | 70.4 ± 5.3 | 32.0 ± 4.6 |
| 853 | ... | ... | 3788 ± 1 | 30 | 10 | 53.0 ± 5.0 | 53.6 ± 2.9 | 10.8 ± 2.1 | 49.5 ± 2.2 | 5.7 ± 1.4 |
| 854 | ... | ... | 8625 ± 1 | 20 | – | 90.9 ± 0.4 | 90.0 ± 4.3 | 8.8 ± 3.0 | 90.0 ± 4.5 | 12.3 ± 2.9 |
| 856 | ... | ... | 4696 ± 1 | 22 | 5 | 91.6 ± 0.7 | 90.0 ± 4.3 | 24.7 ± 7.1 | 93.7 ± 3.7 | 20.2 ± 3.9 |
| 857 | ... | ... | 8453 ± 1 | 15 | – | 36.1 ± 0.4 | 47.8 ± 3.9 | 12.4 ± 3.5 | 45.0 ± 0.2 | 11.9 ± 2.8 |
| 862 | ... | ... | 6704 ± 1 | 25 | – | 32.1 ± 0.4 | 30.2 ± 3.4 | 13.2 ± 2.1 | 31.7 ± 2.2 | 10.1 ± 1.9 |
| 869 | -0.6 ± 0.5 | 0.9 ± 0.5 | 6157 ± 7 | 22 | 7 | 121.8 ± 1.8 | 130.8 ± 4.2 | 25.8 ± 3.8 | 141.4 ± 3.9 | 12.5 ± 2.8 |
| 872 | -0.2 ± 0.7 | -1.3 ± 0.7 | 3767 ± 11 | 20 | 7 | 85.4 ± 3.0 | 64.2 ± 6.3 | 21.5 ± 3.8 | 56.3 ± 6.9 | 23.1 ± 4.3 |
| 876 | -0.6 ± 0.8 | 1.4 ± 0.8 | 5740 ± 13 | 20 | 5 | 106.9 ± 1.3 | 94.2 ± 4.6 | 19.6 ± 5.0 | 95.6 ± 9.2 | 29.9 ± 5.4 |
| 886 | -1.4 ± 0.3 | -0.1 ± 0.2 | 4488 ± 5 | 27 | 7 | 12.8 ± 0.3 | 4.2 ± 1.8 | 8.0 ± 1.6 | 20.0 ± 2.2 | 9.0 ± 2.0 |
| 887 | 0.3 ± 0.4 | 0.4 ± 0.3 | 7065 ± 9 | 25 | 5 | 25.2 ± 1.4 | 12.6 ± 2.9 | 9.7 ± 2.1 | 16.7 ± 4.4 | 17.6 ± 2.5 |
| 889 | -1.2 ± 0.4 | -0.9 ± 0.4 | 4852 ± 7 | 20 | 10 | 64.4 ± 0.7 | 73.4 ± 3.9 | 9.9 ± 2.1 | 58.6 ± 2.9 | 14.8 ± 3.1 |
| 890 | 0.4 ± 0.5 | -0.1 ± 0.4 | 6541 ± 10 | 15 | – | 142.6 ± 0.5 | 157.5 ± 4.2 | 11.0 ± 2.6 | 162.8 ± 5.4 | 14.1 ± 2.8 |
| 896 | 0.3 ± 0.5 | 1.7 ± 0.6 | 7439 ± 11 | 18 | – | 19.6 ± 0.5 | 18.7 ± 6.9 | 20.0 ± 5.5 | 29.6 ± 5.6 | 23.0 ± 4.6 |
| 904 | -0.5 ± 0.5 | -0.0 ± 0.5 | 4913 ± 13 | 30 | 6 | 148.2 ± 1.1 | 149.8 ± 2.5 | 14.2 ± 2.6 | 145.1 ± 2.6 | 12.7 ± 2.6 |
| 924 | -1.0 ± 0.0 | -1.0 ± 0.0 | 2571 ± 1 | 22 | 7 | 24.6 ± 0.8 | 37.4 ± 1.8 | 12.0 ± 1.7 | 51.4 ± 3.2 | 14.7 ± 3.7 |
| 929 | 1.4 ± 0.8 | 0.1 ± 0.7 | 7977 ± 17 | 20 | – | 43.4 ± 0.8 | 54.9 ± 4.6 | 16.8 ± 3.6 | 58.2 ± 4.0 | 15.5 ± 3.6 |
| 938 | 1.0 ± 0.6 | 1.7 ± 0.5 | 5896 ± 4 | 15 | 7 | 51.1 ± 5.9 | 75.3 ± 10.7 | 34.0 ± 6.3 | 73.2 ± 8.1 | 26.1 ± 5.4 |

(1) CALIFA identifier. (2) and (3) Location of the kinematic centre. The value listed is the gradient peak (GP) with respect to the optical nucleus (ON) if not, ON is used as kinematic centre (see section **??** for details). (4) Systemic velocity derived from integrated the velocities in a 2.7$''$ aperture centred in the kinematic centre. (5) Radius used to average the polar coordinates of the positions from the lines of nodes (see section 2.4.3 for details). (6) Radius used to average the polar coordinates of the positions from the zero-velocity line (see section 2.4.3 for details). (7) Morphological PA inferred by fitting an elipse to an isophote at radius $r_{max}$ in the r-band SDSS image. (8) Kinematic position angle at radius r for the approaching side (see section 2.4.3 for details). (9) Standard deviation of the kinematic position angle of the approaching side (see section 2.4.3 for details). (10) Kinematic position angle at radius r for the receding side. (11) Standard deviation of the kinematic position angle of the receding side. Values in parenthesis for each row represent the errors obtained from Monte Carlo simulations.

Table A.3: Ionized gas kinematic properties of the non-interacting sample selected for this study included in the CALIFA survey.

| id | $\Delta\alpha$ | $\Delta\delta$ | $V_{sys}$ | $r_{max}$ | $r_{min}$ | $PA_{morph}$ | PA approaching | | PA receding | |
|---|---|---|---|---|---|---|---|---|---|---|
| | | | | | | | $PA_{kin}$ | $\delta PA_{kin}$ | $PA_{kin}$ | $\delta PA_{kin}$ |
| | ($''$) | ($''$) | (km $s^{-1}$) | ($''$) | ($''$) | ($^\circ$) | ($^\circ$) | ($^\circ$) | ($^\circ$) | ($^\circ$) |
| (1) | (2) | (3) | (4) | (5) | (6) | (7) | (8) | (9) | (10) | (11) |
| 1 | ... | ... | 4990 ± 2 | 22 | ... | 3.7 ± 0.4 | 4.5 ± 1.2 | 3.1 ± 1.0 | 3.5 ± 1.6 | 3.5 ± 1.3 |
| 2 | 0.2 ± 0.1 | -2.3 ± 0.1 | 7247 ± 1 | 22 | ... | 45.2 ± 0.9 | 55.0 ± 1.4 | 6.1 ± 0.7 | 44.6 ± 1.0 | 6.5 ± 1.5 |
| 7 | -1.4 ± 0.3 | -0.5 ± 0.4 | 6299 ± 18 | 20 | ... | 17.4 ± 0.2 | 27.8 ± 2.7 | 8.6 ± 2.1 | 10.3 ± 2.4 | 6.8 ± 1.7 |
| 8 | 0.1 ± 0.1 | 0.9 ± 0.1 | 4534 ± 0 | 20 | 7 | 106.0 ± 1.1 | 116.2 ± 2.1 | 7.4 ± 1.0 | 115.7 ± 1.7 | 7.3 ± 1.0 |
| 10 | 0.1 ± 0.2 | -0.7 ± 0.3 | 5974 ± 8 | 25 | 10 | 179.3 ± 0.6 | 16.4 ± 1.4 | 8.3 ± 1.5 | 18.9 ± 2.3 | 13.9 ± 2.5 |
| 23 | -0.5 ± 0.6 | -0.9 ± 0.6 | 3859 ± 6 | 20 | 10 | 126.0 ± 0.7 | 69.9 ± 16.1 | 91.4 ± 9.2 | 108.2 ± 33.0 | 91.4 ± 21.9 |
| 25 | -1.8 ± 0.5 | -1.2 ± 0.6 | 5239 ± 10 | 30 | 7 | 167.1 ± 1.0 | 174.6 ± 2.4 | 14.5 ± 3.2 | 165.6 ± 1.8 | 19.8 ± 2.7 |
| 28 | -0.4 ± 0.2 | 0.0 ± 0.3 | 4486 ± 4 | 12 | 5 | 60.4 ± 0.8 | 56.2 ± 2.3 | 11.0 ± 2.6 | 47.3 ± 2.4 | 8.6 ± 2.5 |
| 30 | 0.1 ± 0.1 | 1.4 ± 0.1 | 4111 ± 2 | 20 | 7 | 177.3 ± 0.8 | 5.7 ± 1.9 | 6.8 ± 1.7 | 179.6 ± 0.6 | 6.9 ± 3.0 |
| 31 | -0.8 ± 0.2 | 1.5 ± 0.2 | 4438 ± 2 | 30 | 5 | 82.2 ± 4.9 | 65.4 ± 1.1 | 7.2 ± 1.3 | 75.9 ± 1.9 | 10.5 ± 2.2 |
| 33 | -0.2 ± 0.2 | 0.5 ± 0.2 | 5213 ± 6 | 20 | 7 | 93.7 ± 1.5 | 91.5 ± 2.1 | 7.5 ± 1.1 | 87.7 ± 1.2 | 6.9 ± 1.3 |
| 41 | ... | ... | 5547 ± 0 | 15 | ... | 53.9 ± 0.2 | 45.9 ± 2.2 | 9.6 ± 2.4 | 60.6 ± 2.2 | 6.1 ± 1.3 |
| 43 | -0.1 ± 0.3 | 1.0 ± 0.4 | 4811 ± 7 | 12 | 7 | 156.4 ± 1.0 | 7.9 ± 4.0 | 12.3 ± 3.8 | 16.1 ± 4.5 | 11.5 ± 4.3 |
| 53 | -1.2 ± 0.3 | -1.8 ± 0.3 | 6356 ± 4 | 20 | ... | 152.2 ± 0.5 | 148.0 ± 1.4 | 4.8 ± 1.0 | 151.7 ± 1.6 | 5.8 ± 1.2 |
| 108 | 0.1 ± 0.2 | -0.1 ± 0.3 | 5235 ± 2 | 20 | 5 | 96.5 ± 1.2 | 100.6 ± 2.2 | 8.5 ± 2.0 | 100.4 ± 2.3 | 9.0 ± 2.4 |
| 116 | -0.7 ± 0.4 | 1.4 ± 0.4 | 7696 ± 12 | 10 | ... | 172.4 ± 1.4 | 159.9 ± 4.9 | 8.3 ± 2.7 | 167.3 ± 7.0 | 12.3 ± 5.0 |
| 131 | -0.1 ± 0.5 | -0.4 ± 0.5 | 3693 ± 7 | 18 | ... | 128.0 ± 0.4 | 130.3 ± 3.5 | 8.2 ± 2.5 | 132.9 ± 2.9 | 7.0 ± 1.9 |
| 147 | 0.1 ± 0.1 | 2.2 ± 0.2 | 3568 ± 2 | 25 | 7 | 141.7 ± 1.9 | 117.7 ± 1.4 | 8.1 ± 1.4 | 116.4 ± 4.3 | 14.3 ± 2.6 |
| 149 | 0.6 ± 0.2 | -0.6 ± 0.2 | 4359 ± 10 | 20 | 5 | 3.9 ± 0.8 | 5.3 ± 1.7 | 4.7 ± 0.9 | 13.8 ± 1.7 | 5.9 ± 1.5 |
| 151 | 0.7 ± 0.3 | -0.3 ± 0.2 | 4574 ± 18 | 29 | ... | 37.0 ± 0.3 | 36.6 ± 1.3 | 4.3 ± 0.8 | 37.3 ± 3.0 | 10.8 ± 3.7 |
| 152 | -0.1 ± 0.3 | -1.1 ± 0.3 | 3916 ± 4 | 20 | ... | 121.9 ± 0.5 | 122.8 ± 1.9 | 8.2 ± 2.2 | 113.9 ± 2.2 | 8.1 ± 1.8 |
| 153 | -0.6 ± 0.4 | -0.7 ± 0.3 | 8081 ± 10 | 20 | ... | 134.9 ± 0.3 | 135.7 ± 2.1 | 7.3 ± 1.8 | 134.0 ± 1.9 | 4.8 ± 1.1 |
| 273 | 2.4 ± 0.9 | -1.9 ± 0.6 | 4270 ± 5 | 33 | ... | 162.9 ± 0.2 | 150.0 ± 2.9 | 10.7 ± 2.1 | 174.1 ± 2.6 | 6.2 ± 1.5 |
| 275 | 1.2 ± 0.2 | 0.6 ± 0.1 | 2086 ± 6 | 27 | 5 | 82.1 ± 0.6 | 83.2 ± 0.9 | 3.9 ± 0.8 | 82.3 ± 1.3 | 8.1 ± 1.9 |
| 277 | 0.9 ± 0.4 | 0.4 ± 0.6 | 3649 ± 6 | 25 | 9 | 22.3 ± 0.7 | 12.8 ± 2.5 | 16.1 ± 2.8 | 32.5 ± 4.0 | 26.6 ± 3.1 |
| 307 | -0.2 ± 0.3 | 0.2 ± 0.3 | 8439 ± 10 | 15 | ... | 95.2 ± 0.5 | 97.2 ± 4.3 | 9.1 ± 3.4 | 92.0 ± 3.2 | 6.3 ± 2.5 |
| 364 | 0.2 ± 0.6 | 1.1 ± 0.6 | 6582 ± 22 | 25 | ... | 99.8 ± 0.4 | 108.6 ± 4.3 | 14.3 ± 2.7 | 98.6 ± 2.8 | 6.4 ± 1.7 |
| 386 | -0.7 ± 0.5 | -0.1 ± 0.6 | 6332 ± 10 | 17 | ... | 48.9 ± 0.9 | 46.6 ± 3.4 | 8.8 ± 2.6 | 44.2 ± 2.9 | 10.6 ± 2.6 |
| 414 | -0.4 ± 0.3 | 0.1 ± 0.3 | 2497 ± 3 | 25 | 7 | 107.9 ± 3.2 | 143.4 ± 2.3 | 13.8 ± 2.6 | 150.5 ± 2.8 | 17.1 ± 3.7 |
| 436 | 0.1 ± 0.3 | -1.5 ± 0.3 | 3158 ± 6 | 20 | 5 | 24.3 ± 1.1 | 171.5 ± 3.1 | 12.1 ± 4.7 | 173.7 ± 2.7 | 7.7 ± 1.9 |
| 489 | 0.8 ± 0.1 | -0.6 ± 0.2 | 3409 ± 1 | 25 | 10 | 104.1 ± 1.0 | 100.8 ± 1.5 | 8.8 ± 1.3 | 104.2 ± 2.0 | 8.1 ± 1.2 |
| 515 | 0.1 ± 0.4 | 0.1 ± 0.3 | 3866 ± 7 | 25 | 10 | 0.2 ± 1.1 | 166.6 ± 3.3 | 10.5 ± 1.9 | 165.4 ± 3.2 | 10.1 ± 1.8 |
| 518 | -0.6 ± 0.5 | -0.5 ± 0.2 | 2690 ± 11 | 30 | 5 | 88.5 ± 1.0 | 98.1 ± 2.9 | 13.7 ± 1.9 | 97.3 ± 2.5 | 14.2 ± 3.1 |
| 580 | 0.0 ± 0.2 | -0.0 ± 0.2 | 4063 ± 2 | 23 | 5 | 43.3 ± 0.5 | 40.1 ± 1.5 | 6.6 ± 1.6 | 35.5 ± 1.6 | 7.8 ± 1.2 |
| 602 | ... | ... | 4799 ± 12 | 15 | ... | 75.2 ± 0.8 | 67.0 ± 3.7 | 23.9 ± 6.9 | 59.3 ± 6.5 | 19.8 ± 4.8 |
| 610 | 0.5 ± 0.4 | 1.1 ± 0.5 | 7223 ± 12 | 20 | ... | 39.4 ± 0.3 | 39.9 ± 2.0 | 5.6 ± 1.3 | 47.0 ± 2.6 | 7.1 ± 1.5 |
| 624 | 0.9 ± 0.6 | -0.3 ± 0.4 | 7309 ± 7 | 25 | 6 | 116.4 ± 1.5 | 87.4 ± 4.6 | 25.9 ± 5.1 | 78.1 ± 7.9 | 38.4 ± 4.2 |
| 630 | -0.1 ± 0.4 | 0.0 ± 0.5 | 1727 ± 7 | 20 | 9 | 146.4 ± 0.7 | 159.5 ± 4.0 | 18.5 ± 4.4 | 163.9 ± 3.7 | 18.1 ± 4.3 |
| 664 | ... | ... | 3204 ± 5 | 25 | ... | 118.7 ± 0.2 | 113.3 ± 3.2 | 19.8 ± 3.3 | 103.6 ± 3.2 | 13.6 ± 3.5 |
| 684 | 0.4 ± 0.4 | 1.2 ± 0.4 | 5439 ± 10 | 27 | 7 | 141.2 ± 2.1 | 109.5 ± 3.8 | 15.3 ± 4.5 | 111.3 ± 4.2 | 15.0 ± 2.0 |
| 714 | -0.2 ± 0.2 | 0.4 ± 0.2 | 7831 ± 10 | 20 | ... | 16.7 ± 0.5 | 12.1 ± 2.4 | 5.6 ± 1.3 | 13.5 ± 1.9 | 4.3 ± 1.0 |
| 715 | -1.0 ± 0.1 | 0.7 ± 0.0 | 1884 ± 1 | 30 | 7 | 66.5 ± 0.4 | 64.9 ± 0.5 | 4.3 ± 0.6 | 66.7 ± 0.8 | 7.3 ± 1.6 |
| 743 | 0.3 ± 0.2 | -0.3 ± 0.1 | 3865 ± 5 | 25 | 5 | 85.9 ± 0.5 | 83.0 ± 1.6 | 6.0 ± 0.9 | 84.9 ± 1.3 | 8.5 ± 1.0 |
| 748 | -0.9 ± 0.1 | -2.7 ± 0.1 | 2350 ± 2 | 25 | 10 | 192.5 ± 0.5 | 10.7 ± 0.7 | 6.1 ± 1.0 | 21.4 ± 1.4 | 10.3 ± 1.4 |
| 753 | 0.8 ± 0.1 | -0.6 ± 0.1 | 3222 ± 4 | 25 | 7 | 56.1 ± 0.6 | 58.4 ± 0.7 | 8.4 ± 0.7 | 55.7 ± 0.6 | 4.0 ± 0.4 |
| 764 | -0.9 ± 0.3 | 0.7 ± 0.2 | 7726 ± 12 | 20 | 7 | 128.4 ± 0.7 | 129.4 ± 2.8 | 10.2 ± 2.4 | 128.4 ± 2.3 | 12.4 ± 3.9 |
| 768 | 0.4 ± 0.2 | -0.0 ± 0.2 | 3765 ± 3 | 15 | 7 | 42.4 ± 0.9 | 36.8 ± 1.5 | 8.5 ± 1.8 | 53.7 ± 1.8 | 7.7 ± 1.8 |
| 771 | 2.2 ± 0.3 | -0.5 ± 0.4 | 3741 ± 9 | 20 | 7 | 98.7 ± 0.9 | 40.7 ± 3.9 | 15.8 ± 2.7 | 44.3 ± 2.8 | 11.5 ± 2.9 |
| 777 | -0.5 ± 0.2 | 0.6 ± 0.2 | 4877 ± 9 | 30 | 10 | 36.1 ± 0.4 | 37.4 ± 1.0 | 4.7 ± 0.9 | 36.4 ± 1.2 | 6.0 ± 1.0 |
| 779 | -0.1 ± 0.3 | -1.1 ± 0.3 | 5559 ± 5 | 23 | ... | 121.8 ± 0.3 | 124.9 ± 2.1 | 6.5 ± 1.3 | 122.5 ± 2.0 | 8.4 ± 1.7 |
| 782 | 0.3 ± 0.5 | 0.5 ± 0.5 | 7878 ± 29 | 12 | ... | 152.9 ± 0.5 | 153.0 ± 3.6 | 10.4 ± 2.9 | 149.0 ± 4.6 | 11.9 ± 3.1 |
| 790 | 1.8 ± 0.3 | 0.9 ± 0.3 | 4717 ± 6 | 12 | 5 | 143.6 ± 1.3 | 145.5 ± 3.7 | 11.1 ± 1.9 | 160.7 ± 5.9 | 12.7 ± 3.3 |
| 791 | -0.5 ± 0.2 | -0.3 ± 0.2 | 3276 ± 4 | 30 | ... | 152.3 ± 0.3 | 154.1 ± 1.1 | 3.8 ± 0.7 | 148.9 ± 1.0 | 3.2 ± 0.4 |
| 804 | -3.1 ± 0.4 | -2.4 ± 0.5 | 3486 ± 7 | 15 | ... | 126.8 ± 0.5 | 124.7 ± 4.7 | 25.2 ± 6.7 | 109.5 ± 15.9 | 71.6 ± 12.6 |
| 810 | 0.7 ± 0.1 | 1.1 ± 0.1 | 4093 ± 1 | 25 | ... | 15.3 ± 0.5 | 15.4 ± 0.7 | 4.1 ± 0.8 | 15.1 ± 0.6 | 5.7 ± 0.8 |
| 813 | -0.6 ± 0.1 | 0.0 ± 0.2 | 3818 ± 1 | 28 | 7 | 113.1 ± 8.8 | 101.9 ± 2.0 | 15.8 ± 2.7 | 90.5 ± 3.0 | 13.8 ± 3.8 |
| 823 | -1.0 ± 0.2 | 1.9 ± 0.3 | 2825 ± 2 | 25 | 7 | 159.2 ± 0.6 | 149.6 ± 2.1 | 8.3 ± 1.4 | 158.6 ± 2.1 | 10.7 ± 2.0 |
| 824 | -0.4 ± 0.1 | -0.6 ± 0.2 | 4732 ± 3 | 27 | ... | 159.8 ± 0.2 | 159.3 ± 1.0 | 5.4 ± 1.2 | 161.7 ± 1.2 | 5.5 ± 1.1 |
| 826 | ... | ... | 5014 ± 2 | 25 | ... | 127.9 ± 0.3 | 123.9 ± 1.8 | 12.4 ± 2.2 | 129.9 ± 2.2 | 17.9 ± 3.3 |
| 831 | 0.2 ± 0.1 | 0.5 ± 0.2 | 4968 ± 4 | 15 | ... | 123.4 ± 0.6 | 124.2 ± 1.5 | 6.6 ± 1.2 | 127.1 ± 1.2 | 5.3 ± 0.9 |
| 834 | -0.4 ± 0.5 | 1.3 ± 0.5 | 8764 ± 14 | 15 | ... | 114.2 ± 0.5 | 101.9 ± 3.7 | 11.8 ± 4.3 | 106.8 ± 3.7 | 7.5 ± 2.1 |
| 836 | 1.1 ± 0.2 | 1.9 ± 0.2 | 2407 ± 0 | 29 | ... | 148.9 ± 0.9 | 120.9 ± 1.7 | 10.9 ± 1.9 | 135.6 ± 2.2 | 17.5 ± 2.6 |
| 842 | 0.0 ± 0.3 | -0.2 ± 0.3 | 2955 ± 6 | 30 | 7 | 54.7 ± 0.4 | 56.8 ± 2.4 | 9.6 ± 1.5 | 63.2 ± 2.6 | 15.6 ± 1.8 |
| 853 | 0.8 ± 0.2 | -1.0 ± 0.2 | 3809 ± 3 | 30 | 10 | 53.0 ± 5.0 | 50.3 ± 0.9 | 2.9 ± 0.3 | 47.3 ± 1.2 | 3.3 ± 0.4 |
| 854 | 0.9 ± 0.4 | 0.2 ± 0.2 | 8654 ± 16 | 20 | ... | 90.9 ± 0.4 | 87.4 ± 2.3 | 10.1 ± 2.8 | 86.2 ± 3.1 | 9.7 ± 2.9 |
| 856 | 0.7 ± 0.1 | 2.1 ± 0.2 | 4700 ± 3 | 22 | 5 | 91.6 ± 0.7 | 94.3 ± 2.6 | 10.4 ± 2.5 | 91.8 ± 2.6 | 6.9 ± 1.8 |
| 857 | -2.0 ± 0.6 | -1.5 ± 0.4 | 8539 ± 8 | 15 | ... | 36.1 ± 0.4 | 60.5 ± 3.7 | 12.6 ± 5.6 | 38.2 ± 4.3 | 11.7 ± 3.1 |
| 862 | -1.3 ± 0.2 | 1.0 ± 0.2 | 6720 ± 4 | 25 | ... | 32.1 ± 0.4 | 27.8 ± 1.2 | 4.9 ± 1.0 | 37.8 ± 1.7 | 7.3 ± 0.7 |
| 869 | 1.3 ± 0.6 | 3.0 ± 0.4 | 6139 ± 18 | 22 | 7 | 121.8 ± 1.8 | 125.9 ± 3.0 | 13.4 ± 3.7 | 133.0 ± 2.7 | 12.3 ± 2.5 |
| 872 | 2.0 ± 0.7 | 1.1 ± 0.6 | 3813 ± 22 | 20 | 7 | 85.4 ± 3.0 | 64.3 ± 5.3 | 36.8 ± 3.2 | 45.3 ± 6.7 | 30.3 ± 5.8 |
| 876 | 0.1 ± 0.3 | -1.2 ± 0.2 | 5743 ± 4 | 20 | 5 | 106.9 ± 1.3 | 98.1 ± 2.4 | 8.8 ± 1.7 | 96.7 ± 3.2 | 14.2 ± 3.8 |
| 886 | -0.3 ± 0.1 | 0.1 ± 0.2 | 4455 ± 5 | 27 | 7 | 12.8 ± 0.3 | 10.3 ± 1.2 | 6.0 ± 1.4 | 17.2 ± 1.1 | 7.0 ± 1.2 |
| 887 | 0.8 ± 0.1 | 0.9 ± 0.1 | 7056 ± 3 | 25 | 5 | 25.2 ± 1.4 | 15.3 ± 1.8 | 8.6 ± 1.2 | 15.0 ± 1.6 | 7.3 ± 1.5 |
| 889 | -0.5 ± 0.0 | 0.5 ± 0.1 | 4883 ± 0 | 20 | 10 | 64.4 ± 0.7 | 61.7 ± 1.2 | 6.3 ± 0.9 | 70.7 ± 1.2 | 5.4 ± 1.2 |
| 890 | 2.1 ± 0.4 | -1.2 ± 0.4 | 6533 ± 5 | 15 | ... | 142.6 ± 0.5 | 144.5 ± 3.0 | 13.9 ± 4.0 | 167.8 ± 4.2 | 9.7 ± 3.8 |
| 896 | 0.9 ± 0.2 | 0.0 ± 0.3 | 7461 ± 6 | 18 | ... | 19.6 ± 0.5 | 18.2 ± 2.7 | 7.7 ± 1.4 | 28.1 ± 1.8 | 6.8 ± 1.7 |
| 904 | -0.6 ± 0.1 | 1.5 ± 0.1 | 4892 ± 0 | 30 | 6 | 148.2 ± 1.1 | 145.1 ± 1.5 | 8.4 ± 1.1 | 147.2 ± 0.7 | 5.9 ± 1.1 |
| 924 | -0.2 ± 0.4 | -0.3 ± 0.4 | 2525 ± 12 | 22 | 7 | 24.6 ± 0.8 | 49.3 ± 3.9 | 13.4 ± 2.9 | 52.0 ± 2.7 | 13.8 ± 3.7 |
| 929 | -2.0 ± 0.3 | 1.4 ± 0.3 | 8103 ± 6 | 20 | ... | 43.4 ± 0.8 | 52.4 ± 1.3 | 7.1 ± 1.5 | 50.7 ± 1.9 | 7.6 ± 1.8 |
| 938 | 0.6 ± 0.2 | 0.7 ± 0.2 | 5913 ± 3 | 15 | 7 | 51.1 ± 5.9 | 64.6 ± 3.9 | 14.6 ± 3.4 | 68.4 ± 5.2 | 12.3 ± 3.4 |

(1) CALIFA identifier. (2) and (3) Location of the kinematic centre. The value listed is the gradient peak (GP) with respect to the optical nucleus (ON) if not, ON is used as kinematic centre (see section **??** for details). (4) systemic velocity derived from integrated the velocities in a 2.7$''$ aperture centred on the kinematic centre. (5) radius used to average the polar coordinates of the positions from the lines of nodes (see section 2.4.3 for details). (6) radius used to average the polar coordinates of the positions from the zero-velocity line (see section 2.4.3 for details). (7) morphological PA inferred by fitting an elipse to an isophote at radius $r_{max}$ in the r-band SDSS image. (8) kinematic position angle at radius r for the approaching side (see section 2.4.3 for details). (9) standard deviation of the kinematic position angle of the approaching side (see section 2.4.3 for details). (10) kinematic position angle at radius r for the receding side. (11) standard deviation of the kinematic position angle of the receding side. Values in parenthesis for each row represent the errors obtained from Monte Carlo simulations.

Table A.4: Kinematic orientation measured at different radius for a sample of low inclined galaxies included in our sample of non-interacting galaxies.

| id | | | | | Stars | | | | Ionized gas | | | |
|---|---|---|---|---|---|---|---|---|---|---|---|---|
| | | | | | $r_{in}$ | | $r_{out}$ | | $r_{in}$ | | $r_{out}$ | |
| (1) | $r^{stars}_{in}$ ($''$) (2) | $r^{stars}_{out}$ ($''$) (3) | $r^{gas}_{in}$ ($''$) (4) | $r^{gas}_{out}$ ($''$) (5) | $PA_{app}$ (deg) (6) | $PA_{rec}$ (deg) (7) | $PA_{app}$ (deg) (8) | $PA_{rec}$ (deg) (9) | $PA_{app}$ (deg) (10) | $PA_{rec}$ (deg) (11) | $PA_{app}$ (deg) (12) | $PA_{rec}$ (deg) (13) |
| 8 | 10 | 20 | 14 | 28 | 114 | 117 | 114 | 112 | 114 | 114 | 114 | 117 |
| 10 | 12 | 25 | 12 | 27 | 27 | 15 | 12 | 12 | 18 | 13 | 15 | 17 |
| 23 | 15 | 25 | 27 | 30 | 81 | 84 | 103 | 89 | 77 | 102 | 76 | 76 |
| 25 | 22 | 30 | 22 | 30 | 170 | 166 | 155 | 171 | 170 | 166 | 168 | 155 |
| 28 | 14 | 17 | 14 | 28 | 52 | 42 | 72 | 52 | 55 | 48 | 49 | 51 |
| 30 | 7 | 20 | 7 | 30 | 183 | 162 | 189 | 168 | 12 | 162 | 6 | 91 |
| 31 | 15 | 30 | 16 | 32 | 57 | 74 | 72 | 64 | 67 | 72 | 65 | 73 |
| 33 | 10 | 20 | 16 | 32 | 93 | 90 | 88 | 95 | 91 | 86 | 90 | 95 |
| 43 | 8 | 17 | 8 | 17 | 22 | 29 | 9 | 20 | 7 | 19 | 99 | 10 |
| 108 | 10 | 20 | 10 | 27 | 86 | 90 | 96 | 107 | 94 | 95 | 100 | 97 |
| 147 | 10 | 20 | 10 | 30 | 117 | 116 | 112 | 125 | 117 | 115 | 117 | 115 |
| 149 | 12 | 25 | 12 | 28 | 10 | 10 | 6 | 4 | 5 | 18 | 5 | 12 |
| 275 | 13 | 27 | 16 | 32 | 78 | 76 | 79 | 94 | 83 | 80 | 82 | 86 |
| 277 | 12 | 25 | 16 | 30 | 15 | 20 | 23 | 13 | 49 | 46 | 12 | 21 |
| 414 | 14 | 25 | 14 | 30 | 137 | 136 | 147 | 144 | 133 | 137 | 146 | 152 |
| 436 | 14 | 25 | 23 | 25 | 164 | 181 | 178 | 175 | 172 | 173 | 178 | 178 |
| 489 | 13 | 27 | 16 | 32 | 102 | 110 | 95 | 102 | 98 | 106 | 105 | 99 |
| 515 | 15 | 25 | 16 | 32 | 162 | 168 | 163 | 172 | 164 | 162 | 166 | 169 |
| 518 | 17 | 30 | 17 | 30 | 105 | 93 | 90 | 98 | 104 | 97 | 95 | 98 |
| 580 | 11 | 23 | 13 | 27 | 35 | 37 | 47 | 33 | 35 | 31 | 42 | 35 |
| 602 | 11 | 22 | 5 | 10 | 68 | 81 | 75 | 84 | 71 | 80 | 65 | 63 |
| 624 | 21 | 25 | 21 | 30 | 90 | 82 | 105 | 100 | 74 | 70 | 92 | 89 |
| 630 | 12 | 22 | 12 | 32 | 160 | 97 | 155 | 158 | 167 | 163 | 159 | 157 |
| 684 | 15 | 27 | 20 | 30 | 119 | 111 | 121 | 105 | 114 | 114 | 107 | 108 |
| 715 | 15 | 30 | 16 | 32 | 72 | 59 | 66 | 61 | 65 | 67 | 64 | 58 |
| 743 | 12 | 25 | 16 | 32 | 80 | 84 | 94 | 78 | 81 | 84 | 81 | 83 |
| 748 | 12 | 25 | 16 | 30 | 12 | 20 | 18 | 19 | 12 | 24 | 13 | 22 |
| 753 | 12 | 25 | 16 | 32 | 54 | 57 | 55 | 54 | 53 | 57 | 62 | 56 |
| 764 | 7 | 20 | 7 | 30 | 132 | 124 | 119 | 138 | 120 | 113 | 130 | 128 |
| 768 | 7 | 15 | 14 | 28 | 38 | 25 | 42 | 42 | 35 | 53 | 38 | 47 |
| 771 | 10 | 20 | 21 | 30 | 21 | 33 | 35 | 38 | 39 | 41 | 48 | 33 |
| 777 | 15 | 30 | 18 | 35 | 36 | 38 | 32 | 38 | 38 | 34 | 36 | 34 |
| 790 | 6 | 12 | 10 | 20 | 137 | 143 | 144 | 146 | 144 | 162 | 149 | 155 |
| 791 | 15 | 30 | 15 | 30 | 151 | 154 | 149 | 154 | 156 | 149 | 153 | 149 |
| 813 | 16 | 28 | 16 | 35 | 106 | 88 | 93 | 88 | 101 | 83 | 99 | 95 |
| 823 | 12 | 25 | 16 | 32 | 156 | 165 | 160 | 161 | 149 | 162 | 152 | 154 |
| 836 | 14 | 29 | 14 | 29 | 144 | 135 | 131 | 129 | 127 | 138 | 119 | 129 |
| 842 | 18 | 30 | 15 | 30 | 90 | 73 | 57 | 60 | 58 | 70 | 55 | 52 |
| 853 | 15 | 30 | 15 | 30 | 53 | 46 | 56 | 50 | 49 | 45 | 50 | 48 |
| 856 | 7 | 22 | 7 | 30 | 84 | 98 | 95 | 89 | 76 | 88 | 94 | 93 |
| 869 | 16 | 22 | 16 | 30 | 130 | 142 | 116 | 132 | 134 | 136 | 124 | 133 |
| 872 | 17 | 20 | 17 | 30 | 63 | 55 | 75 | 65 | 61 | 39 | 73 | 71 |
| 876 | 10 | 20 | 15 | 25 | 94 | 79 | 96 | 110 | 102 | 89 | 92 | 101 |
| 886 | 13 | 27 | 16 | 32 | 2 | 24 | 4 | 18 | 15 | 16 | 7 | 15 |
| 887 | 10 | 25 | 10 | 35 | 10 | 10 | 15 | 24 | 11 | 15 | 14 | 13 |
| 889 | 11 | 22 | 11 | 28 | 71 | 58 | 74 | 58 | 57 | 66 | 63 | 69 |
| 904 | 11 | 30 | 11 | 30 | 143 | 138 | 152 | 146 | 142 | 143 | 145 | 148 |
| 924 | 11 | 22 | 16 | 32 | 39 | 48 | 33 | 51 | 43 | 53 | 46 | 48 |
| 938 | 11 | 20 | 11 | 30 | 78 | 72 | 67 | 74 | 64 | 69 | 66 | 66 |

(1) CALIFA identifier. (2) and (3) internal and external radii used to measured the kinematic PA in the stellar component (see section 3.2.6 for details). (4) and (5) internal and external radii used to measured the kinematic PA in the ionized gas component. (6) and (7) internal approaching and receding kinematic position angles for the stellar component (see section 3.2.6 for details). (8) and (9) external approaching and receding kinematic position angles for the stellar component. (10) and (11) internal approaching and receding kinematic position angles for the ionized gas. (12) and (13) external approaching and receding kinematic position angles for the ionized gas.

Table A.5: Morphological parameters of the sample of interacting CALIFA galaxies used in this study.

| CALIFA id (1) | Name (2) | Morphological type (3) | Interaction stage (4) | Stellar mass $\log(M/M_{\odot})$ (5) |
|---|---|---|---|---|
| 14 | UGC00312 | Sd | 1 | 9.64 |
| 17 | UGC00335NED02 | E4 | 2 | 10.73 |
| 22 | NGC0169 | Sab | 2 | 10.87 |
| 26 | NGC0192 | Sab | 1 | 10.73 |
| 39 | NGC0444 | Scd | 1 | 9.82 |
| 42 | NGC0477 | Sbc | 1 (2) | 10.38 |
| 44 | NGC0499 | E5 | 1 | 11.26 |
| 119 | NGC1167 | S0 | 4 | 11.58 |
| 127 | NGC1349 | E6 | 4 | 11.14 |
| 155 | UGC03995 | Sb | 2 | 10.81 |
| 156 | NGC2449 | Sab | 1 | 10.74 |
| 165 | UGC04132 | Sbc | 1 | 10.65 |
| 186 | IC2247 | Sab | 1 | 10.39 |
| 213 | NGC2623 | Scd | 3 | 10.33 |
| 274 | IC0540 | Sab | 1 | 9.78 |
| 311 | NGC3106 | Sab | 4 | 11.21 |
| 314 | UGC05498NED01 | Sa | 1 | 10.69 |
| 340 | NGC3303 | S0a | 2 | 11.03 |
| 360 | NGC3406NED01 | S0 | 2 | 11.34 |
| 475 | NGC3991 | Sm | 2 | 9.53 |
| 479 | NGC4003 | S0a | 1 | 10.98 |
| 486 | UGC07012 | Scd | 1 | 9.35 |
| 520 | NGC4211NED02 | S0a | 2 | 10.42 |
| 577 | NGC4676 | Sdm | 2 | 10.73 |
| 589 | NGC4841A | E3 | 2 (1) | 10.94 |
| 593 | UGC08107 | Sa | 3 | 10.96 |
| 633 | NGC5216 | E0 | 2 | 10.48 |
| 634 | NGC5218 | Sab | 2 | 10.57 |
| 663 | IC0944 | Sab | 1 | 11.16 |
| 676 | NGC5378 | Sb | 1 | 10.52 |
| 680 | NGC5394 | Sbc | 2 | 10.38 |
| 740 | NGC5614 | Sa | 2 | 11.28 |
| 746 | NGC5623 | E7 | 4 (0) | 10.80 |
| 758 | NGC5682 | Scd | 1 | 9.33 |
| 766 | NGC5730 | Scd | 1 | 9.61 |
| 767 | NGC5731 | Sd | 1 | 9.30 |
| 769 | UGC09476 | Sbc | 1 | 10.10 |
| 770 | NGC5739 | S0a | 4 | 11.40 |
| 778 | NGC5784 | S0 | 4 | 11.14 |
| 780 | NGC5797 | E7 | 1 | 10.59 |
| 781 | IC1079 | E4 | 1 | 11.06 |
| 785 | UGC09711 | Sab | 1 | 10.76 |
| 795 | NGC5930 | Sab | 2 | 10.55 |
| 796 | NGC5934 | Sb | 2 | 10.93 |
| 797 | UGC09873 | Sb | 1 | 9.96 |
| 801 | NGC5953 | Sa | 2 | 10.33 |
| 802 | ARP220 | Sd | 3 | 10.83 |
| 803 | NGC5957 | Sb | 1 | 10.18 |
| 806 | NGC5966 | E4 | 1 | 11.10 |
| 807 | IC4566 | Sb | 1 | 10.84 |
| 816 | NGC6021 | E5 | 1 | 10.87 |

(1) CALIFA ID number. For the objects not included in the CALIFA mother sample, we tag them as the ID of the CALIFA companion plus 1000. (2) Name of the galaxy. (3) Morphological type from visual clasification (see Walcher et al. 2014, for details). (4) Interaction stage: 0, 1, 2, 3, 4 represent non-interacting galaxies, objects include in a pair, galaxy in a binary system with clear signatures of interaction, merger remnant with evident tidal features, and merger remnant, respectively. For galaxies with uncertain interaction stage the alternative stage is present in parenthesis (see details of the definition in Sec. 2.3.1). (5) Stellar masses (see Walcher et al. 2014, for details).

Table A.5: continue

| CALIFA id (1) | Name (2) | Morphological type (3) | Interaction stage (4) | Stellar mass $\log(M/M_{\odot})$ (5) |
|---|---|---|---|---|
| 822 | UGC10205 | S0a | 3 (0) | 10.86 |
| 828 | UGC10331 | Sc | 1 (1) | 9.73 |
| 832 | NGC6146 | E5 | 1 | 11.50 |
| 833 | NGC6154 | Sab | 4 | 10.84 |
| 843 | UGC10650 | Scd | 1 | 9.07 |
| 844 | NGC6278 | S0a | 1 | 10.48 |
| 846 | UGC10695 | E5 | 2 (1) | 11.28 |
| 850 | NGC6314 | Sab | 1 | 11.15 |
| 852 | UGC10796 | Scd | 1 (2) | 9.24 |
| 858 | UGC10905 | S0a | 4 | 11.28 |
| 860 | NGC6427 | S0 | 1 | 10.60 |
| 871 | NGC6978 | Sb | 1 | 10.97 |
| 873 | UGC11680NED01 | Sb | 2 | 10.96 |
| 874 | NGC7025 | S0a | 3 (0) | 11.26 |
| 877 | UGC11717 | Sab | 1 (2) | 10.80 |
| 882 | NGC7236 | S0 | 2 | 11.12 |
| 883 | UGC11958 | S0 | 2 | 11.19 |
| 892 | VV488NED02 | Sb | 1 | 10.19 |
| 900 | NGC7550 | E4 | 2 | 11.49 |
| 901 | NGC7549 | Sbc | 2 | 10.32 |
| 903 | NGC7562 | E4 | 1 | 11.23 |
| 905 | UGC12494 | Sd | 1 | 9.34 |
| 907 | NGC7608 | Sbc | 1 | 9.98 |
| 913 | NGC7625 | Sa | 3 (0) | 9.97 |
| 915 | NGC7653 | Sb | 1 | 10.39 |
| 916 | NGC7671 | S0 | 1 | 10.85 |
| 922 | UGC12688 | Scd | 2 (4) | 9.91 |
| 923 | NGC7711 | E7 | 4 | 10.96 |
| 925 | NGC7722 | Sab | 3 (0) | 11.24 |
| 927 | NGC7738 | Sb | 4 (0) | 11.01 |
| 932 | NGC7783NED01 | Sa | 2 (1) | 11.31 |
| 935 | UGC12864 | Sc | 3 (0) | 9.94 |
| 939 | NGC4676B | S0a | 2 | 10.02 |
| 1014 | UGC00312NOTES01 | S0a | 1 | 9.71 |
| 1017 | UGC00335NED01 | E4 | 2 | 10.19 |
| 1022 | NGC0169A | S0 | 2 | 10.21 |
| 1026 | NGC0197 | S0a | 1 | 9.12 |
| 1042 | CGCG536-030 | Sc | 1 (2) | 9.69 |
| 1044 | NGC0495 | S0a | 1 | 9.75 |
| 1340 | NGC3303NED01 | Sb | 2 | 10.33 |
| 1360 | NGC3406NED02 | S0 | 2 | 10.23 |
| 1520 | NGC4211NED01 | S0a | 2 | 10.85 |
| 1589 | NGC4841B | E0 | 2 (1) | 10.82 |
| 1663 | KUG1349+143 | Sb | 1 | 10.16 |
| 1740 | NGC5615 | Ir | 2 | 9.28 |
| 1780 | NGC5794 | S0 | 1 | 10.69 |
| 1781 | IC1078 | Sa | 1 | 10.45 |
| 1795 | NGC5929 | Sa | 2 | 10.47 |
| 1796 | NGC5935 | S0a | 2 | 10.80 |
| 1801 | NGC5954 | Sc | 2 | 7.45 |
| 1871 | NGC6977 | Sa | 1 | 10.85 |
| 1873 | UGC11680NED02 | E0 | 2 | 9.45 |

Table A.6: Stellar Kinematic properties of the interacting sample selected for this study included in the CALIFA survey.

| id | $V_{sys}$ | r | $PA_{morph}$ (r) | PA approaching | | PA receding | | $\Psi_{morph-kin}$ | | $\Psi_{kin-kin}$ |
|---|---|---|---|---|---|---|---|---|---|---|
| | | | | $PA_{kin}$ | $\delta PA_{kin}$ | $PA_{kin}$ | $\delta PA_{kin}$ | approaching | receding | |
| | (km $s^{-1}$) | (arcsec) | (°) | (°) | (°) | (°) | (°) | (°) | (°) | (°) |
| (1) | (2) | (3) | (4) | (5) | (6) | (7) | (8) | (9) | (10) | (11) |
| 14 | – | – | – | – | – | – | – | – | – | – |
| 17 | 5409 ± 5 | 5 | 148.8 ± 0.5 | 142.6 ± 16.6 | 29.5 ± 15.5 | 145.9 ± 11.8 | 15.7 ± 8.3 | 6.2 ± 16.6 | 2.9 ± 11.8 | 3.3 ± 20.4 |
| 22 | 4562 ± 8 | 25 | 87.5 ± 0.5 | 85.4 ± 1.7 | 4.6 ± 1.2 | 89.3 ± 2.0 | 7.5 ± 2.2 | 2.0 ± 1.7 | 1.9 ± 2.1 | 3.9 ± 2.6 |
| 26 | 4180 ± 1 | 25 | 164.0 ± 0.2 | 178.2 ± 3.0 | 10.3 ± 1.6 | 4.6 ± 2.4 | 12.4 ± 2.2 | 14.2 ± 3.0 | 20.5 ± 2.4 | 6.3 ± 3.8 |
| 39 | – | – | – | – | – | – | – | – | – | – |
| 42 | 5828 ± 6 | 15 | 115.5 ± 1.3 | 125.7 ± 5.2 | 18.2 ± 4.8 | 135.2 ± 5.8 | 19.2 ± 3.9 | 10.2 ± 5.4 | 19.7 ± 5.9 | 9.5 ± 7.8 |
| 44 | 4375 ± 1 | 25 | 73.5 ± 0.3 | 97.0 ± 9.0 | 45.1 ± 11.0 | 84.8 ± 6.2 | 35.0 ± 9.4 | 23.4 ± 9.0 | 11.3 ± 6.2 | 12.1 ± 11.0 |
| 119 | 4919 ± 4 | 10 | 70.3 ± 1.2 | 65.6 ± 10.4 | 20.7 ± 6.0 | 73.1 ± 6.8 | 14.9 ± 4.9 | 4.6 ± 10.5 | 2.8 ± 6.9 | 7.4 ± 12.4 |
| 127 | 6534 ± 3 | 17 | 35.6 ± 2.3 | 36.1 ± 5.2 | 19.5 ± 4.0 | 43.4 ± 4.7 | 20.6 ± 4.4 | 0.5 ± 5.7 | 7.8 ± 5.2 | 7.4 ± 7.0 |
| 155 | 4753 ± 6 | 22 | 109.2 ± 0.8 | 80.4 ± 2.9 | 13.5 ± 3.2 | 73.7 ± 3.9 | 16.8 ± 2.2 | 28.8 ± 3.0 | 35.5 ± 3.9 | 6.7 ± 4.8 |
| 156 | 4892 ± 4 | 25 | 127.7 ± 0.2 | 134.7 ± 2.4 | 10.4 ± 1.3 | 130.1 ± 2.1 | 8.9 ± 1.6 | 6.9 ± 2.4 | 2.3 ± 2.1 | 4.6 ± 3.2 |
| 165 | 5154 ± 6 | 22 | 23.4 ± 0.8 | 34.9 ± 2.4 | 7.6 ± 1.6 | 22.1 ± 2.9 | 8.4 ± 1.8 | 11.5 ± 2.6 | 1.3 ± 3.0 | 12.8 ± 3.8 |
| 186 | 4257 ± 2 | 20 | 149.0 ± 0.6 | 152.4 ± 2.2 | 7.5 ± 1.7 | 143.4 ± 2.9 | 10.7 ± 2.1 | 3.3 ± 2.3 | 5.6 ± 2.9 | 9.0 ± 3.6 |
| 213 | 5469 ± 5 | 7 | 81.3 ± 1.6 | 77.8 ± 10.0 | 24.8 ± 13.5 | 112.7 ± 14.3 | 29.5 ± 14.4 | 3.5 ± 10.1 | 31.4 ± 14.4 | 34.9 ± 17.5 |
| 274 | 2068 ± 3 | 12 | 169.8 ± 0.7 | 173.3 ± 4.6 | 16.6 ± 5.5 | 10.2 ± 5.5 | 14.5 ± 6.2 | 3.5 ± 5.1 | 20.4 ± 5.8 | 16.9 ± 7.3 |
| 311 | 6155 ± 2 | 20 | 132.2 ± 2.4 | 142.0 ± 4.6 | 27.7 ± 4.1 | 152.1 ± 5.3 | 22.8 ± 4.9 | 9.8 ± 5.2 | 19.9 ± 5.8 | 10.1 ± 7.0 |
| 314 | 6248 ± 4 | 20 | 59.4 ± 0.8 | 61.7 ± 2.6 | 7.2 ± 1.5 | 59.0 ± 2.4 | 7.1 ± 1.5 | 2.3 ± 2.7 | 0.5 ± 2.5 | 2.8 ± 3.5 |
| 340 | 6138 ± 7 | 12 | 153.2 ± 0.8 | 16.9 ± 7.6 | 18.1 ± 3.3 | 11.9 ± 6.7 | 19.6 ± 5.8 | 43.7 ± 7.6 | 38.7 ± 6.8 | 5.1 ± 10.1 |
| 360 | 7422 ± 4 | 15 | 73.0 ± 1.8 | 48.0 ± 2.2 | 10.0 ± 2.7 | 71.1 ± 5.5 | 19.9 ± 4.0 | 25.0 ± 2.8 | 1.8 ± 5.8 | 23.1 ± 5.9 |
| 475 | – | – | – | – | – | – | – | – | – | – |
| 479 | 6527 ± 4 | 22 | 146.0 ± 0.4 | 169.8 ± 3.0 | 10.5 ± 2.1 | 176.2 ± 2.5 | 11.2 ± 2.3 | 23.8 ± 3.0 | 30.2 ± 2.5 | 6.4 ± 3.9 |
| 486 | 3093 ± 1 | 18 | 14.0 ± 1.0 | 5.1 ± 12.0 | 47.5 ± 11.8 | 23.5 ± 10.6 | 25.1 ± 6.8 | 8.9 ± 12.0 | 9.6 ± 10.7 | 18.4 ± 16.0 |
| 520 | 6607 ± 4 | 7 | 170.0 ± 0.0 | 24.1 ± 10.2 | 20.2 ± 5.7 | 20.4 ± 9.0 | 18.6 ± 10.1 | 34.1 ± 10.2 | 30.4 ± 9.0 | 3.6 ± 13.6 |
| 577 | 6591 ± 4 | 10 | 2.8 ± 0.9 | 33.7 ± 5.7 | 14.9 ± 4.1 | 27.1 ± 6.8 | 17.4 ± 5.8 | 30.9 ± 5.8 | 24.3 ± 6.9 | 6.6 ± 8.9 |
| 589 | – | – | – | – | – | – | – | – | – | – |
| 593 | 8218 ± 2 | 20 | 48.0 ± 0.8 | 47.9 ± 2.4 | 12.2 ± 2.6 | 49.8 ± 3.1 | 17.7 ± 3.6 | 0.1 ± 2.5 | 1.8 ± 3.2 | 1.9 ± 3.9 |
| 633 | 2940 ± 1 | 12 | 88.8 ± 2.3 | 98.5 ± 7.9 | 25.8 ± 7.4 | 103.9 ± 5.2 | 12.1 ± 4.3 | 9.8 ± 8.2 | 15.1 ± 5.7 | 5.4 ± 9.4 |
| 634 | 2916 ± 4 | 20 | 91.3 ± 0.7 | 70.9 ± 2.6 | 10.0 ± 2.3 | 55.9 ± 3.2 | 9.5 ± 1.8 | 20.4 ± 2.7 | 35.4 ± 3.2 | 15.1 ± 4.1 |
| 663 | 6901 ± 6 | 20 | 108.3 ± 0.3 | 106.4 ± 2.1 | 7.7 ± 2.3 | 104.8 ± 2.1 | 6.2 ± 1.6 | 2.0 ± 2.1 | 3.6 ± 2.1 | 1.6 ± 3.0 |
| 676 | 2964 ± 2 | 6 | 65.6 ± 0.7 | 80.5 ± 12.8 | 22.2 ± 12.0 | 101.9 ± 13.8 | 21.1 ± 13.9 | 14.9 ± 12.8 | 36.3 ± 13.8 | 21.4 ± 18.8 |
| 680 | – | – | – | – | – | – | – | – * | – * | – * |
| 740 | 3866 ± 3 | 20 | 2.2 ± 2.7 | 64.4 ± 4.6 | 17.7 ± 3.5 | 64.7 ± 4.9 | 18.7 ± 3.7 | 62.2 ± 5.3 | 62.4 ± 5.6 | 0.2 ± 6.7 |
| 746 | 3403 ± 2 | 10 | 26.6 ± 0.3 | 35.5 ± 3.7 | 11.5 ± 3.2 | 27.7 ± 3.4 | 7.8 ± 3.0 | 8.9 ± 3.7 | 1.0 ± 3.4 | 7.8 ± 5.0 |
| 758 | – | – | – | – | – | – | – | – | – | – |
| 767 | – | – | – | – | – | – | – | – | – | – |
| 769 | 3248 ± 2 | 20 | 101.9 ± 1.0 | 128.9 ± 4.6 | 24.5 ± 4.0 | 138.0 ± 6.3 | 26.9 ± 5.2 | 27.1 ± 4.7 | 36.2 ± 6.4 | 9.1 ± 7.8 |
| 770 | 5461 ± 6 | 12 | 30.6 ± 0.6 | 40.3 ± 5.1 | 14.3 ± 3.6 | 34.1 ± 6.8 | 17.2 ± 3.6 | 9.7 ± 5.1 | 3.6 ± 6.8 | 6.2 ± 8.4 |
| 778 | 5459 ± 1 | 15 | 65.8 ± 0.8 | 63.0 ± 4.6 | 15.7 ± 2.8 | 70.1 ± 3.4 | 17.4 ± 4.1 | 2.9 ± 4.6 | 4.3 ± 3.5 | 7.2 ± 5.7 |
| 780 | 4024 ± 3 | 17 | 112.0 ± 0.3 | 107.9 ± 3.1 | 10.2 ± 2.4 | 113.9 ± 4.4 | 11.6 ± 2.1 | 4.2 ± 3.2 | 1.9 ± 4.4 | 6.1 ± 5.4 |
| 781 | – | – | – | – | – | – | – | – * | – * | – * |
| 785 | – | – | – | – | – | – | – | – | – | – |
| 795 | 2629 ± 2 | 15 | 163.9 ± 0.7 | 158.0 ± 3.4 | 7.7 ± 1.9 | 157.3 ± 4.9 | 12.5 ± 2.5 | 6.0 ± 3.5 | 6.6 ± 5.0 | 0.6 ± 6.0 |
| 796 | 5584 ± 7 | 15 | 2.0 ± 0.6 | 170.7 ± 3.3 | 9.5 ± 2.7 | 179.6 ± 3.0 | 9.0 ± 3.9 | 11.3 ± 3.4 | 2.4 ± 3.0 | 8.9 ± 4.5 |
| 797 | 5577 ± 2 | 15 | 121.4 ± 0.4 | 130.6 ± 3.7 | 11.5 ± 2.9 | 125.9 ± 6.9 | 19.2 ± 4.5 | 9.2 ± 3.7 | 4.5 ± 6.9 | 4.7 ± 7.8 |
| 801 | 2010 ± 1 | 11 | 31.2 ± 1.6 | 63.1 ± 9.6 | 32.5 ± 18.0 | 55.7 ± 17.1 | 58.2 ± 18.0 | 31.8 ± 9.7 | 24.4 ± 17.2 | 7.4 ± 19.6 |
| 802 | 5433 ± 2 | 11 | 178.2 ± 2.5 | 34.2 ± 11.9 | 37.1 ± 9.0 | 38.9 ± 19.1 | 35.7 ± 11.3 | 36.0 ± 12.2 | 40.7 ± 19.2 | 4.7 ± 22.5 |
| 803 | 1823 ± 0 | 27 | 96.6 ± 0.9 | 34.2 ± 4.7 | 29.4 ± 5.2 | 62.1 ± 18.6 | 65.6 ± 40.9 | 62.4 ± 4.8 | 34.5 ± 18.6 | 27.9 ± 19.2 |
| 806 | 4483 ± 1 | 12 | 92.1 ± 0.3 | 89.3 ± 3.9 | 17.8 ± 7.5 | 85.8 ± 6.4 | 21.1 ± 6.5 | 2.8 ± 3.9 | 6.3 ± 6.4 | 3.5 ± 7.5 |
| 807 | 5549 ± 1 | 20 | 154.5 ± 0.6 | 151.9 ± 3.0 | 17.9 ± 3.7 | 151.5 ± 3.4 | 14.9 ± 2.5 | 2.6 ± 3.0 | 3.0 ± 3.5 | 0.4 ± 4.5 |
| 816 | 4762 ± 2 | 12 | 149.9 ± 0.5 | 146.4 ± 3.1 | 10.0 ± 2.7 | 144.1 ± 6.6 | 17.5 ± 5.4 | 3.5 ± 3.2 | 5.7 ± 6.6 | 2.2 ± 7.3 |
| 822 | 6499 ± 2 | 15 | 132.4 ± 1.6 | 141.9 ± 6.1 | 30.2 ± 5.7 | 127.0 ± 6.7 | 23.0 ± 5.2 | 9.4 ± 6.3 | 5.5 ± 6.9 | 14.9 ± 9.0 |

(1) CALIFA id. (2) Systemic velocity derived from integrated the velocities in a 2.7″ aperture centred in the kinematic centre. (3) Radius used to average the polar coordinates of the positions from the lines of nodes (see Sec. 2.4.3 for details). (4) Morphological PA inferred by fitting an elipse to an isophote at radius r in the r-band SDSS image. (5) and (6) Kinematic PA and its standard deviation at radius r for the approaching side (see Sec. 2.4.3 for details). (7) and (8) Kinematic PA and its standard deviation at radius r for the receding side. (9) and (10) Morpho-kinematic misalignment for the receding and the approaching sides. (11) Kinematic misalignment between the receding and the approaching sides. The * symbol tag the objects where it is not posible to determine any kinematic property using our method (see Sec. 2.4.3 for details).

Table A.6: continue A.2

| id | $V_{sys}$ | r | $PA_{morph}$ (r) | PA approaching | | PA receding | | $\Psi_{morph-kin}$ | | $\Psi_{kin-kin}$ |
|---|---|---|---|---|---|---|---|---|---|---|
| | | | | $PA_{kin}$ | $\delta PA_{kin}$ | $PA_{kin}$ | $\delta PA_{kin}$ | approaching | receding | |
| | (km $s^{-1}$) | (arcsec) | (°) | (°) | (°) | (°) | (°) | (°) | (°) | (°) |
| (1) | (4) | (5) | (7) | (8) | (9) | (10) | (11) | (10) | (11) | (10) |
| 828 | – | – | – | – | – | – | – | – | – | – |
| 832 | 8699 ± 5 | 25 | 74.5 ± 0.5 | 72.6 ± 3.9 | 16.3 ± 2.9 | 70.4 ± 4.5 | 15.6 ± 2.1 | 1.9 ± 4.0 | 4.1 ± 4.6 | 2.2 ± 6.0 |
| 833 | 5931 ± 1 | 20 | 135.6 ± 0.9 | 21.2 ± 3.0 | 16.8 ± 4.2 | 11.4 ± 7.7 | 23.5 ± 5.1 | 65.6 ± 3.1 | 55.8 ± 7.7 | 9.8 ± 8.2 |
| 843 | – | – | – | – | – | – | – | – | – | – |
| 844 | 2837 ± 3 | 25 | 125.6 ± 0.3 | 128.5 ± 2.3 | 9.9 ± 1.4 | 128.7 ± 2.0 | 9.3 ± 1.5 | 2.9 ± 2.4 | 3.1 ± 2.0 | 0.2 ± 3.1 |
| 846 | – | – | – | – | – | – | – | – | – | – |
| 850 | 6551 ± 1 | 20 | 173.1 ± 0.7 | 173.8 ± 3.5 | 19.8 ± 3.4 | 174.4 ± 2.5 | 11.8 ± 3.7 | 0.7 ± 3.5 | 1.3 ± 2.6 | 0.6 ± 4.3 |
| 852 | – | – | – | – | – | – | – | – | – | – |
| 858 | 7651 ± 6 | 12 | 177.9 ± 0.6 | 171.2 ± 3.3 | 10.1 ± 3.2 | 2.0 ± 2.2 | 8.0 ± 4.6 | 6.6 ± 3.3 | 4.1 ± 2.3 | 10.7 ± 4.0 |
| 860 | 3253 ± 1 | 25 | 35.9 ± 0.3 | 37.5 ± 1.3 | 7.2 ± 1.2 | 34.2 ± 1.3 | 5.9 ± 1.3 | 1.7 ± 1.4 | 1.7 ± 1.4 | 3.3 ± 1.9 |
| 871 | 5923 ± 6 | 20 | 128.4 ± 0.4 | 129.0 ± 2.3 | 10.1 ± 2.4 | 125.0 ± 2.8 | 9.5 ± 1.8 | 0.6 ± 2.3 | 3.4 ± 2.8 | 4.0 ± 3.6 |
| 873 | 7674 ± 7 | 10 | 15.2 ± 1.4 | 76.6 ± 8.3 | 16.4 ± 4.3 | 80.6 ± 6.7 | 16.9 ± 6.5 | 61.3 ± 8.4 | 65.3 ± 6.8 | 4.0 ± 10.7 |
| 874 | 4920 ± 6 | 25 | 49.0 ± 0.7 | 45.4 ± 1.7 | 14.5 ± 3.0 | 39.7 ± 3.4 | 14.5 ± 2.2 | 3.6 ± 1.9 | 9.3 ± 3.5 | 5.7 ± 3.8 |
| 877 | 6294 ± 9 | 13 | 38.5 ± 0.6 | 32.1 ± 4.6 | 17.5 ± 3.2 | 38.4 ± 3.7 | 8.7 ± 2.5 | 6.5 ± 4.7 | 0.2 ± 3.7 | 6.3 ± 5.9 |
| 882 | 7786 ± 2 | 13 | 149.7 ± 3.8 | 40.2 ± 4.3 | 16.6 ± 2.7 | 56.4 ± 2.9 | 9.9 ± 3.0 | 70.5 ± 5.7 | 86.7 ± 4.8 | 16.2 ± 5.2 |
| 883 | – | – | – | – | – | – | – | – * | – * | – * |
| 892 | 4910 ± 4 | 15 | 70.6 ± 0.5 | 69.4 ± 5.1 | 13.3 ± 2.7 | 71.2 ± 3.1 | 7.5 ± 2.3 | 1.3 ± 5.1 | 0.6 ± 3.1 | 1.9 ± 5.9 |
| 900 | – | – | – | – | – | – | – | – | – | – |
| 901 | 4651 ± 3 | 15 | 139.4 ± 1.3 | 15.5 ± 3.7 | 14.3 ± 3.4 | 172.0 ± 4.7 | 19.4 ± 5.1 | 56.1 ± 3.9 | 32.6 ± 4.9 | 23.5 ± 6.0 |
| 903 | 3579 ± 0 | 25 | 81.0 ± 0.3 | 92.1 ± 2.7 | 27.7 ± 5.0 | 79.8 ± 7.1 | 30.6 ± 6.2 | 11.1 ± 2.7 | 1.2 ± 7.1 | 12.3 ± 7.6 |
| 905 | – | – | – | – | – | – | – | – | – | – |
| 907 | 3476 ± 2 | 15 | 19.4 ± 0.6 | 23.2 ± 5.7 | 23.6 ± 7.5 | 23.1 ± 6.3 | 27.2 ± 7.3 | 3.8 ± 5.8 | 3.7 ± 6.3 | 0.1 ± 8.5 |
| 913 | 1632 ± 3 | 23 | 27.8 ± 1.2 | 33.4 ± 5.2 | 20.9 ± 4.0 | 38.9 ± 6.8 | 28.6 ± 4.8 | 5.6 ± 5.3 | 11.1 ± 6.9 | 5.5 ± 8.6 |
| 915 | 4227 ± 3 | 20 | 160.3 ± 3.2 | 169.3 ± 5.5 | 22.7 ± 4.2 | 174.1 ± 4.3 | 17.5 ± 5.1 | 9.0 ± 6.3 | 13.8 ± 5.3 | 4.8 ± 6.9 |
| 916 | 3856 ± 6 | 20 | 134.7 ± 0.2 | 133.9 ± 2.6 | 9.9 ± 1.9 | 134.3 ± 2.5 | 10.0 ± 1.8 | 0.9 ± 2.6 | 0.4 ± 2.5 | 0.4 ± 3.6 |
| 922 | 5222 ± 2 | 15 | 91.7 ± 0.7 | 93.1 ± 5.1 | 27.6 ± 10.0 | 90.9 ± 6.6 | 24.0 ± 7.4 | 1.4 ± 5.1 | 0.8 ± 6.7 | 2.2 ± 8.3 |
| 923 | 4065 ± 3 | 7 | 93.2 ± 0.7 | 108.0 ± 14.6 | 30.4 ± 15.6 | 107.1 ± 13.4 | 27.3 ± 12.2 | 14.8 ± 14.6 | 14.0 ± 13.5 | 0.9 ± 19.8 |
| 925 | 4018 ± 8 | 15 | 129.4 ± 11.7 | 139.3 ± 4.6 | 15.5 ± 3.3 | 147.2 ± 5.8 | 15.1 ± 2.7 | 9.9 ± 12.6 | 17.7 ± 13.1 | 7.8 ± 7.4 |
| 927 | 6704 ± 2 | 15 | 43.2 ± 0.7 | 74.8 ± 4.1 | 14.3 ± 2.8 | 67.6 ± 5.3 | 19.3 ± 3.8 | 31.5 ± 4.2 | 24.3 ± 5.3 | 7.2 ± 6.7 |
| 932 | 7747 ± 5 | 15 | 103.9 ± 0.2 | 105.2 ± 2.6 | 8.2 ± 3.0 | 106.8 ± 2.1 | 6.3 ± 1.7 | 1.3 ± 2.6 | 2.8 ± 2.1 | 1.5 ± 3.3 |
| 935 | – | – | – | – | – | – | – | – | – | – |
| 939 | 6483 ± 3 | 10 | 33.2 ± 0.8 | 164.7 ± 9.4 | 25.5 ± 5.5 | 150.6 ± 6.3 | 16.0 ± 5.0 | 48.5 ± 9.5 | 62.5 ± 6.4 | 14.0 ± 11.4 |
| 1014 | – | – | – | – | – | – | – | – | – | – |
| 1017 | 5428 ± 2 | 10 | 127.1 ± 8.9 | 121.4 ± 7.0 | 21.2 ± 6.7 | 121.1 ± 7.4 | 20.7 ± 8.6 | 5.7 ± 11.3 | 6.0 ± 11.6 | 0.3 ± 10.2 |
| 1022 | 4559 ± 7 | 5 | 10.0 ± 0.0 | 38.3 ± 8.8 | 16.6 ± 6.3 | 19.6 ± 13.4 | 12.8 ± 7.9 | 28.3 ± 8.8 | 9.6 ± 13.4 | 18.7 ± 16.0 |
| 1026 | – | – | – | – | – | – | – | – | – | – |
| 1042 | – | – | – | – | – | – | – | – | – | – |
| 1044 | 4067 ± 3 | 15 | 169.9 ± 1.2 | 136.7 ± 5.4 | 16.2 ± 3.5 | 137.3 ± 5.5 | 18.3 ± 4.1 | 33.2 ± 5.5 | 32.6 ± 5.6 | 0.6 ± 7.7 |
| 1340 | 6145 ± 1 | 7 | 140.0 ± 0.0 | 81.9 ± 7.2 | 17.5 ± 6.9 | 113.2 ± 7.7 | 17.1 ± 8.6 | 58.1 ± 7.2 | 26.8 ± 7.7 | 31.2 ± 10.5 |
| 1360 | 7044 ± 1 | 7 | 10.0 ± 0.0 | 58.4 ± 9.5 | 16.3 ± 5.4 | 49.3 ± 10.0 | 18.9 ± 7.8 | 48.4 ± 9.5 | 39.3 ± 10.0 | 9.1 ± 13.8 |
| 1520 | 6534 ± 1 | 7 | 125.0 ± 0.0 | 80.6 ± 13.1 | 28.7 ± 8.5 | 81.7 ± 14.7 | 26.5 ± 11.9 | 44.4 ± 13.1 | 43.3 ± 14.7 | 1.1 ± 19.7 |
| 1589 | 6262 ± 1 | 7 | – | 96.5 ± 11.1 | 30.4 ± 13.1 | 89.7 ± 12.6 | 27.3 ± 17.7 | 90.5 ± 11.1 | 83.7 ± 12.6 | 6.8 ± 16.8 |
| 1663 | – | – | – | – | – | – | – | – | – | – |
| 1740 | – | – | – | – | – | – | – | – * | – * | – * |
| 1780 | 4195 ± 3 | 14 | 109.1 ± 7.1 | 3.1 ± 3.9 | 16.8 ± 5.3 | 174.3 ± 5.9 | 17.8 ± 4.7 | 74.0 ± 8.1 | 65.3 ± 8.1 | 8.7 ± 5.5 |
| 1781 | 8508 ± 4 | 12 | 43.6 ± 1.0 | 20.7 ± 12.9 | 42.0 ± 10.2 | 19.1 ± 6.4 | 12.8 ± 5.0 | 22.9 ± 12.9 | 24.5 ± 6.5 | 1.6 ± 14.4 |
| 1795 | 2505 ± 2 | 10 | 45.2 ± 4.2 | 59.0 ± 9.0 | 21.2 ± 6.5 | 46.0 ± 8.1 | 23.7 ± 5.0 | 13.7 ± 9.9 | 0.7 ± 9.1 | 13.0 ± 12.1 |
| 1796 | 5362 ± 8 | 10 | 26.5 ± 0.6 | 29.8 ± 3.6 | 9.5 ± 3.1 | 23.2 ± 4.0 | 9.5 ± 3.8 | 3.3 ± 3.6 | 3.3 ± 4.0 | 6.6 ± 5.4 |
| 1801 | 1944 ± 4 | 20 | 1.7 ± 0.9 | 8.4 ± 4.2 | 11.5 ± 2.4 | 165.9 ± 4.6 | 23.3 ± 10.5 | 6.7 ± 4.3 | 15.8 ± 4.7 | 22.4 ± 6.2 |
| 1871 | 6072 ± 3 | 20 | 139.0 ± 0.0 | 164.7 ± 3.6 | 32.1 ± 4.1 | 156.0 ± 3.0 | 11.8 ± 2.3 | 25.7 ± 3.6 | 17.0 ± 3.0 | 8.7 ± 4.7 |
| 1873 | 7806 ± 6 | 8 | 55.8 ± 10.3 | 135.9 ± 20.6 | 66.1 ± 17.4 | 143.0 ± 21.4 | 27.8 ± 12.5 | 80.2 ± 23.0 | 87.2 ± 23.8 | 7.0 ± 29.7 |

Table A.7: Ionised Gas Kinematic properties of the interacting sample selected for this study included in the CALIFA survey.

| id | $V_{sys}$ | r | $PA_{morph}$ (r) | PA approaching | | PA receding | | $\Psi_{morph-kin}$ | | $\Psi_{kin-kin}$ |
|---|---|---|---|---|---|---|---|---|---|---|
| | | | | $PA_{kin}$ | $\delta PA_{kin}$ | $PA_{kin}$ | $\delta PA_{kin}$ | approaching | receding | |
| | (km $s^{-1}$) | (arcsec) | (°) | (°) | (°) | (°) | (°) | (°) | (°) | (°) |
| (1) | (4) | (5) | (7) | (8) | (9) | (10) | (11) | (10) | (11) | (10) |
| 14 | 4323 ± 0 | 30 | 9.5 ± 0.9 | 38.4 ± 0.7 | 23.8 ± 1.6 | 36.2 ± 1.5 | 13.2 ± 2.9 | 28.9 ± 1.1 | 26.7 ± 1.7 | 2.2 ± 1.6 |
| 17 | 5402 ± 4 | 5 | 148.8 ± 0.5 | 87.7 ± 15.3 | 26.1 ± 13.1 | 96.6 ± 22.5 | 36.7 ± 18.4 | 61.1 ± 15.3 | 52.2 ± 22.5 | 8.9 ± 27.2 |
| 22 | 4552 ± 8 | 25 | 87.5 ± 0.5 | 79.0 ± 1.4 | 7.4 ± 1.4 | 79.1 ± 4.4 | 22.6 ± 2.4 | 8.5 ± 1.5 | 8.4 ± 4.5 | 0.1 ± 4.7 |
| 26 | 4185 ± 0 | 25 | 164.0 ± 0.2 | 173.6 ± 1.0 | 5.7 ± 0.7 | 1.8 ± 1.8 | 12.1 ± 1.4 | 9.6 ± 1.1 | 17.8 ± 1.8 | 8.2 ± 2.1 |
| 39 | 4811 ± 1 | 27 | 160.2 ± 0.3 | 158.4 ± 2.0 | 10.1 ± 2.2 | 159.4 ± 1.7 | 5.8 ± 1.1 | 1.8 ± 2.0 | 0.8 ± 1.7 | 1.0 ± 2.6 |
| 42 | 5860 ± 8 | 15 | 115.5 ± 1.3 | 133.1 ± 3.3 | 12.3 ± 3.5 | 144.1 ± 3.7 | 11.1 ± 2.8 | 17.6 ± 3.5 | 28.6 ± 3.9 | 11.0 ± 5.0 |
| 44 | – | – | – | – | – | – | – | – | – | – |
| 119 | 4906 ± 8 | 10 | 70.3 ± 1.2 | 85.8 ± 4.9 | 15.7 ± 6.1 | 82.9 ± 11.9 | 35.8 ± 12.6 | 15.5 ± 5.0 | 12.6 ± 12.0 | 2.9 ± 12.9 |
| 127 | 6564 ± 3 | 17 | 35.6 ± 2.3 | 52.0 ± 12.0 | 35.4 ± 11.8 | 39.0 ± 6.4 | 60.3 ± 10.0 | 16.4 ± 12.2 | 3.4 ± 6.8 | 13.0 ± 13.6 |
| 155 | 4689 ± 9 | 22 | 109.2 ± 0.8 | 80.3 ± 3.3 | 9.8 ± 2.3 | 76.4 ± 3.2 | 19.7 ± 3.4 | 28.9 ± 3.4 | 32.8 ± 3.3 | 3.9 ± 4.6 |
| 156 | 4883 ± 8 | 25 | 127.7 ± 0.2 | 133.3 ± 1.8 | 7.2 ± 1.4 | 133.5 ± 2.1 | 7.2 ± 1.2 | 5.6 ± 1.8 | 5.8 ± 2.1 | 0.2 ± 2.8 |
| 165 | 5162 ± 3 | 22 | 23.4 ± 0.8 | 30.6 ± 1.0 | 4.1 ± 0.6 | 32.3 ± 0.8 | 3.8 ± 0.5 | 7.2 ± 1.3 | 8.9 ± 1.2 | 1.7 ± 1.3 |
| 186 | 4266 ± 1 | 20 | 149.0 ± 0.6 | 149.8 ± 1.3 | 11.1 ± 3.4 | 148.2 ± 1.0 | 4.9 ± 1.0 | 0.8 ± 1.4 | 0.9 ± 1.2 | 1.7 ± 1.7 |
| 213 | 5528 ± 10 | 7 | 81.3 ± 1.6 | 83.1 ± 5.9 | 15.6 ± 7.3 | 115.1 ± 11.4 | 20.7 ± 9.0 | 1.9 ± 6.1 | 33.8 ± 11.5 | 32.0 ± 12.9 |
| 274 | 2062 ± 1 | 12 | 169.8 ± 0.7 | 12.0 ± 7.0 | 16.8 ± 4.2 | 11.3 ± 3.4 | 10.3 ± 4.5 | 22.2 ± 7.0 | 21.5 ± 3.5 | 0.7 ± 4.7 |
| 311 | 6173 ± 3 | 20 | 132.2 ± 2.4 | 153.7 ± 8.1 | 40.2 ± 5.0 | 132.8 ± 5.4 | 27.2 ± 5.3 | 21.5 ± 8.5 | 0.6 ± 5.9 | 20.9 ± 9.8 |
| 314 | 6279 ± 3 | 20 | 59.4 ± 0.8 | 66.6 ± 2.0 | 7.4 ± 1.9 | 67.1 ± 2.4 | 9.9 ± 2.3 | 7.2 ± 2.1 | 7.7 ± 2.5 | 0.5 ± 3.1 |
| 340 | 6143 ± 4 | 12 | 153.2 ± 0.8 | 18.2 ± 8.8 | 41.7 ± 14.1 | 21.1 ± 19.0 | 55.8 ± 13.3 | 45.0 ± 8.8 | 47.9 ± 19.0 | 2.9 ± 20.9 |
| 360 | – | – | – | – | – | – | – | – | – | – |
| 475 | 3165 ± 1 | 22 | 31.1 ± 0.5 | 40.5 ± 3.0 | 12.6 ± 2.0 | 56.0 ± 5.6 | 25.3 ± 2.5 | 9.4 ± 3.0 | 24.9 ± 5.6 | 15.5 ± 6.4 |
| 479 | 6589 ± 10 | 22 | 146.0 ± 0.4 | 163.4 ± 2.3 | 36.4 ± 9.8 | 158.2 ± 5.0 | 31.4 ± 3.9 | 17.4 ± 2.3 | 12.2 ± 5.0 | 5.2 ± 5.5 |
| 486 | 3077 ± 1 | 18 | 14.0 ± 1.0 | 9.9 ± 2.6 | 12.6 ± 3.0 | 13.5 ± 3.1 | 15.1 ± 2.2 | 4.0 ± 2.8 | 0.4 ± 3.2 | 3.6 ± 4.0 |
| 520 | 6627 ± 0 | 7 | 170.0 ± 0.0 | 44.5 ± 4.0 | 12.3 ± 6.2 | 37.4 ± 10.5 | 17.8 ± 5.1 | 54.5 ± 4.0 | 47.4 ± 10.5 | 7.1 ± 11.2 |
| 577 | 6588 ± 1 | 10 | 2.8 ± 0.9 | 32.0 ± 2.7 | 8.1 ± 1.2 | 24.1 ± 3.3 | 24.8 ± 4.2 | 29.2 ± 2.9 | 21.3 ± 3.4 | 7.9 ± 4.3 |
| 589 | – | – | – | – | – | – | – | – | – | – |
| 593 | 8291 ± 0 | 20 | 48.0 ± 0.8 | 52.8 ± 0.6 | 6.8 ± 0.9 | 51.2 ± 0.9 | 8.5 ± 0.5 | 4.7 ± 1.0 | 3.1 ± 1.2 | 1.6 ± 1.1 |
| 633 | 2920 ± 9 | 12 | 88.8 ± 2.3 | 22.5 ± 11.5 | 24.1 ± 4.4 | 63.8 ± 6.5 | 38.5 ± 12.4 | 66.2 ± 11.7 | 25.0 ± 6.9 | 41.3 ± 13.2 |
| 634 | 2876 ± 4 | 20 | 91.3 ± 0.7 | 60.3 ± 1.8 | 8.1 ± 2.2 | 55.1 ± 2.5 | 12.6 ± 2.1 | 31.0 ± 1.9 | 36.3 ± 2.6 | 5.3 ± 3.1 |
| 663 | 6937 ± 2 | 20 | 108.3 ± 0.3 | 104.5 ± 1.1 | 4.4 ± 1.0 | 106.7 ± 1.2 | 4.1 ± 0.8 | 3.9 ± 1.2 | 1.7 ± 1.2 | 2.2 ± 1.6 |
| 676 | 2964 ± 3 | 6 | 65.6 ± 0.7 | 107.5 ± 7.4 | 15.4 ± 7.4 | 93.3 ± 18.7 | 31.8 ± 11.7 | 42.0 ± 7.5 | 27.7 ± 18.8 | 14.3 ± 20.2 |
| 680 | 3438 ± 1 | 20 | 29.5 ± 1.3 | 24.0 ± 9.4 | 37.6 ± 6.2 | 19.8 ± 15.5 | 42.5 ± 6.8 | 5.5 ± 9.5 | 9.7 ± 15.5 | 4.2 ± 18.1 |
| 740 | 3852 ± 2 | 20 | 2.2 ± 2.7 | 74.5 ± 5.6 | 36.8 ± 10.3 | 81.0 ± 6.6 | 30.1 ± 3.7 | 72.3 ± 6.2 | 78.8 ± 7.1 | 6.5 ± 8.6 |
| 746 | 3388 ± 12 | 10 | 26.6 ± 0.3 | 126.2 ± 4.6 | 19.6 ± 8.5 | 125.7 ± 4.6 | 14.3 ± 5.2 | 80.4 ± 4.7 | 80.9 ± 4.6 | 0.5 ± 6.5 |
| 758 | 2281 ± 0 | 20 | 120.1 ± 0.4 | 142.9 ± 1.2 | 8.0 ± 1.3 | 129.0 ± 1.1 | 6.0 ± 1.9 | 22.8 ± 1.2 | 8.9 ± 1.2 | 13.9 ± 1.6 |
| 767 | 2531 ± 0 | 25 | 115.2 ± 0.3 | 109.4 ± 1.3 | 9.6 ± 1.5 | 111.4 ± 1.2 | 6.9 ± 1.9 | 5.8 ± 1.3 | 3.8 ± 1.2 | 2.0 ± 1.8 |
| 769 | 3246 ± 0 | 20 | 101.9 ± 1.0 | 128.3 ± 2.5 | 13.8 ± 3.2 | 129.5 ± 3.4 | 10.8 ± 1.4 | 26.4 ± 2.7 | 27.7 ± 3.5 | 1.3 ± 4.2 |
| 770 | 5505 ± 2 | 12 | 30.6 ± 0.6 | 145.4 ± 3.1 | 33.0 ± 9.5 | 90.7 ± 6.2 | 20.2 ± 4.0 | 65.2 ± 3.2 | 60.1 ± 6.2 | 54.7 ± 6.9 |
| 778 | 5500 ± 3 | 15 | 65.8 ± 0.8 | 70.9 ± 1.7 | 7.1 ± 1.4 | 74.7 ± 1.7 | 5.5 ± 1.2 | 5.1 ± 1.9 | 8.9 ± 1.8 | 3.8 ± 2.4 |
| 780 | – | – | – | – | – | – | – | – | – | – |
| 781 | – | – | – | – | – | – | – | – | – | – |
| 785 | 8404 ± 5 | 7 | 105.5 ± 0.0 | 116.2 ± 16.0 | 32.5 ± 10.8 | 126.2 ± 7.9 | 14.0 ± 4.5 | 10.7 ± 16.0 | 20.7 ± 7.9 | 10.0 ± 17.8 |
| 795 | 2643 ± 0 | 15 | 163.9 ± 0.7 | 161.9 ± 4.6 | 13.6 ± 3.3 | 148.7 ± 1.0 | 4.3 ± 0.8 | 2.1 ± 4.6 | 15.2 ± 1.3 | 13.1 ± 4.7 |
| 796 | 5627 ± 2 | 15 | 2.0 ± 0.6 | 6.0 ± 1.2 | 8.0 ± 1.6 | 2.6 ± 2.0 | 7.0 ± 4.0 | 4.0 ± 1.3 | 0.6 ± 2.1 | 3.4 ± 2.3 |
| 797 | 5592 ± 1 | 15 | 121.4 ± 0.4 | 121.7 ± 2.0 | 9.7 ± 3.4 | 138.8 ± 2.8 | 9.6 ± 1.9 | 0.3 ± 2.0 | 17.4 ± 2.8 | 17.1 ± 3.4 |
| 801 | 2020 ± 0 | 11 | 31.2 ± 1.6 | 56.2 ± 2.6 | 13.3 ± 1.2 | 41.9 ± 0.5 | 8.1 ± 0.4 | 25.0 ± 3.0 | 10.6 ± 1.6 | 14.4 ± 2.6 |
| 802 | 5435 ± 12 | 11 | 178.2 ± 2.5 | 31.3 ± 16.2 | 57.1 ± 10.2 | 21.4 ± 3.3 | 10.5 ± 3.2 | 33.1 ± 16.4 | 23.2 ± 4.2 | 9.9 ± 16.5 |
| 803 | 1791 ± 1 | 27 | 96.6 ± 0.9 | 33.6 ± 6.2 | 41.2 ± 5.8 | 43.2 ± 12.5 | 34.9 ± 6.2 | 63.0 ± 6.3 | 53.4 ± 12.5 | 9.6 ± 13.9 |
| 806 | 4501 ± 3 | 12 | 92.1 ± 0.3 | 21.3 ± 4.8 | 15.1 ± 3.6 | 16.7 ± 4.5 | 12.3 ± 3.6 | 70.8 ± 4.8 | 75.4 ± 4.5 | 4.6 ± 6.6 |
| 807 | 5561 ± 2 | 20 | 154.5 ± 0.6 | 144.5 ± 3.8 | 16.9 ± 2.7 | 150.9 ± 2.7 | 14.9 ± 3.6 | 9.9 ± 3.9 | 3.6 ± 2.8 | 6.4 ± 4.7 |
| 816 | 4780 ± 4 | 12 | 149.9 ± 0.5 | 141.8 ± 4.1 | 14.3 ± 3.1 | 146.4 ± 4.6 | 16.6 ± 3.6 | 8.1 ± 4.1 | 3.5 ± 4.6 | 4.6 ± 6.1 |
| 822 | 6520 ± 1 | 15 | 132.4 ± 1.6 | 120.3 ± 2.7 | 11.3 ± 1.1 | 129.4 ± 1.5 | 6.0 ± 1.2 | 12.1 ± 3.1 | 3.1 ± 2.2 | 9.1 ± 3.1 |

(1) CALIFA id. (2) Systemic velocity derived from integrated the velocities in a 2.7″ aperture centred in the kinematic centre. (3) Radius used to average the polar coordinates of the positions from the lines of nodes (see Sec. 2.4.3 for details). (4) Morphological PA inferred by fitting an elipse to an isophote at radius r in the r-band SDSS image. (5) and (6) Kinematic PA and its standard deviation at radius r for the approaching side (see Sec. 2.4.3 for details). (7) and (8) Kinematic PA and its standard deviation at radius r for the receding side. (9) and (10) Morpho-kinematic misalignments for the receding and approaching sides, respectively. (11) Kinematic misalignment between the receding and the approaching sides. The * symbol tag the objects where it is not posible to determine any kinematic property using our method (see Sec. 2.4.3 for details).

Table A.7: continue A.3

| id | $V_{sys}$ | r | $PA_{morph}$ (r) | PA approaching | | PA receding | | $\Psi_{morph-kin}$ | | $\Psi_{kin-kin}$ |
|---|---|---|---|---|---|---|---|---|---|---|
| | | | | $PA_{kin}$ | $\delta PA_{kin}$ | $PA_{kin}$ | $\delta PA_{kin}$ | approaching | receding | |
| | (km $s^{-1}$) | (arcsec) | (°) | (°) | (°) | (°) | (°) | (°) | (°) | (°) |
| (1) | (4) | (5) | (7) | (8) | (9) | (10) | (11) | (10) | (11) | (10) |
| 828 | 4464 ± 0 | 22 | 137.3 ± 0.4 | 147.2 ± 1.1 | 9.6 ± 4.2 | 160.8 ± 1.4 | 13.0 ± 1.9 | 9.9 ± 1.2 | 23.6 ± 1.4 | 13.7 ± 1.8 |
| 832 | – | – | – | – | – | – | – | – | – | – |
| 833 | 5952 ± 5 | 20 | 135.6 ± 0.9 | 29.5 ± 4.4 | 29.3 ± 7.7 | 31.6 ± 7.5 | 25.9 ± 6.4 | 73.9 ± 4.5 | 76.1 ± 7.6 | 2.2 ± 8.7 |
| 843 | – | – | – | – | – | – | – | – * | – * | – * |
| 844 | – | – | – | – | – | – | – | – | – | – |
| 846 | 8258 ± 14 | 8 | 105.2 ± 0.6 | 12.6 ± 8.7 | 14.3 ± 6.7 | 2.9 ± 8.5 | 17.4 ± 7.3 | 87.4 ± 8.7 | 77.6 ± 8.5 | 9.8 ± 12.1 |
| 850 | 6564 ± 4 | 20 | 173.1 ± 0.7 | 176.2 ± 2.6 | 7.0 ± 1.6 | 170.5 ± 1.5 | 6.2 ± 1.4 | 3.1 ± 2.7 | 2.7 ± 1.6 | 5.8 ± 3.0 |
| 852 | 3066 ± 3 | 12 | 99.4 ± 0.6 | 155.1 ± 7.5 | 16.7 ± 6.9 | 166.1 ± 8.9 | 25.9 ± 7.2 | 55.6 ± 7.5 | 66.7 ± 8.9 | 11.1 ± 11.6 |
| 858 | 7741 ± 19 | 12 | 177.9 ± 0.6 | 180.0 ± 0.0 | 6.5 ± 1.9 | 174.3 ± 3.5 | 12.0 ± 5.8 | 2.2 ± 0.6 | 3.5 ± 3.5 | 5.7 ± 3.5 |
| 860 | – | – | – | – | – | – | – | – | – | – |
| 871 | 5944 ± 3 | 20 | 128.4 ± 0.4 | 126.8 ± 1.1 | 5.7 ± 1.1 | 130.3 ± 1.6 | 7.0 ± 1.3 | 1.7 ± 1.1 | 1.8 ± 1.6 | 3.5 ± 1.9 |
| 873 | 7720 ± 3 | 10 | 15.2 ± 1.4 | 66.6 ± 5.4 | 22.0 ± 5.3 | 69.9 ± 4.0 | 9.6 ± 2.8 | 51.4 ± 5.5 | 54.7 ± 4.2 | 3.3 ± 6.7 |
| 874 | 4901 ± 9 | 25 | 49.0 ± 0.7 | 43.6 ± 2.4 | 18.0 ± 1.9 | 49.6 ± 2.5 | 13.8 ± 1.1 | 5.4 ± 2.5 | 0.6 ± 2.6 | 6.1 ± 3.5 |
| 877 | 6281 ± 0 | 13 | 38.5 ± 0.6 | 36.6 ± 2.0 | 13.4 ± 4.8 | 43.1 ± 0.5 | 9.7 ± 1.9 | 1.9 ± 2.1 | 4.6 ± 0.8 | 6.5 ± 2.1 |
| 882 | – | – | – | – | – | – | – | – | – | – |
| 883 | – | – | – | – | – | – | – | – | – | – |
| 892 | 4920 ± 2 | 15 | 70.6 ± 0.5 | 69.7 ± 2.5 | 7.0 ± 2.2 | 67.3 ± 2.2 | 6.0 ± 1.8 | 0.9 ± 2.6 | 3.4 ± 2.2 | 2.4 ± 3.3 |
| 900 | 5048 ± 7 | 5 | 166.9 ± 2.8 | 68.5 ± 12.8 | 20.2 ± 10.1 | 64.6 ± 14.5 | 19.5 ± 11.0 | 81.6 ± 13.1 | 77.7 ± 14.7 | 4.0 ± 19.3 |
| 901 | 4651 ± 0 | 15 | 139.4 ± 1.3 | 7.0 ± 2.7 | 14.7 ± 2.4 | 7.2 ± 1.0 | 8.4 ± 3.1 | 47.6 ± 3.0 | 47.8 ± 1.6 | 0.2 ± 2.9 |
| 903 | – | – | – | – | – | – | – | – | – | – |
| 905 | – | – | – | – | – | – | – | – | – | – |
| 907 | 3478 ± 1 | 15 | 19.4 ± 0.6 | 17.4 ± 3.2 | 12.4 ± 3.6 | 21.5 ± 3.5 | 11.7 ± 4.8 | 2.0 ± 3.2 | 2.1 ± 3.6 | 4.1 ± 4.7 |
| 913 | 1612 ± 0 | 23 | 27.8 ± 1.2 | 38.2 ± 2.5 | 20.7 ± 2.0 | 71.1 ± 0.5 | 37.1 ± 1.0 | 10.3 ± 2.8 | 43.3 ± 1.3 | 33.0 ± 2.6 |
| 915 | 4259 ± 2 | 20 | 160.3 ± 3.2 | 164.6 ± 2.0 | 5.5 ± 1.2 | 177.6 ± 3.0 | 10.9 ± 2.1 | 4.3 ± 3.7 | 17.4 ± 4.4 | 13.1 ± 3.6 |
| 916 | – | – | – | – | – | – | – | – | – | – |
| 922 | 5212 ± 1 | 15 | 91.7 ± 0.7 | 118.2 ± 3.0 | 11.9 ± 1.4 | 109.0 ± 1.9 | 10.8 ± 1.3 | 26.5 ± 3.1 | 17.4 ± 2.0 | 9.1 ± 3.6 |
| 923 | – | – | – | – | – | – | – | – | – | – |
| 925 | 4021 ± 11 | 15 | 129.4 ± 11.7 | 139.4 ± 2.0 | 6.7 ± 1.5 | 142.6 ± 2.2 | 7.3 ± 2.0 | 10.0 ± 11.9 | 13.2 ± 11.9 | 3.3 ± 2.9 |
| 927 | 6722 ± 0 | 15 | 43.2 ± 0.7 | 45.9 ± 2.1 | 20.3 ± 1.8 | 47.9 ± 2.3 | 12.6 ± 5.1 | 2.7 ± 2.2 | 4.6 ± 2.4 | 1.9 ± 3.1 |
| 932 | – | – | – | – | – | – | – | – | – | – |
| 935 | 4674 ± 2 | 25 | 80.4 ± 0.4 | 99.0 ± 3.6 | 17.9 ± 5.6 | 104.3 ± 4.1 | 17.7 ± 2.7 | 18.6 ± 3.6 | 24.0 ± 4.1 | 5.4 ± 5.4 |
| 939 | 6540 ± 2 | 10 | 33.2 ± 0.8 | 154.8 ± 5.8 | 20.4 ± 4.5 | 165.1 ± 7.2 | 17.1 ± 4.1 | 58.3 ± 5.9 | 48.1 ± 7.3 | 10.2 ± 9.3 |
| 1014 | 4332 ± 2 | 12 | 12.6 ± 6.1 | 177.7 ± 5.8 | 14.7 ± 2.7 | 159.6 ± 10.3 | 19.9 ± 6.8 | 15.0 ± 8.4 | 33.1 ± 12.0 | 18.1 ± 11.8 |
| 1017 | – | – | – | – | – | – | – | – | – | – |
| 1022 | 4605 ± 3 | 5 | 10.0 ± 0.0 | 57.7 ± 20.5 | 33.3 ± 11.5 | 59.3 ± 24.2 | 35.3 ± 23.8 | 47.7 ± 20.5 | 49.3 ± 24.2 | 1.6 ± 31.7 |
| 1026 | 4092 ± 1 | 15 | 68.0 ± 9.6 | 29.3 ± 23.1 | 56.4 ± 9.3 | 75.7 ± 10.7 | 29.1 ± 5.9 | 38.8 ± 25.1 | 7.6 ± 14.4 | 46.4 ± 25.5 |
| 1042 | 5927 ± 3 | 17 | 21.1 ± 1.8 | 20.2 ± 2.8 | 9.4 ± 2.0 | 25.9 ± 4.0 | 15.4 ± 3.4 | 0.9 ± 3.4 | 4.8 ± 4.4 | 5.7 ± 4.9 |
| 1044 | – | – | – | – | – | – | – | – | – | – |
| 1340 | – | – | – | – | – | – | – | – * | – * | – * |
| 1360 | – | – | – | – | – | – | – | – | – | – |
| 1520 | 6567 ± 3 | 7 | 125.0 ± 0.0 | 104.9 ± 11.2 | 27.4 ± 12.3 | 57.7 ± 15.5 | 32.0 ± 16.2 | 20.1 ± 11.2 | 67.3 ± 15.5 | 47.2 ± 19.1 |
| 1589 | – | – | – | – | – | – | – | – | – | – |
| 1663 | 7377 ± 0 | 15 | 107.5 ± 4.2 | 99.0 ± 9.5 | 44.3 ± 10.2 | 113.8 ± 7.7 | 28.9 ± 12.3 | 8.5 ± 10.4 | 6.3 ± 8.8 | 14.8 ± 12.2 |
| 1740 | – | – | – | – | – | – | – | – * | – * | – * |
| 1780 | – | – | – | – | – | – | – | – | – | – |
| 1781 | 8626 ± 2 | 12 | 43.6 ± 1.0 | 0.9 ± 16.5 | 49.2 ± 10.6 | 18.4 ± 20.1 | 55.8 ± 23.3 | 42.7 ± 16.5 | 25.2 ± 20.1 | 17.5 ± 26.0 |
| 1795 | 2480 ± 0 | 10 | 45.2 ± 4.2 | 97.0 ± 0.2 | 32.0 ± 2.8 | 70.1 ± 0.2 | 20.2 ± 2.8 | 51.8 ± 4.2 | 24.9 ± 4.2 | 26.9 ± 0.3 |
| 1796 | 5377 ± 11 | 10 | 26.5 ± 0.6 | 27.8 ± 4.6 | 12.6 ± 4.0 | 26.1 ± 5.0 | 22.0 ± 6.7 | 1.3 ± 4.6 | 0.3 ± 5.0 | 1.6 ± 6.8 |
| 1801 | 1891 ± 1 | 20 | 1.7 ± 0.9 | 177.3 ± 0.5 | 15.4 ± 1.8 | 174.0 ± 1.6 | 16.1 ± 4.9 | 4.4 ± 1.0 | 7.7 ± 1.8 | 3.3 ± 1.6 |
| 1871 | 6155 ± 5 | 20 | 139.0 ± 0.0 | 158.1 ± 3.2 | 22.4 ± 5.2 | 155.0 ± 2.9 | 15.5 ± 3.6 | 19.1 ± 3.2 | 16.0 ± 2.9 | 3.1 ± 4.3 |
| 1873 | 7849 ± 0 | 8 | 55.8 ± 10.3 | 133.7 ± 1.0 | 16.1 ± 4.7 | 164.5 ± 2.8 | 18.2 ± 2.0 | 77.9 ± 10.4 | 71.2 ± 10.7 | 30.9 ± 3.0 |

Table A.8: Kinematic (mis)alignment between the stellar and the ionised gas components for the galaxies included in this study.

| id | $\Psi_{\rm gas-star}$ | |
|---|---|---|
| | approaching | receding |
| | (°) | (°) |
| (1) | (2) | (3) |
| 14 | – | – |
| 17 | 54.9 ± 22.6 | 49.3 ± 25.4 |
| 22 | 6.4 ± 2.2 | 10.2 ± 4.9 |
| 26 | 4.6 ± 3.2 | 2.8 ± 3.0 |
| 39 | – | – |
| 42 | 7.4 ± 6.2 | 8.9 ± 6.9 |
| 44 | – | – |
| 119 | 20.2 ± 11.5 | 9.8 ± 13.7 |
| 127 | 15.9 ± 13.1 | 4.4 ± 7.9 |
| 155 | 0.1 ± 4.4 | 2.7 ± 5.0 |
| 156 | 1.4 ± 3.1 | 3.5 ± 3.0 |
| 165 | 4.3 ± 2.6 | 10.2 ± 3.0 |
| 186 | 2.5 ± 2.6 | 4.8 ± 3.0 |
| 213 | 5.4 ± 11.6 | 2.4 ± 18.3 |
| 274 | 18.7 ± 5.8 | 1.1 ± 6.8 |
| 311 | 11.7 ± 9.3 | 19.3 ± 7.6 |
| 314 | 4.9 ± 3.3 | 8.1 ± 3.4 |
| 340 | 181.2 ± 11.6 | 170.8 ± 20.2 |
| 360 | – | – |
| 475 | – | – |
| 479 | 6.4 ± 3.8 | 18.0 ± 5.6 |
| 486 | 4.8 ± 12.3 | 10.0 ± 11.1 |
| 520 | 20.5 ± 11.0 | 17.0 ± 13.8 |
| 577 | 1.7 ± 6.3 | 2.9 ± 7.6 |
| 589 | – | – |
| 593 | 4.9 ± 2.4 | 1.3 ± 3.3 |
| 633 | 76.0 ± 13.9 | 40.1 ± 8.3 |
| 634 | 10.6 ± 3.1 | 0.8 ± 4.1 |
| 663 | 1.9 ± 2.4 | 1.9 ± 2.4 |
| 676 | 27.0 ± 14.8 | 8.6 ± 23.3 |
| 680 | – | – |
| 740 | 10.0 ± 7.2 | 16.3 ± 8.2 |
| 746 | 90.7 ± 5.9 | 98.0 ± 5.7 |
| 758 | – | – |
| 767 | – | – |
| 769 | 0.7 ± 5.3 | 8.5 ± 7.2 |
| 770 | 105.1 ± 5.9 | 56.6 ± 9.2 |
| 778 | 8.0 ± 4.9 | 4.5 ± 3.8 |
| 780 | – | – |
| 781 | – | – |
| 785 | – | – |
| 795 | 3.9 ± 5.7 | 8.6 ± 5.0 |
| 796 | 15.4 ± 3.5 | 3.0 ± 3.6 |
| 797 | 8.9 ± 4.2 | 12.9 ± 7.5 |
| 801 | 6.9 ± 9.9 | 13.8 ± 17.1 |
| 802 | 2.9 ± 20.1 | 17.5 ± 19.4 |
| 803 | 0.6 ± 7.8 | 18.9 ± 22.4 |
| 806 | 68.0 ± 6.2 | 69.1 ± 7.9 |
| 807 | 7.3 ± 4.8 | 0.5 ± 4.4 |
| 816 | 4.6 ± 5.1 | 2.3 ± 8.0 |
| 822 | 21.6 ± 6.6 | 2.4 ± 6.8 |

Table A.8: continue A.2

| id | $\Psi_{\mathrm{gas-star}}$ | |
|---|---|---|
| | approaching | receding |
| | (°) | (°) |
| (1) | (2) | (3) |
| 828 | – | – |
| 832 | – | – |
| 833 | 8.3 ± 5.3 | 20.3 ± 10.7 |
| 843 | – | – |
| 844 | – | – |
| 846 | – | – |
| 850 | 2.4 ± 4.3 | 3.9 ± 2.9 |
| 852 | – | – |
| 858 | 8.8 ± 3.3 | 7.6 ± 4.1 |
| 860 | – | – |
| 871 | 2.2 ± 2.5 | 5.2 ± 3.2 |
| 873 | 10.0 ± 9.9 | 10.7 ± 7.8 |
| 874 | 1.8 ± 3.0 | 9.9 ± 4.3 |
| 877 | 4.5 ± 5.1 | 4.7 ± 3.7 |
| 882 | – | – |
| 883 | – | – |
| 892 | 0.3 ± 5.6 | 4.0 ± 3.8 |
| 900 | – | – |
| 901 | 8.5 ± 4.6 | 15.2 ± 4.9 |
| 903 | – | – |
| 905 | – | – |
| 907 | 5.9 ± 6.6 | 1.6 ± 7.2 |
| 913 | 4.8 ± 5.8 | 32.3 ± 6.8 |
| 915 | 4.7 ± 5.8 | 3.6 ± 5.2 |
| 916 | – | – |
| 922 | 25.1 ± 5.9 | 18.2 ± 6.9 |
| 923 | – | – |
| 925 | 0.1 ± 5.0 | 4.5 ± 6.2 |
| 927 | 28.8 ± 4.6 | 19.7 ± 5.7 |
| 932 | – | – |
| 935 | – | – |
| 939 | 9.8 ± 11.1 | 14.4 ± 9.6 |
| 1014 | – | – |
| 1017 | – | – |
| 1022 | 19.4 ± 22.3 | 39.7 ± 27.7 |
| 1026 | – | – |
| 1042 | – | – |
| 1044 | – | – |
| 1340 | – | – |
| 1360 | – | – |
| 1520 | 24.4 ± 17.3 | 24.0 ± 21.3 |
| 1589 | – | – |
| 1663 | – | – |
| 1740 | – | – |
| 1780 | – | – |
| 1781 | 19.8 ± 20.9 | 0.7 ± 21.1 |
| 1795 | 141.9 ± 9.0 | 155.9 ± 8.1 |
| 1796 | 2.0 ± 5.8 | 2.9 ± 6.4 |
| 1801 | 11.1 ± 4.2 | 8.1 ± 4.9 |
| 1871 | 6.6 ± 4.8 | 0.9 ± 4.2 |
| 1873 | 2.3 ± 20.6 | 21.6 ± 21.6 |

## A.3 Stellar and Ionized Velocity Fields for the Non-interacting Sample

In this appendix we present the velocity field of the 80 non-interacting galaxies. Each row present one galaxy similar to the one in Fig.2.10, from left to right: SDSS r-band image of the galaxy. The white solid line represents the photometric PA measured at the same galactocentric distance as the kinematic PA ($PA_{morph}$, see section 2.4.3). The dashed line represents the photometric PA measured at the outermost isophote of the image ($PA^{out}_{morph}$, see section 3.2). The next two panels show the stellar and ionized gas velocity maps, respectively. Green points highlight the locations where the maximum velocity is located at a given radius, determined from the position-velocity diagram. Black lines for each kinematic side represent the average kinematic PA ($PA_{kin}$), while white thin lines along the zero-velocity curve show the average minor kinematic PA. The next panel shows the distance from the galactic centre versus the maximum for the stellar (blue) and ionized gas (red) components. The curve along $0\,km\,s^{-1}$ represents the velocities along the zero-velocity curve. Uncertainty in velocity are determined from Monte Carlo simulations. The last panel shows the dependence of the different PA with respect to the radius. $PA_{morph}$, $PA^{stellar}_{kin}$, and $PA^{gas}_{kin}$ are represented by open circles, filled blue diamonds, and filled red squares, respectively. For barred galaxies, we highlight the length of the bar and its orientation with dashed lines.

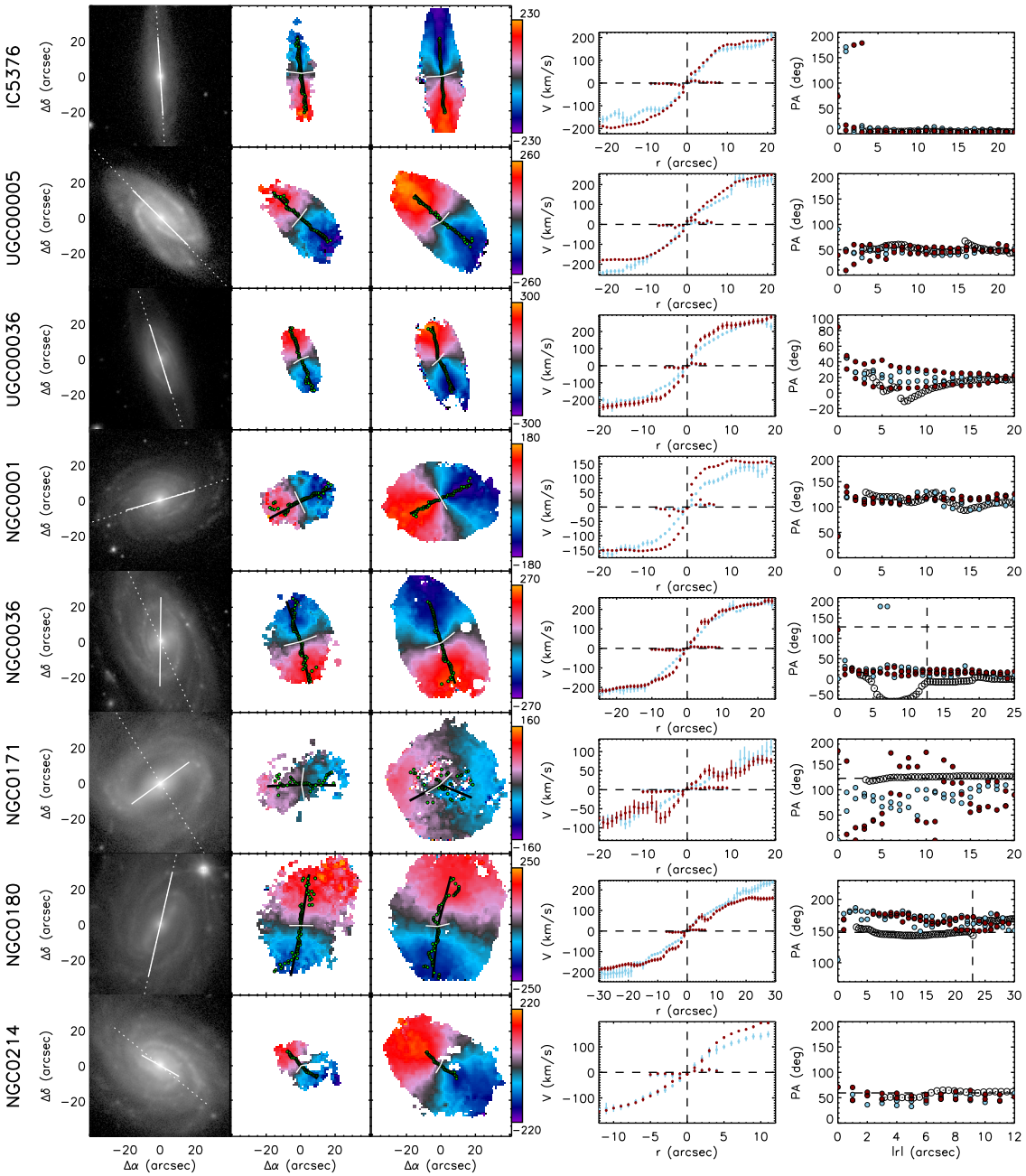


Figure A.5: Stellar and ionised gas velocity fields for the sample of galaxies used in this study.

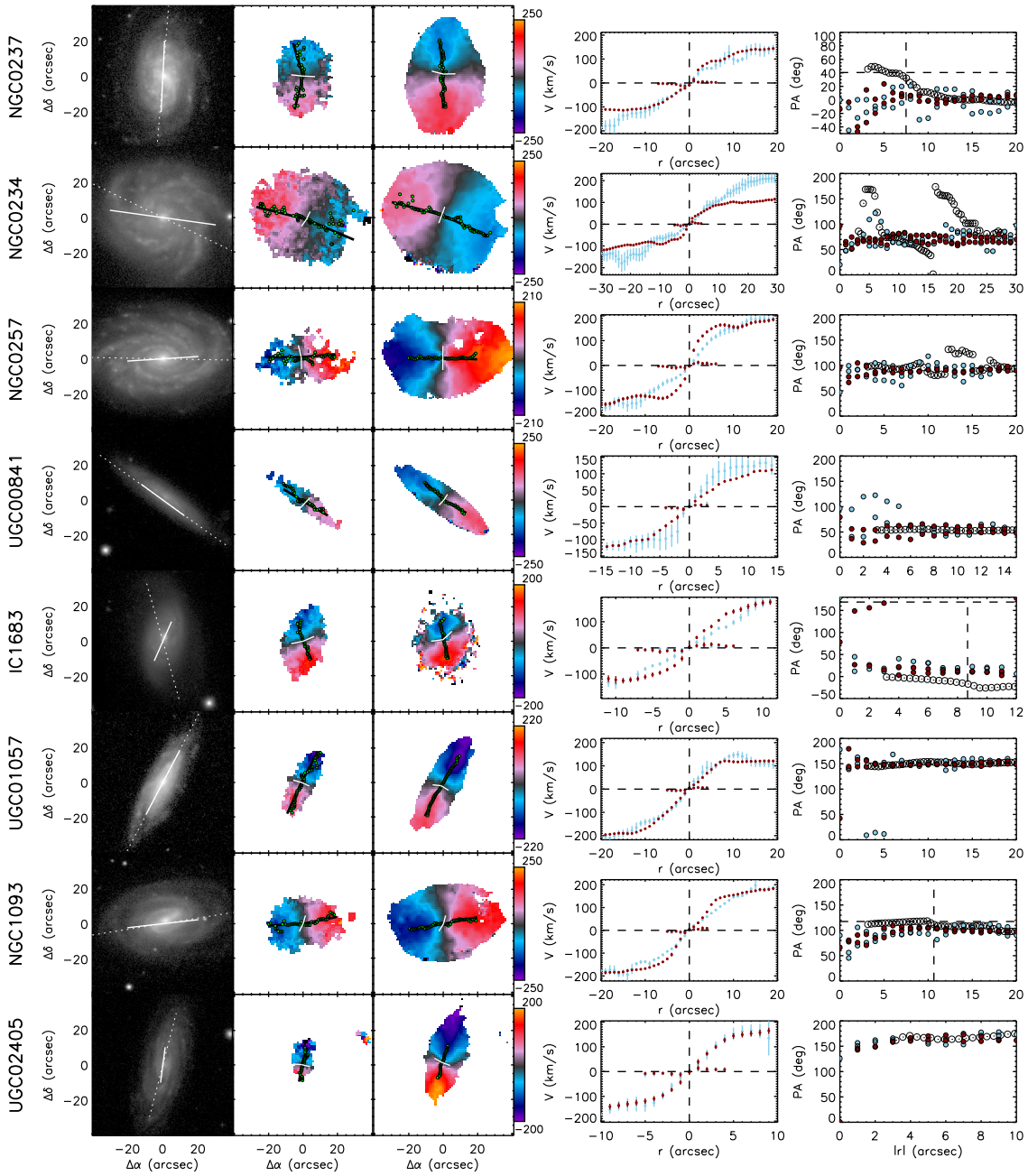


Figure A.5: - *continued*

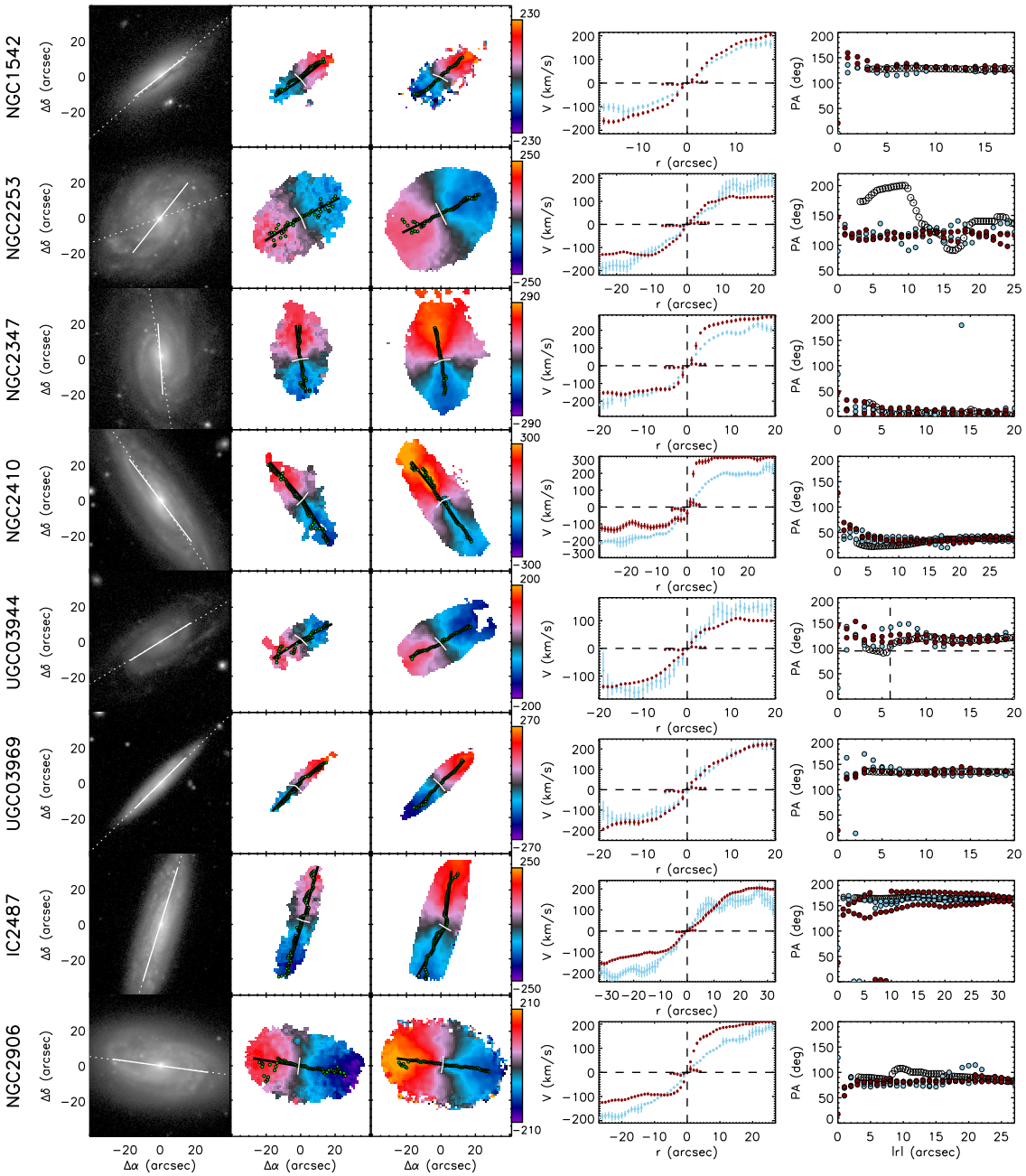


Figure A.5: - *continued*

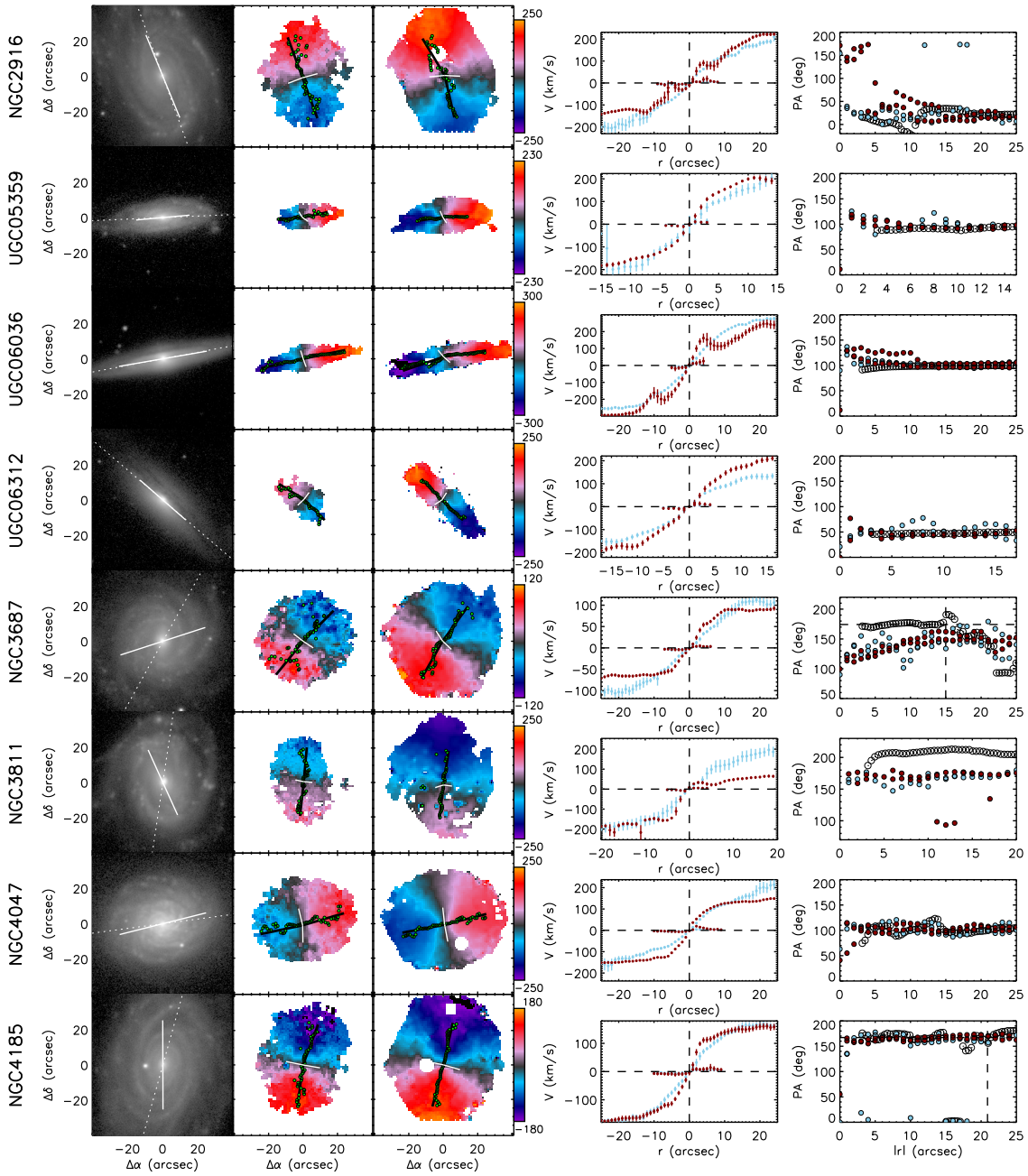


Figure A.5: - *continued*

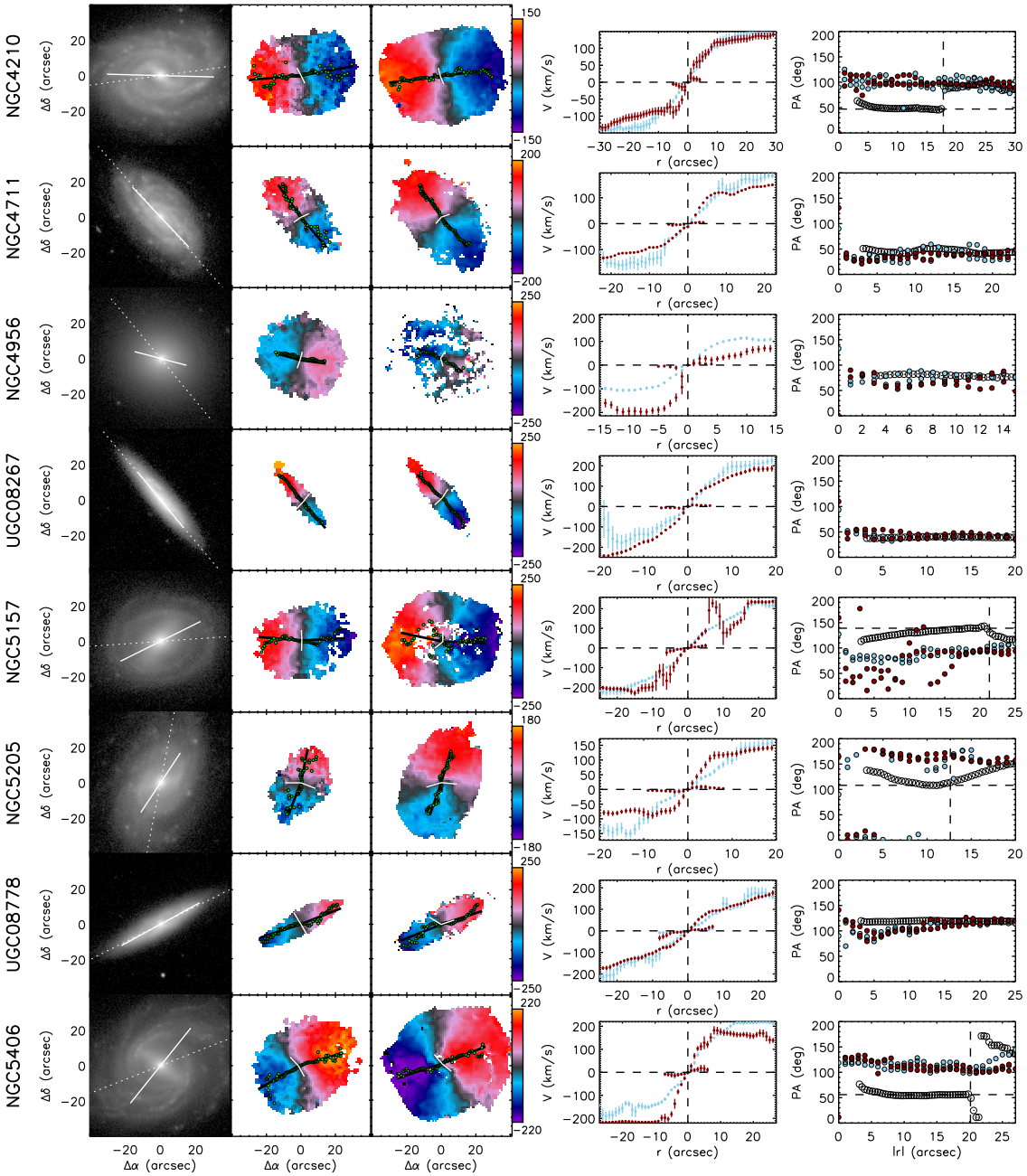


Figure A.5: - *continued*

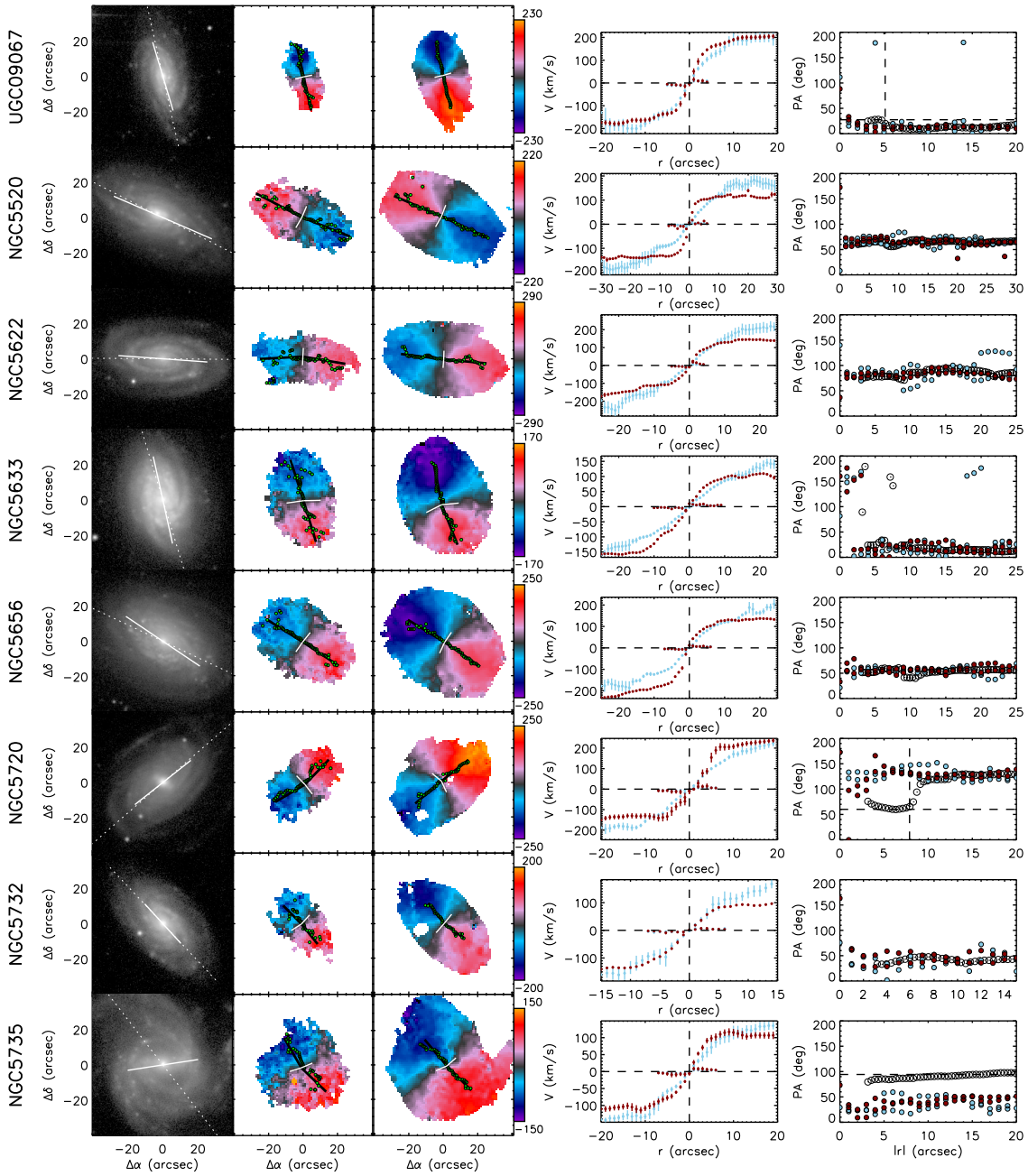


Figure A.5: - *continued*

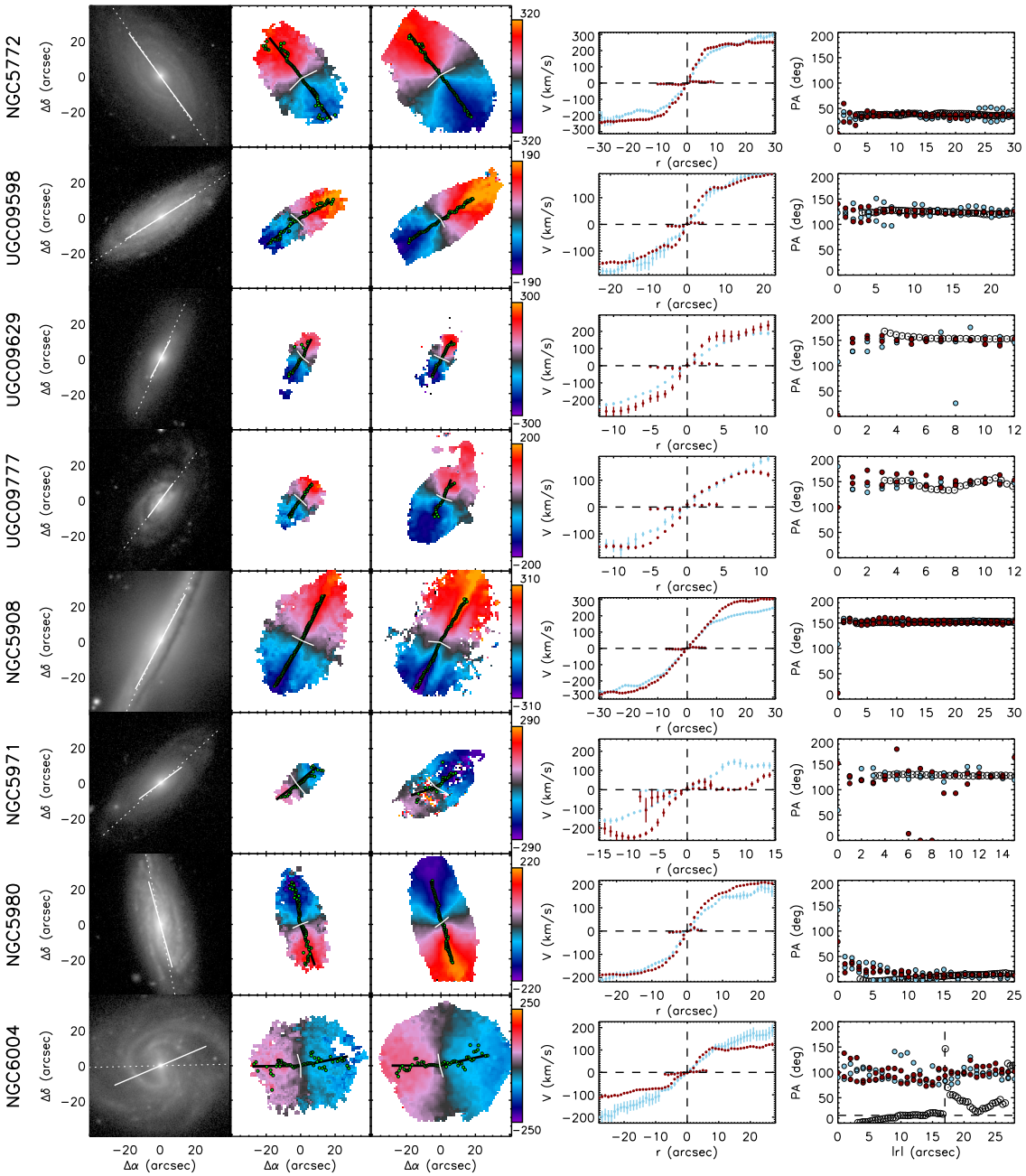


Figure A.5: - *continued*

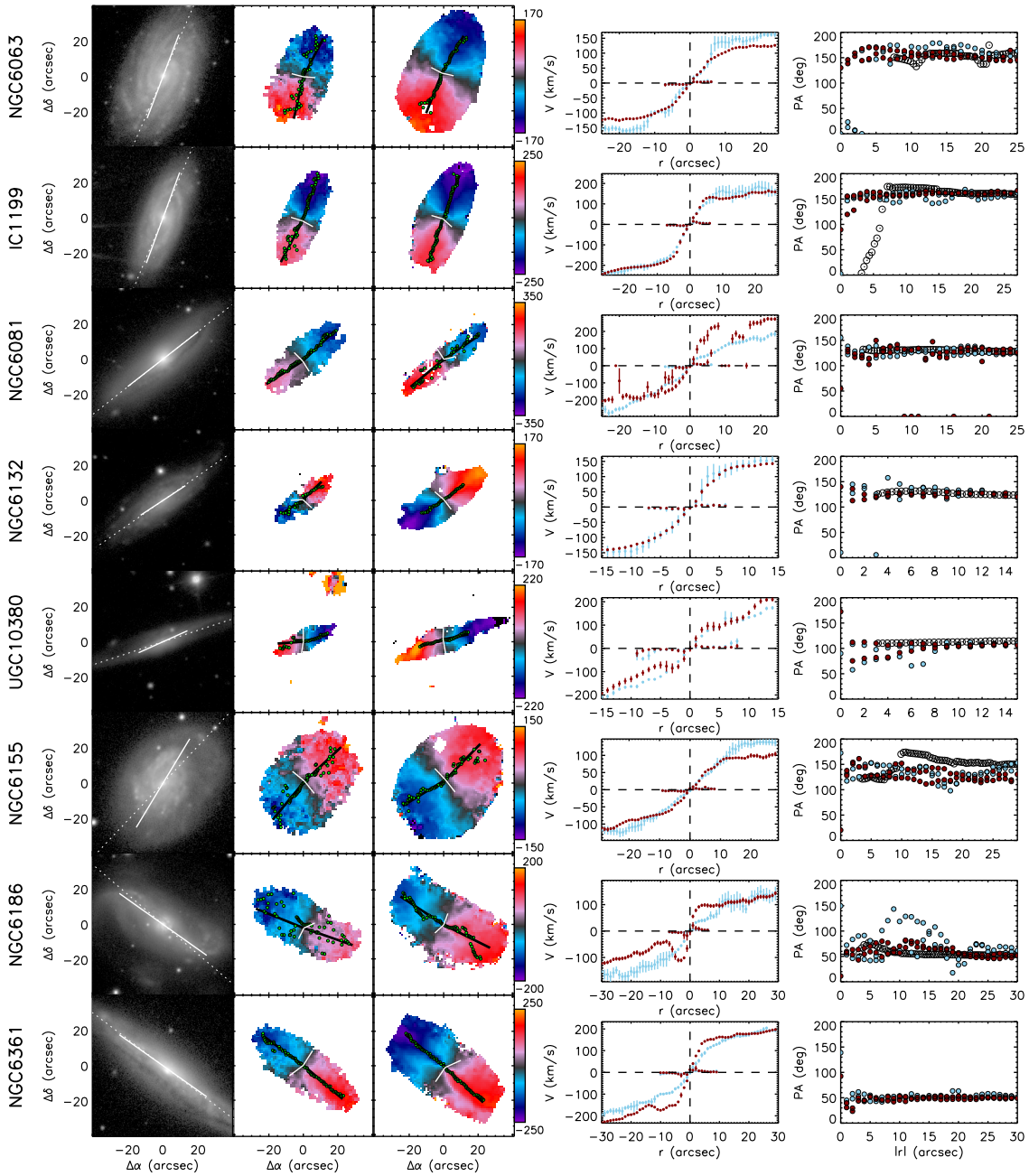


Figure A.5: - *continued*

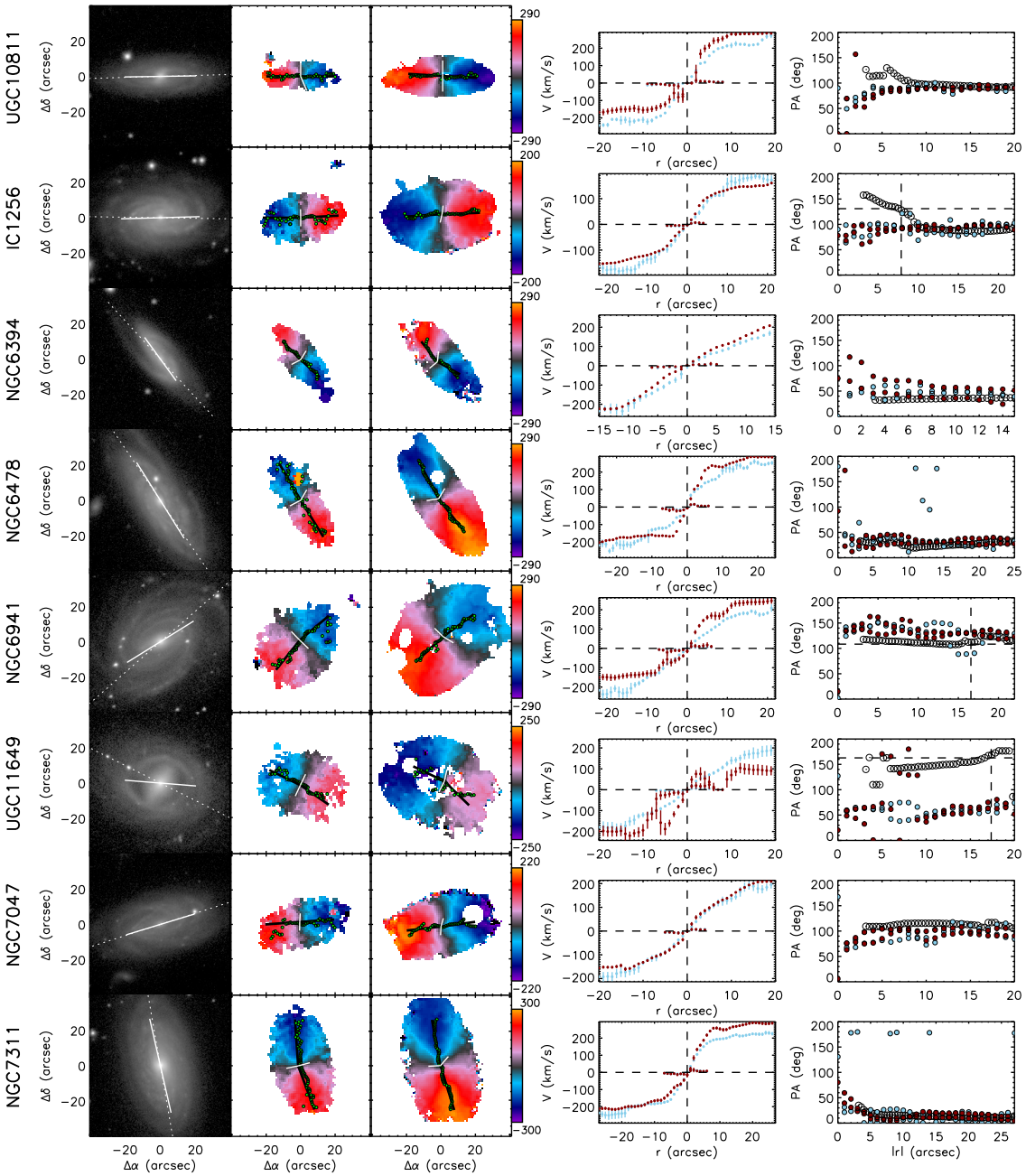


Figure A.5: - *continued*

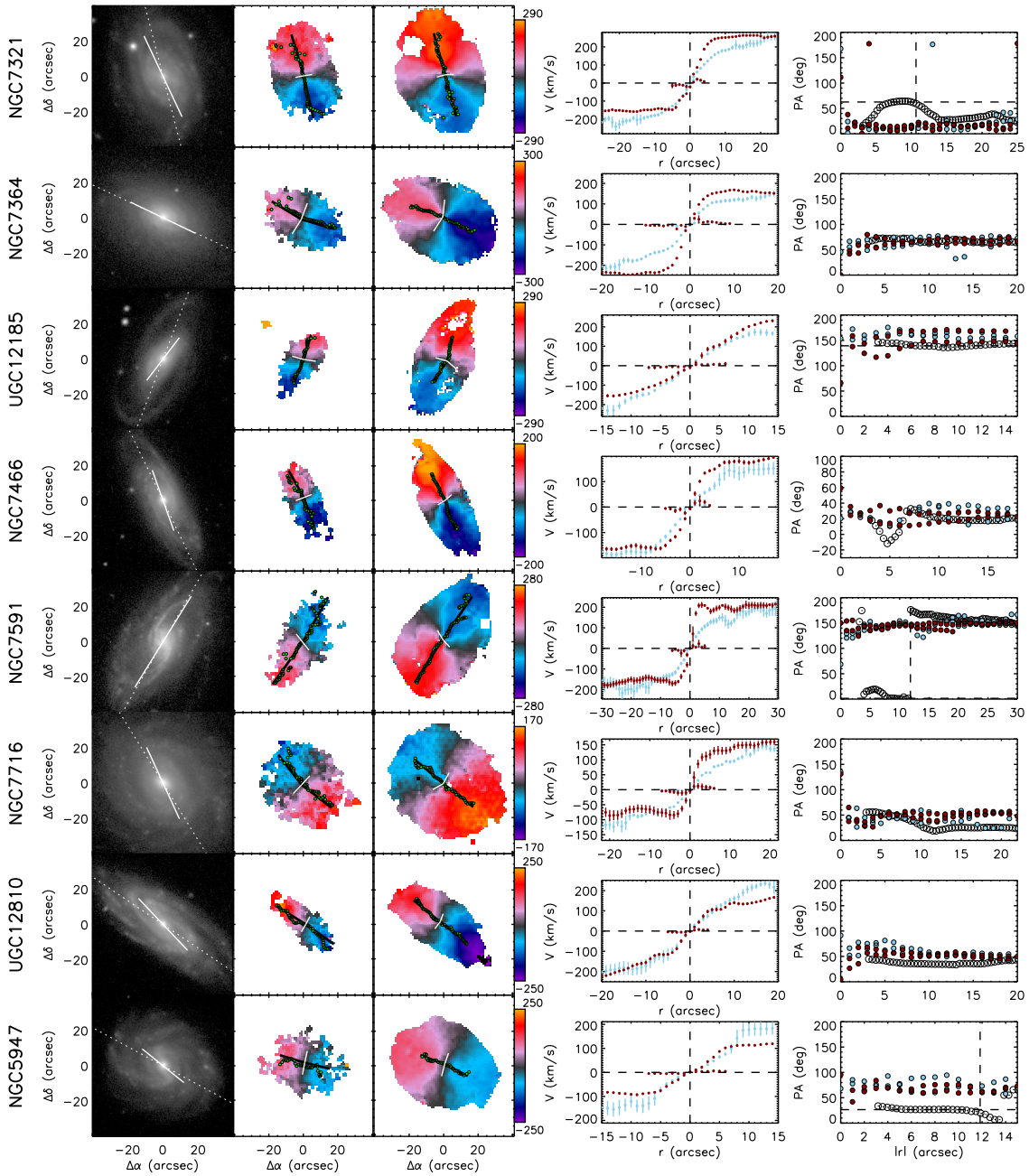


Figure A.5: - *continued*

## A.4 Stellar and Ionized velocity fields for the interacting sample

In this appendix we present the stellar and ionized gas kinematic maps of the interacting sample used in this study. We group from Fig. A.6 to A.10 the galaxies in the different interaction stages described in section 2.3. For each interacting galaxy (system) we show from left to right: SDSS $r$-band image. For post-merger and merger remnants we enhance the contrast of the images to highlight their morphological features. The white hexagon represents the area covered by the CALIFA field-of-view. White line in the left-bottom corner represent 10 kpc scale. In systems where both objects are observed, two hexagons are plotted. Next panel shows the SDSS $r$-band image at the same area for which the kinematic velocity distributions has been observed. White line represents the morphological PA. Next two panels show the stellar and the ionized gas velocity fields. The green dots in each of these panels represent the position of maximum velocity for that galactocentric distance. Black lines represent the mean kinematic PA derived from these points (see details in section 2.4.3). Last panel shows the velocity curve derived directly from the velocity field (see details in section 2.4.3), blue and red curves represent the stellar and the ionized gas components, respectively. The thickness of the lines represent the uncertainty in the determination of the maximum velocity for each galactocentric distance by means of Monte Carlo simulations (see details in section 2.4.3). Note that for galaxies where the kinematic PA was not possible to determine for any component, neither the velocity curves nor the positions are plotted in the velocity fields.

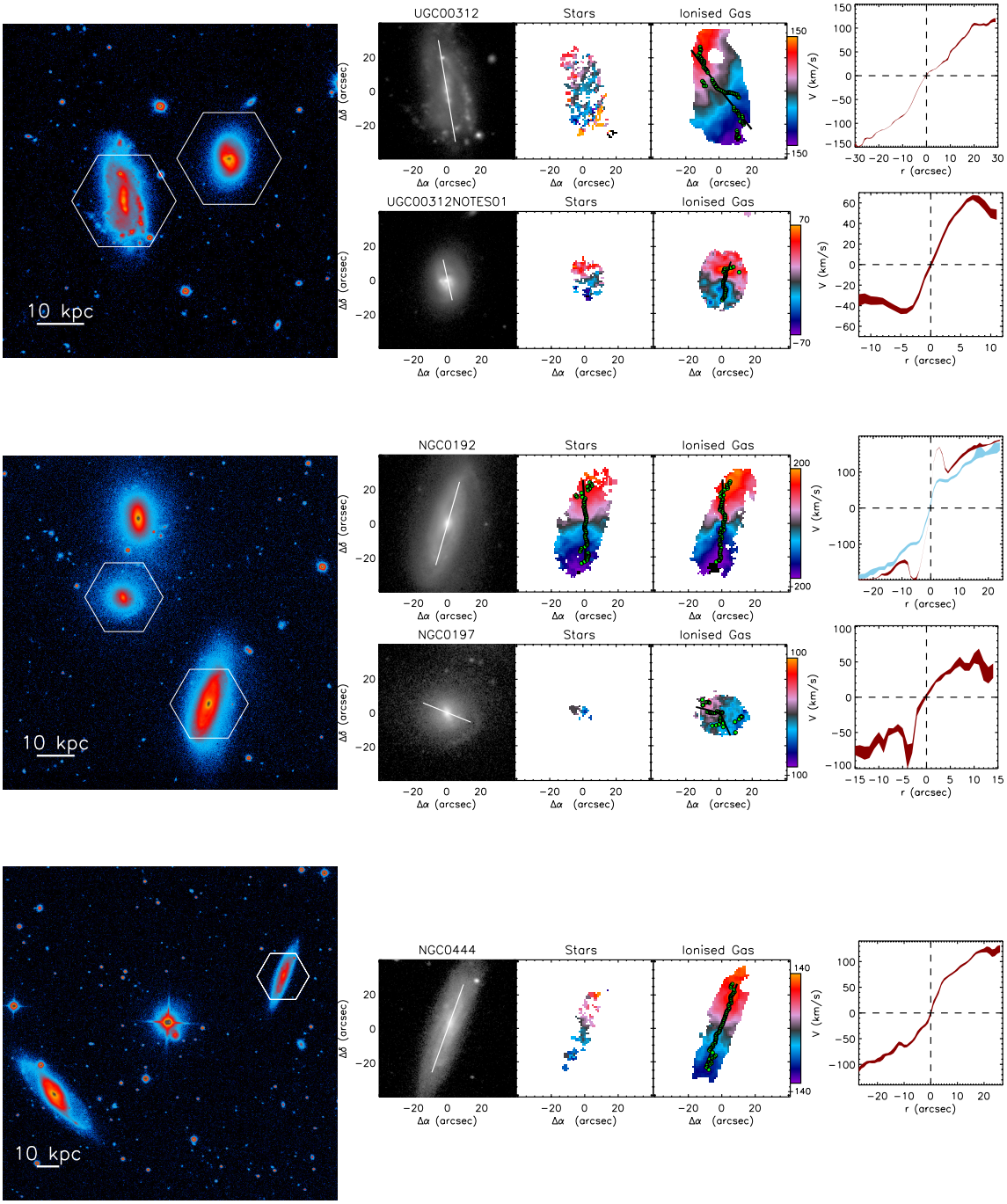


Figure A.6: Objects in the pre-merger stage. From top to bottom the pairs UGC00312 and UGC00312NOTES01; NGC0192 and NGC0197 and NGC0444

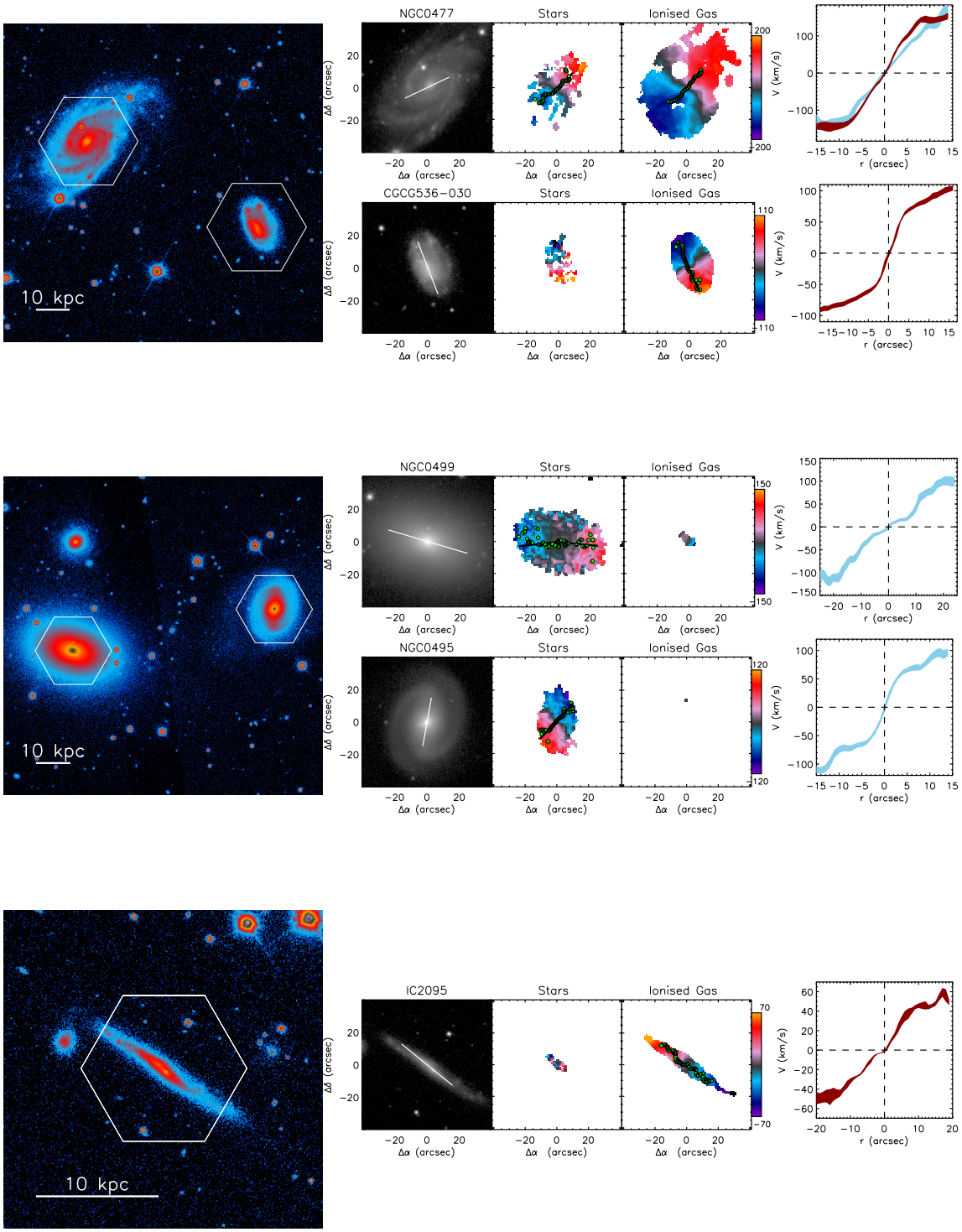


Figure A.6: Continuation Fig.A.6. From top to bottom the pairs NGC 477 and CGCG536-030; NGC 499 and NGC 495; and IC 2095

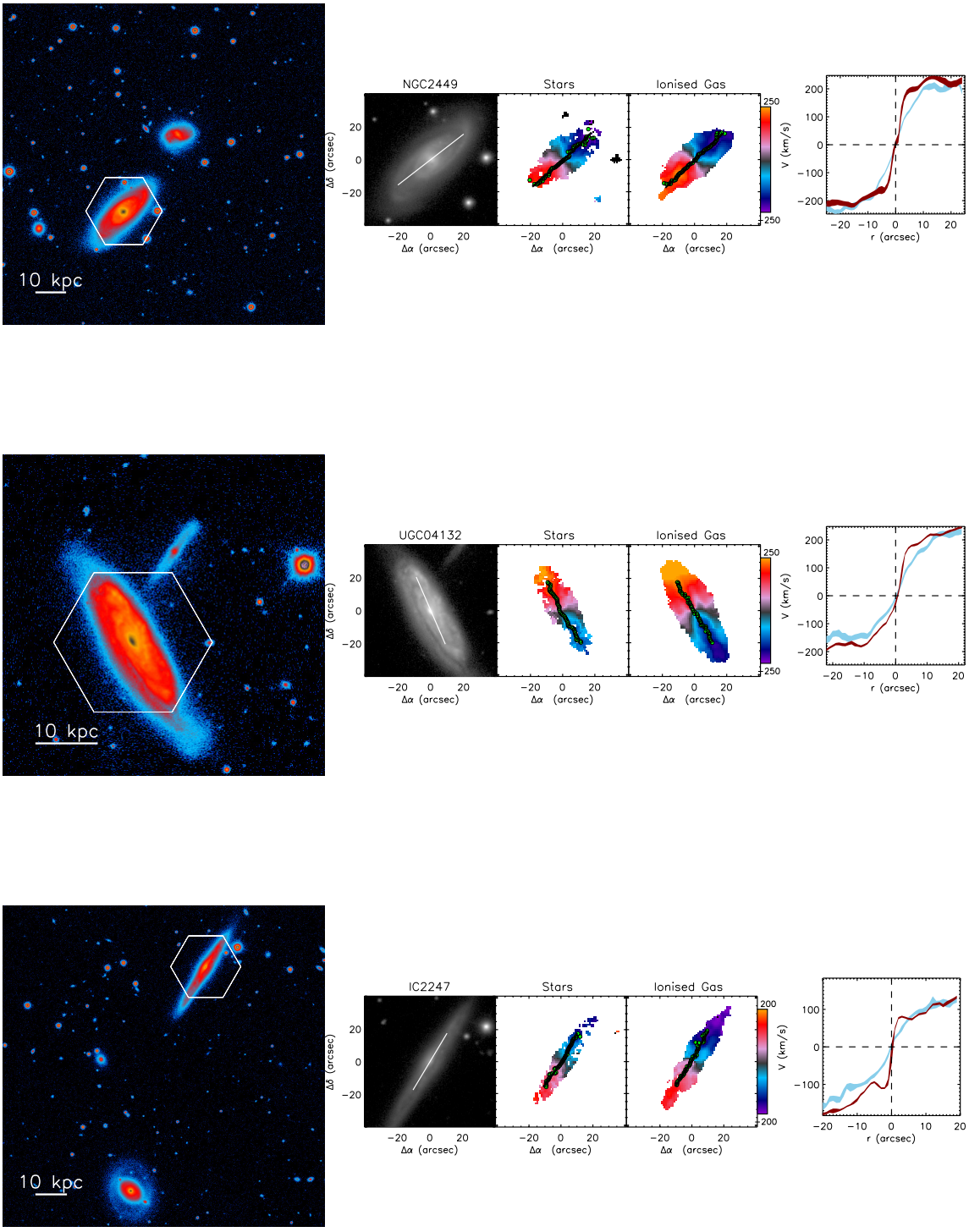


Figure A.6: Continuation Fig.A.6. Top: NGC 2499. Middle: UGC 0432. Bottom: IC 2247

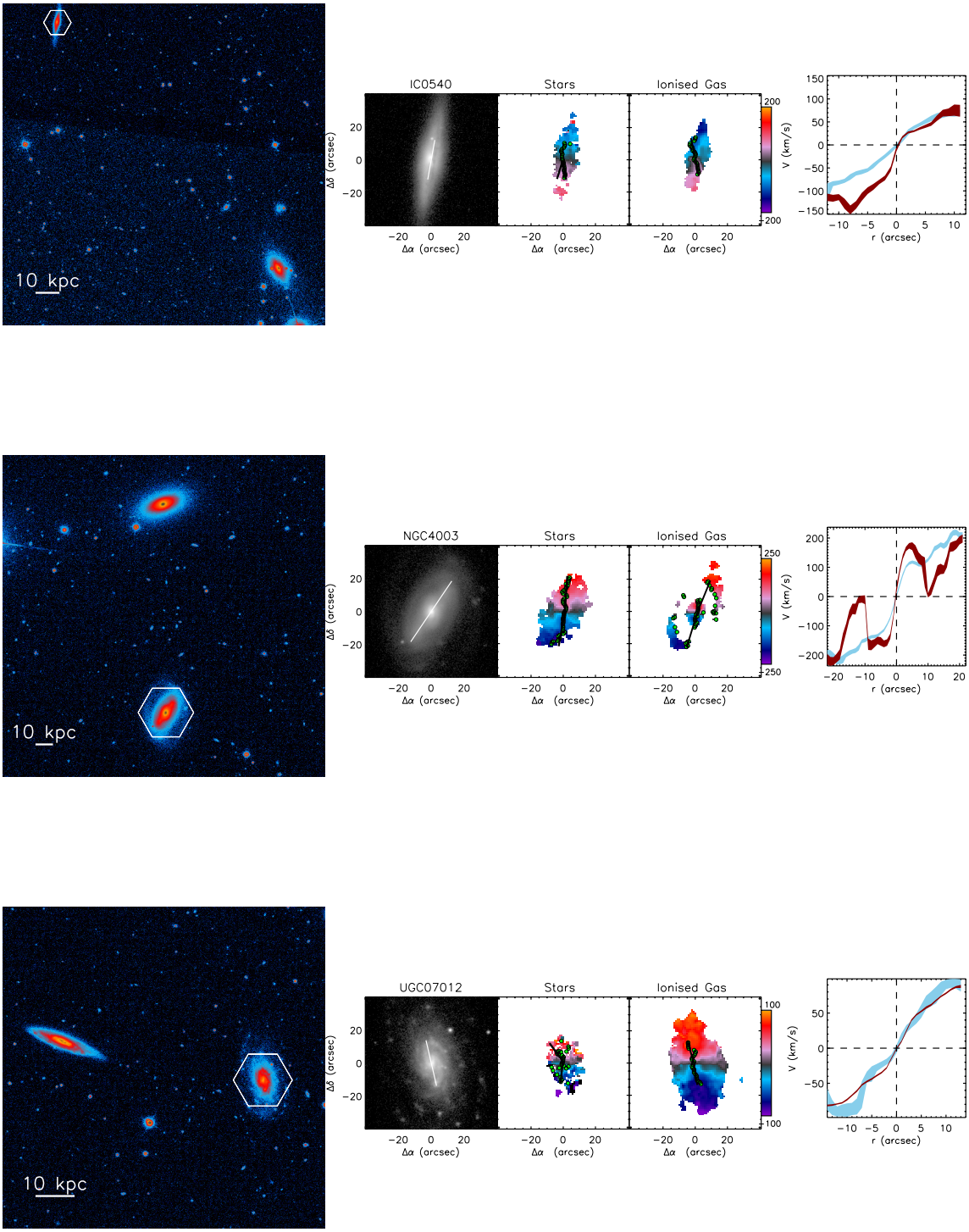


Figure A.6: Continuation Fig.A.6. Top: IC 540. Middle: NGC 4003. Bottom: UGC 7012

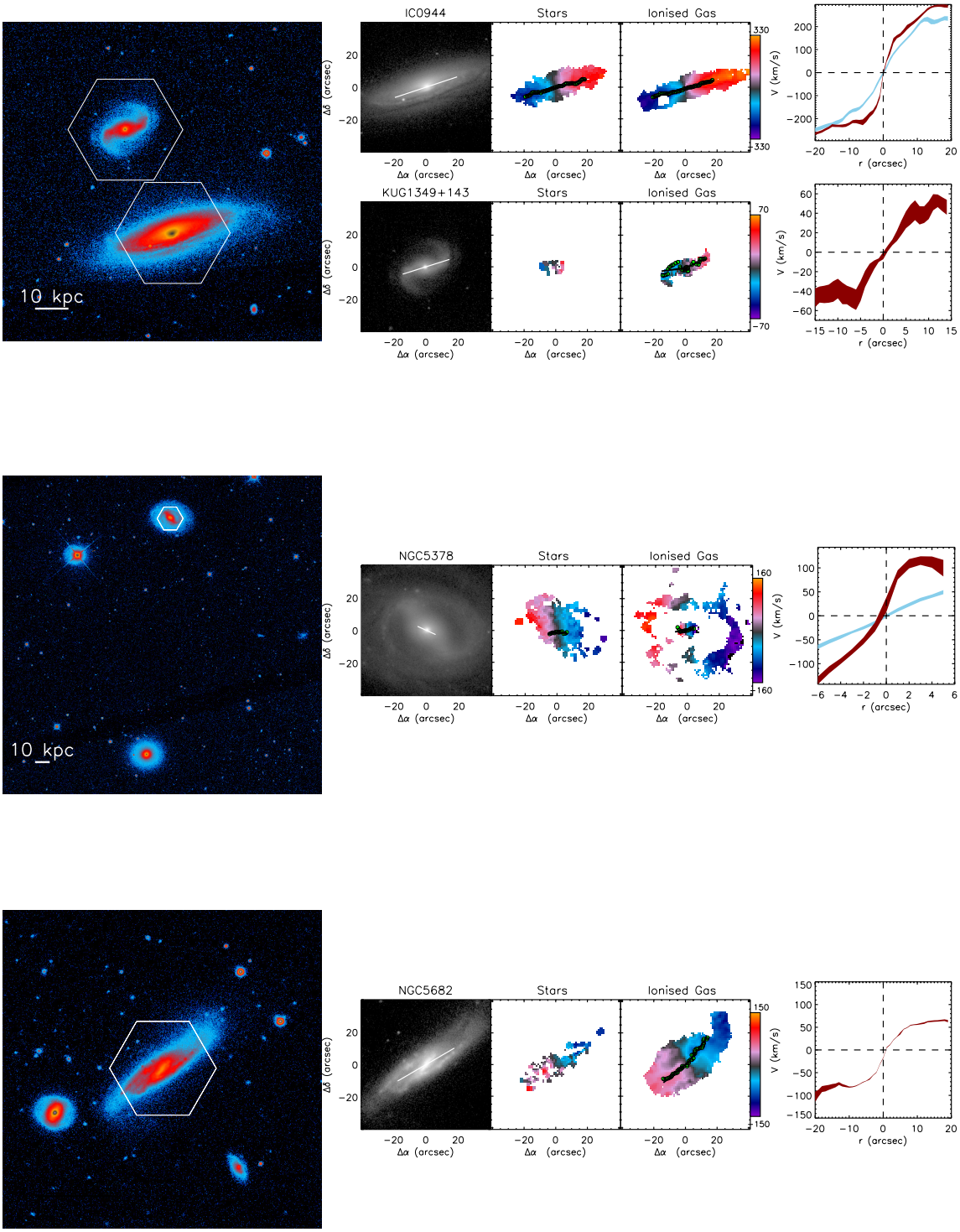


Figure A.6: Continuation Fig.A.6. Top: IC 944. Middle: NGC 5378. Bottom: NGC 5682

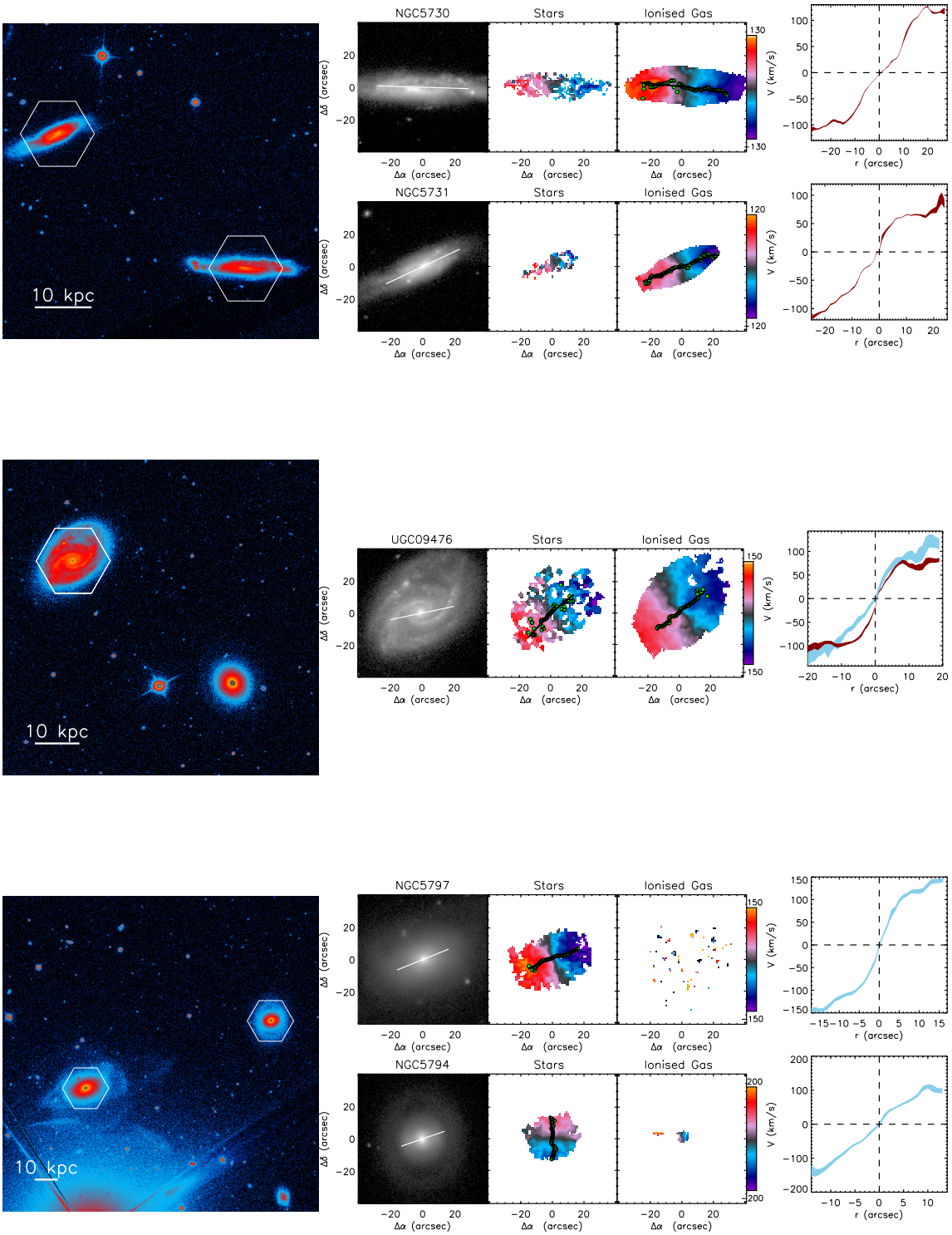


Figure A.6: Continuation Fig.A.6. Top: NGC 5730. Middle: UGC 9476. Bottom: NGC 5797 and NGC 5794

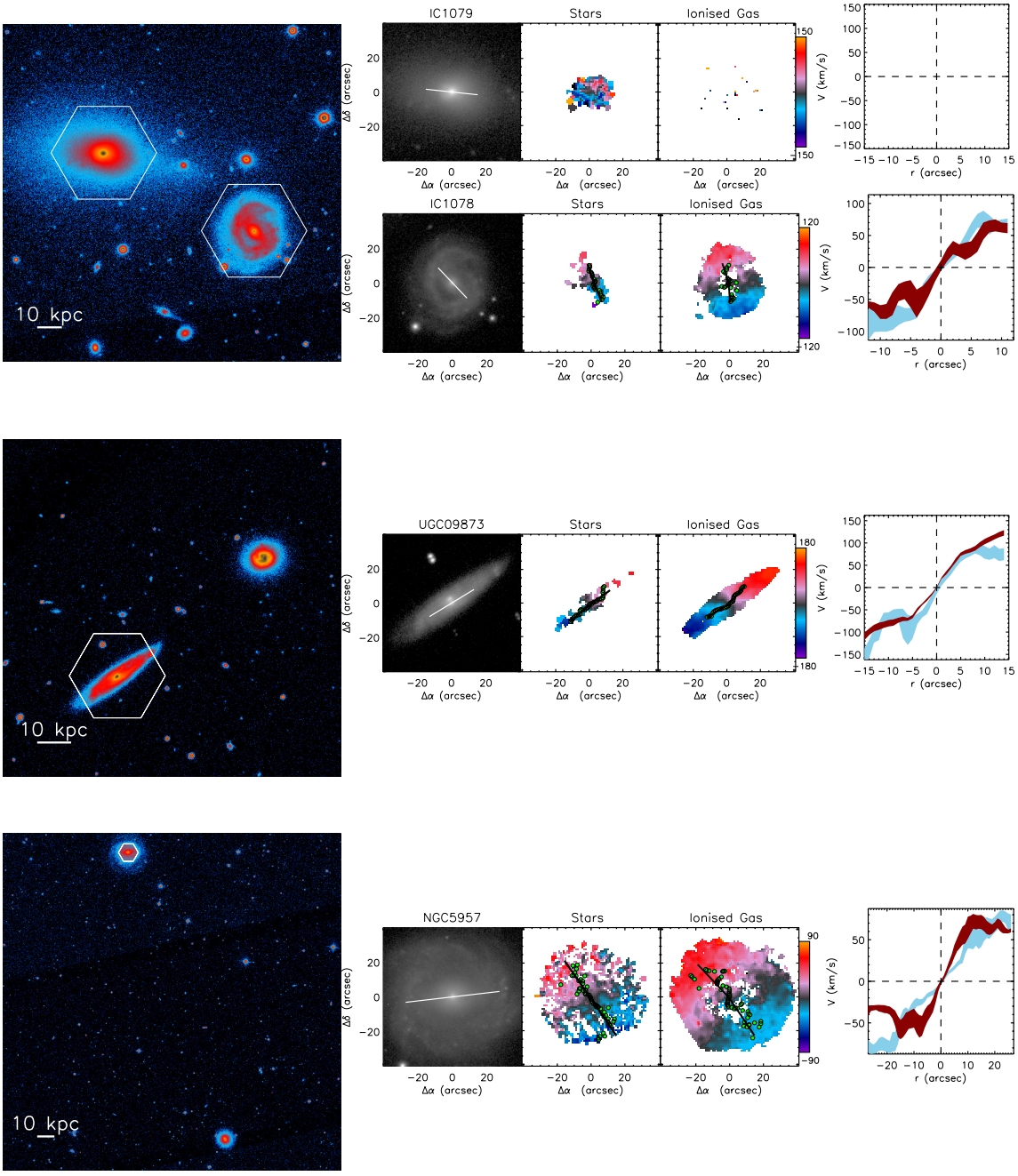


Figure A.6: Continuation Fig.A.6. Top: Pairs of galaxies IC 1079 and IC 1078. Middle: UGC 9873. Bottom: NGC 5957.

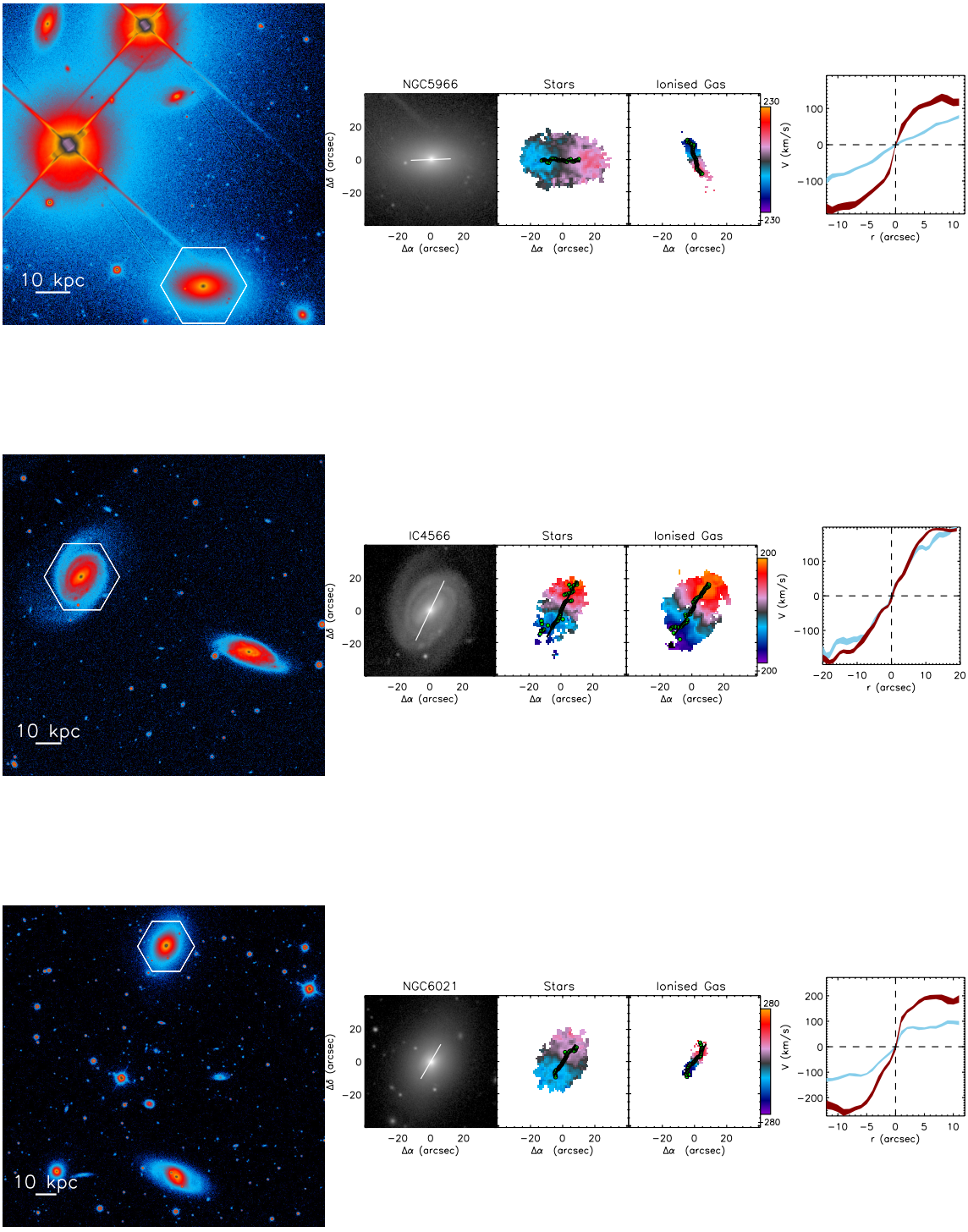


Figure A.6: Continuation Fig.A.6. Top: NGC 5966, Middle: IC 4566, Bottom: NGC 6021.

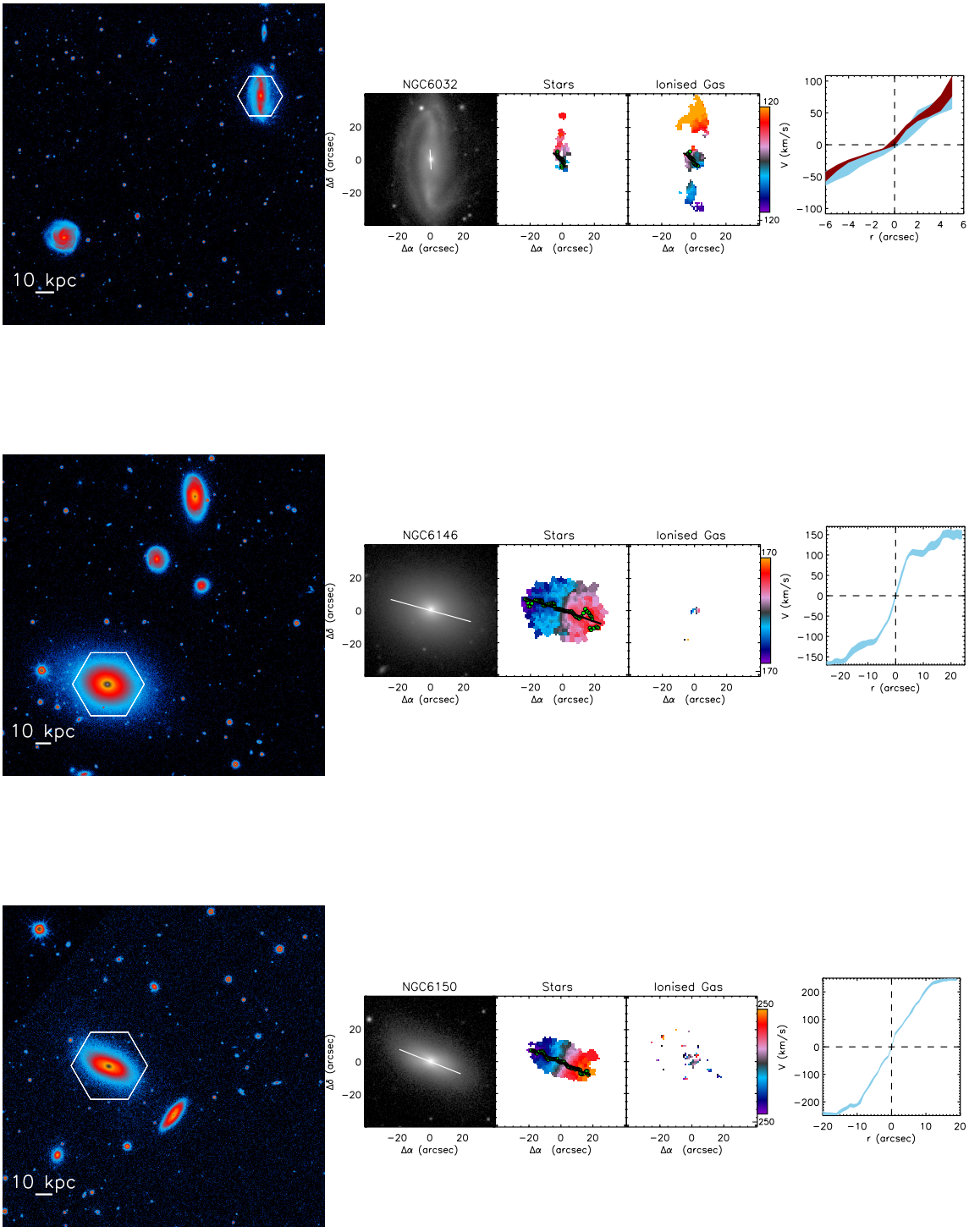


Figure A.6: Continuation Fig.A.6. Top: NGC 6032. Middle: NGC 6146. Bottom: NGC 6150.

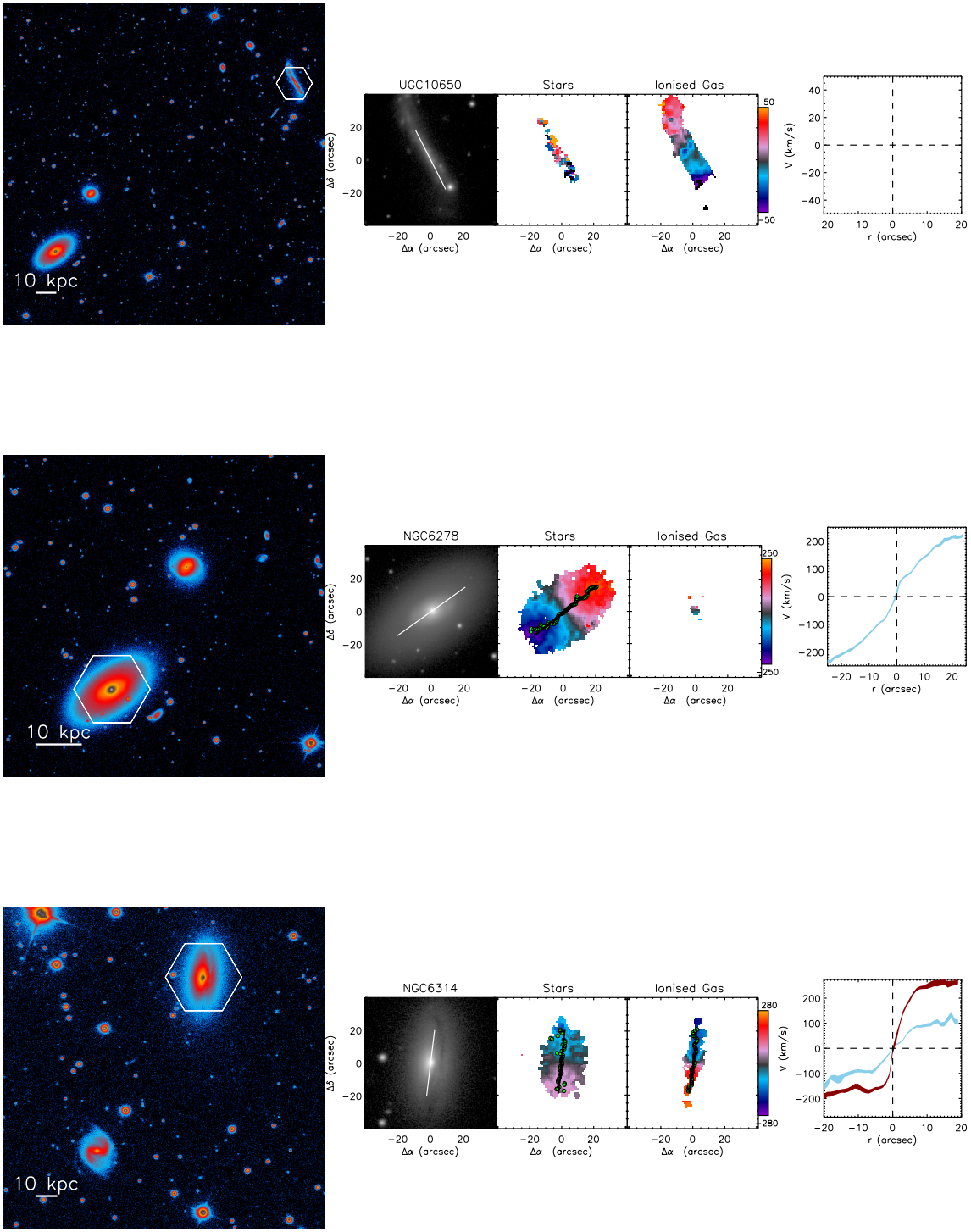


Figure A.6: Continuation Fig.A.6. Top: UGC 10650. Middle: NGC 6278. Bottom: NGC 6314.

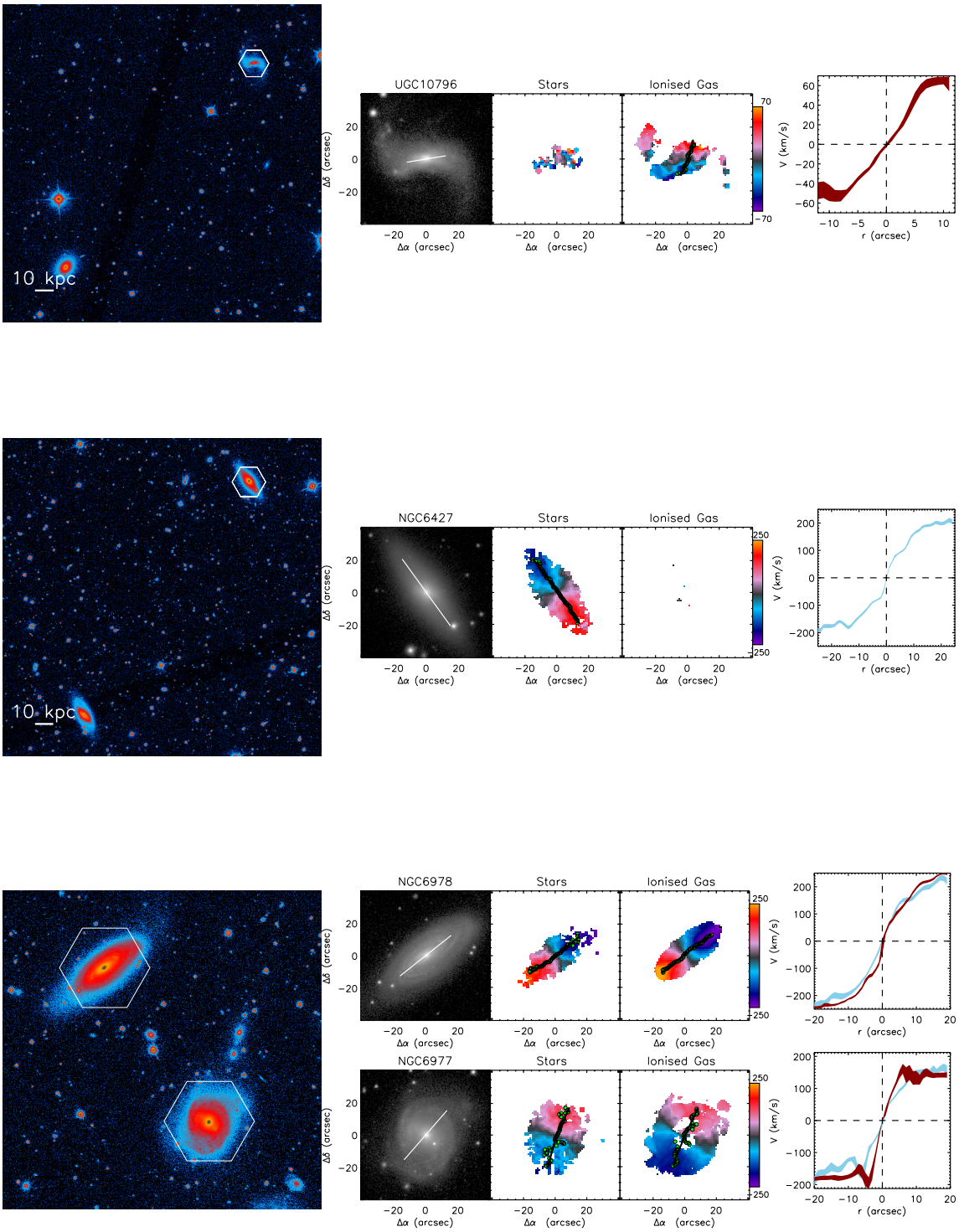


Figure A.6: Continuation Fig.A.6. Top: UGC 10796. Middle: NGC 6427. Bottom: NGC 6978 and NGC 6977.

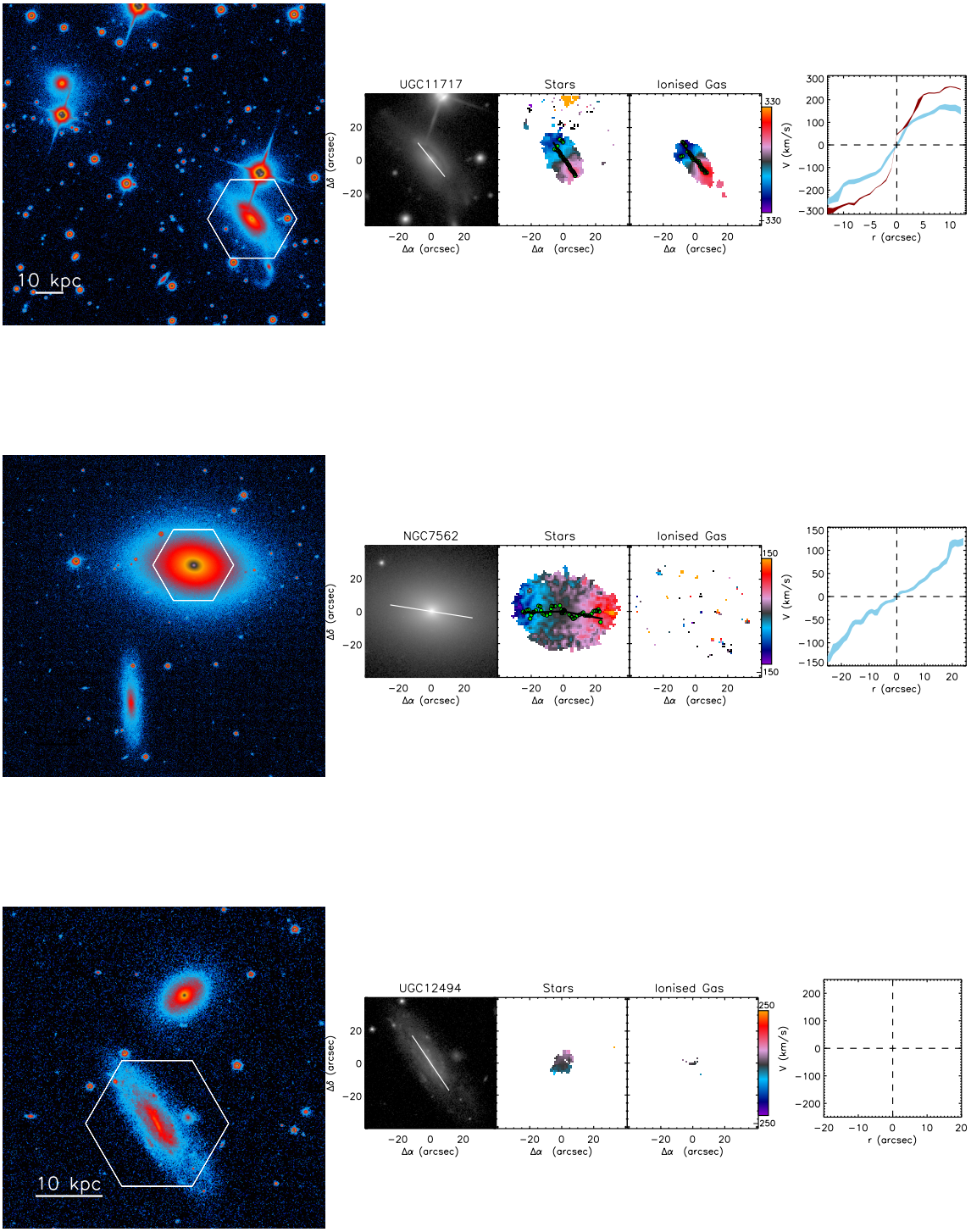


Figure A.6: Continuation Fig.A.6. Top: UGC 11717. Middle: NGC 7562 Bottom: UGC 12494

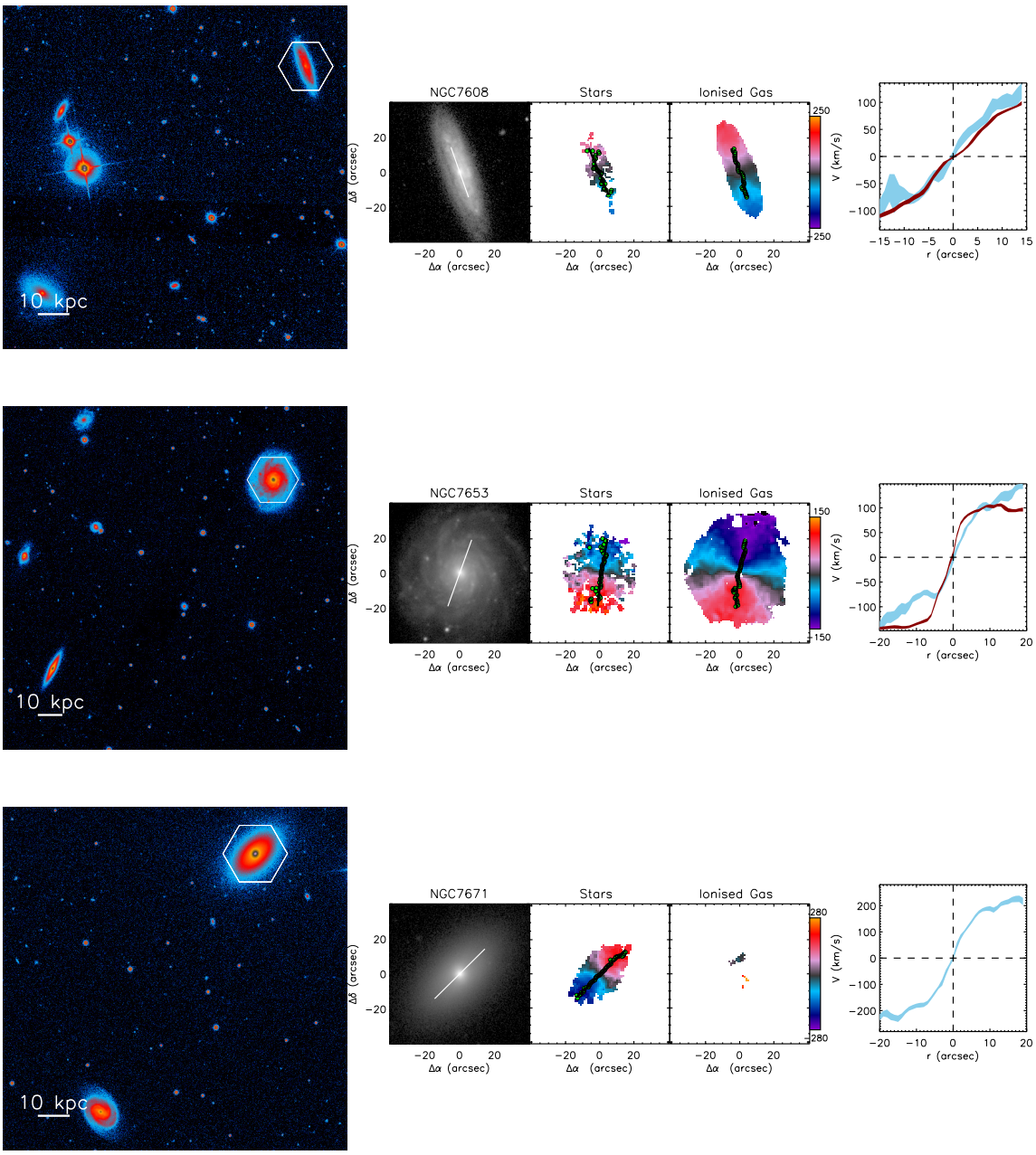


Figure A.6: Continuation Fig.A.6. Top: NGC 7608. Middle: NGC 7653. Bottom: NGC 7671

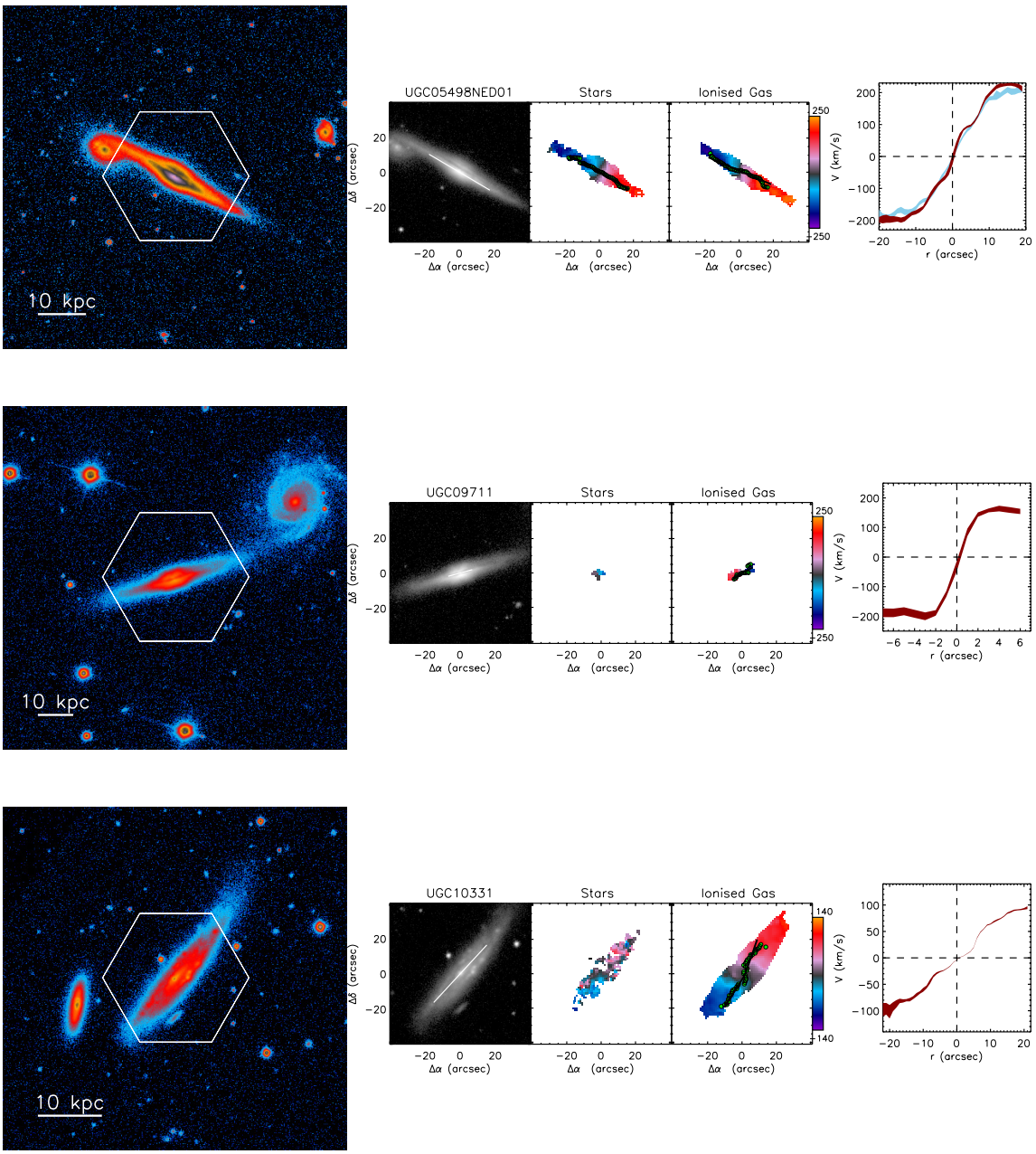


Figure A.6: Continuation Fig.A.6. Top panel: UGC 5498NED01. Middle: UGC 9711. Bottom: UGC 10331.

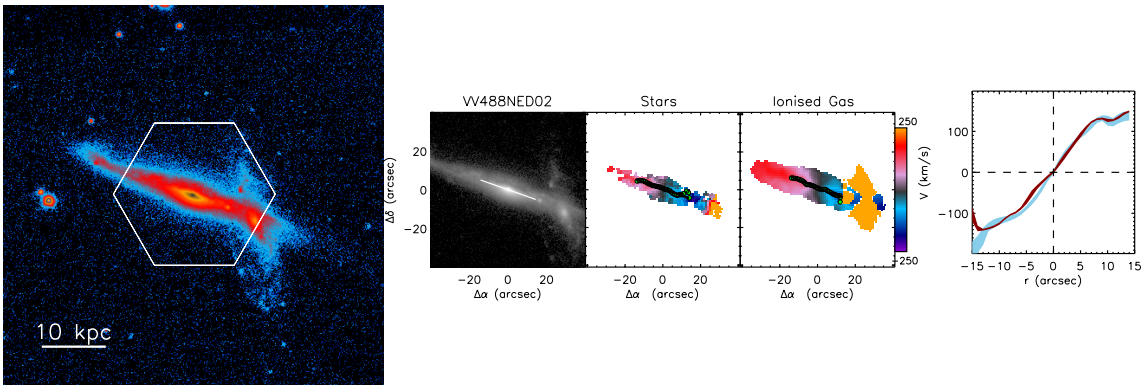


Figure A.7: Continuation Fig.A.6. VV488NED02.

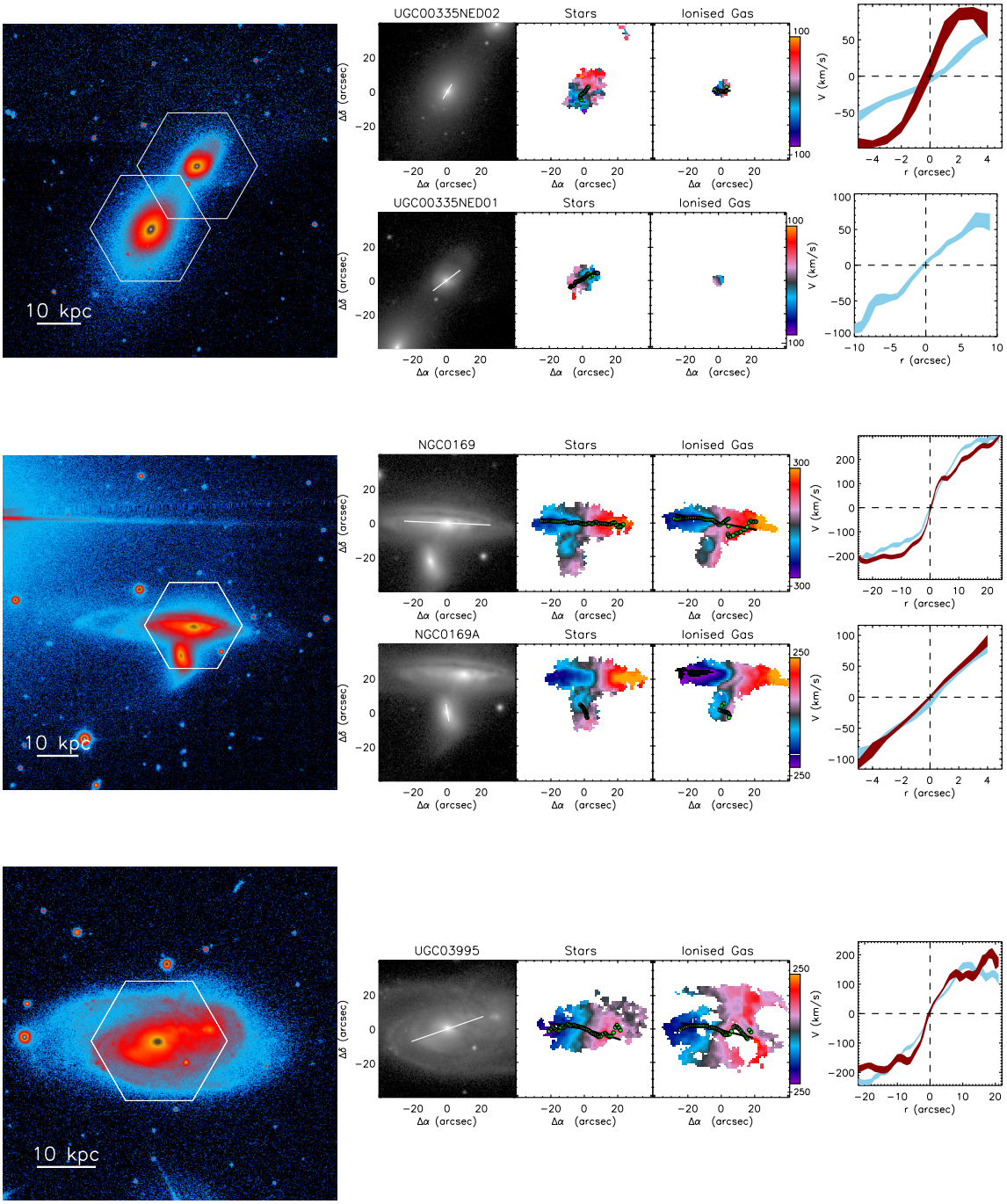


Figure A.8: Pairs of Galaxies with signatures of interactions. Top: Pair UGC 335NED02 and NED01. Middle: Pair of galaxies NGC 169 and NGC 169A. Bottom: UGC 3995.

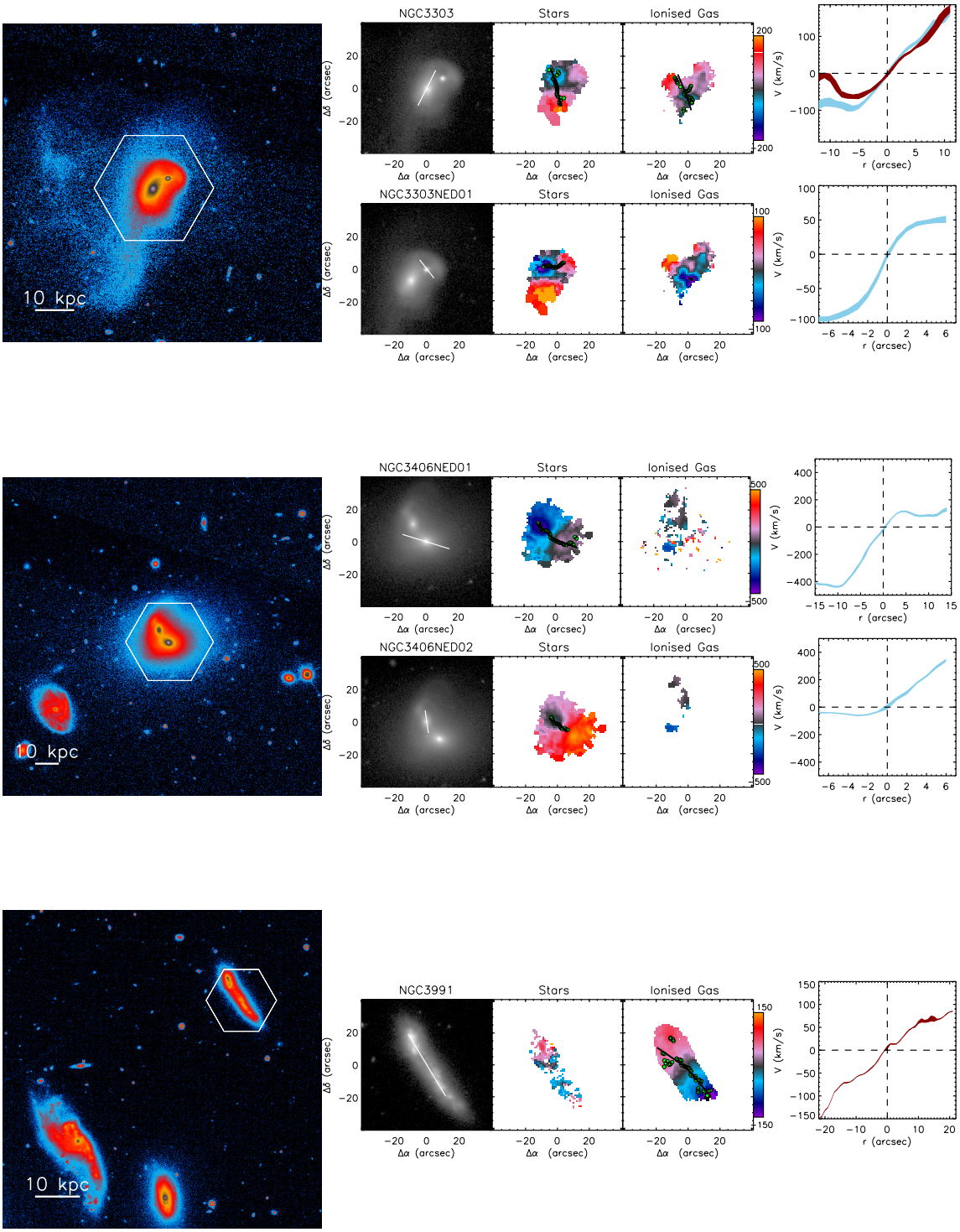


Figure A.8: Continuation Fig.A.8. Top: Pair NGC 3303 and NGC 3303NED01. Middle: NGC 3406NED01 and NGC 3406NED02 . Bottom: Companion NGC 3991.

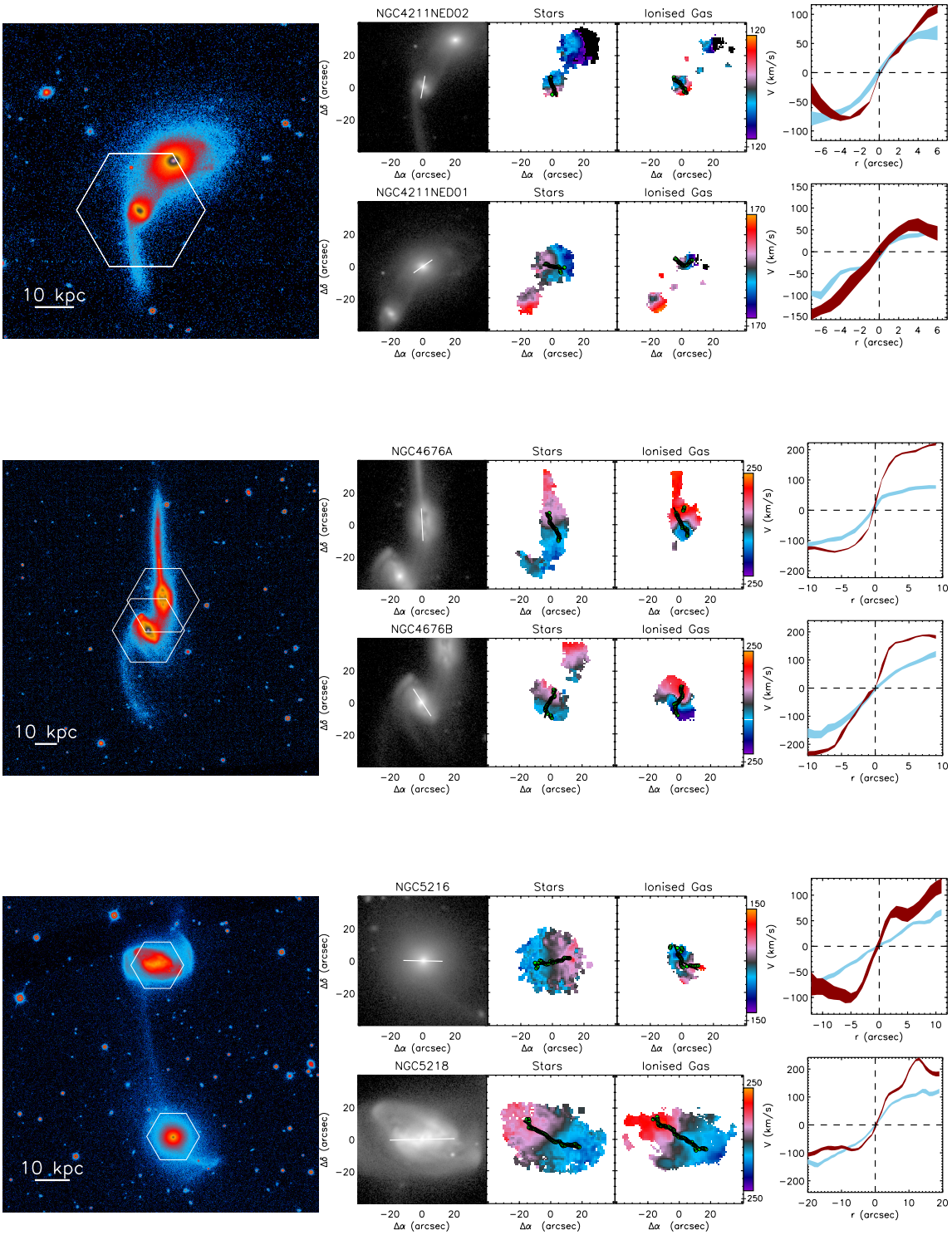


Figure A.8: Continuation Fig.A.8. Top: NGC 4211NED02 and NGC 4211NED01. Middle: NGC 4676A and NGC 4676B. Bottom: NGC 5216 and NGC 5218

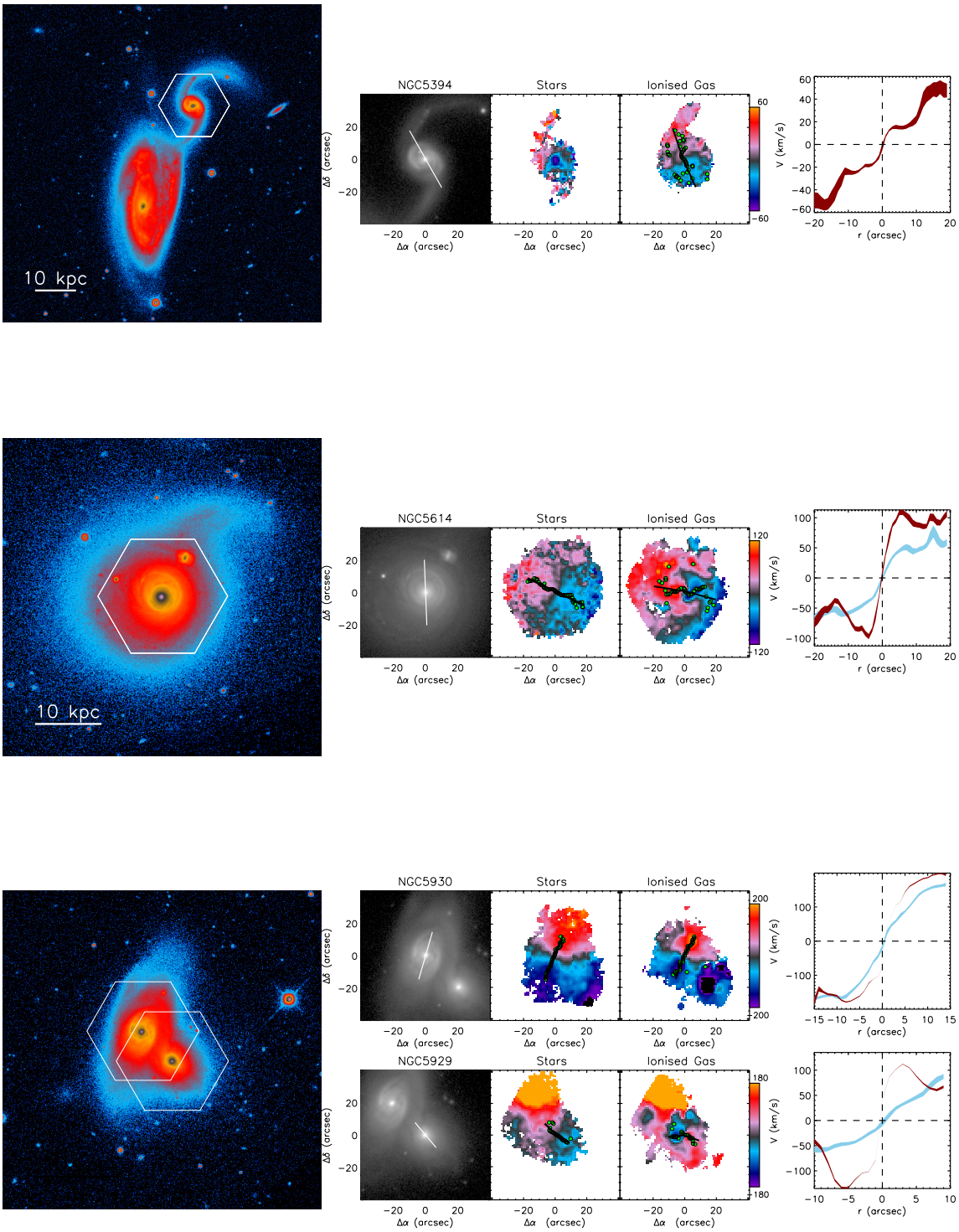


Figure A.8: Continuation Fig.A.8. Top: NGC 5394. Middle: NGC 5614. Bottom:NGC 5930 and NGC 5929

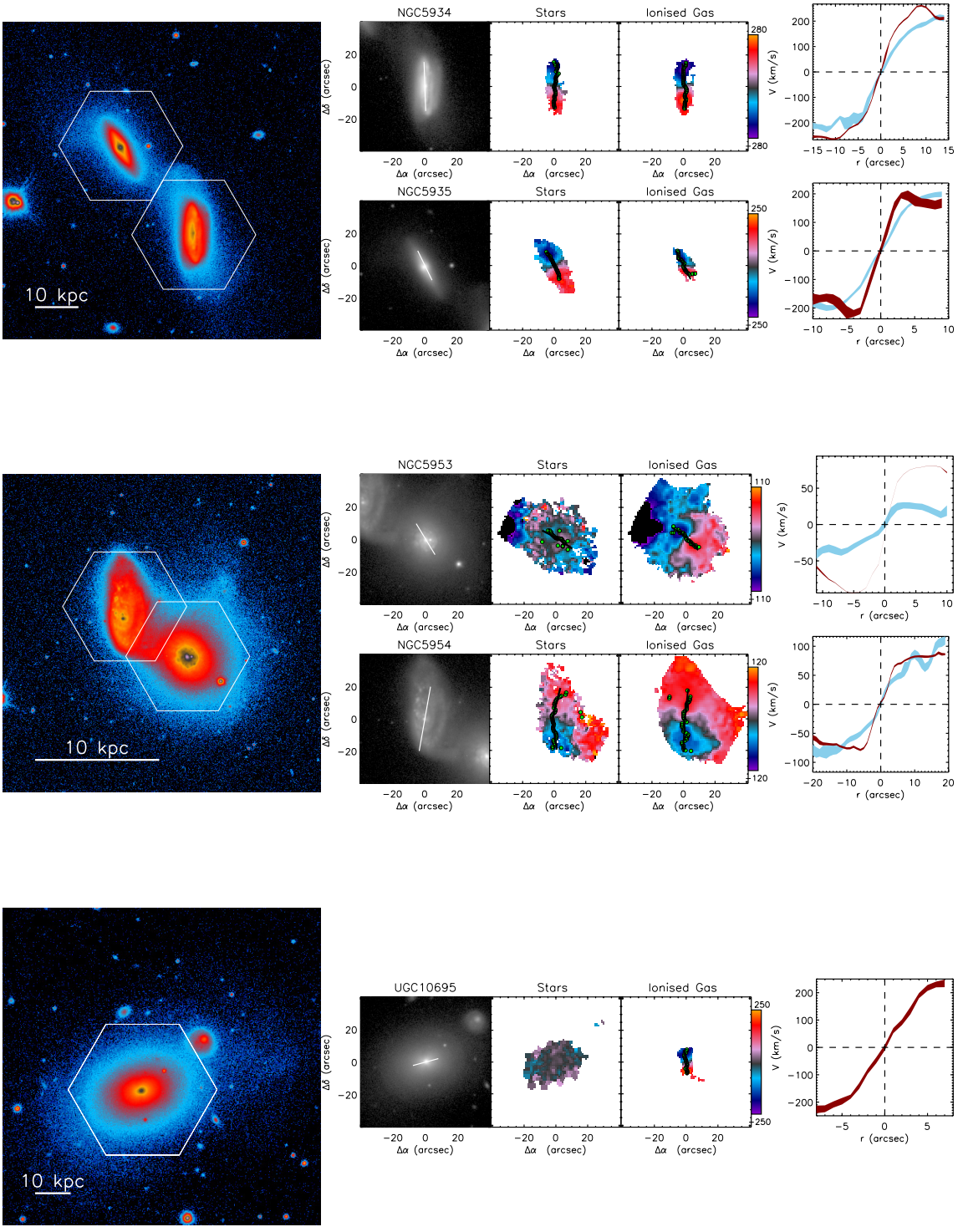


Figure A.8: Continuation Fig.A.8. Top: NGC 5934 and NGC 5935. Middle: NGC 5953 and NGC 5954. Bottom: UGC 10695.

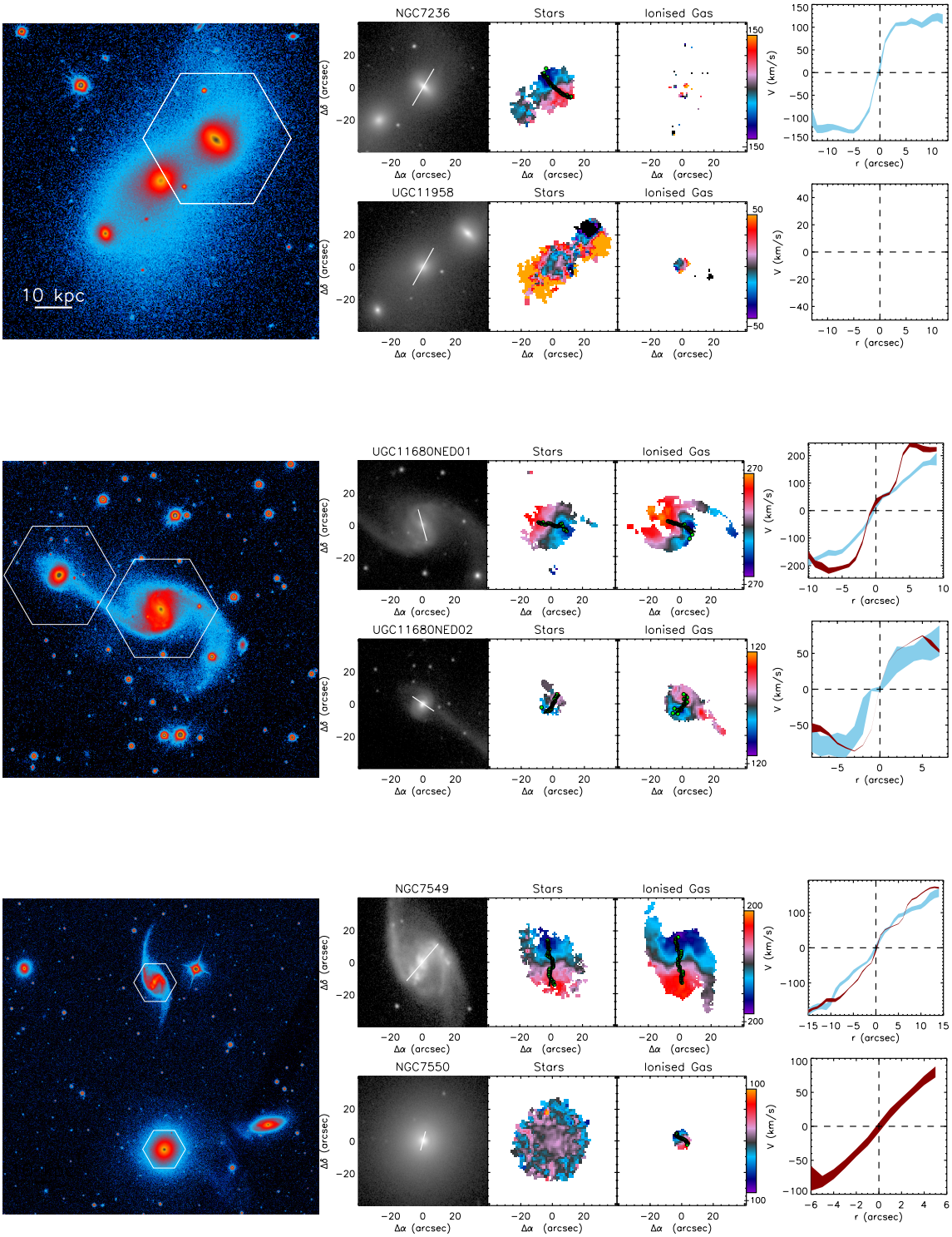


Figure A.8: Continuation Fig.A.8. Top: NGC 7236 and UGC 11958. Middle: UGC 11680 NED01 and NED02. Bottom: NGC 7549 and NGC 7550.

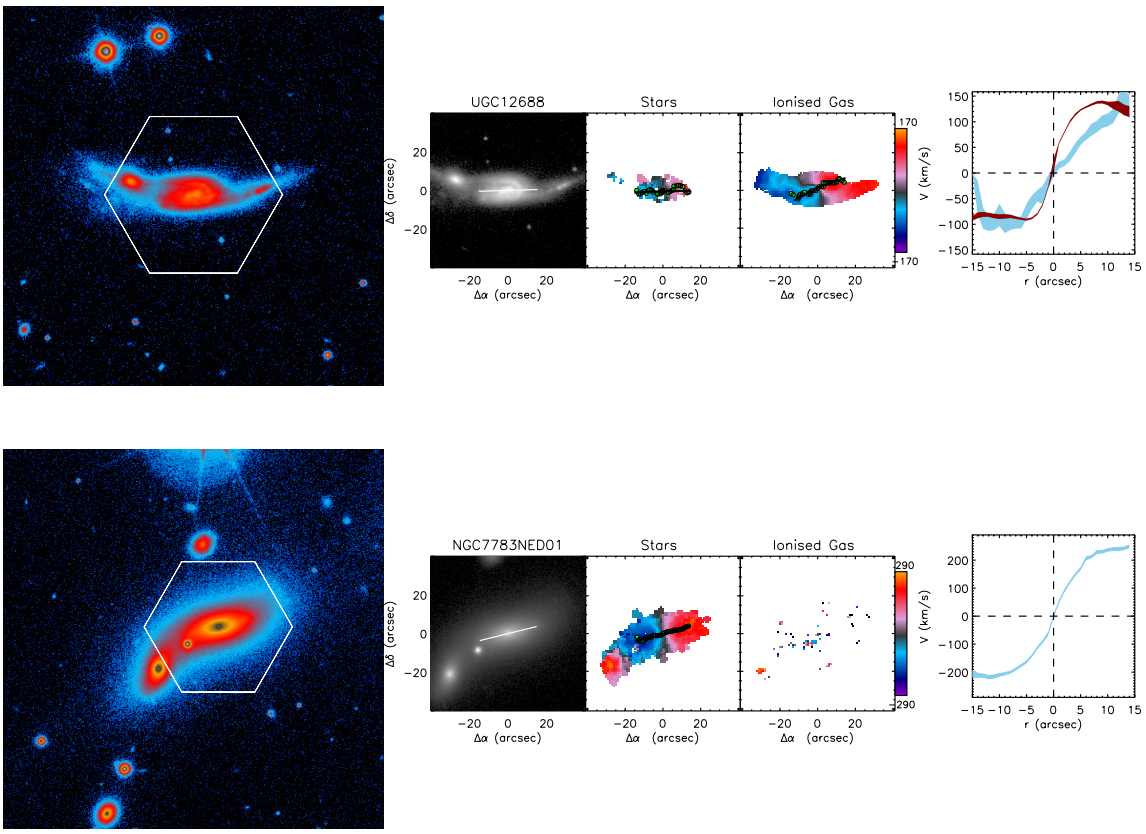


Figure A.8: Continuation Fig.A.8. Top: UGC 12688. Bottom: NGC 7783NED01

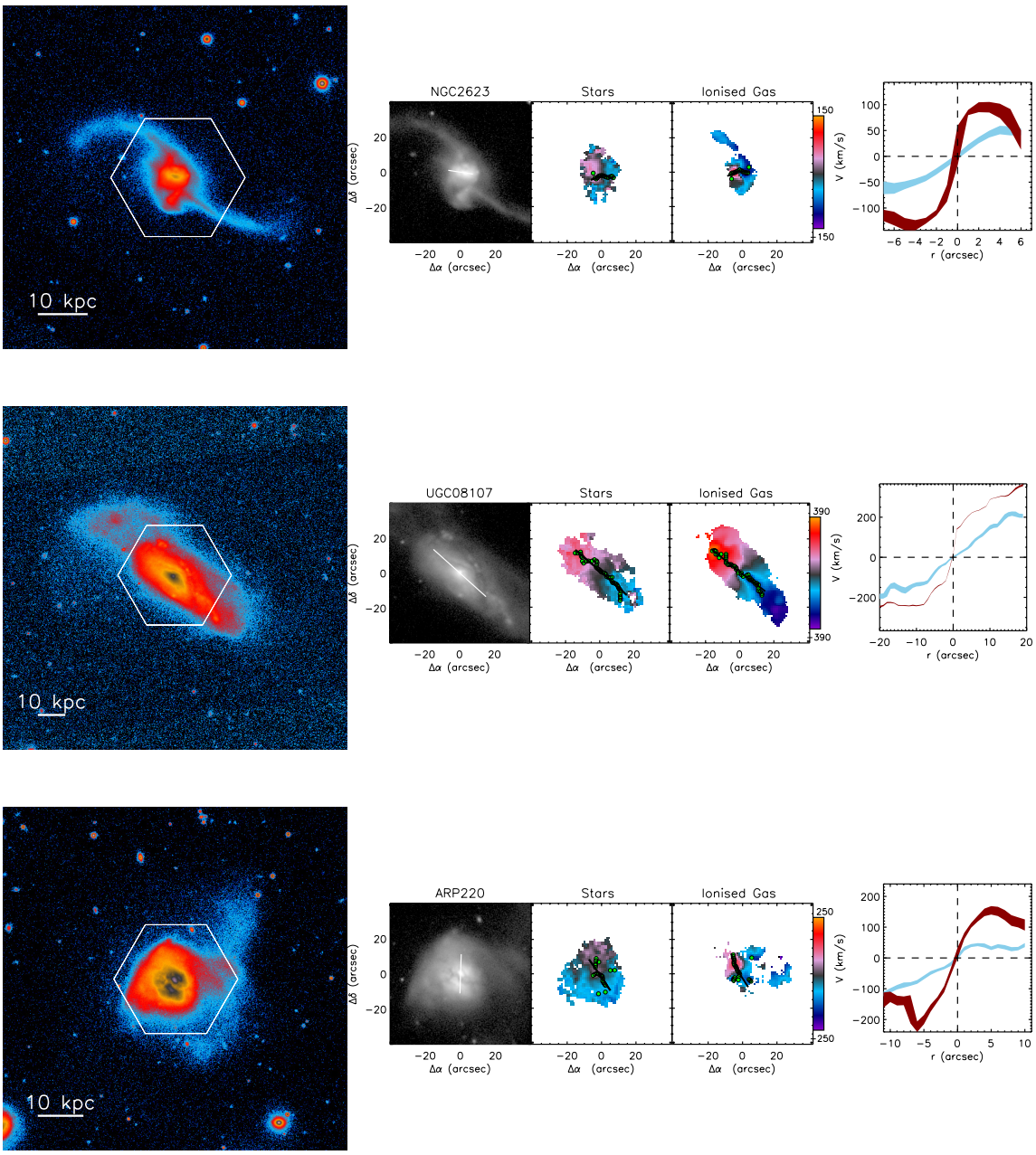


Figure A.9: Post-merger galaxies. Top: NGC 2623 . Middle: UGC 8107. Bottom: Arp 220.

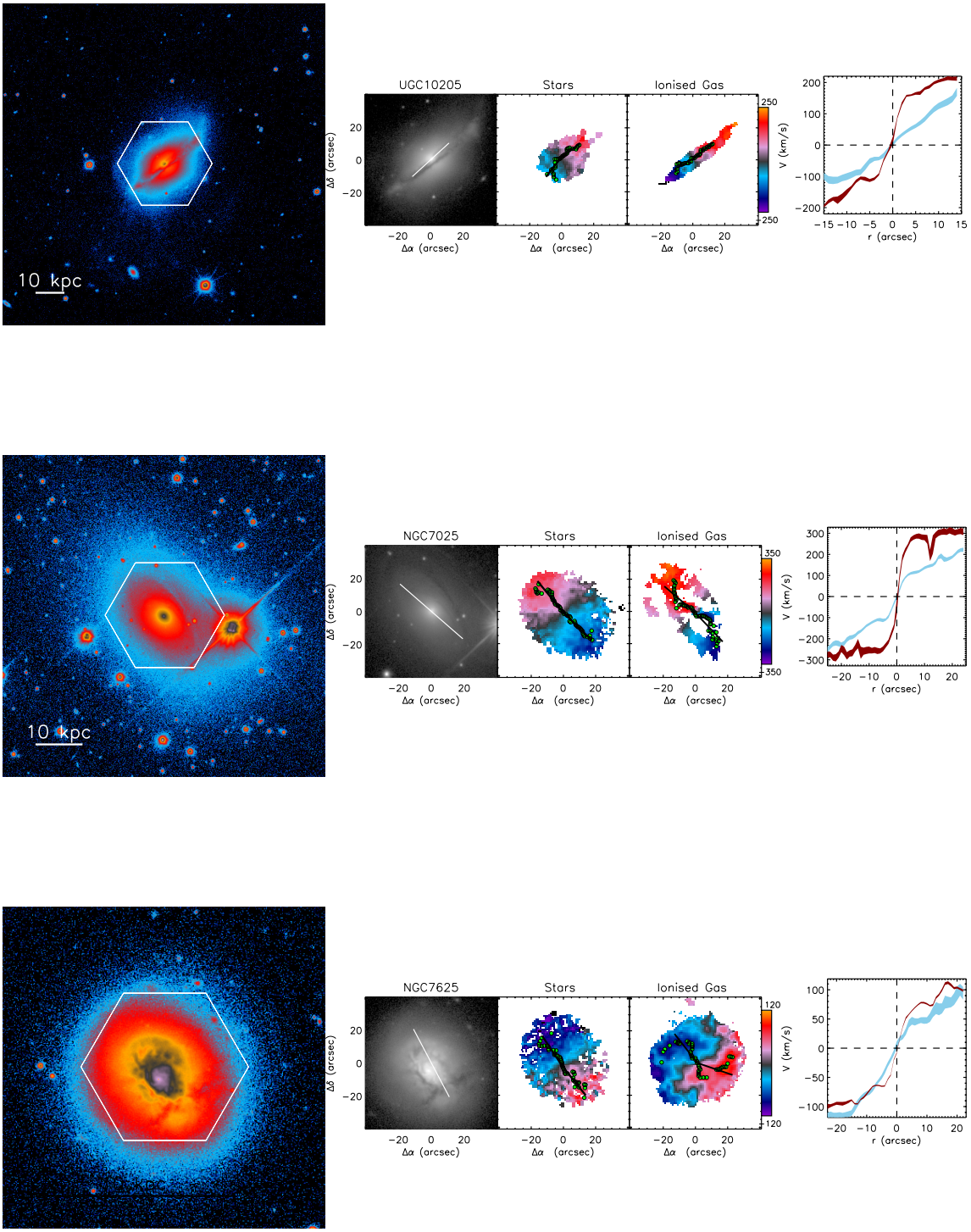


Figure A.9: Continuation Fig.A.9. Post-merger galaxies. Top: UGC 10205. Middle: NGC 7025. Bottom: NGC 7625.

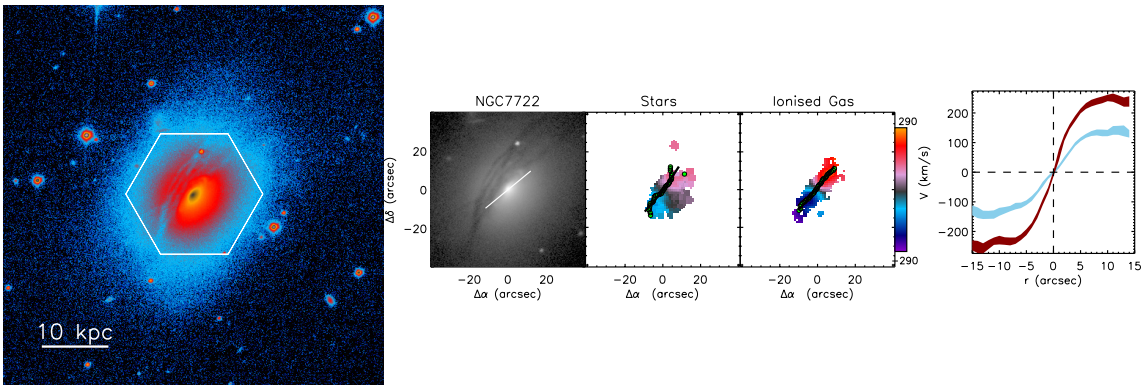


Figure A.9: Continuation Fig.A.9. Post-merger galaxies. NGC 7722.

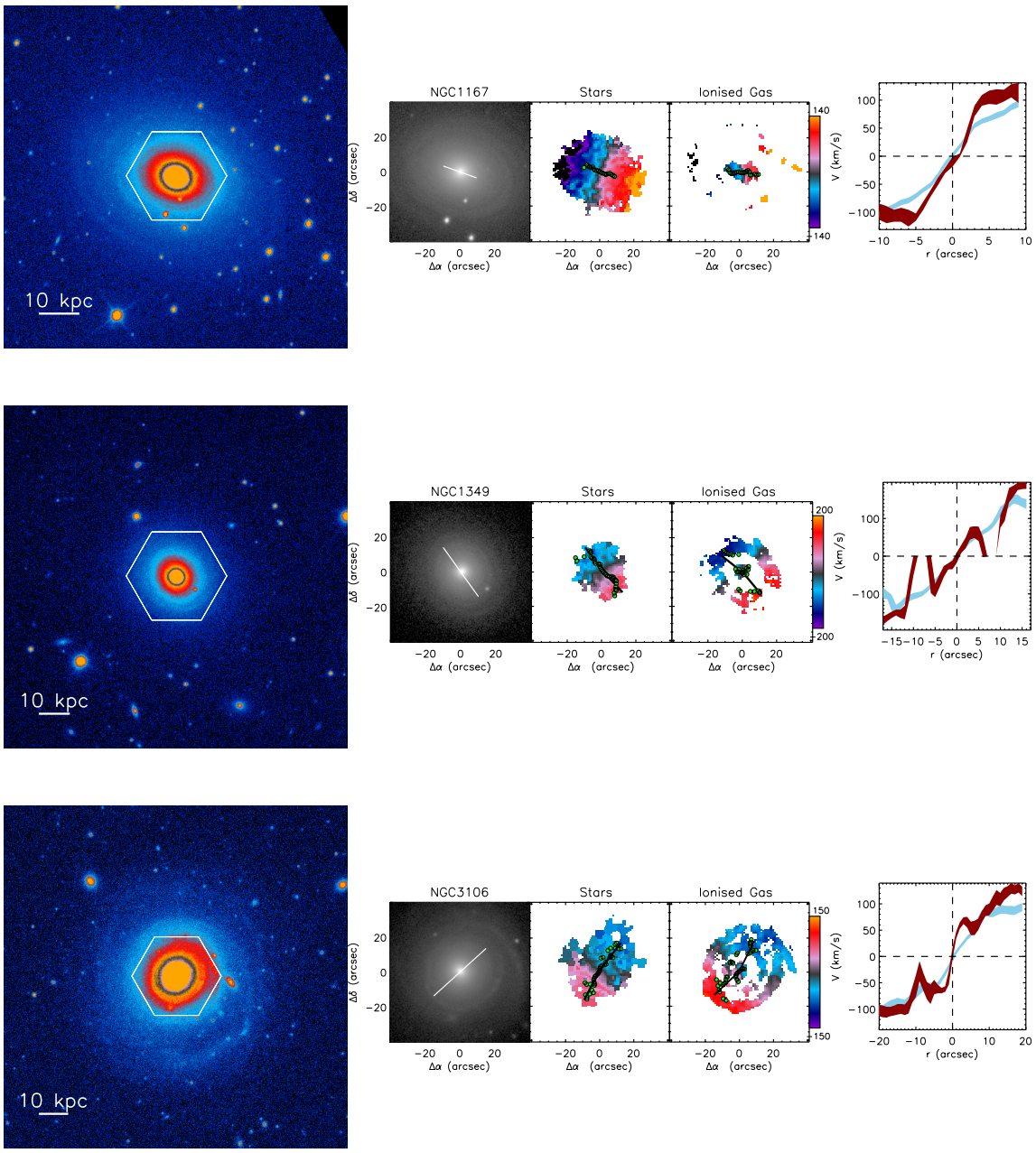


Figure A.10: Late merger remnants galaxies. Top: NGC 1167. Middle: NGC 1349. Bottom: NGC3106.

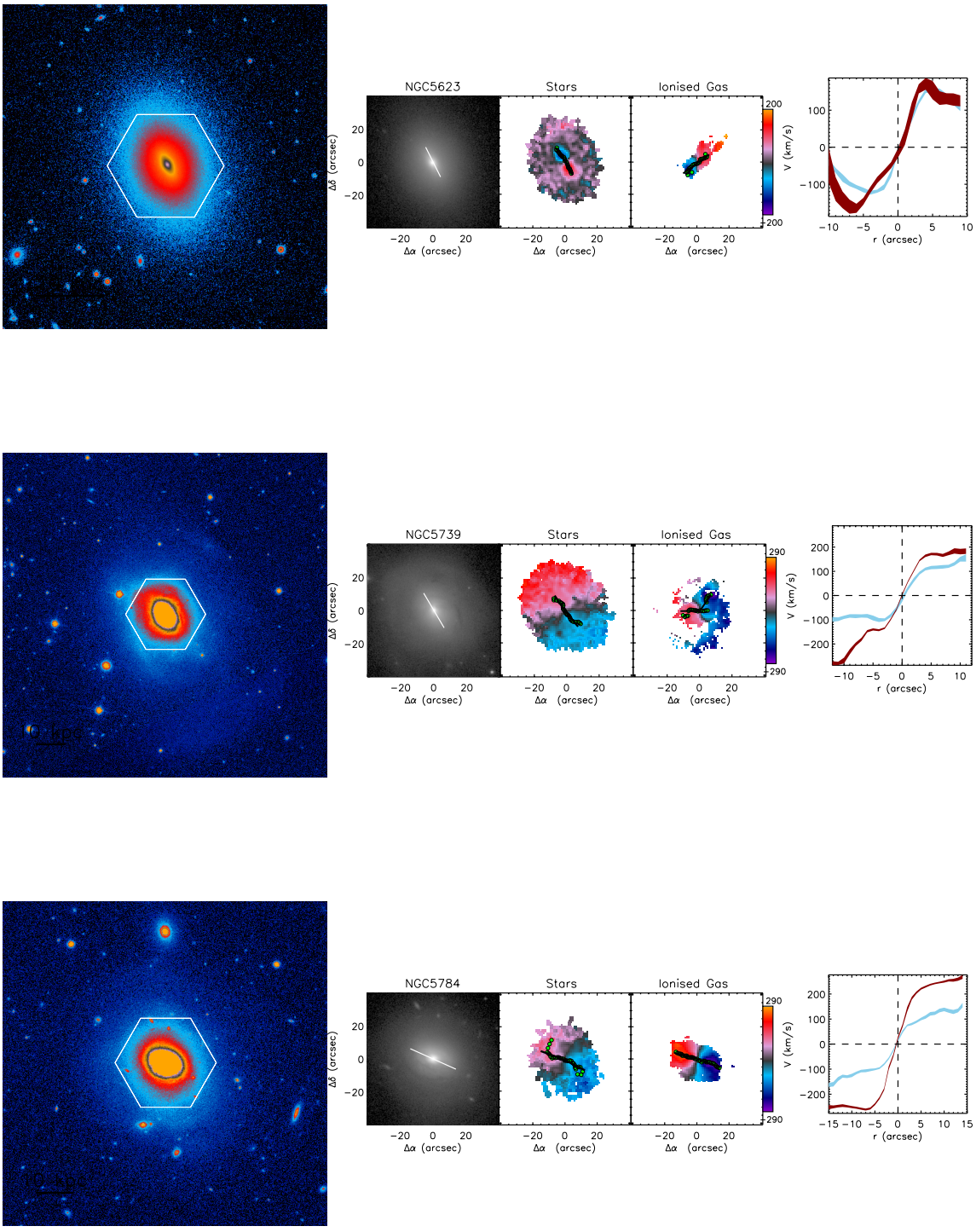


Figure A.10: Continuation Fig.A.10 Late merger remnants galaxies. Top: NGC 5623. Middle: NGC 5739. Bottom: NGC 5784.

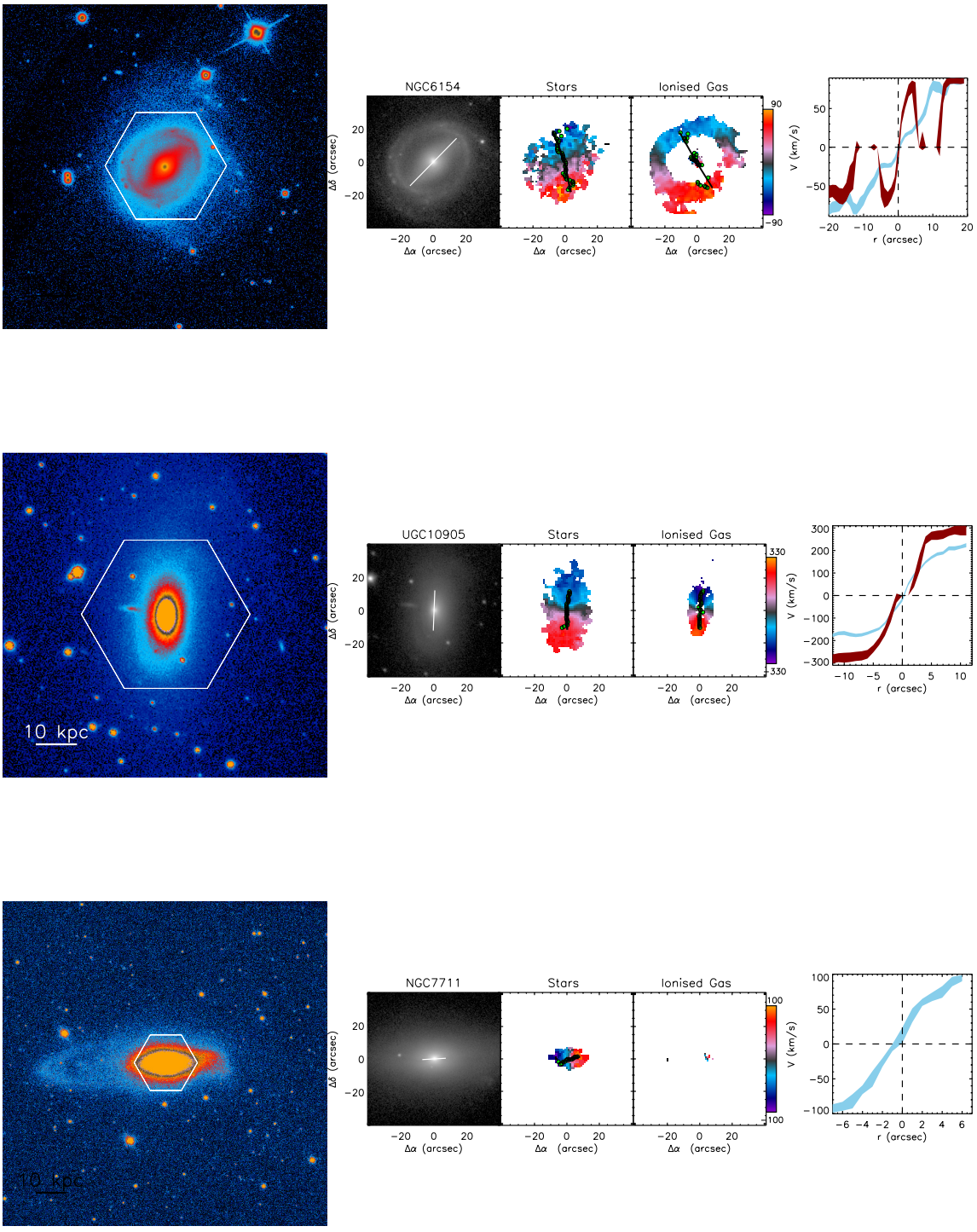


Figure A.10: Continuation Fig.A.10 Late merger remnants galaxies. Top: NGC 6154. Middle: UGC 10905. Bottom: NGC 7711.

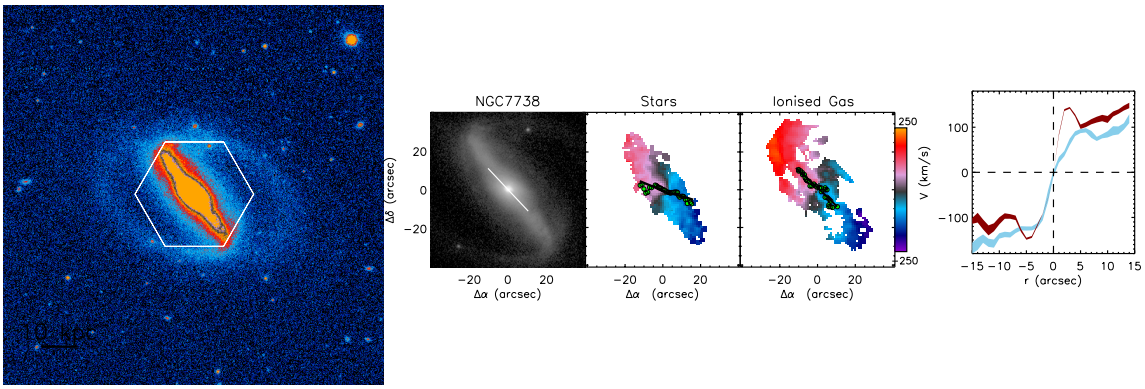


Figure A.10: Continuation Fig.A.10. NGC 7738.